ME

JOURNAL OF THE
AERO/SPACE SCIENCES

VOLUME 26 NOVEMBER, 1959 NUMBER 11

CONTENTS

Experiments on Porous-Wall Cooling and Flow Separation Control in a Supersonic Nozzle ..... LEON GREEN, JR., AND KENNETH L. NALL 689

An Experimental Study of Jet-Flap Compressor Blades ..... EDWARD L. CLARK, JR., AND DONALD EARL ORDWAY 698

The Equation of Energy Balance for Fluttering Systems With Some Applications in the Supersonic Regime ..... JOHN D. C. CRISP 703

Some Effects of Sound-Reduction Devices on a Turbulent Jet ... GILLES M. CORCOS 717

Hypersonic Viscous Flow Over Slender Cones ..... L. TALBOT, T. KOGA, AND P. M. SHERMAN 723

Heat Transfer in Separated Flows ..... HOWARD K. LARSON 731

An Actuator Disc Analysis of Inlet Distortion and Rotating Stall in Axial Flow Turbomachines ..... HSUAN YEH 739

Readers' Forum 754

Published by
INSTITUTE OF THE AERONAUTICAL SCIENCES, INC.

JOURNAL OF THE AERO/SPACE SCIENCES

Editor: W. R. SEARS

Director, Graduate School of Aeronautical Engineering, Cornell University

Associate Editor: ROBERT R. DEXTER *Managing Editor:* RITA J. TURINO

Editorial Assistant: CAROLINE TAYLOR

Editorial Committee

Aerodynamics and Fluid Mechanics

H. Julian Allen
Holt Ashley
Dean R. Chapman
Francis H. Clauser
Hugh L. Dryden
John C. Evvard
Antonio Ferri
Alexander Flax
Wallace D. Hayes
R. T. Jones
Carl Kaplan
H. W. Liepmann
C. C. Lin
H. F. Ludloff
Harold Luskin
Clark B. Millikan
Henry T. Nagamatsu
H. J. E. Reid
George S. Schairer
G. B. Schubauer
John Stack
Theodore Theodorsen
Arthur N. Tifford
Th. von Kármán

Flight Testing

R. R. Gilruth
Melvin N. Gough
W. L. Howland
W. F. Milliken, Jr.

Rotating Wing Aircraft

F. B. Gustafson
K. H. Hohenemser
Bartram Kelley
R. B. Maloy
Ralph McClarren
R. H. Miller
R. H. Prewitt
Igor I. Sikorsky

Structures

John E. Duberg
R. R. Heldenfels
N. J. Hoff
Samuel Levy
J. F. McBrearty
W. Ramberg
E. E. Sechler
F. R. Shanley
C. R. Strang
S. Timoshenko

Meteorology

C. F. Brooks
D. M. Little
F. W. Reichelderfer
K. C. Spengler

Vibration and Flutter

Lee Arnold
M. A. Biot
R. L. Bisplinghoff
Harold A. Cheilek
I. E. Garrick
Martin Goland

Aircraft Design

W. E. Beall
E. H. Heinemann
Hall L. Hibbard
Richard Hutton
C. L. Johnson
A. A. Kartveli
F. K. Teichmann

Electronics

K. C. Black
M. V. Kiebert, Jr.
David S. Little
Paul Rosenberg
Giles J. Strickroth

Physiologic Problems

H. G. Armstrong
Louis H. Bauer
Robert J. Benford
W. Randolph Lovelace, II
Ross A. MacFarland

Flight Propulsion

William Bollay
George W. Brady
R. P. Kroon
Frank E. Marble
Abe Silverstein
E. S. Taylor

Instruments

Alan G. Binnie
Charles H. Colvin
Frank R. Cook
C. S. Draper
S. G. Eskin
C. F. Savage
R. C. Sylvander

SUBSCRIPTION RATES

JOURNAL OF THE AERO/SPACE SCIENCES (formerly Journal of the Aeronautical Sciences), Published Monthly. United States and Possessions: 1 Year, $15.00; Single Copies, $1.50. Foreign Countries Including Canada (American Currency Rates): 1 Year, $16.00; Single Copies, $1.50.

AERO/SPACE ENGINEERING, Published Monthly. United States and Possessions: 1 Year, $5.00; Single Copies, $0.50. Foreign Countries Including Canada (American Currency Rates): 1 Year, $6.00; Single Copies, $0.50.

Notices of change of address should be sent to the Institute at least 30 days prior to actual change of address.

Manuscripts for publication, proofs, and all correspondence should be addressed to the Editorial Office of the JOURNAL.

Publication Office, 20th and Northampton Sts., Easton, Pa. Correspondence regarding subscriptions may be addressed to the Editorial Office of the JOURNAL OF THE AERO/SPACE SCIENCES, 2 East 64th Street, New York 21, N. Y.

© *Copyright, 1959, by the Institute of the Aeronautical Sciences, Inc.*

Second-Class Mail Privileges Authorized at Easton, Penna. Acceptance for mailing at a special rate of postage provided for in Section 1103, Act of October 3, 1917, authorized April 29, 1937.

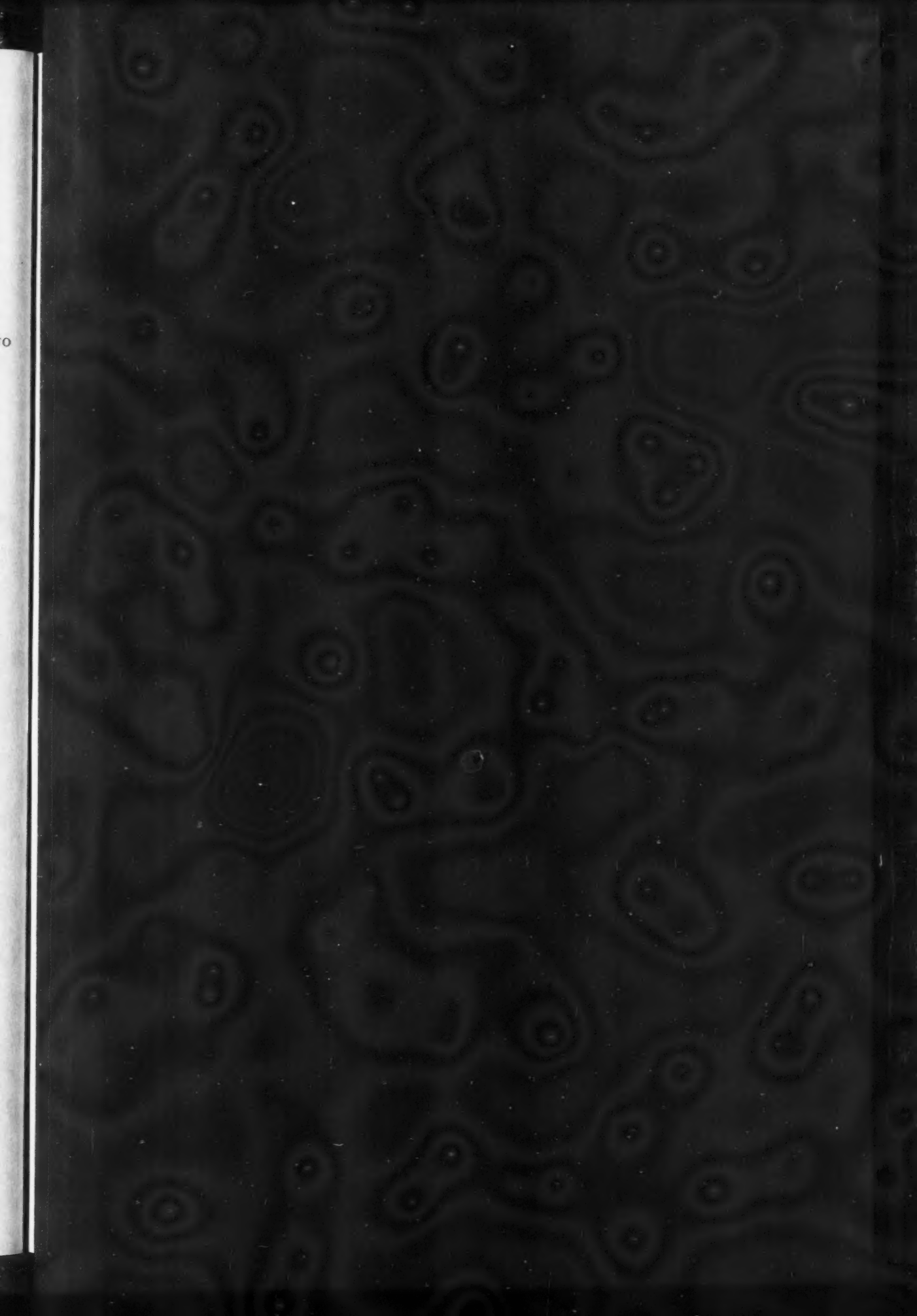

VOL

Fl

Contr
boundar
nozzle w
nitrogen
(ambien
Injection
the use o
diameter
forced b
addition
tion mea
boundar
approach
could be
velocity
mass ve
noticeab
asymmet
degrees a
wall heat
ture did
perature
tion, toge
sin analy
noninject
heat-tran
of the tra
tures der
porous m

A =
A^* =
a =
b =
c_f =

Present
Meeting,
25, 1959.
* Now,
Motor Co
** Assi
ects.

JOURNAL OF THE AERO/SPACE SCIENCES

VOLUME 26 NOVEMBER, 1959 NUMBER 11

Experiments on Porous-Wall Cooling and Flow Separation Control in a Supersonic Nozzle

LEON GREEN, JR.,* AND KENNETH L. NALL**

Aerojet-General Corporation

Summary

Control of flow separation by fluid injection at one diverging boundary of a two-dimensional, transparent-walled de Laval nozzle was investigated by spark schlieren photography of dry nitrogen flows expanded from two stagnation temperatures (ambient and 500°F.) and several stagnation pressure levels. Injection conditions at the permeable boundary were varied by the use of three grades of porous stainless steel with nominal pore diameters of 10, 20, and 30 microns, through which nitrogen was forced by coolant reservoir pressures of 25, 50, and 100 psig, in addition to the case of no forced injection. Pressure distribution measurements were made along the nonpermeable diverging boundary. It was found that flow separation at expansion ratios approaching the optimum value for maximum thrust coefficient could be induced at the porous wall by a local injection mass velocity of the order of a few per cent of the local main-stream mass velocity. Separation at the solid boundary was not noticeably influenced by injection at the opposite wall, and the asymmetrical separation thus effected jet deflections of up to 10 degrees at the lower stagnation-pressure levels. Variation of the wall heat-transfer condition by changing the stagnation temperature did not significantly influence separation behavior. Temperature measurements at the reservoir face of the porous section, together with use of published correlations and of the Rubesin analysis for estimation of stream-side Stanton Numbers under noninjection and injection conditions, respectively, permitted heat-transfer calculations which indicated that the effectiveness of the transpiration technique in controlling nozzle wall temperatures derives primarily from intimate fluid-solid contact in a porous material of high specific surface.

Symbols

A = area of channel cross section
A^* = throat area
a = speed of sound
b = channel width
c_f = friction coefficient
c_p = specific heat of coolant gas
Eu = Euler Number
h = heat-transfer coefficient
K = mixing-length constant
k = thermal conductivity
L = thickness of porous wall
M = molecular weight
M = Mach Number
m = exponent
$\dot{m}$ = mass flow rate of main stream
p = pressure
Pr = Prandtl Number
R = gas constant
r = temperature recovery factor
Re_s = length Reynolds Number
s = distance from throat, measured along wall
St = Stanton Number
T = temperature
u = stream velocity
v = normal injection velocity
x = distance from throat, measured axially
y = distance from manifold face of porous wall
α = viscous resistance coefficient of porous wall
β = inertial resistance coefficient of porous wall
μ = viscosity
ρ = density

Subscripts

0 = stagnation conditions
1 = main-stream conditions
c = coolant
i = stream-side surface
o = coolant-side surface
r = recovery
w = porous wall
$*$ = zero injection

Presented at the Aerodynamics—II Session, IAS 27th Annual Meeting, N.Y., Jan. 26–29, 1959. Revised and received February 25, 1959.

* Now, Senior Staff Member, Aeronutronic, a Division of Ford Motor Company.

** Assistant Senior Engineer, Applied Research, Rover Projects.

Introduction

IN THE DEVELOPMENT of long-duration rocket engines, the problem of nozzle cooling has been prominent. The available approaches for effecting controlled, steady-state wall temperatures may be categorized as convective cooling, in which heat transferred to the wall is removed by a coolant flowing through internal

passages; film cooling, in which coolant fluid streams injected at discrete locations coalesce to form a thin protective film adjacent to the wall; and porous-wall effusion cooling (also called "sweat" or "transpiration" cooling) in which a permeable wall material is employed and an effectively continuous fluid injection distribution is achieved. The cooling action of the effusion method, which is now generally agreed to be the most efficient in terms of degree of cooling effected by a given expenditure of coolant, derives from three factors: efficient transfer of heat from the wall to the infiltrating coolant is achieved because of intimate fluid-solid contact in a porous medium of high specific surface; if still in liquid phase on emerging from the wall, the fluid forms a cool insulating layer adjacent to the surface; the local ejection of mass into the boundary layer alters the velocity profile in a manner which decreases local heat (and momentum) transfer from the stream.

It is of historical interest to note that the first reported experiments with the effusion or transpiration technique concerned nozzle cooling—in 1940 Meyer-Hartwig[1] successfully employed porous copper nozzles subjected to stream temperatures of 4,500°F. Porous-wall cooling of rocket combustion chambers for aircraft had been suggested by Goddard[2] in 1938, and its application to nozzle cooling was independently proposed by Skoglund[3] in 1942. A brief series of *ad hoc* experiments was conducted by Jakob and Fieldhouse in 1943, using a small disc of porous brass subjected to a parallel flow of hot air, but the results were not reported until 1949.[4] The first comprehensive investigation of porous-wall cooling was independently initiated in 1944 by Duwez and his associates[5, 6] at the California Institute of Technology. In 1946, Moore and Grootenhuis[7] proposed the technique for cooling gas-turbine blades. Since that time the effusion technique has become the subject of a voluminous and rapidly growing literature. It has been considered for application to flight structures (both for cooling of hypersonic vehicles and for heating to prevent ice formation on leading edges) and to the unit operations of chemical engineering. The field has been reviewed by Grootenhuis and Moore[8] for the period up to 1950, to 1952 by Eckert[9] and Broadwell and Sherman,[10] to 1955 by Berger,[11] through 1957 by Eckert, *et al.*,[12, 13] and into 1958 by the present authors.[14] Experimental studies published as of this writing have employed bounded channel flows and unbounded flows along plates, cones, and blades. Analytical studies, which, with a few notable exceptions, generally deal with the more tractable case of laminar flow, have considered the above-mentioned situations, plus others, including constant-area channel flows with nonzero Euler Number, flows around blunt bodies, and flows with chemical reaction. No recent study of the nozzle problem appears to have been reported in the open literature.

Although continued investigation of nozzle cooling by porous-wall effusion was thus desired, the principal objective of the present study was to determine the feasibility of achieving controlled nozzle flow separation. Boundary-layer control by distributed surface suction had long been recognized as an effective means of delaying or preventing flow separation from an airfoil, and it was desired to evaluate the effectiveness of the inverse technique of surface injection in promoting jet detachment from the walls of an exhaust nozzle. Interest in the nozzle flow separation problem is due to the loss in nozzle thrust coefficient resulting from overexpansion of the flow to pressures below that of the surrounding atmosphere, an overexpansion which subjects single-stage rocket-propelled vehicles with nozzles designed for efficient high-altitude operation to a substantial performance penalty during take-off and low-altitude operation.

The nozzle flow separation phenomenon has been the subject of several experimental and analytical investigations, which have been reviewed by the present authors.[15] The experiments may be classified in two groups: those employing the hot combusion products from rocket motors and those using air or nitrogen expanded from ambient stagnation temperature to low static temperatures in the exit section. It was found that the results of nozzle pressure-distribution measurements from the various "hot flow" experiments could be unified by an empirical correlation in terms of chamber pressure, atmospheric pressure, and pressure at the point of separation, independent of the gas properties and nozzle divergence angle.[16, 15] The "cold-flow" studies, however, yielded results which conflicted concerning the divergence-angle effect and at best deviated slightly from the above-mentioned correlation. It was thought that this difference in behavior might be attributed to the different heat-transfer condition at the nozzle wall prevailing in the two types of tests—i.e., the stabilizing influence of a large heat flux from the stream to the wall might mask other effects. In view of the above situation, it was desired to study nozzle flow separation behavior under controlled stagnation conditions, and, particularly, to investigate the effectiveness of boundary-layer injection in promoting incipient separation.

Design of Experiment

For this purpose, a two-dimensional, transparent-walled, de Laval nozzle similar to that of McKenney[17] was designed. Transparent walls of glass and later fused quartz were used. To promote smooth flow conditions at the throat, a converging nozzle entrance section was used to provide a continuous transition from the circular plenum cross section to the rectangular nozzle cross section. The entrance section was designed to be water-cooled if necessary, but this feature was not needed during the program described here. The nozzle flow-channel width was 0.5 in., the throat height, 0.2 in., the divergence half-angle 15°, and the exit expansion ratio 10. The nozzle-exit blocks were fabricated from stainless steel and were positioned by dowel pins. One block was tapped for static-pressure

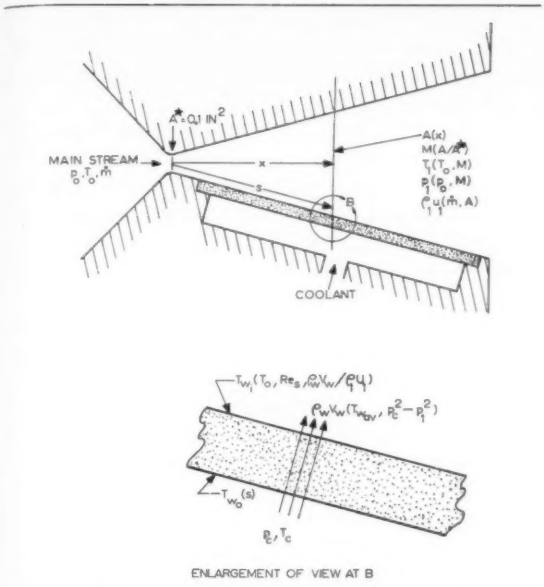

FIG. 1. Schematic diagram of two-dimensional nozzle with porous-wall injection (porous section actually was located in upper block).

measurements along the diverging exit section. The other was provided with a section of porous stainless steel through which cold nitrogen could be injected from a manifold, as indicated schematically in Fig. 1. The assembled nozzle section is shown in Fig. 2.

Previous investigations indicated that the measurement of the stream-side temperature of a porous wall was a source of difficulty, because the installation of thermocouple stations at this surface involved some perturbation of the permeability and coolant-flow distribution, and hence of the local heat-flow pattern. Because it was desired to use three easily exchangeable injection blocks employing porous sections of different permeability (each with five thermocouple stations) and because any perturbation of the coolant injection pattern was undesirable in that it might influence local separation behavior in a complicated manner, it was decided to measure the temperature of the manifold side of the porous-wall section and calculate the stream-side temperature. The injection nozzle blocks were, therefore, provided with ports through which spring-loaded, iron-constantan thermocouples could press firmly against the coolant-side porous surface. This method of porous-surface temperature measurement had previously been demonstrated by Grootenhuis, Mackworth, and Saunders.[18]

Three porous-walled nozzle blocks were fabricated, employing 0.12-in. thick permeable sections of Micro-Metallic Type 316 porous stainless steel media with the properties tabulated in Table 1. The viscous and inertial-resistance coefficients, α and β, which characterize the flow resistance of porous media over an extended range of Reynolds Numbers according to the relation[19]

$$\Delta(p^2)/L = \alpha(2RT/M)\mu\rho_w v_w + \beta(2RT/M)(\rho_w v_w)^2 \quad (1)$$

TABLE 1

Nominal pore dia. (microns)	Surface roughness (RMS microin.)	Viscous resistance coefficient, (in.$^{-2}$)	Inertial resistance coefficient, (in.$^{-1}$)
10	160	7.41×10^8	2.25×10^5
20	165	2.48	1.08
30	210	0.42	0.51

were determined from isothermal-flow calibrations of the individual sections, as shown in Fig. 3.

Both the primary working fluid and the secondary injected fluid used in the present experiments were dry nitrogen gas from a liquid nitrogen supply. The flow rates and pressure levels were controlled by a system of Grove regulators and Fischer-Porter Flowrators capable of metering flows up to 1.0 lbm./sec. The nozzle-entrance stagnation temperature was controlled by varying the power input to the heat-transfer section, in which the gas flowed radially inward through a D.C. resistance-heated, porous graphite cylinder, as shown schematically in Fig. 4. The flow and temperature control systems, together with the manometer bank used to display the pressure distribution in the nozzle, the spark schlieren apparatus used to visualize the nozzle flow field, and the associated photographic and recording equipment, are described in detail elsewhere.[15, 20]

Experimental Conditions

Systematic flow-separation experiments were performed at two main-stream stagnation temperatures, ambient (about 40°F.) and 500°F. A few tests were completed using a stagnation temperature of 990°F., but fissure of one of the quartz walls (initiated during the 500°F. runs) under combined thermal and mechanical stresses prevented completion of a systematic series at this level. Nominal stagnation pressures of 250, 300, 350, and 400 psig were employed in the 500°F. tests, but flow system capacity limited the pressure

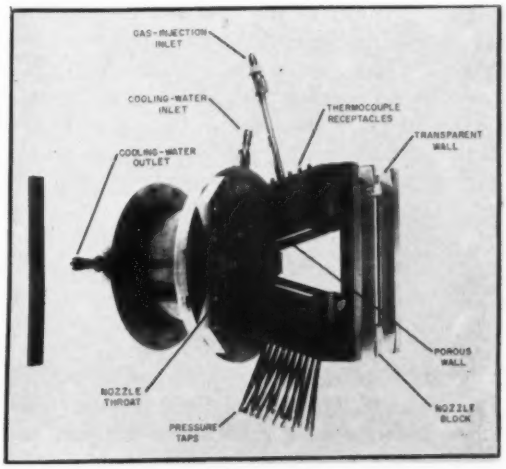

FIG. 2. View of assembled nozzle.

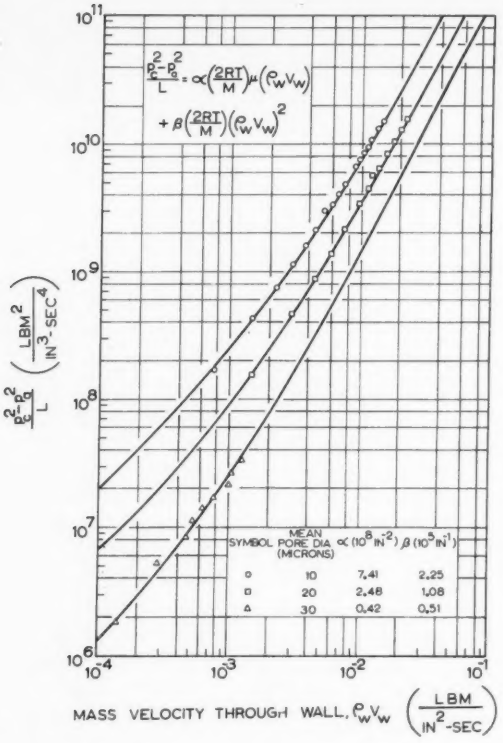
$\frac{P_c^2-P_0^2}{L}=\alpha\left(\frac{2RT}{M}\right)\mu\left(\rho_w V_w\right)+\beta\left(\frac{2RT}{M}\right)\left(\rho_w V_w\right)^2$
$\frac{P_c^2-P_0^2}{L}\left(\frac{LBM^2}{IN^3\text{-}SEC^4}\right)$
MEAN
SYMBOL PORE DIA (MICRONS) $\alpha\,(10^8\ IN^{-2})$ $\beta\,(10^5\ IN^{-1})$
○ 10 7.41 2.25
□ 20 2.48 1.08
△ 30 0.42 0.51
MASS VELOCITY THROUGH WALL, $\rho_w V_w$ $\left(\frac{LBM}{IN^2\text{-}SEC}\right)$

FIG. 3. Flow resistance characteristics of porous wall media.

levels in the ambient-temperature tests to the range 200, 250, and 300 psig. Four injection conditions were employed, with coolant at ambient temperature forced by manifold pressures of 25, 50, and 100 psig in addition to the case of no forced injection (manifold sealed). Coolant-side porous-wall temperatures were measured only in the tests with heated main-stream flows.

The pressure and velocity conditions prevailing in the nozzle are indicated by the profiles presented in Fig. 5, which were computed from the known area-ratio variation by standard one-dimensional gas-dynamic methods assuming isentropic flow and neglecting the small mass addition through the porous wall section. The Euler Number of the flow was calculated from the pressure and velocity profiles of Fig. 6 and is shown in Fig. 7. The apparent discrepancy between the results from differentiation of the pressure profile and those from the slope $m = Eu$ of the velocity profile on logarithmic coordinates is attributed to the fact that m is the average slope of a flat but slightly inflected curve. The length Reynolds Number distribution for the various stagnation conditions employed is shown in Fig. 7.

Experimental Results

Schlieren Observations

The nozzle flow fields observed by spark schlieren photography for flows expanded from ambient stagnation temperature are typified by the examples shown in Fig. 8 for the particular case of the medium-grained (20 micron nominal pore dia.) wall section and a nominal stagnation pressure of 300 psig. Fig. 9 presents similar photographs of flows expanded from stagnation conditions of 500°F. and 350 psig. In each figure, the nozzle locations corresponding to the throat, the point of optimum expansion to one atmosphere pressure, the point of jet detachment from the porous wall, and the detachment point on the nonporous wall predicted by the empirical correlation of separation-pressure data[16] are indicated. The separation point predictions appear to be more accurate in the case of the heated flows than for the unheated flows. It may be noted that even in the case of no forced injection some asymmetry of the separation pattern is evident. This behavior is attributable to the strong streamwise pressure gradient in the flow. Hence, gas forced outward through the porous wall in a region near the nozzle throat re-emerges downstream in a region of lower static pressure, thus producing some injection effect.

The results shown in Figs. 8 and 9 indicate that as the injection velocity is increased, the point of jet detachment from the porous wall approaches the optimum separation point—i.e., that where the local static pressure equals 1 atm. Within the range of conditions studied, the effectiveness of injection was not noticeably influenced by the stagnation temperature. It should also be noted that the rate of fluid injection required to promote early separation is not great; the injection ratios at the point of jet detachment varied over a range from about 0.5 per cent to about 3 per cent in the 88 different combinations of stagnation conditions, injection pressure, and wall material employed in the investigation.[14, 15] As indicated in Fig. 10, integration of the injection velocity distribution—calculated from the nozzle pressure distribution by Eq. (1)—from the leading edge of porous insert (s = 0.38 in.) up to the point of separation (s_{sep}) revealed that the total coolant expenditure amounted to only a few per cent of the main-stream flow rate, and no effort had been made to minimize this fraction.

TABLE 2
Experimental Conditions Under Which Typical Nozzle Flow Fields Shown in Figs. 8 and 9 Were Obtained
(Porous wall media: 20-micron nominal pore diameter; atmospheric pressure 14.4 psia)

	Fig. 8	Fig. 9
stagnation temperature (°F.)	48	500
stagnation pressure (psig)	300	350
main stream flow rate (lbm./sec.)	0.68	0.59
coolant temperature (°F.)	43	44
coolant manifold pressure (psig)		
A	*	*
B	25	25
C	50	50
D	100	100
local injection ratio ($\rho_w v_w/\rho_1 u_1$) at point of separation from porous wall (per cent)		
A	*	*
B	0.51	0.68
C	0.83	1.01
D	1.21	1.58

* Coolant manifold sealed.

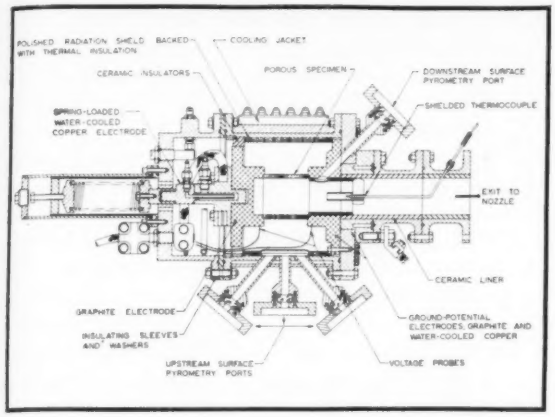

FIG. 4. Schematic diagram of heat-transfer section.

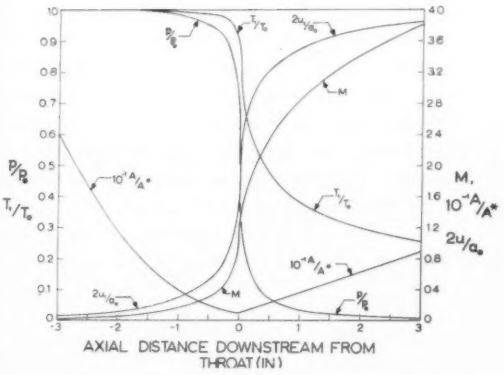

FIG. 5. Distribution of gas-dynamic parameters in nozzle (neglecting mass addition).

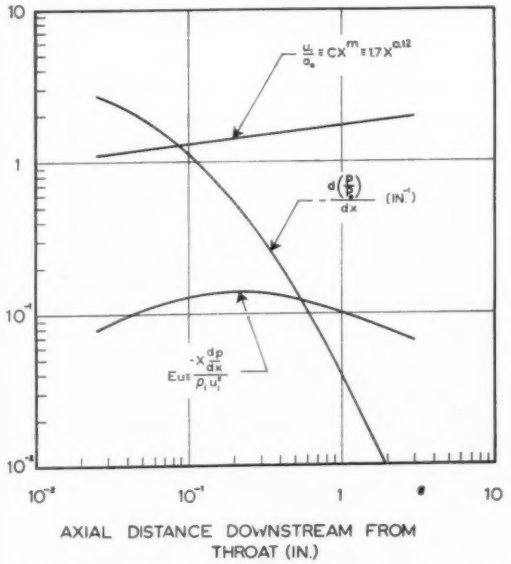

FIG. 6. Distribution of pressure gradient, velocity gradient, and Euler Number in expansion section.

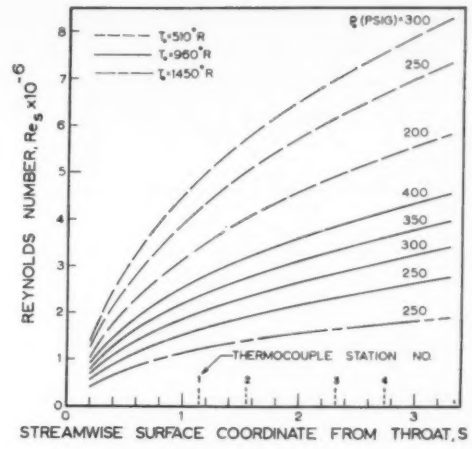

FIG. 7. Reynolds Number distribution in nozzle exit section for various stagnation conditions.

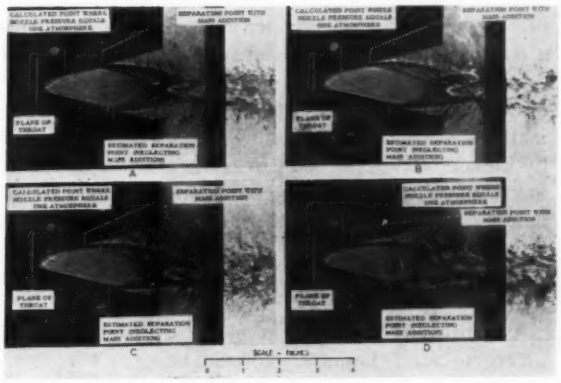

FIG. 8. Schlieren photographs of typical nozzle flows expanded from ambient temperature.

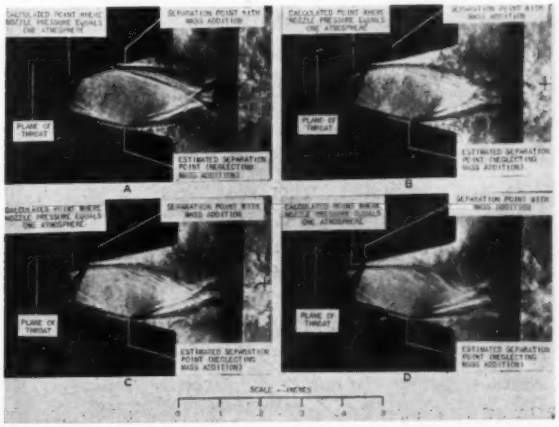

FIG. 9. Schlieren photographs of typical nozzle flows expanded from 500°F.

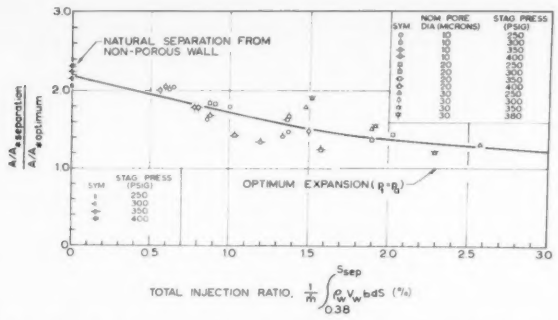
NATURAL SEPARATION FROM NON-POROUS WALL
OPTIMUM EXPANSION ($P_t = P_0$)
NOM. PORE DIA (MICRONS)
STAG. PRESS (PSIG)
A/A separation / A/A optimum
TOTAL INJECTION RATIO, $\frac{1}{\dot{m}}\int_{0.38}^{S_{sep}} \rho_w V_w b\,dS$ (%)

FIG. 10. Nozzle expansion ratios at separation vs. total injection ratio.

From the above semiquantitative studies, it is concluded that the porous-wall injection technique holds promise as a method of achieving controlled flow separation in supersonic exhaust nozzles. Also noteworthy is the angle of jet deflection effected by the asymmetrical separation pattern. Deflections up to 10 degrees were observed in tests at the lower stagnation pressure levels. It appears possible that the use of locally-variable boundary injection from segmented manifolds with pressures regulated by a valve system might constitute a means of thrust vector control under altitude conditions permitting flow overexpansion. Such an arrangement would enjoy advantages over the conventional methods of control by chamber or nozzle gimballing or by the use of vanes or jetevators[21] in that the actuating forces and inertia of moving parts would be low, and no moving parts would be subjected to heating and erosion by the stream.

Static Pressure Measurements

The pressure distribution along the nonpermeable diverging nozzle boundary corresponding to the photographs of Fig. 9 are shown in Fig. 11, which also indicates the location of the optically-observed points of natural separation from the nonporous walls (as well as those of forced separation from the porous wall) for comparison with the estimated separation point. The results, which are typical of those observed under other conditions, indicate that the estimated separation station agress well with the points of minimum pressure, whereas the flow actually detaches from the wall slightly further downstream in a region of adverse pressure gradient.

Heat-Transfer Calculations

It was mentioned earlier that measurements of the temperature of the coolant manifold side of the porous wall were substituted for more difficult measurements of the stream-side temperature. The situation involved in calculation of the stream-side temperature was shown schematically in Fig. 1. The quantities which are known or measured directly are the porous-wall permeability characteristics; the nozzle geometry, A^* and $A(x)/A^*$; the stream mass flow rate, ˙ ; the stagna ion pressure and temperature, p_0 and T_0; the coolant pressure and temperature, p_c and T_c; and individual values of the manifold-side porous-wall temperature, T_{w_0}, at five stations. The quantities which may then be directly calculated are the distributions of mass velocity, Mach Number, static pressure, and static temperature in the main stream, and, hence, length Reynolds Number Re_s based on fluid properties evaluated at main-stream conditions. In addition, the distribution of coolant injection mass velocity through the wall may be calculated from a knowledge of the distribution of pressure-square difference $p_c^2 - p_1^2$ across it because the temperature difference across the wall is small, and (in so far as fluid properties entering the injection-rate calculation is concerned) no significant error is introduced by considering it to be isothermal at known temperature T_{w_0}.

However, the stream-side wall temperature T_{w_i} cannot be precisely calculated without knowledge of the temperature recovery factor, r, and the heat-transfer coefficient, h. Thus, there is required a solution of the heat-conduction problem in the wall simultaneous with an evaluation of the effect of injection upon r and h. In view of the relatively fine texture and high specific surface of even the coarsest porous-wall medium, it may be safely assumed that the difference in temperature between the porous solid and the gas permeating it is negligible compared to the total temperature levels involved. The heat conduction in the wall (assumed to take place only in the high-conductivity solid phase) thus is governed by the boundary-value problem

$$k_w(d^2T_w/dy^2) - \rho_w v_w c_p(dT_w/dy) = 0 \qquad (2)$$

$$T_w(0) = T_{w_0} \qquad (3a)$$

$$k_w \left.\frac{dT_w}{dy}\right|_L = h(T_r - T_{w_i}) \qquad (3b)$$

Using average values for the thermal properties k_w and c_p in the wall, the solution to this problem is

$$(T_{w_i} - T_{w_0})/(T_r - T_{w_i}) = (h/\rho_w v_w c_p)[1 - e^{-(\rho_w v_w c_p L/k_w)}] \qquad (4)$$

Of the various analyses of transpiration cooling which have been reported, that of Rubesin[22] was selected for evaluation of the effect of injection upon h and r, owing

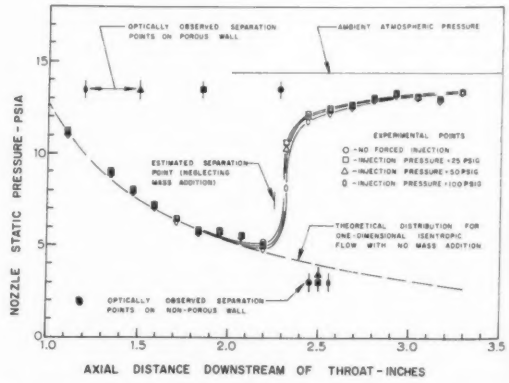
OPTICALLY OBSERVED SEPARATION POINTS ON POROUS WALL
AMBIENT ATMOSPHERIC PRESSURE
EXPERIMENTAL POINTS
ESTIMATED SEPARATION POINT (NEGLECTING MASS ADDITION)
THEORETICAL DISTRIBUTION FOR ONE-DIMENSIONAL ISENTROPIC FLOW WITH NO MASS ADDITION
OPTICALLY OBSERVED SEPARATION POINTS ON NON-POROUS WALL
NOZZLE STATIC PRESSURE - PSIA
AXIAL DISTANCE DOWNSTREAM OF THROAT - INCHES

FIG. 11. Pressure distribution in nozzle exit section corresponding to flow fields shown in Fig. 9.

to its success in correlation of experimental data on heat and momentum transfer in turbulent, compressible boundary layers in supersonic as well as subsonic flows with injection and with positive Euler Numbers. In view of the large Reynolds Numbers involved (10^6 to 10^7), the roughness of the porous walls, the destabilizing effect of injection, and the results of conventional nozzle heat-transfer experiments by Saunders and Calder[23] and Pefley,[24] the conclusion that the boundary layer on the porous section would be turbulent appeared safe. Although Rubesin's method involves many steps, it was adaptable to an iterative calculation procedure which could be programed for machine solution on an Electrodata E-102 digital computer. This procedure is described in detail elsewhere[14] and will only be outlined here.

The starting point of the calculation was to assume an initial value of T_{w_i} ($T_{w_i} = T_{w_o}$ was used at first, but experience soon permitted a better first approximation and, hence, more rapid convergence of the iteration) in order to evaluate the various parameters involved in Rubesin's analysis. With the distributions of stream mass velocity, injection mass velocity, and length Reynolds Number determined as described previously, the subsonic-flow data of Mickley and Davis[25] were extrapolated to higher injection ratios to obtain a starting approximation for the friction coefficient $c_f/2$. This estimate provided the basis for an iterative calculation which converged upon a value of $c_f/2$ satisfying all relations for the initial estimate of T_{w_i}. Although the basic analysis assumed that the Prandtl-Kármán mixing-length constant K was fixed at a value of 0.392, unaffected by transpiration, the present calculation arbitrarily employed variable values of K again by extrapolating the results of Mickley and Davis to higher injection ratios. The validity of the process has not been assessed, but it appears as defensible as does the assumption of constant value of K in the region adjacent to an effusion-cooled wall with large injection.

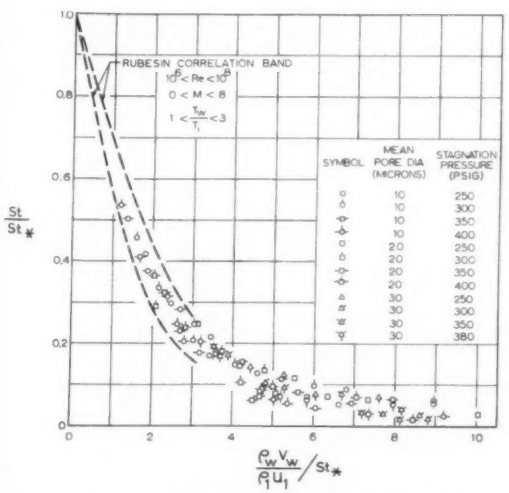

FIG. 12. Stanton Number ratio vs. Mickley-Rubesin injection parameter.

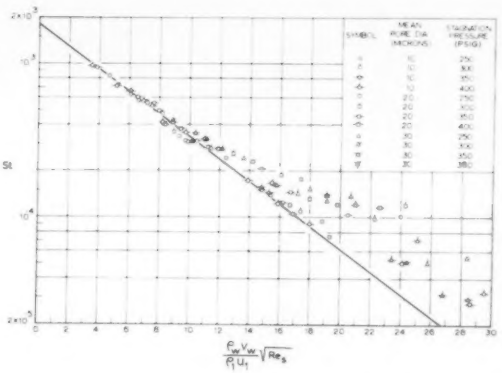

FIG. 13. Stanton Number vs. alternative injection parameter.

The calculation of $c_f/2$, however, constituted but one step in a larger iteration loop for determination of T_{w_i}. Values of $c_f/2$ from the internal iteration loop were used to evaluate Rubesin's expressions for the Stanton Number, taking the turbulent Prandtl Number as unity and evaluating the molecular Prandtl Number at local main-stream conditions. At this point, the external iteration loop was closed by calculation of T_{w_i} from Eq. (4), and the process (including the internal iteration for $c_f/2$) was repeated until convergence was achieved.

The results of the Stanton Number calculations from all the heated-flow tests are presented in Fig. 12 in terms of the ratio St/St_* vs. $(\rho_w v_w/\rho_1 u_1)/St_*$. Only data corresponding to stations within the nonseparated zone (as established by comparison with the schlieren photographs) are included. It was found that the injection ratios employed were so large that a long, nonlinear extrapolation to the zero-injection condition would be required to establish values of St_* from the experimental data. Therefore, St_* was estimated from the expression

$$St_* = 0.0285\, Re_s^{-1/5} Pr^{-2/3} \tag{5}$$

where Re_s is the Reynolds Number based on the distance downstream from the throat measured along the wall. This type of approximation has been found satisfactory for correlation of conventional nozzle heat-transfer data.[23, 24] The calculations indicate that the injection ratios employed were sufficient to reduce the heat-transfer ratios by more than one order of magnitude. It is seen that, despite the drastic mixing-length extrapolation involved in the modified application of Rubesin's method, the St/St_* points appear to fall within the band calculated by Rubesin[26] to cover the range of variables $0 \leq M \leq 8$, $1 \leq T_w/T_1 \leq 3$, and $10^6 \leq Re \leq 10^8$. An alternative presentation of the Stanton Number calculations in terms of an alternative injection parameter, $(\rho_w v_w/\rho_1 u_1)\sqrt{Re_s}$, is shown in Fig. 13. This parameter is of significance in analyses of laminar-flow situations where it is proportional to the Blasius function evaluated at the wall. It is used here only for correlative purposes because it permits a linear extrapolation of the data in the range of low-to-moderate injection ratios which is of greatest practical interest.

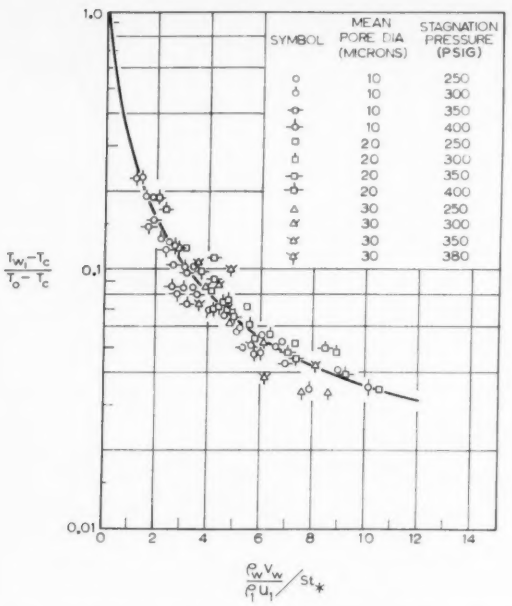

FIG. 14. Wall-temperature ratio vs. Mickley-Rubesin injection parameter.

The wall-temperature ratios $(T_{w_1} - T_c)/(T_o - T_c)$ obtained from the calculations are presented as a function of $(\rho_w v_w/\rho_1 u_1)/St_*$ in Fig. 14. It is seen that the effect of injection is to reduce the stream-side surface temperature by more than an order of magnitude compared to that which would be experienced under adiabatic recovery conditions. The apparent divergence of the points is magnified by the logarithmic ordinate scale (which was necessary to distinguish the small temperature-ratio values which otherwise clustered close to zero) and is not regarded as significant.

Corresponding values of the friction coefficient and temperature recovery factor derived from the calculation procedure are shown in Figs. 15 and 16. The recovery factor is seen to increase slightly with increasing injection ratios. This trend is surprising in view of the results of other (laminar-flow) analyses of single-component boundary-layer injection. However, Rubesin advises that his analysis probably does not yield precisely valid results for the influence of injection on recovery factor, and that the most positive statement possible is that the effect is small, with an approximate value of $r \cong 0.9$ being representative for the regime of low-to-moderate injection rates which is of practical interest.

Concluding Recommendations

The experiments described in the foregoing discussion indicate that the technique of effusion cooling by injection of a gaseous coolant through a porous wall is highly efficient under conditions of strong flow expansion (high positive Euler Number). In addition, it was demonstrated that, when the injection technique is applied to one diverging wall of a two-dimensional, supersonic de Laval nozzle, early separation of the flow from the porous wall may be promoted under expansion conditions approaching the optimum. By means of such controlled, asymmetrical flow separation, controlled jet deflections up to 10° (depending upon the chamber pressure and injection ratio) could be effected. Since the experiments were not designed to investigate this behavior over a wide range of conditions, it is recommended that the attractive possibility of using porous-wall injection techniques for control of the magnitude and direction of the nozzle thrust vector be evaluated experimentally by small-scale rocket thrust chamber tests using axially-symmetric nozzles with segmented injection manifolds.

Effect of Film-Coefficient and Recovery Factor Assumptions

As a means of evaluating the sensitivity of the heat-transfer calculations summarized above to the arbitrary assumptions required, a second set of solutions to Eq. (4) was performed subject to the assumption that the film coefficient and recovery factor are not affected by injection—i.e., $St = St_*$ and $r = Pr^{1/3}$. The wall-temperature ratios so derived are presented in Fig. 17 for comparison with the correlating line from Fig. 14 and with the line estimated by Rubesin[26] for the case of conventional cooling of 100 per cent effectiveness—i.e., when the coolant achieves full wall temperature. It is seen that the data reduced in this fashion fall somewhat below Rubesin's estimate in the range of low injection rates.

Fig. 17 indicates that the effectiveness of the effusion cooling technique derives principally from the efficient heat transfer between the porous solid and the infiltrating fluid during its passage through the wall, a conclusion supporting that of Lifton.[27] The additional beneficial effect of mass addition to the stream upon the

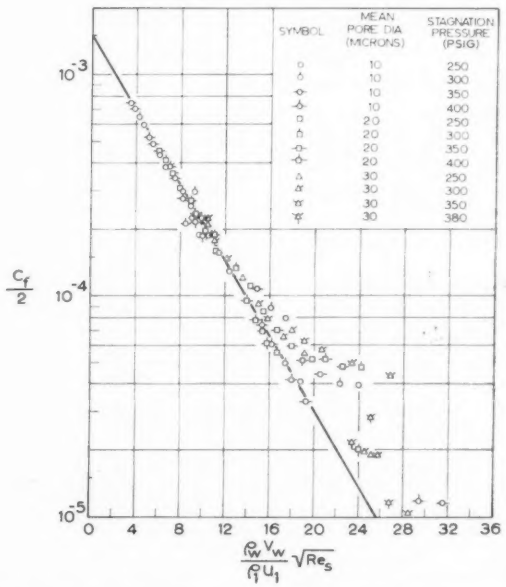

FIG. 15. Friction coefficient vs. alternative injection parameter.

boundary-layer conditions governing the film coefficient is thus illustrated by the first-order difference between the two lower curves of Fig. 17. It would thus appear that differences in prediction of the effect of mass transfer on the film coefficient by the various analyses currently available may be considered to be of second-order importance in the design of porous-wall cooling systems. In cases where the transfer coefficient per se (rather than the wall-temperature reduction effected) is of primary concern, as in the case of skin-friction estimates, these differences between the various analytical predictions, of course, become significant.

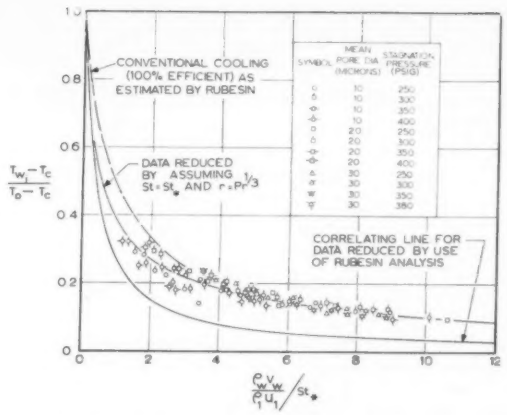
CONVENTIONAL COOLING (100% EFFICIENT) AS ESTIMATED BY RUBESIN
DATA REDUCED BY ASSUMING St=St* AND r=Pr^1/3
CORRELATING LINE FOR DATA REDUCED BY USE OF RUBESIN ANALYSIS
MEAN PORE DIA (MICRONS)
STAGNATION PRESSURE (PSIG)
$\frac{T_w - T_c}{T_o - T_c}$
$\frac{\rho_w v_w}{\rho_1 u_1}/St_o$

FIG. 17. Effect of film-coefficient and recovery-factor assumptions on wall-temperature ratios.

References

[1] Meyer-Hartwig, F., *Kühlung hochhitzbeanspruchter Oberflächen mit einem durch Poren im Werkstoff zugeführten Kühlmittel (Schwitzbaustoffe)*, Luftfahrtforschungsanstalt Hermann Göring, Institut für Motorenforschung, Braunschweig, Zentrale für Wissenschaftliches Berichtwesen (Berlin-Adlershof) Rep. No. FB 1470, December 1, 1940. Air Materiel Command Translation No. F-TS-2067-RE, ATI No. 22204, September, 1948.

[2] Goddard, R. H., *Combustion Chambers for Aircraft*, U.S. Patent 2,183,313 (1938).

[3] Skoglund, V. G., *Fluid Nozzle*, U.S. Patent 2,354,151 (1942).

[4] Jakob, M., and Fieldhouse, I. B., *Cooling by Forcing a Fluid through a Porous Plate in Contact with a Hot Gas Stream*, p. 191; Heat Transfer and Fluid Mechanics Institute, Berkeley, Calif., June, 1949 (publ. by ASME).

[5] Duwez, P., *Experimental Study of Cooling by Infiltration of a Fluid through a Porous Material*, Sixth International Congress for Applied Mechanics, Paris, France, September, 1946.

[6] Duwez, P., and Wheeler, H. L., Jr., *Experimental Study of Cooling by Injection of a Fluid through a Porous Material*, Journal of the Aeronautical Sciences, Vol. 15, No. 9, pp. 509–552, September, 1948.

[7] Moore, N. P. W., and Grootenhuis, P., *Improvement Relating to Internal Combustion Turbines and Like Apparatus Working with Gases at High Temperatures*, British Patent 619,634 (1946).

[8] Grootenhuis, P., and Moore, N. P. W., *Sweat Cooling: A Review of Present Knowledge and Its Application to the Gas Turbine*, Symposium on High-Temperature Steels and Alloys for Gas Turbines, Special Rep. No. 43, pp. 281–288, The Iron and Steel Institute, London, 1951.

[9] Eckert, E. R. G., *Transpiration and Film Cooling*, Heat Transfer Symposium, pp. 195–210, Engineering Research Institute, University of Michigan, Ann Arbor, Mich., 1953.

[10] Broadwell, J. E., and Sherman, P., *Survey of Porous-Wall Heat-Transfer Literature*, Engineering Research Institute Project M992-7, University of Michigan, Ann Arbor, Mich., April, 1953

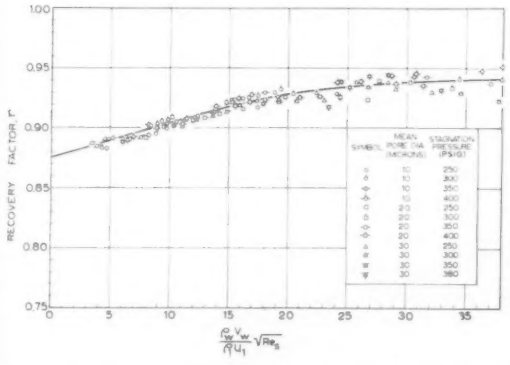

FIG. 16. Temperature recovery factor vs. alternative injection parameter.

[11] J. Berger, *Contribution a l'Etude de l'Injection Pariétale*, Doctor's thesis, University of Paris, Poudres Memorial, Vol. 38 (Annex), p. 1, Imprimerie Nationale, Paris, 1956.

[12] Eckert, E. R. G., Hartnett, J. P., Irvine, T. F., Jr., and Schneider, P. J., *Review of Heat Transfer Literature—1956*, Mech. Eng., pp. 433–444, May, 1957.

[13] Eckert, E. R. G., Hartnett, J. P., and Irvine, T. F., Jr., *A Review of Heat Transfer Literature—1957*, Mech. Eng., pp. 64–76, June, 1958.

[14] Green, L., Jr., and Nall, K. L., *Experiments on Porous-Wall Cooling and Flow Separation Control in a Supersonic Nozzle*, Aerojet-General Rep. No 1490, December, 1958.

[15] Green, L., Jr., and Nall, K. L., *Control of Nozzle Flow Separation by Boundary-Layer Injection*, Aerojet-General Rep. No. 1381, December 31, 1957.

[16] Green, L., Jr., *Flow Separation in Rocket Nozzles*, J. Amer. Rocket Soc., Vol. 23, p. 34, 1953.

[17] McKenney, J. D., *An Investigation of Flow Separation in a Two-Dimensional Transparent Nozzle*, Jet Propulsion Laboratory Progress Rep. No. 20-129, California Institute of Technology, April, 1953.

[18] Grootenhuis, P., Mackworth, R. C. A., and Saunders, O. A., *Heat Transfer to Air Passing Through Heated Porous Metals*, General Discussions on Heat Transfer, p. 363, The Institution of Mechanical Engineers, London, 1951.

[19] Green, L., Jr., and Duwez, P., *Fluid Flow Through Porous Metals*, Trans. ASME (J. Appl. Mech.) Vol. 72, pp. 39–45, 1951.

[20] Green, L., Jr., and Nall, K. L., *Heat Removal from a Resistance-Heated Porous Solid*, Aerojet-General Rep. No. 1380, December, 1957.

[21] Fraser, R. P., and Rowe, P. N., *Supersonic Jet Deflection*, J. Roy. Aero. Soc., Vol. 62, No. 565, pp. 43–59, January, 1958.

[22] Rubesin, M. W., *An Analytical Estimation of the Effect of Transpiration Cooling on the Heat-Transfer and Skin-Friction Characteristics of a Compressible, Turbulent Boundary Layer*, NACA TN 3341, December, 1954.

[23] Saunders, O. A., and Calder, P. H., *Heat Transfer in Nozzle at Supersonic Speeds*, Engineering, pp. 281–284, August 29, 1952.

[24] Pefley, R. K., *Convection Heat Transfer Coefficients in de Laval Nozzles*, Technical Report No. HS-3, Department of Mechanical Engineering, Stanford University, October 1, 1951.

[25] Mickley, H. S., and Davis, R. S., *Momentum Transfer for Flow over a Flat Plate with Blowing*, NACA TN 4017, November, 1957.

[26] Rubesin, M. W., *The Influence of Surface Injection on Heat Transfer and Skin Friction Associated with the High-Speed Turbulent Boundary Layer*, NACA RM A55L13, February 20, 1956.

[27] Lifton, D., *Experimental Investigation of Sweat Cooling with Nitrogen*, Jet Propulsion Laboratory Progress Rep. No. 20-199, California Institute of Technology, October 12, 1953.

An Experimental Study of Jet-Flap Compressor Blades†

EDWARD L. CLARK, JR.,* AND DONALD EARL ORDWAY**
Cornell University

Summary

The results of a preliminary experimental investigation to determine the feasibility of using the jet flap to improve the section characteristics of an axial-flow compressor blade are presented and discussed. The airfoil tested was the NACA 65-(12)10 blower blade with a thickened trailing edge. Internal design of the blade is described and details of the resulting jet flow are given. Also included are wind-tunnel design and test procedures for the two-dimensional cascade used in the test.

Test results are presented in the form of the measured turning angle, pressure rise, and lift coefficient. They are examined with particular reference to the prevention of rotating stall.

Symbols

b	= blade span
c	= blade chord
C_F	= force coefficient
C_j	= jet-momentum coefficient
C_l	= section lift coefficient
F	= force
g	= coordinate parallel to tangential direction
g_0	= tangential spacing between blades
M_j	= jet momentum
p	= static pressure
p_a	= atmospheric pressure
p_t	= total pressure
p_{tj}	= total pressure in the jet
q	= dynamic pressure
V	= flow velocity
y	= coordinate perpendicular to downstream flow direction
y_0	= defined as $g_0 \cos \beta_2$
$\Delta p/q_1$	= nondimensional static-pressure-rise parameter
α	= angle between upstream flow direction and blade chord
β	= angle between flow direction and cascade axis
δ	= angle between jet direction and blade chord
ϑ	= flow turning angle, $(\beta_1 - \beta_2)$
ρ	= mass density of air
σ	= solidity; ratio of blade chord to blade tangential spacing

Subscripts

a	= component in axial direction
m	= referred to vector-mean velocity
t	= component in tangential direction
1	= upstream of blade row
2	= downstream of blade row

Superscript

*	= referred to equivalent downstream velocity

Introduction

ONE of the most serious problems involved in the design of high performance axial-flow compressors is the problem of rotating stall. The phenomenon of rotating stall has been widely discussed in the literature[1, 2] and is given only briefly here. The stalling occurs when a row of blades, such as the rotor or stator of a compressor, has a high angle of attack relative to the upstream flow, as shown in Fig. 1. This frequently happens during rapid acceleration of a turbojet engine—for example, prior to take-off or during in-flight throttle adjustments. A small disturbance can then increase the flow angle of one of the blades to the point where it will stall. This stalled condition may create a region of separated flow which will deflect the upstream flow. The next blade will then have a higher effective angle of attack and it may also stall. At the same time, the deflected flow decreases the angle of attack of the blade below and tends to prevent or remove the stalled condition. In this manner, the stall region "rotates" around the blade row.

One approach to the elimination of rotating stall would be the use of boundary-layer control to delay flow separation and, hence, increase the stall angle of the blade. However, while boundary-layer control

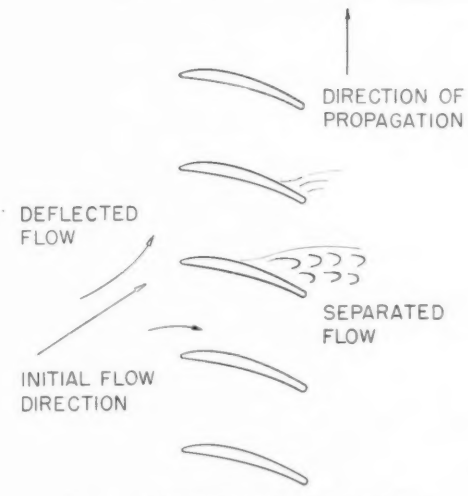

FIG. 1. Mechanism of stall propagation.

Received October 29, 1958.

† This research was partially supported by Therm Advanced Research Division of THERM, Inc.

* Formerly, Graduate Student in Aeronautical Engineering. Now with ARO, Inc.

** Formerly, Assistant Professor of Aeronautical Engineering. Now, Head, Aerophysics Section, Therm Advanced Research Division.

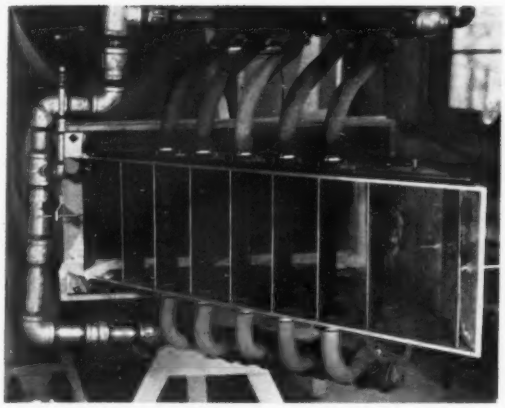

FIG. 2. Cascade test section as viewed from tunnel exit.

has been extensively studied and tested on isolated airfoils, only a few attempts have been made to apply it to the blades of turbomachines. Three of these which have been examined are: (1) suction through slots,[3] (2) suction through porous walls,[4] and (3) slotted blades.[5] None of these references give data which can be related to the specific problem of rotating stall, although Schultz's experiment[4] showed that there was an increase in lift for an angle of attack less than the stall angle.

Another possibility was suggested to the authors by Prof. F. E. Marble of the California Institute of Technology. His idea was to utilize the jet flap which has been successfully tested on isolated airfoils, for example, see reference 6. This consists of a high-speed stream of air blown from the trailing edge of an airfoil, usually at an angle to the chord. The jet of air, similar to a solid flap, increases the airfoil circulation. Furthermore, it reduces separation effects by adding high energy air to a region which would normally have a low velocity. Therefore, these effects should allow a jet-flap blade in cascade to operate at a lower angle of attack than a conventional blade with the same load. They should also give a higher stall angle if the jet deflection angle is not too large.[7]

Description of the Cascade Tunnel

It was of prime interest to isolate airfoil characteristics, such as turning angle and lift coefficient. Therefore, the airfoils were tested in a two-dimensional cascade tunnel rather than in an actual compressor.

The Cornell 10 × 25 in. low-speed cascade tunnel is of open circuit design.[8] It utilizes a large settling chamber with eight fine-mesh screens to provide uniform flow at the test section. No method was employed for removing the test section wall boundary layer although this would have been desirable.

The inlet air angle β_1 was 45° and the solidity σ was 1.0. The cascade was composed of seven airfoils. Each had a 4 in. chord and an aspect ratio of $2^1/_2$. Although it would have been advantageous to have had all airfoils of the jet flap type, tunnel construction necessitated a conventional airfoil at either end of the cascade. The test section end walls were cambered and could be adjusted to match the cascade.

Compressed air for the jet flaps was supplied from two manifolds to both ends of the five "blowing" airfoils. An overall view of the cascade test section is shown in Fig. 2.

Description of Airfoils

The airfoils selected for this test were NACA 65-(12)10 compressor blades with trailing edges thickened to a 2 per cent radius.[9] This airfoil section was used since it has a trailing edge suitable for the internal construction desired and is representative of compressor blades having well-known characteristics.

To avoid three-dimensional effects, it was necessary that the internal duct provide a constant exit jet velocity along the span. In an effort to achieve this result, the internal channel converged from a relatively large plenum chamber to a small parallel slot. This spanwise slot was 1/2 in. long and 0.013 in. thick. As shown in Fig. 3, the slot was inclined at an angle of 15.9° to the chord. Preliminary tests showed that it was essential for the exit slot to be of uniform thickness across the span. Therefore, the airfoils were cast of Meehanite to avoid residual stresses associated with materials such as cold-rolled steel. For structural strength, 1/10 in. thick internal ribs were placed at one-third and two-thirds of the span.

The spanwise total-pressure distribution, as measured by a probe inserted one-tenth of an inch into the slot, was fairly uniform as shown in (a) of Fig. 4. From this measurement, it was assumed that the jet effects except at the rib stations were essentially two-dimensional along the span. However, it is to be noted that the total-pressure distribution one chord downstream of the trailing edge was not as uniform, see (b) of Fig. 4 for the test airfoil. An earlier "test block" used in developing the internal configuration showed better results, (b) in Fig. 4. It also had internal ribs but a lower ratio of rib to slot thickness than the test airfoil. Limited experiments indicate that the downstream uniformity of the jet sheet depends critically on this ratio, among other variables.

Test Procedures and Measurements

Initial tests at the design angle of attack indicated that the airfoil characteristics became practically independent of Reynolds Number at a value of 270,000,

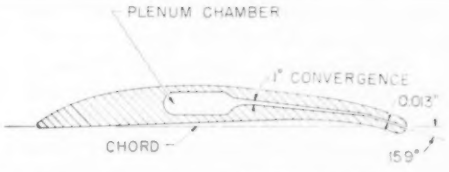

FIG. 3. Cross section of the NACA 65-(12)10 compressor blade, with 2 per cent trailing-edge radius, showing internal duct design.

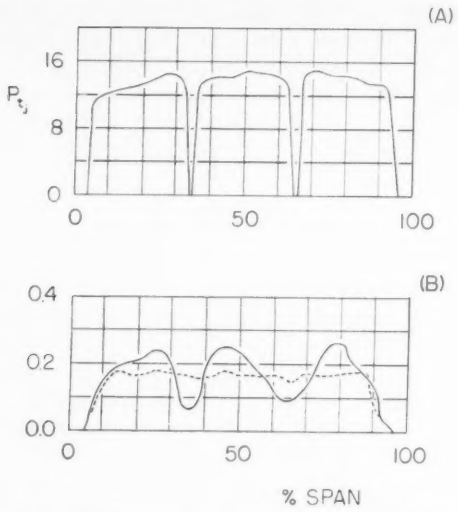

FIG. 4. Spanwise total-pressure (in in. of Hg) distribution with zero tunnel velocity and an airfoil plenum pressure of 20.4 in. of Hg: (a) inside exit slot and (b) one chord downstream of exit slot of airfoil (solid line) and "test block" (dotted line).

which is typical for cascade tests.[10, 11] With a blade chord of 4 in., this allowed an upstream velocity of 140 ft. per sec. that was low enough to avoid compressibility effects. The corresponding dynamic pressure was 22.1 lbs. per ft.^{2}, and all tests were made at this pressure.

The cambered end walls were adjusted for each airfoil angle-of-attack setting. This was necessary in order to satisfy as well as possible the criteria of infinite blade row conditions. These criteria are: (1) the upstream and downstream flow directions should be uniform along the blade row, usually with the upstream direction set parallel to the tunnel axis at one chord, and (2) the upstream static pressure should be uniform along the blade row. It was found that the end walls could be positioned to satisfy either of the conditions, but not both. An initial test showed, however, that best results were obtained with uniform static pressure so this criterion was used. This required, of course, that the upstream flow direction be measured and included in the turning angle. Because of the two conventional end blades in the cascade, it was found that neither of the infinite blade row conditions could be rigorously satisfied with jet coefficients other than zero. The test procedure used was to set the end walls for optimum conditions with the jets off and then leave them in that position when the jets were on.

The upstream flow direction was measured with a cobra-head yaw probe.[12] The probe head was placed at mid-span of the airfoils, one chord upstream of the cascade. Readings were taken with it located on the tunnel centerline and then $2^1/_2$ in. on either side of this position. The upstream static pressure was measured with wall orifices located along the bottom cascade wall, one-half chord ahead of the blade row. At this position, any "local" influences ot the airfoils were found to be negligible. Total pressure ahead of the cascade was measured by two probes located at mid-height of the tunnel, 1 in. from the end walls.

Downstream of the cascade, the flow direction was also measured with a cobra-head yaw probe. The probe was set at mid-span of the airfoils, one chord downstream of the cascade. All measurements were made in the airfoil passages adjoining the center airfoil. However, since the yaw probe gives erroneous results in the presence of a total pressure gradient, all measurements were taken outside of the airfoil wake regions. The total pressure distribution one chord downstream of the cascade was determined with a seven-tube nonintegrating rake.

As defined, the jet coefficient is the nondimensional momentum of the jet. Thus, the coefficient can be determined by direct measurement of the jet momentum. With zero tunnel velocity, the jet total pressure, and, hence, momentum, was measured with the total-head rake at mid-span of the airfoil. Measurements were made one-half chord and one chord downstream of the airfoil trailing edge. These results, practically equal, were averaged. The resultant momentum was converted to a nondimensional form by using the product of blade area and upstream dynamic pressure. Jet coefficient values used in the present test were 0.15, 0.33, and 0.52.

Data Reduction

Calculation of the forces on a cascade was based on pressure and momentum changes as determined from measurements taken upstream and downstream of the cascade. As anticipated, the results were not in exact agreement with the results expected from an ideal, two-dimensional, infinite cascade.

To begin with, the flow in the cascade test section was not actually two-dimensional. This was principally due to the nonuniform jet sheet, secondary flow in the blade channels, and the interaction of wall and airfoil boundary layers at the airfoil tips. This last effect introduced a large error in measurements of the static-pressure rise through the cascade. Fig. 5, showing the theoretical pressure rise, gives an indication of the magnitude of this error. The measured value is less than the theoretical because the walls experience the same pressure rise as the airfoils and, in addition,

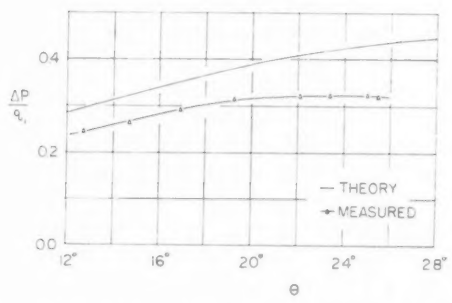

FIG. 5. Variation of cascade-pressure-rise coefficient with turning angle for $C_j = 0$.

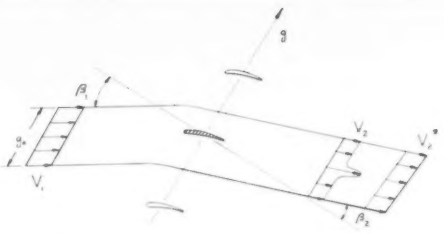

FIG. 6. Momentum control surface for a cascade of jet-flap airfoils.

have a well-developed boundary layer prior to the cascade. Hence, a thick boundary layer is produced, creating a smaller effective cross section downstream of the cascade. This "contraction" causes the exit velocity to be larger than that predicted by continuity relations based on a constant tunnel height. Therefore, a lower pressure is obtained.

On the other hand, the jets issuing from the trailing edges of the airfoils entrain part of the main flow downstream of the cascade. This lowers the velocity of the main flow there, and so increases the static pressure rise. In fact, subsequent examination of the test data will show that the measured pressure increment is greater than would be expected from the increase in the measured turning angle. Hence, it would be interesting to calculate the entrainment but this is difficult because of the flow acceleration by the exit "contraction."

Finally, as it was previously mentioned, the tests were actually run with an inlet air angle which was as much as 4° greater (one chord upstream) than the geometric angle of 45°, since the upstream flow could not be set parallel to the tunnel axis. However, the turning angle and lift coefficient change only very slowly with inlet angle in this range.

The force on a cascade is frequently resolved into axial and tangential components. To calculate these forces, consider a control surface containing one airfoil as shown in Fig. 6. The axial force F_a, taken positive in the upstream direction, is given by the momentum equation, or

$$F_a = \rho \int_0^{g_0} (V_2 \cos \beta_2)^2 b dg - \rho(V_1 \cos \beta_1)^2 b g_0 + (p_2 - p_1) b g_0 \quad (1)$$

where the density ρ is assumed constant. Also, letting the tangential force F_t be positive if the velocity change is in the usual direction, shown in Fig. 7, we have, similarly,

$$F_t = \rho\, V_1^2 b g_0 \cos \beta_1 \sin \beta_1 - \rho b \int_0^{g_0} V_2^2 \cos \beta_2 \sin \beta_2\, dg \quad (2)$$

It is now convenient to define an "equivalent" downstream velocity V_2^* which will give the same resultant force but will be independent of tangential position. Assuming the flow direction in the wake to be the same as the flow direction outside of the wake and taking the equivalent velocity in this direction, we find

$$(V_2^*)^2 = (1/g_0) \int_0^{g_0} V_2^2 dg \quad (3)$$

Now, far downstream of the cascade the static pressure is atmospheric,† so for incompressible flow, Eq. (3) may be rewritten,

$$(V_2^*)^2 = (2/\rho g_0 \cos \beta_2) \int_0^{y_0} (p_{t_1} - p_a) dy \quad (4)$$

where the y axis is taken perpendicular to the flow direction—that is, $y_0 = g_0 \cos \beta_2$. The integrand $(p_{t_1} - p_a)$ was determined by a survey with the total-head rake, and the integral evaluated graphically.

The force coefficients C_{F_a} and C_{F_t} based on the upstream dynamic pressure q_1 and the blade area bc are then,

$$C_{F_a} \equiv F_a/q_1 bc = (2/\sigma)[(V_2^*/V_1)^2 \cos^2 \beta_2 - \cos^2 \beta_1 + (\Delta p/2q_1)] \quad (5)$$

$$C_{F_t} \equiv F_t/q_1 bc = (2/\sigma)[\cos \beta_1 \sin \beta_1 - (V_2^*/V_1)^2 \cos \beta_2 \sin \beta_2] \quad (6)$$

where $\Delta p \equiv (p_2 - p_1)$ and $\sigma \equiv c/g_0$, the cascade solidity.

A standard procedure in cascade tests is to define the lift and drag as components of the resultant force perpendicular and parallel, respectively, to the vector mean velocity V_m. Since this velocity is the vector average of V_1 and V_2^*, its position is determined by

$$\beta_m = \arctan [(V_{t_1} + V_{t_2}^*)/(V_{a_1} + V_{a_2}^*)] \quad (7)$$

as shown in Fig. 7. Hence, the axial and tangential force coefficients may be resolved into lift and drag coefficients.

The jet coefficient C_j is defined as

$$C_j = M_j/q_1 bc \quad (8)$$

where the jet momentum M_j is given by

$$M_j = \int_{\text{jet}} \rho V^2 b dy \quad (9)$$

† In order to observe the pressure recovery due to the "ejector effect," the sidewalls should be extended further downstream as practiced for highly loaded turbine blades.[13]

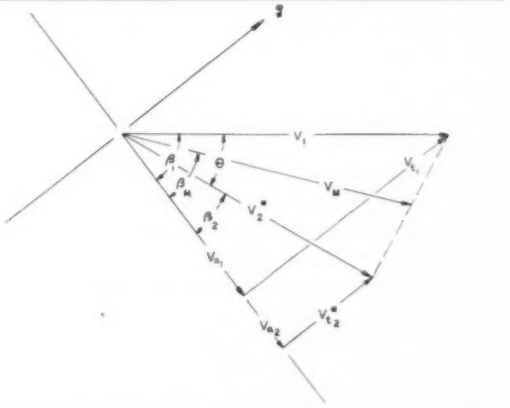

FIG. 7. Typical velocity diagram for an axial compressor.

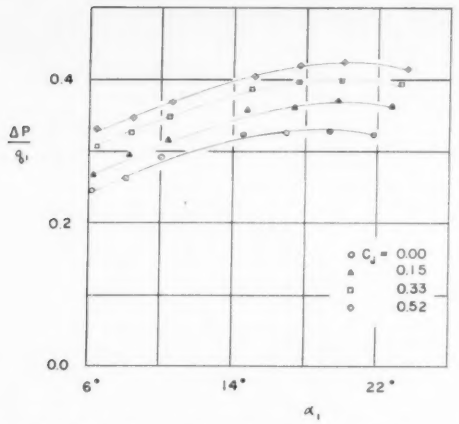

FIG. 8. Variation of cascade static pressure rise with angle of attack for $\beta_1 = 45°$, $\sigma = 1.0$, and NACA 65-(12)10 blade section with $\delta = 15.9°$.

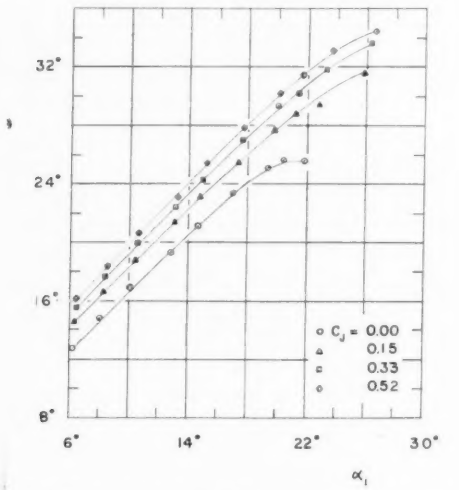

FIG. 9. Variation of turning angle with angle of attack for $\beta_1 = 45°$, $\sigma = 1.0$, and NACA 65-(12)10 blade section with $\delta = 15.9°$.

Far downstream of the airfoil, the flow is essentially incompressible; therefore,

$$C_j = (2/q_1 c) \int_{\text{jet}} (p_{tj} - p_a) dy \qquad (10)$$

The integral of Eq. (10) and, hence, Eq. (10) is evaluated from a total-pressure traverse of the jet with zero tunnel velocity.

Results and Discussion

The blade section characteristics are given in Figs. 8–10. The present tunnel configuration did not afford sufficient accuracy to determine the drag coefficient.

It can be seen that the stall angle was increased by the use of the jet flap. Since measurements near the stall condition were difficult to make with the present tunnel, the actual increase was not determined. However, the important result obtained was that at the maximum jet coefficient of 0.52 the lift was increased more than 30 per cent throughout the angle-of-attack range. Or, a comparable lift coefficient can be obtained at a much lower angle of attack. For example, if the blades were normally operated at a design angle of attack of 14°, they could now be used at an angle of 7° with a jet coefficient of 0.52 to obtain the same lift. Thus, through the increase in stall angle and increase in lift, a row of jet flap blades would have a greatly improved chance of avoiding rotating stall.

The efficiency of the jet flap blade would be an important factor if the blowing were used continuously. The most likely source of air for the jets would be a bleed from the later stages of the compressor. Therefore, with continuous blowing it is possible that the increased pressure rise due to the jets would be offset by the losses incurred in supplying the jet air. However, if the jets were used only at critical periods, the benefits gained by prevention of rotating stall would outweigh any losses in efficiency. It should be noted, though, that the blade design does not take advantage of the increase in circulation at high speeds when the jet flap is not used at design speed. Therefore, all of the gain in angle-of-attack range discussed above cannot be realized.

The present tests constituted only a preliminary investigation and, hence, were crude in many ways. Future tests will include a porous wall cascade test section with flexible end walls and a single-stage, axial-flow jet-flap compressor. These tests, which will include measurements of the loss coefficient and efficiency, will help to determine if the jet-flap blade can be a solution to the rotating-stall problem.

References

[1] Emmons, H. W., Pearson, C. E., and Grant, H. P., *Compressor Surge, and Stall Propagation*, Trans. ASME, Vol. 77, pp. 455–467, 1955.

(*Continued on page 738*)

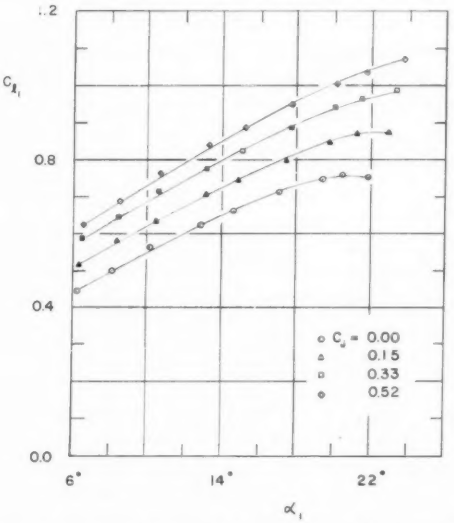

FIG. 10. Variation of lift coefficient with angle of attack for $\beta_1 = 45°$, $\sigma = 1.0$, and NACA 65-(12)10 blade section with $\delta = 15.9°$.

The Equation of Energy Balance for Fluttering Systems With Some Applications in the Supersonic Regime

JOHN D. C. CRISP*

Massachusetts Institute of Technology

Introduction

IT IS WELL KNOWN that the development of a critical flutter oscillation can be attributed to the existence, at an appropriate air speed, of a right (characteristic) set of amplitude ratios and phase angles (eigenmodes) between certain component motions—being then neutrally stable, the system is *potentially* capable of energy gain (or loss) as a result of some further perturbation. It seems natural then that a study of the *eigenmodes*, rather than the eigenvalues (critical flutter speed and frequency parameter) should lead to a clearer understanding of the flutter mechanism and of those system parameters which are most significant in allowing it. This is indeed the case; and it will be shown how such a study leads to some useful tools of assessment for the practicing aeroelastician. The emphasis in analysis here passes from interest in the solution, by whatever means, of the characteristic flutter determinant for the eigenvalues to an assessment of the eigenmodes which is best made by consideration of the equation of energy balance. This, in turn, illuminates the equations of motion themselves so that a cursory inspection of the matrices of the flutter coefficients can be very revealing as to the system behavior and stability. Such assessment as is possible with the concepts outlined below provides a useful guide in formulating and interpreting conventional flutter analyses.

These considerations are particularly pertinent today when the inevitable complexity of multi-degree of freedom systems tends to obscure the basic mechanisms, and the flutter engineer is in danger of losing his physical understanding of the problem.

For a harmonically oscillating conservative system, the Integral of Energy is a first integral of the equations of motion and, in fact, is a statement of the law of conservation of energy. A fluttering system, on the other hand, is subject, *inter alia*, to dissipative forces so that the integral of energy leads to an equation of balance relating the total energy of the system to the energy of the impressed aerodynamic forces or generalized forces, as they are customarily termed. Whereas the conventional analysis of the equations of motion leads to a complete statement of system behavior, the equation of energy balance, being a first integral of the equations of motion, is less informative in this sense. It states, in essence, those amplitude and phase relations necessary for the existence of flutter when the system displacement is represented by a truncated modal series. It does, however, reveal those system properties which are basic and significant in flutter in a general way which elucidates the results of the more pedestrian parametric solutions of the equations of motion; and it is capable of development as a criterion of stability which finds useful practical application.

The equation of energy balance has been used in various restricted forms since Routh[1] applied it to stability considerations of mechanical systems, a topic further elaborated by Rayleigh.[2] Their work formed the basis of its application, by Frazer and Duncan,[3] to stability determinations for some rather special forms of two-dimensional binary flutter. Garrick[4] used a two-dimensional form of it to investigate propulsive effects of a flutter-like wing motion, while Barton,[6] Greidanus,[7] Rott,[9] and Lambourne[11] employed it to derive limiting reduced frequencies for flutter to exist in the case of two-dimensional wing bending-torsion flutter. Of these authors, Rott carried the ideas furthest, to a point, in fact, where he deduced a simple criterion of flutter stability. This was expressed in geometric terms as a "limit circle" in the complex amplitude ratio plane which is a special case of the "energy circle" derived independently by the present author[13] from a criterion of "ultimate stability" for binary fluttering systems of any type of coupling, and two- or three-dimensional in nature.

Two experimental applications of the energy balance equation are to be found in the "flutter engine" of Ellis and Duncan,[5] and the wind-tunnel measurements of Halfman.[12]

The generalization of the statement of the equation of energy balance to any finite number of degrees of freedom of a three-dimensional system was elegantly made by Duncan,[8] and he emphasized the importance of the "skew-symmetric aerodynamic stiffness components" of the generalized forces, which will be elaborated below. The development given here is quite general; it is applicable to any finite number of degrees of freedom of a three- (or two-) dimensional

Presented at the Aeroelasticity Session, IAS 27th Annual Meeting, N.Y., Jan. 26–29, 1959.

* Formerly, Research Engineer. Now, Research Assistant Professor of Applied Mechanics, Polytechnic Institute of Brooklyn.

linear system, caters for time-dependence of system parameters, is valid for divergent and subsident oscillations. Specialization is then made to neutrally stable oscillation, thence to binary three-dimensional flutter. A criterion of "ultimate stability" is established for this case. Several examples of supersonic flutter include wing-bending-torsion flutter, wing-aileron flutter, and panel flutter, and are designed to illustrate the application and limitations of the equation of energy balance, both as a means of understanding the essential behavior of fluttering systems and as a design tool.

Equations of Motion

A familiar form of the equations of motion can be written in matrix form as

$$[\delta_{jk}]\{q_k\} = 0 \tag{1}$$

where the matrix of q is a column of n generalized coordinates and the elements δ_{jk} of the $n \times n$ square matrix are

$$\delta_{jk} = -[1 - (1 + ig_j)\Psi^2\Omega^2]a_{jk}k^2 + Q_{ik} \tag{2}$$

Here a_{jk} are generalized masses, g_j are modal damping coefficients, $\Psi_j = \omega_j/\omega_0$ the modal frequency ratio, while $\Omega = \omega_0/\omega$ and $k = \omega b/U$ are the required eigenvalues. The generalized (aerodynamic) forces Q_{jk} are, of course, complex. It will be convenient at first to ignore structural damping (place $g_j = 0$) and to rewrite Eqs. (1) and (2) in a general matrix form more amenable to energy derivations, thus:

$$A\ddot{q} + B\dot{q} + Cq = 0 \tag{3}$$

where A, B, C are square matrices containing as elements the generalized masses, the imaginary, and the real part of the generalized forces added to the structural stiffness forces, respectively. Thus, $Q_{jk} = c_{jk} + 2ikb_{jk}$ when the motion is sinusoidal. The q and its derivatives are to be understood, therefore, as column matrices. It will add little complication to generalize the situation to allow a time dependence of all system parameters so that Eq. (3) becomes

$$A(t)\ddot{q} + [\dot{A}(t) + B(t)]\dot{q} + C(t)q = 0 \tag{4}$$

It is worth while now relating the forces of Eq. (4) to the basic work functions from which they may in part be derived, thereby gaining a formal description of the system.

The Force Potentials

Quite formally, the forces implied by the matrices A, B, C are derivable in part from scalar functions or potentials T, F, V, respectively. We define

$$\begin{aligned} T &= [\dot{q}'A(t)\dot{q}]/2 \\ F &= [\dot{q}'B(t)\dot{q}]/2 \\ V &= [q'C(t)q]/2 \end{aligned} \tag{5}$$

where T is the kinetic energy quadratic in the generalized velocities, F is Rayleigh's dissipation function, and V is a "generalized potential energy." The prime q', etc., indicates the transpose of q, etc. For a fluttering system, the matrix A is symmetric, and for the usual choice of generalized coordinates, diagonal. The matrix B, in the absence of any mechanical or structural damping, is of aerodynamic origin and usually nonsymmetric; in particular cases it too may be symmetric, as, for example, when piston theory oscillatory forces are applicable, the only restriction being the need for profile symmetry about the mean profile chord. The matrix C is almost without exception nonsymmetric, and consists of aerodynamic and also structural components, the latter of which by themselves usually form a diagonal matrix. It is of vital interest to take note of the form of these matrices of elements because it reveals in a general way the importance of couplings as well as the probable behavior of the system.

It is a great convenience to write the matrices B, C as a sum

$$B = B_1 + B_2; \quad C = C_1 + C_2 \tag{6}$$

where B_1, C_1, are symmetric and B_2, C_2 are skew-symmetric—i.e., ${}_2b_{jk} = -{}_2b_{kj}$ or ${}_2b_{jk} = (b_{jk} - b_{kj})/2$. It will transpire that the skew-symmetric components* of the "stiffness" matrix C are of great significance in flutter.

The definitions (6) substituted in Eq. (5) lead, by a property of operations on skew-matrices, to a form of the potentials T, F, V which involve only the symmetric A, B_1, C_1; since $x'B_2x = x'C_2x = 0$. The scalar V thus has as its coefficients both structural and (symmetric) aerodynamic parts and is a "generalized" potential energy in this sense.

It remains to recall that the coefficients A, B, C, $\dot{A}$ of Eq. (4) are in general functions of the reduced frequency k and Mach Number M. This is not always so, however; for piston theory they are all independent of k.

The Total Energy Gradient

The total energy of the system is given[16] by

$$\sum_{j=1}^{n} p_j\dot{q}_j - L(\dot{q}_j, q, t) = E \tag{7}$$

where p_j are the generalized momenta $\partial L/\partial\dot{q}_j$, and L is the generalized kinetic potential T-V. Because of the nonconservative nature of a fluttering system (through the dissipation function F and the explicit time dependence of L), the total energy E is not a constant. Using an expression for $\ddot{q}$ from Eq. (4) substituted in the relation

$$dL/dt = \sum_{j=1}^{n} [(\partial L/\partial\dot{q}_j)\ddot{q}_j + (\partial L/\partial q_j)\dot{q}_j] + (\partial L/\partial t) \tag{8}$$

it is straightforward to show that

* Rayleigh[2] calls these gyrostatic terms.

$$(d/dt)(E) = -[2\Phi + \dot{q}'C_2q - (q'\dot{C}_1q)/2] \quad (9)$$

$$E = T + V$$

for the special forms (5) of the potentials, where there arises a new generalized dissipation function

$$\Phi = (1/2)\dot{q}'(B + \dot{A}/2)\dot{q} = (1/2)\dot{q}'(B_1 + \dot{A}/2)\dot{q} \quad (10)$$

which degenerates to F when the generalized masses are time independent—i.e., $\dot{A} = 0$. Thus, the rate of change with time of the total energy of the system is determined by the nature of the generalized *dissipation*, the magnitude of the *skew-symmetric components of the aerodynamic "stiffness" forces*, and the *time variation of the symmetric components* of those same forces. It is clear that the stability of the system is likewise dependent on the same factors, inasmuch as increasing/decreasing E implies gain/loss of energy to the system. It is of interest to note that the time rate of change of the damping forces, $\dot{B}$, does not appear in Eq. (9). In fact, for a fluttering system experiencing acceleration or undergoing structural stiffness changes due to kinetic heating it is the last term which primarily governs the transient behavior. For conventional flutter, $\dot{C}_1 = 0$, it is the second term involving C_2 which dominates and primarily determines system stability. This is because *fluttering systems are characterized by large skew-symmetric aerodynamic stiffness couplings and the system can often be assessed by a scrutiny of these.*

It is only in the single degree of freedom system that the dissipation function Φ or F is the prime behavior determinant, since then the right-hand side of Eq. (9) becomes $-[(b_{11} + \dot{a}_{11}/2)\dot{q}_1^2 - \dot{c}_{11}q_1^2/2]$. For $\dot{a}_{11} = \dot{c}_{11} = 0$ this implies the well-known result that stability is determined by the sign of the damping coefficient b_{11}.

In the conventional flutter case, $\dot{A} = \dot{C}_1 = 0$,

$$(d/dt)(E) = (d/dt)(T + V) = -(2F + \dot{q}'C_2q) \quad (11)$$

which is equivalent to Duncan's result.[8]

Energy and Stability

Eqs. (9) and (11) indicate that system stability is assured if the expressions within the respective brackets of the right-hand side are always positive for the whole range of a system parameter (such as airspeed) of interest. (T is necessarily positive definite, and we assume for the moment that so also is V.) Looking first at Eq. (11), we note that for aerodynamic (flutter) systems the dissipation function is not necessarily positive definite (as is usually the case for mechanical systems) but is so in most cases. The quantity $\dot{q}'C_2q$, on the other hand, is as likely to be negative as positive, and it is the behavior of this quantity which almost invariably dominates system stability, and may, for example, vitiate all attempts to induce stability by artificial increase of damping—i.e., by algebraically increasing the value of the dissipation function.

We may state these ideas more explicitly, on the basis that both T and V are positive definite, by writing $G = \dot{q}'C_2q$, thus:

(a) If $G = 0$, for which a sufficient condition is $C_2 = 0$, i.e., if there are no skew-symmetric stiffness couplings, then, provided F is positive definite (or $|B_1|_J > 0$), the system is stable irrespective of the skew-symmetric damping couplings B_2.

(b) If $B_2 = 0$, i.e., if there are no skew-symmetric damping couplings, then, provided F is positive definite (or $|B_1|_J > 0$), the system may be stable or unstable.

Similar considerations apply to the more general Eq. (9) from which three conclusions can immediately be drawn. Firstly, we note the complete absence of the time-variation of the dissipative forces, $\dot{B}$. Secondly, the time rate of change of the stiffness forces clearly dominates the transient behavior, and it is of interest that of these the *symmetric* components ($\dot{C}_1$) are the significant ones and, moreover, they act in a sense opposite to the skew-symmetric components C_2. Finally, time rate of change of generalized masses provides an effective additional damping effect, which may be positive or negative. An example is later given incorporating some of these phenomena. Suffice it to say here that they are readily interpretable physically. The variation $\pm|\dot{A}|$, for example, may be due to time-variation of the density ratio μ induced either by altitude or mass changes. The variation $\pm|\dot{C}_1|$ could arise simply through accelerated flight or, additionally, through structural stiffness changes due to kinetic heating. For example, in the case that $\dot{A} = 0$, transient effects on stability are governed by the sign of $q'\dot{C}_1q$. Positive discriminants of this expression assure its positive definiteness. For a binary system, $n = 2$, for example, this requires

$$(\dot{c}_{11}\dot{c}_{22} - \dot{c}_{12}\dot{c}_{21})_1 > 0; \quad (\dot{c}_{11})_1 > 0 \quad (12)$$

If satisfied, Eq. (12) implies a *destabilizing* influence.

It should be noted that the definition of instability as the increase of system total energy is an "instantaneous" one in the sense that it ignores the system condition with indefinite increase of time, and, in fact, avoids the difficulty of interpreting stability in physical terms. This leads to no ambiguity for linear systems with time-independent coefficients, but when these conditions are not met, the absorption of energy, if time-limited, may not necessarily result in unacceptable system motion or catastrophic failure. For such systems, our definition of instability then strictly applies only for the time interval of energy absorption, it still being necessary to interpret the resultant state of the system after the cease of energy-absorption as one of structural integrity or its lack. With this proviso the definition stands, and is used in the sequel.

For aerodynamic systems, the generalized potential energy V need not be of positive definite form. In this case, the system may be subject to instabilities of a nonoscillatory nature, so-called divergence. Since flutter instabilities are of prime importance only in the absence of such divergence, we assume throughout that these do not exist so that the earlier assumption of positive definiteness of V is retained.

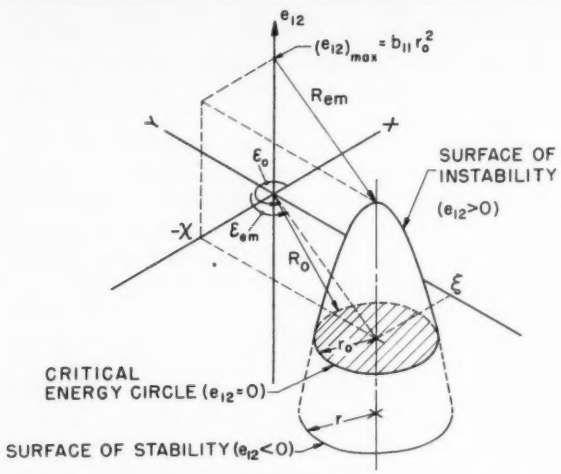

FIG. 1. Paraboloid surface of stability for binary flutter.

The Equation of Energy Balance

The integral with respect to time of Eq. (9) between limits t_0 and t_1 yields the gain or loss of total energy of the system over that time interval. Thus:

$$\Delta E = [T + V]_{t_0}^{t_1} = -\int_{t_0}^{t_1} [2\Phi + \dot{q}'C_2 q - (1/2)q'\dot{C}_1 q]dt \quad (13)$$

which is the equation of energy balance, relating the system total energy change to the external work. When the motion is periodic, and harmonic of circular frequency k, it is permissible to place $t_0 = 0$, $t_1 = 2\pi/k$. It follows by virtue of the form of the potentials T and V that *for no transient effects* (A, C independent of time), Eq. (13) reduces to

$$\Delta E = -\int_0^{2\pi/k} (2F + \dot{q}'C_2 q)dt = 0 \quad (14)$$

which is a *necessary condition* for flutter to exist. This expression depends only on certain of the aerodynamic forces, the modal amplitude ratios and phase angles, and involves no inertia or structural parameters explicitly.

Kinematically Admissible Flutter Configurations

The implications of Eq. (14) become clearer upon the specification of the type of motion. For neutrally stable flutter oscillations, we may define the motion, in matrix form, as*

$$[q_j] = [Q_j \sin (kt + \epsilon_j)]; \quad j = 1, 2, \ldots, n \quad (15)$$

which upon substitution in Eq. (14) and after integration yields

$$0 = \Delta E = -\pi k \sum_{j=1}^{n} \sum_{j=1}^{n} Q_j Q_k [b_{jk}^{(1)} k \cos (\epsilon_j - \epsilon_k) - c_{jk}^{(2)} \sin (\epsilon_j - \epsilon_k)] \quad (16)$$

* t here can be regarded as the nondimensional time Ut/b.

where the suffixes (1) and (2) refer to symmetric and skew-symmetric components, respectively, and k is the reduced frequency. Define now the amplitude ratio R_j and phase difference λ_{jk}:

$$R_j = Q_j/Q_r; \quad \lambda_{jk} = \epsilon_j - \epsilon_k \quad (17)$$

and the mean energy per cycle becomes

$$e = \Delta E/\pi k^2 Q_r^2 = -\sum_{j=1}^{n} \sum_{j=1}^{n} R_j R_k [b_{jk}^{(1)} \cos \lambda_{jk} - (c_{jk}^{(2)}/k) \sin \lambda_{jk}] = 0 \quad (18)$$

Eq. (18) is simply a statement of a condition that the $n - 1$ amplitude ratios R and the $n - 1$ phase angles λ must satisfy for flutter to exist at a given reduced frequency k. It thus defines all kinematically admissible flutter configurations, which are determined by the symmetric (aerodynamic) damping forces and the skew-symmetric stiffness forces. The latter will, in general, be solely of aerodynamic origin, inasmuch as the matrix of *structural* stiffness force coefficients is symmetric (usually diagonal, in fact). In order to see how Eq. (18) can be developed toward practical ends, it is convenient to consider the simple binary flutter case.

Binary Flutter and the Energy Circle

In the event that only two degrees of freedom are coupled, $n = 2$, Eq. (18) is reducible to a simple form by placing $Q_r = Q_2$, $\epsilon_2 = 0$ which normalization implies no loss of generality. Then $R_2 = 1$ and for simplicity let $R_1 = R$, $\lambda_{12} = \epsilon$. Eq. (18) becomes

$$e_{12} = -b_{11}\{R^2 + 2(\chi \cos \epsilon - \xi \sin \epsilon)R + \zeta\} = 0 \quad (19)$$

where

$$\chi = (b_{12} + b_{21})/2b_{11}$$
$$\xi = (c_{12} - c_{21})/2b_{11}k$$
$$\zeta = b_{22}/b_{11} \quad (20)$$

This is the polar equation of a circle, such that a vector of modulus R and argument ϵ based on the origin of cartesian coordinates traces the circle of center $(-\chi, \xi)$ and radius r_0 given by

$$r_0^2 = \chi^2 + \xi^2 - \zeta \quad (21)$$

In other words, this circle defines kinematically admissible flutter configurations of R, ϵ. (There exist actually two further restrictions on admissible R, ϵ pairs. First, because R is by definition positive, Eq. (19) indicates that $Z = \chi \cos \epsilon - \xi \sin \epsilon < 0$. Secondly, in addition Eq. (19) considered as quadratic in R can have real positive roots only if $Z^2 - \zeta \geqslant 0$. Both inequalities place bounds on the phase angle ϵ but they are seldom of significant interest in relation to the energy circle.) Such are transitional between configurations lying within the circle (when $e_{12} > 0$) which permit energy gain/instability, and those without the circle (when $e_{12} < 0$) which require energy loss/stability. Consider now the left-hand side of Eq. (19) and the value of e_{12} as R, ϵ range arbitrarily. It can be shown that e_{12} is a maximum at the center of the circle and further that

$$(e_{12})_{max} = b_{11}r_0^2 \tag{22}$$

where r_0 is, as above, the radius of the energy circle for $e_{12} = 0$. It follows that e_{12} can be represented geometrically as a paraboloidal surface horizontal sections of which are the loci of the vector R, ϵ; see Fig. 1, in which the subscript "*em*" refers to values appropriate to $(e_{12})_{max}$. Clearly, Fig. 1 can be interpreted also as the influence on the critical energy circle ($e_{12} = 0$) of variation of the damping ratio or, more precisely, of the direct aerodynamic damping coefficient* b_{22}.

Ultimate Stability

For $e_{12} = 0$, the energy circle defines physically possible configurations which permit flutter—it represents a necessary condition for flutter. Whether flutter actually occurs and if so, to which *point* of the circle it corresponds, is determined by system parameters involving generalized masses and structural stiffness or modal frequencies, which are absent from Eq. (19). In order to determine the necessary and sufficient configuration, one must use a variational principle of least Action which normally means solving the Lagrangian equations of motion for the eigenvalues and then seeking the eigenmodes. (The setting up of such auxiliary conditions using the equations of motion, for example, can lead to a complete solution for the eigenvalues as demonstrated by Pulos[24] for a binary system.) Lacking this knowledge, we note that Eqs. (19) and (21), and Fig. 1 indicate that there are some configurations represented as lying outside the critical energy circle for which the Action is such that the system can never absorb energy and therefore never flutter, *irrespective of the mass and structural stiffness characteristics.* It follows that if the critical energy circle can be made to vanish by manipulation of the significant aerodynamic couplings, then stability is always assured. We can then define a *criterion of "ultimate stability"* which states that if

$$r_0^2 < 0 \tag{23}$$

flutter instability is impossible.

In view of Eq. (22) and the fact that the absolute values of

$$(\partial e_{12}/\partial X)_{e_{12}=0} = (\partial e_{12}/\partial Y)_{e_{12}=0} = 2b_{11}r_0 \tag{24}$$

where $X = R\cos\epsilon$, $Y = R\sin\epsilon$, it is plausible to attempt an interpretation of the significance of the size of the critical energy circle. It should first be realized that the paraboloidal surface of stability (or instability) strictly has no physical validity except at $e_{12} = 0$ inasmuch as the expression for the energy exchange e_{12} is derived from considerations of sinusoidal motion. Let us suppose, however, that this surface is an adequate approximation of the true one which results from a correct representation of the motion as exponentially damped (positively or negatively). Then any nonzero value e_{12} can be regarded as the quantity of energy which must artificially be added to (or subtracted from) the system to ensure satisfaction of the equation of energy balance and so a critical flutter motion. Alternatively, the maximum value of e_{12} can be thought of as the maximum available energy which the system is capable of absorbing. This suggests that the nature of any flutter occurring for $e_{12} = 0$ should be related to the quantity $(e_{12})_{max}$ in such a way that the flutter can be described as "violent" if the configuration is potentially capable of large energy gains and "mild" if small. Through Eq. (24), this means that a large energy circle radius r_0 implies violent flutter whereas a small r_0 implies mild flutter. Thus, the question of the degree of violence of flutter is transferred from the usual considerations of decay rate of amplitude or the rate of change of this rate with airspeed say, to the consideration of the capability of a neutrally stable configuration of absorbing energy. On the basis of our suppositions, this can be stated in terms of the radius of the energy circle so that any parametric change which increases/decreases r_0 can be described as destabilizing/stabilizing.

We look more closely now at the assumption concerning the validity of the paraboloidal surface for nonzero e_{12}. If Eq. (15) is replaced by the motion

$$[q_j] = [Q_j e^{\mu t}\sin(kt + \epsilon_j)];\quad j = 1, 2, \ldots, n \tag{25}$$

the equation of energy balance (14), which will now involve T and V, yields for the binary system $n = 2$, with $R_2 = 1$, $R_1 = R$, $\epsilon_2 = 0$, $\epsilon_1 = \epsilon$, $A = 1 + 2\lambda^2$, $\lambda = \mu/k$:

$$\begin{aligned}\Delta E = [T + V]_0^{2\pi/k} = -[(e^{4\pi\lambda} - 1)b_{11}kQ_2^2/2\lambda] \times \\ [AR^2\cos^2\epsilon + R^2\sin^2\epsilon - \lambda R^2\sin 2\epsilon + \\ 2A\chi R\cos\epsilon - 2(\xi + \lambda\chi)R\sin\epsilon + Ab_{22}]\end{aligned} \tag{26}$$

which is the polar equation of a central conic traced by the radius vector R, ϵ in the $X = R\cos\epsilon$, $Y = R\sin\epsilon$ plane. The ellipse center is given by [compare Eq. (20)]

$$\begin{aligned}X_c &= -\chi + \xi\lambda/(1 + \lambda^2) \\ Y_c &= \xi(1 + 2\lambda^2)/(1 + \lambda^2)\end{aligned} \tag{27}$$

the inclination of the major axis to OX is $\alpha = -(1/2)\tan^{-1}(1/\lambda)$, while the square of the major and minor axes are given by

$$\begin{aligned}(1 + \lambda^2 \pm \lambda\sqrt{1 + \lambda^2})\{-4\pi\lambda\Gamma/b_{11}(e^{4\pi\lambda} - 1) + \\ (1 + 2\lambda^2)[r_0^2 - \lambda^2\xi^2/(1 + \lambda^2)]\}^{-1}\end{aligned} \tag{28}$$

where $\Gamma = \Delta E/2\pi kQ_2^2$; see Fig. 2. The total energy exchange can be maximized by considering $\partial\Gamma/\partial X = \partial\Gamma/\partial Y = \partial\Gamma/\partial\lambda = 0$, the first two conditions of which lead to the location in the X, Y plane of Γ_{max}; thus X_{max}, Y_{max} are found from Eq. (27) by letting $\lambda = \lambda_{max}$. The third condition written as

$$(\partial\Gamma/\partial\lambda)_{X=X_{max},Y=Y_{max}} = 0 \tag{29}$$

* One would expect Eqs. (19) and (20) to show cyclic behavior with respect to the subscripts 1 and 2, so that b_{22} is not a preferred quantity. The cyclic nature of the results is achieved by recasting Eq. (19) by placing $R_2 = R$. Succinctly, as formulated the analysis deals with $R = Q_1/Q_2$ and not its inverse Q_2/Q_1, which corresponds to a definition of $\xi = \xi' = b_{11}/b_{22}$.

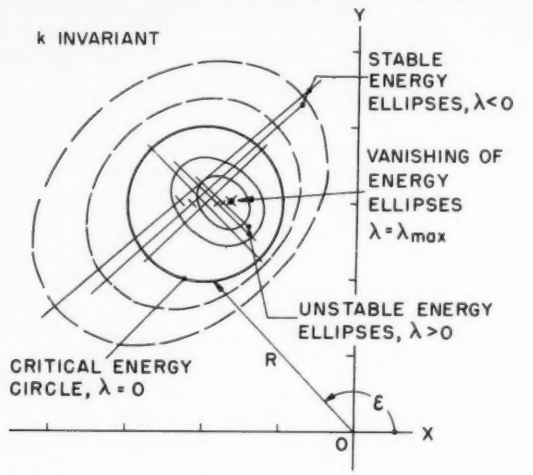

FIG. 2. Energy balance ellipses for super- and subcritical motion; λ = damping ratio.

reduces ultimately to

$$[(1 + 5\lambda^2 + 2\lambda^4)/(1 + \lambda^2)^2 + (1 - 2\lambda^2)(r_0/\xi)^2/\lambda^2][(1 - e^{-4\pi\lambda})/4\pi\lambda] + Y_m/\xi - (1 + 2\lambda^2)(r_0/\xi)^2/\lambda^2 = 0 \quad (30)$$

It is realistic now to limit λ so that λ is small compared with unity, so that

$$1 \pm 2\lambda^2 \approx 1 \pm \lambda^2 \approx 1, \quad e^{4\lambda\pi} = 1 + 4\pi\lambda + 8(\pi\lambda)^2 \quad (31)$$

and those quantities, χ, ξ, r_0 dependent on the flutter coefficients may assume their sinusoidal values for which rigorously $\lambda = 0$. By Eq. (30), it follows that

$$\begin{aligned} \lambda_{max} &= (1/6\pi)[-1 + \sqrt{1 + 3(2\pi r_0/\xi)^2}] \approx r_0/\xi\sqrt{3} \\ \Gamma_{max} &= (1/3)b_{11}r_0^2[2 + \sqrt{1 + 3(2\pi r_0/\xi)^2}] \\ X_{max} &= -\chi + \xi\lambda_{max} \\ Y_{max} &= \xi \end{aligned} \quad (32)$$

Expression (28) for the ellipse axes reduces simply to

$$(1 \pm \lambda)[-\Gamma/b_{11}(1 + 2\pi\lambda) + r_0^2]^{-1} \quad (33)$$

Eqs. (32) form the basis of the claim that qualitatively the representation of Fig. 1 (based on $\lambda = 0$) and the interpretation placed on the significance of the magnitude of the energy circle radius r_0 is an adequate one. But we may state further that, for small λ, the magnitude of the maximum energy capable of absorption is a simple function of r_0 defined by the second of Eqs. (32); and, in fact, there corresponds to this condition a maximum (positive) damping ratio λ_m which the system can attain which is related to r_0 in the manner of the first of Eqs. (32). We choose then to define the nature of a system's critical flutter oscillation in terms of its energy absorption potentiality.

We conclude then that if in practice it is not possible to satisfy the criterion (23), it is at least desirable to minimize the energy circle radius by adjustment of the parameters involved in χ, ξ, ζ.

Higher Order Systems and Stability

For systems with many degrees of freedom, $n > 2$, Eq. (18) does not prove as tractable as for the binary case. It is often no restriction to limit considerations to a single pair of freedoms as an approximate representation of the fluttering system since such degenerate binary forms contain all the essential characteristics of the more general system. It is important, of course, to select the appropriate parent binary form and this is not always an easy choice for today's configurations. Then again it is increasingly the case that a binary system is an inadequate approximation for modern configurations. It is of interest, therefore, to look briefly at the general Eq. (18), and it proves fortuitous that this can be rewritten quite rigorously in a form involving the $n(n-1)/2$ principal binary constituents. We define e_{jk} as the expression—see, for example, Eq. (19)—for energy for the binary constituent formed from the system whose two displacements are q_j and q_k, all other q being zero. Then Eq. (18) can be written, without approximation,

$$e = \sum_{j=1}^{n} \sum_{k>j}^{n} e_{jk} + (n-2) \sum_{j=1}^{n} b_{jj}R_j^2 = 0 \quad (34)$$

in which for all damping coefficients $b_{jj} > 0$, which is the usual case, the single summation is always positive. This equation simply states that the total energy balance is the sum of the energies of the constituent binary systems and the individual modal dissipation energies. For simplicity, consider the ternary system, $n = 3$:

$$e_{123} = e_{12} + e_{13} + e_{23} + b_{11}R_1^2 + b_{22}R_2^2 + b_{33}R_3^2 \quad (35)$$

Suppose flight conditions are such that all three binary systems are unstable—i.e., each $e_{jk} > 0$; then clearly $e_{123} > 0$ and the ternary system is also unstable. The same result applies to the general Eq. (34). On the other hand, suppose all binary systems are stable—i.e., all $e_{jk} < 0$; the higher order systems are not necessarily stable and provided some or all of the direct (positive) *damping coefficients* are sufficiently *large* they may be *unstable*. Other corollaries are simply deduced, viz.:

(a) If all binary systems are critical ($e_{jk} = 0$), all higher order systems are stable/unstable provided all dampings $b_{jj} \lesseqgtr 0$.

(b) If one binary system is critical (say, $e_{12} = 0$) and both the other binaries are unstable ($e_{13}, e_{23} > 0$) for the same flight conditions, then for these conditions of flight the ternary system is necessarily unstable. In other words, the addition of the third degree of freedom is destabilizing. However, the converse is not necessarily true.

Eq. (34) thus offers a guide to the relevance of higher modes. Béatrix[14] has suggested a method directed to the same end based on a study of the way in which constituent modal energies change with airspeed. See also Van de Vooren.[10]

Structural Damping

Structural damping is variously represented.[17] If a viscous type damping force is an adequate representation, then these forces appear in Eqs. (3) or (4) simply as added components of the damping matrix. Thus, B is replaced by $B + D$ where D is a diagonal matrix of modal damping coefficients; $b_{jj} \to b_{jj} + d_{jj}$; $d_{jk} = 0$, $j \neq k$. This substitution carries right through the analysis of the energy balance. The more usual "hysteretic" representation of structural damping—see Eq. (2)—stems from modal damping forces of the form[17] $d_{jj}\dot{q}/\omega$ or $d_{jj}\dot{q}\,|q/\dot{q}|$. Energy dissipation per cycle of oscillation arising from such forces is then, *respectively*,

$$\left.\begin{aligned} e_d &= \pi \sum_{j=1}^{n} d_{jj}Q_j^2 \\ \text{or} \qquad e_d &= 2 \sum_{j=1}^{n} d_{jj}Q_j^2 \end{aligned}\right\} \tag{36}$$

which differ only in a constant multiplier. Eqs. (16), (18), and (19) then possess a right-hand side of the form $\Sigma\, d_{jj}Q_j^2 \cos(\epsilon_j - \epsilon_j)$, $\Sigma R_j^2 d_{jj} \cos \lambda_{jj}$, and $(d_{11}R^2 + d_{22})/k$, respectively, where the constant factor of Eq. (36) has been absorbed in d_{jj}. It is possible then to absorb the effects of structural damping simply by defining new damping coefficients

$$\bar{b}_{jj} = b_{jj} + d_{jj}/k \tag{37}$$

which influence system stability through the parameters of Eq. (21) for the energy circle radius. By considering $\partial r_0^2/\partial \bar{b}_{22}$ and $\partial r_0^2/\partial \bar{b}_{11}$ the variation of r_0 due to changes in b_{11}, b_{22} is given by

$$\delta r_0^2 = -[\delta \bar{b}_{22} + (2r_0^2 + \bar{\xi})\delta \bar{b}_{11}]/\bar{b}_{11} \tag{38}$$

Assuming, as usual, $\bar{\xi} > 0$, $\bar{b}_{11} > 0$, it follows that for $r_0^2 \gtrless 0$ increases (decreases) of either or both b_{11} and b_{22} cause reductions (augmentations) in r_0^2 and, therefore, are stabilizing (destabilizing). [It is of interest to compare this result with that deduced from Eq. (35) for ternary flutter—there is no paradox since the stability determining quantities are essentially χ, ξ of Eq. (20), not the direct damping coefficients.] For $r_0^2 < 0$—i.e., for an ultimately stable system changes in dampings can cause stabilization or destabilization according as $2r_0^2/\bar{\xi}$ is $\lesssim 1$. Either possibility exists also when $\delta \bar{b}_{11}$, $\delta \bar{b}_{22}$ have opposite signs—see also the results of Salaün.[15]

Degenerate Binary Systems

In the unusual event that a system has $\xi = 0$—i.e., the aerodynamic stiffness matrix is symmetric, the energy circle radius becomes $r_0^2 = \chi^2 - \zeta$, so involving only damping coefficients. Stability questions are then related only to the dissipation function F, as previously noted. This can be shown in a direct way by noting that for $n = 2$, F is a positive definite form if all discriminants $|b_{jk}^{(1)}| > 0$; i.e.,

$$\left.\begin{aligned} b_{11} > 0 \text{ and } b_{11}b_{22} - [(b_{12} + b_{21})/2]^2 > 0 \\ \text{which is} \qquad b_{11}^2(\zeta - \chi^2) > 0 \\ -b_{11}^2 r_0^2 > 0 \\ \text{or, finally,} \qquad r_0^2 < 0 \end{aligned}\right\} \tag{39}$$

It is more often the case that $\chi^2 - \zeta$ is small and negative and ξ^2 is so large as to dominate the magnitude of r_0^2. In this case, a reasonable approximation for the purposes of assessing the system is to place $\chi^2 - \zeta = 0$ so that the skew-symmetric stiffness components are a direct indication of system stability. Mere inspection of these flutter coefficients will suggest which binary couplings are significant. The neglect[23] of the damping terms leads to a conservative approximation.

Aerodynamic Balancing

The application of the principles above to the prevention or elimination of flutter can be thought of as aerodynamic balancing. Early techniques of flutter prevention often consisted essentially of dynamic balancing—i.e., the elimination or optimization of inertial couplings. Here we are primarily concerned with bringing within acceptable bounds the aerodynamic couplings. Mass and structural stiffness distribution are not *explicitly* involved, but their implicit role appears in the dependence of the aerodynamic coefficients b_{jk}, c_{jk} on mode shapes as well as their influence on the reduced frequency k at flutter.

In subsequent sections, we proceed to examine some examples of supersonic flutter in order both to gain an insight into the essential mechanism and to discover in what way useful application of the ultimate stability concept may result.

General Supersonic Flutter

Consider the regime[18] for which piston theory oscillatory airforces are appropriate. The generalized forces can be put in the nondimensional form

$$Q_{jk} = c_{jk} + 2ikb_{jk} =$$

$$(2/M)\int_{\eta}\int_{\psi} (1 + \Gamma)[f_j f_k' + 2ikf_j f_k]\,d\psi\,d\eta \tag{40}$$

in which $f_j = f_j(\psi, \eta)$ define nondimensional modes as functions of the nondimensional coordinates ψ (streamwise; $\psi = x/2b$) and η (spanwise; $\eta = y/s$) and the prime means $\partial/\partial\psi$. Γ is a streamwise profile parameter, such that

$$\Gamma = (1/2)(\gamma + 1)M \cdot \partial z_0(\psi)/\partial\psi \tag{41}$$

when the binomial expression[18] for the pressure coefficient is truncated to exclude downwash terms of degree $\geqslant 3$. In Eq. (41), $z_0(\psi)$ defines the profile shape. It follows* immediately from Eq. (40) that the dissipation matrix $[b_{jk}]$ is symmetric and that for $f_k' = 0$; i.e., for any pure bending mode, $c_{jk} = 0$ so that there exist

* The *only* restriction on profile shape implicit in the derivation of the form (40) is the requirement of profile symmetry about the mean chord-line. "Fore and aft" symmetry is not necessary.

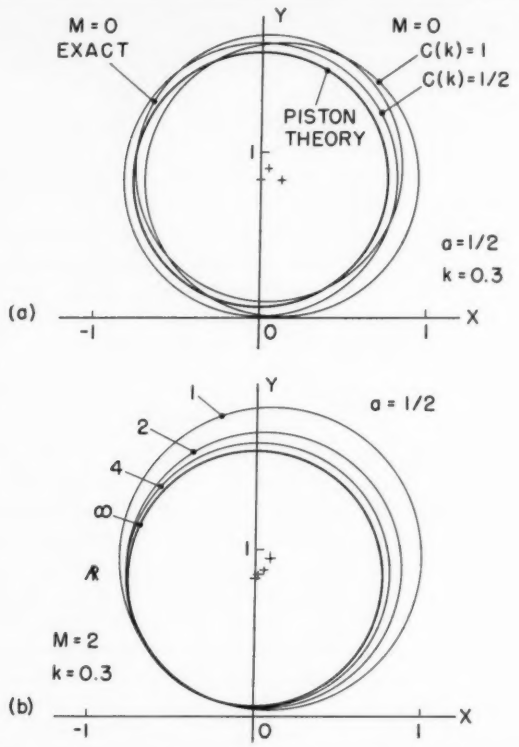

FIG. 3. Energy circles for binary wing bending-torsion flutter. (a) Supersonic flutter compared with incompressible for midchord pitch axis of two-dimensional section. (b) Effect of aspect ratio on flutter of rigid flat plate at $M = 2$.

likely large skew-symmetric components $c_{jk} - c_{kj}$. Interpreting this in binary terms, we find that

$$\chi = b_{jk}/b_{jj}; \quad \xi = -c_{jk}/4kb_{jj}; \quad \zeta = b_{kk}/b_{jj} \quad (42)$$

For a surface of (near) uniform mass distribution, the orthogonal modal coupling integral $\int\int f_j f_k$ is (small) zero so that for no thickness effects, $\Gamma = 0$, $b_{jk} = \chi = 0$. It can be expected then that the skew-symmetric effects embodied in ξ will dominate the magnitude of the energy circle radius for any binary coupling involving a bending type mode, in such a case. This result is closely true for more general modal configurations.

Binary Bending-Torsion Wing Flutter

If the above expressions are developed for the simple two-dimensional, infinite aspect ratio wing with a bending mode $f_1 = 1$, and torsion mode $f_2 = x/2b - a$, where $x = 2ba$ defines the pitch axis position aft of the leading edge we find

$$\begin{aligned} \chi &= 1/2 - a - (\gamma + 1)MA_w/16b^2 \\ \xi &= 1/4k \\ \zeta &= 1/3 - a + a^2 - (\gamma + 1)MA_w(1/2 - a)/8b^2 \end{aligned} \quad (43)$$

$$\text{so that} \quad \zeta - \chi^2 = 1/12 - [(\gamma + 1)MA_w/16b^2]^2 \quad (44)$$

$$\text{and} \quad r_0^2 = \xi^2 - (\zeta - \chi^2) \quad (45)$$

By inequality (39), the dissipation F is positive definite, from Eq. (44), provided $(\gamma + 1)MA_w/b^2 < 8/\sqrt{3}$, which for a doubly symmetric wedge profile in air reduces to $M\tau < 5/3\sqrt{3} \approx 1$. It is clear then that for practical profiles F is a positive definite form, $\zeta - \chi^2$ is small compared with ξ^2 for the small values of k experienced in this type of flutter, and the energy circle radius is predominantly determined by ξ. For the flat plate profile, specifically, and rigorously,

$$r_0 = (1/2)\sqrt{1/4k^2 - 1/3} \quad (46)$$

a result independent of both Mach Number and pitching axis, which vanishes for $k = k_{cr} \geqslant \sqrt{3}/2$ when flutter is impossible, the system having attained ultimate stability. For the general profile, it transpires that the influence of thickness on the energy circle is very small *for a prescribed k*. It is always mildly destabilizing when k is invariant with change in the thickness parameter $MA_w/16b^2$. However, in practice, changing thickness normally results in a change in k the nature of which is not revealed by the equation of energy balance approach. The qualitative effect can be estimated by looking at the change in the modal aerodynamic stiffnesses which will influence the flutter frequency and therefore k. Thus, $c_{11} = 0$ and $c_{22} = [4(1 - 2a) - (\gamma + 1)M\tau]/4M$ for the double wedge section which decreases with increasing $M\tau$. Accordingly, k can be expected also to decrease so leading to increased r_0 and destabilization. For a pitch axis near midchord, $a \to 1/2$, the effect may well be significant.[18]

It is of some interest to compare the results (43) and (46) with those arising from another quasi-steady theory,[19] viz., two-dimensional incompressible flow. By arbitrarily placing the Theodorsen function $C(k) = 1/2$, 1 we derive two approximate formulations of the critical energy circle. We find in both cases that like the piston theory result (46) the radius is independent of pitch axis position whereas the coordinates of the center are given, respectively, by $[(1/2 - a)/2, 1/4k]$, $[(1/4 - a)/2, 1/4k]$—compare Eq. (43) for zero thickness. The energy circles are graphed in Fig. 3(a) for the pitch axis at midchord and $k = 0.3$, where, in addition, is given that for the exact linearized theory for $M = 0$. We note that for $C(k) = 1/2$ the energy circle passes through the origin since $\zeta = 0$, where $R = 0$ and ϵ is indeterminate. (This result is independent of k for $a = 1/2$.) This is interpretable as a zero airspeed natural oscillation of a single mode.

Fig. 3(b) illustrates the effect of aspect ratio on the energy circle for a rectangular flat plate fluttering in rigid translation and pitching about the midchord. It is assumed that for $\mathcal{R} = \infty$ piston theory is acceptable at $M = 2$. The finite $\mathcal{R}$ circles are based on corrections to the $\mathcal{R} = \infty$ case defined by a linearized theory[20] which is considered valid for $\mathcal{R} > 1/\sqrt{M^2 - 1} = 0.58$. Decreasing $\mathcal{R}$ is seen to be destabilizing in this case. In Fig. 4 are given further results for pitching about the leading edge ($a = 0$); Fig. 4(a) depicts the effect of Mach Number for $\mathcal{R} = \infty$, while Fig. 4(b) shows the influence of $\mathcal{R}$ for $M = 1.4$, $k = 0.3$. In both cases,

exact linearized theory is used. It appears that M variation has little influence on the energy circle radius whereas decreasing $\mathcal{R}$ is strongly stabilizing.

Binary Wing-Aileron Flutter

Let $2bh$ define the chordwise location of the aileron hingeline aft of the wing leading edge. Consider first wing translation-aileron rotation coupling according to piston theory in which now an additional downwash term is allowed in the expression for the pressure coefficient so that effects of mean aileron displacement are included. It is found that, for a double-wedge profile,

$$\begin{aligned} \chi &= (1-h)^2/C \\ \xi &= \chi/2k(1-h) \\ \zeta &= 2\chi(1-h)/3 \\ A &= -(\gamma+1)M\tau + B/2 \\ B &= (\gamma+1)M^2(\tau^2+\beta_0^2) \\ C &= (4+B)/(2+A) \end{aligned} \tag{47}$$

by which the energy circle is defined (β_0 = initial aileron deflection). Stability boundaries defined by $r_0^2 = 0$ are shown in Fig. 5 as a function of aileron chord $(1-h)$ and reduced frequency k, for the zero thickness case, $A = B = 0$. For $k \leqslant 3/4$, for example, it is impossible to achieve ultimate stability.

When thickness and initial aileron deflection are allowed with k invariance, it is possible to deduce that the former by itself is stabilizing, the latter mildly destabilizing. Together the overall effect is destabilizing only when β_0 is large compared with τ.

Consider now the case of wing pitch-aileron rotation coupling for the double wedge profile. Analogous to Eq. (47), we then have

$$\left.\begin{aligned} \chi &= (1-h)^2[h-a+2(1-h)/3]/D \\ \xi &= (1-h)(h-a)/2kD \\ \zeta &= 2(1-h)^3/3D \\ D &= C(a^2-a/2+1/12)+(1-2a)/2 \\ C &= (4+B)/(2+A) \end{aligned}\right\} \tag{48}$$

and the vanishing of the energy circle, $r_0^2 = 0$, leads to a functional relation between the hinge-line location h and the pitch axis a, thus:

$$\begin{aligned} 3(1-h)a^2 - 2(1-h-h^2)a - \\ (1+h+h^2)/3 - [2a^2-a+1/6]D + \\ 3(a-h)^2/4k^2(1-h) = 0 \end{aligned} \tag{49}$$

Graphical solutions of this condition for the flat plate $A = B = 0$ are given in Figs. 6 and 7. The former applies to a quarter-chord aileron, $h = 3/4$ and the shaded area indicates ultimate stability, $r^2 < 0$. The contours $r^2 \neq 0$ reveal the existence of a worst siting of the pitch axis, viz., $a = 1/4$ where for a given k, the energy circle radius is a maximum. If increasing k is regarded as being due to increasing a modal stiffness (the aileron circuit, say), then the contours suggest that in the region $a = 1/4$ such a measure is not effectively stabilizing. Rearward positions of the pitch axis appear more favorable. Fig. 7 summarizes the critical condition for $0 \leqslant h \leqslant 1$, $0 \leqslant a \leqslant 2$ for a variety of k, reflecting a general behavior similar to that for $h = 3/4$, Fig. 6. For $h = a$, the system possesses ultimate stability for all k.

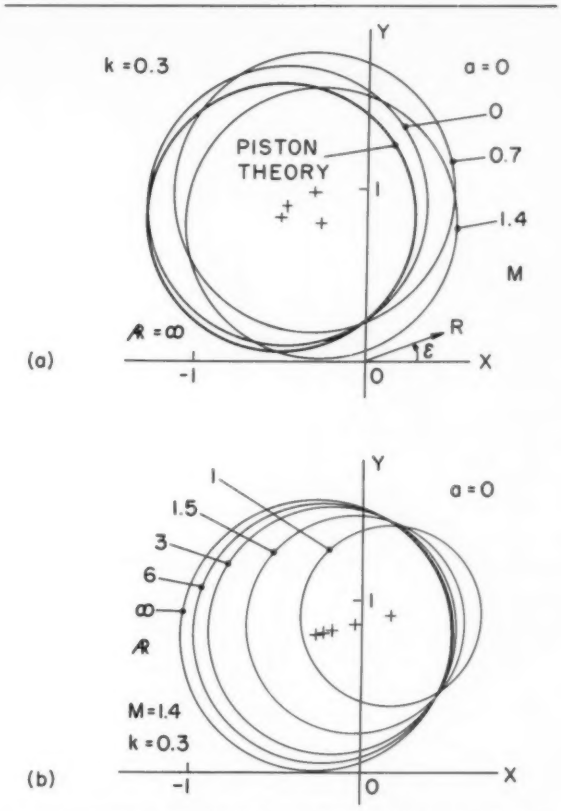

FIG. 4. Energy circles for binary wing bending-torsion flutter. (a) Effect of Mach Number on two-dimensional section pitching at leading edge. (b) Effect of aspect ratio at $M = 1.4$ for rigid flat plate pitching at leading edge.

Flutter of All-Moving Surfaces

The configuration used here consists of a finite wing symmetrically tapered about the locus of midchord stations, having a taper ratio t = tip chord/root chord. Two modes are considered, the first being rigid body pitch about an axis $2ba$ aft of the root leading edge, the second being a bending mode represented by the nondimensional modal function $f = (\eta^2 - \bar{\eta}^2)/(1 - \bar{\eta}^2)$. The value $\bar{\eta}$ of the spanwise coordinate η thus defines the spanwise position of the bending nodal line. For the delta wing, $t = 0$, the use of piston strip theory will yield correct values[21] of many of the generalized forces for the modes considered, while those remaining will be closely correct. For $t > 0$, the approximation is less good because of the parallel tip effect, but for the purpose of illustrating the principle of ultimate stability this error is neglected.

Fig. 8 depicts the critical stability surface, $r^2 = 0$ in terms of pitch axis location a, bending nodal line position $\bar{\eta}$, and reduced frequency k based on the root chord for the delta wing $t = 0$. The surface is symmetrical about the $\bar{\eta}$:k plane at $a = 1/2$ which for in-

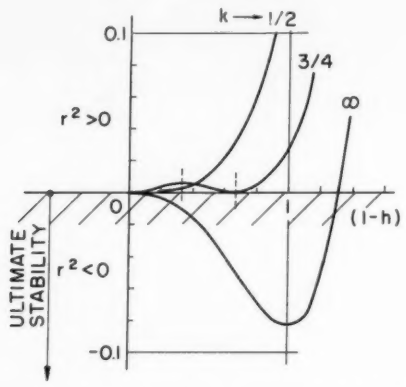

FIG. 5. Binary wing bending-aileron supersonic flutter showing ultimate stability boundaries as function of aileron chord $(1 - h)$ and reduced frequency.

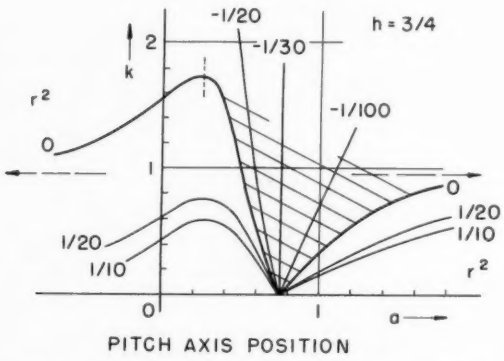

FIG. 6. Binary wing torsion-aileron supersonic flutter showing contours of the energy circle radius squared as function of pitch axis position and reduced frequency for hinge position of 3/4 chord.

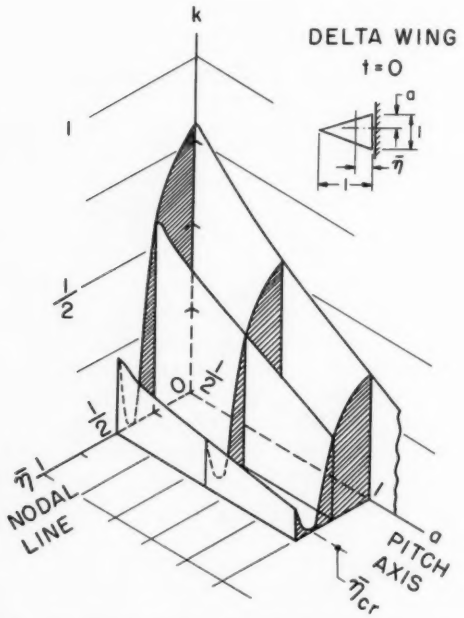

FIG. 8. Supersonic binary flutter of all-moving delta showing stability surface as function of nodal line and pitch axis positions. Ultimate stability exists above the surface.

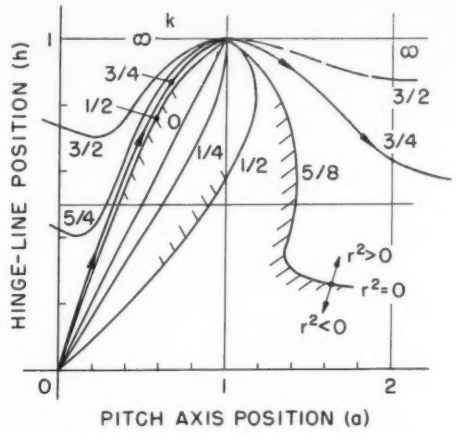

FIG. 7. Binary wing torsion-aileron supersonic flutter showing limiting reduced frequencies for ultimate stability as function of pitch axis and hinge-line positions.

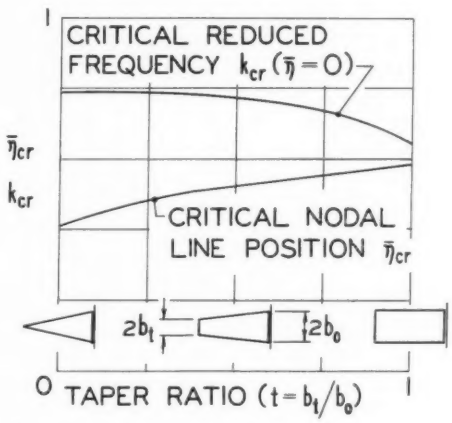

FIG. 9. Flutter of all-moving surfaces showing variation of critical nodal line position and reduced frequency for $\bar{\eta}_{cr} = 0$ with taper ratio.

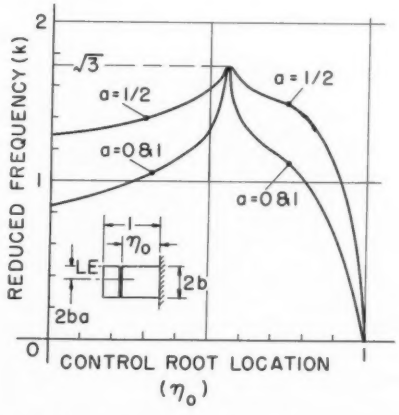

FIG. 10. Flutter of carried all-moving rectangular control showing limiting reduced frequency as function of pitch axis position a and control span. Ultimate stability exists above the curves.

board locations of the bending nodal line is clearly the worst situation for the pitch axis. Ultimate stability exists *above* the surface. It is of interest to note that there exists an $\eta = \eta_{cr}$ for which ultimate stability is assured irrespective of k. Its value in this case is $\bar{\eta}_{cr} = 1/\sqrt{6}$ and is the optimum nodal line location—the system will never flutter. The effect of taper ratio on the value of η_{cr} is shown in Fig. 9 where also is plotted for $\bar{\eta} = 0$ the value of k_{cr} which always occurs at the worst pitch axis position ($a = 1/2$). Increasing taper ratio is seen, in this case, to be mildly stabilizing.

When the all-moving control is carried by a wing surface, the binary flutter is conveniently formulated in terms of the same bending mode and rigid control pitch outboard of the spanwise station η_0 which defines the control root chord position. For the case of $\bar{\eta} = 0$—i.e., the nodal line of the bending mode is at the wing root, and a zero thickness profile, the critical stability boundaries are shown in Figs. 10 and 11. The former relates to a rectangular planform, the latter to a delta. Ultimate stability exists above the boundaries. In both cases, it is clear that from the ultimate flutter stability viewpoint the carried control is superior to the all-moving wing only for a limited range of extreme outboard positions of the carried control. For the delta wing, for example, ultimate stability can *never* be achieved for a control span one quarter of the wing-span—i.e., for $\eta_0 = 3/4$.

Panel Flutter

Let us consider the two-dimensional panel subject to piston theory type forces for which we shall assume zero thickness. Further, we use a modal representation of the displacements so that for simply-supported edge conditions (normal to airstream) the mth mode is simply

$$f_m = \sin m\pi\theta, \quad m \geq 1 \tag{50}$$

and we make no distinction between a "membrane" and a "plate" panel. The streamwise coordinate is here $x = 2b\theta$, b being the panel semilength, so that the panel is defined between $\theta = 0, 1$. Using Eq. (40), it is readily shown that the aerodynamic damping coefficients are (omitting the common multiplier $2/M$)

$$b_{mn} = 1/2; \quad b_{mn} = 0, \text{ all } m, n \tag{51}$$

The damping matrix is thus *diagonal*. The aerodynamic stiffness coefficients are found to be

$$c_{mn} = \begin{cases} 0; & m \neq n, \text{ both odd or even} \\ 2mn/(m^2 - n^2); & m + n \text{ odd} \end{cases} \tag{52}$$
$$c_{mn} = 0$$

The skew-symmetric stiffness components, therefore, are

$$c_{mn}^{(2)} = (c_{mn} - c_{nm})/2 = 2mn/(m^2 - n^2) \tag{53}$$

For any binary coupling, the energy circle radius becomes

$$r_0^2 = 4[mn/(m^2 - n^2)]^2/k^2 - 1 \tag{54}$$

and the critical value of reduced frequency corresponding to ultimate stability is derived from $r_0^2 = 0$ as

$$k_{cr} = \pm 2mn/(m^2 - n^2) \text{ and } r_0^2 = (k_{cr}/k)^2 - 1 \tag{55}$$

Eqs. (51) and (52) indicate that the results (52)–(55) apply only for m even, n odd, or vice versa. In all other cases, the modes are completely uncoupled, and flutter considerations do not arise.

Under prescribed airstream conditions or for prescribed k, Eq. (55) shows k_{cr} to be a direct indication of the energy circle radius and, therefore, of the significance of coupling of any two modes. In Fig. 12 are plotted* values of k_{cr} for some of the lower modes,

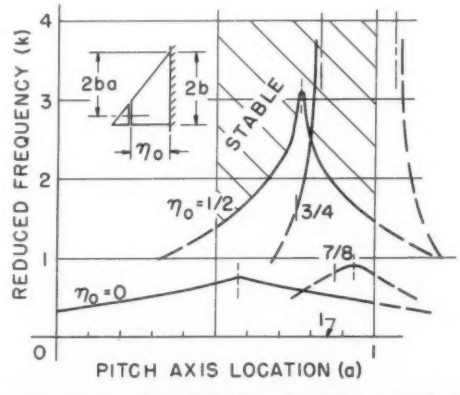

FIG. 11. Flutter of carried all-moving delta control showing limiting reduced frequency as function of pitch axis position a and control span.

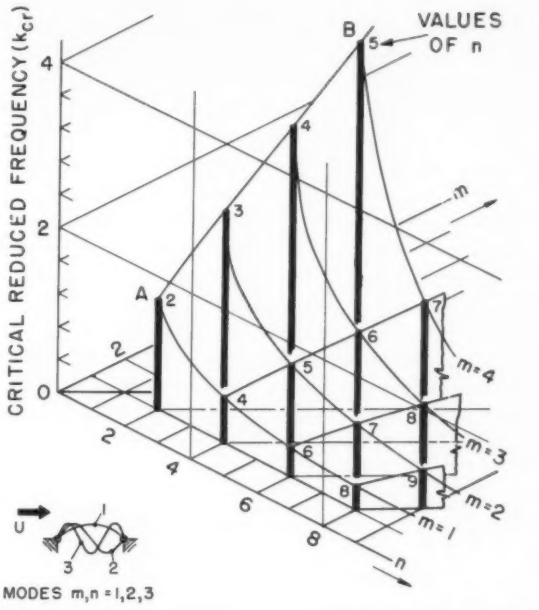

FIG. 12. Two-dimensional panel flutter showing limiting reduced frequency for binary couplings of modes $f_m = \sin m\pi\theta$ and $f_n = \sin n\pi\theta$.

* In Fig. 12, the continuous curves are for convenience of visualization only; m and n are, of course, integers.

and it is at once evident that whereas for increasing n the energy circle radius rapidly decreases (toward zero), for increasing m the radius increases rapidly for low n. This suggests that such higher modes are of vital significance in a modal-type analysis but it is not clear how this significance is manifest; and it is of interest that the analysis so far takes no cognizance of any difference between the behavior of a membrane and a plate. The discrimination of the two structures arises solely in the disparity of their respective actual flutter reduced frequencies k in Eq. (55) due to differing modal frequencies for the same mode. This is most clearly seen by an assessment of the flutter reduced frequency k_f by means of a conventional solution of the binary flutter determinant. The separated characteristic equation yields finally, for any two modes m, n:

$$k_f^2 = (k_m^2 + k_n^2)/2 \tag{56}$$

where k_m and k_n are reduced *modal* frequencies, and

$$(\mu M)^2(k_m^2 - k_n^2)^2 = k_{cr}^2 - k_f^2 = k_f^2 r_0^2 \tag{57}$$

where μ is the density ratio, the exact definition of which is immaterial. Eq. (56) allows discrimination of a membrane and plate by use of the k_m and k_n appropriate to each. Eq. (57) shows that for flutter to exist

$$k_f^2 \leq k_{cr}^2 \tag{58}$$

which is *exactly* the condition derivable from the criterion of ultimate stability through Eq. (55). In other words, ultimate stability is here synonymous with stability in the usual sense. From Eqs. (56) and (57), provided Eq. (58) is satisfied, the flutter speed is given by

$$U_f = \mu M b(\omega_m^2 - \omega_n^2)/\omega_f r_0 \tag{59}$$

Consider now the values of k_f, Eq. (56). The modal frequencies and, therefore, modal reduced frequencies k_m are proportional to m and m^2, respectively, for the membrane and plate. The constants of proportionality depend on membrane and plate mass and stiffness properties. Let these be so chosen that for both plate and membrane k_f assumes the value of k_{cr}, for binary coupling of the lowest modes—i.e., $k_f = k_{cr} = 4/3$ for both structures for $m = 1$, $n = 2$. It is simple to show then that for the plate $k_f(m, n) > k_{cr}(m, n)$ for all other m, n; while for the membrane $k_f(m, n) < k_{cr}(m, n)$ for all couplings m, $n = m + 1$ but exceeds $k_{cr}(m, n)$ for all remaining binary couplings. Interpreting this in terms of Fig. 12, the "Surface" formed by k_f for the plate lies everywhere above the "Surface" of k_{cr} shown in that figure, excepting at $m = 1$, $n = 2$. In other words, all the higher mode binaries are stable. For the membrane this is not so, and for all binary couplings corresponding to the line AB of Fig. 12, $k_f < k_{cr}$, and all such binaries are unstable at some finite airspeed; elsewhere all binaries are stable for the membrane. The two structures are thus basically different, and it appears intuitively that whereas for the plate the higher modes become increasingly less significant, for the membrane *all* the higher modes attain importance in a Rayleigh-Ritz type analysis.[18] Unfortunately, the results above do not allow a rigorous demonstration of this.

Chordwise Flexible Surfaces

The flutter of an extremely small aspect ratio delta wing provides an example† of the limitations of the energy balance approach when dealing with multi-degree of freedom systems as well as highlighting the dangers of disregarding structural parameters. The wing is regarded as possessing no spanwise deformation, the vibration modes being polynomial functions only of the streamwise coordinate. Calculated by an iteration process, the first three elastic modes are considered and shown sketched in Fig. 13. In addition, the two rigid body modes of translation and pitch are included in the analysis. The modes, designated 1, 2, . . . , 5 have modal frequency parameters which can be represented, respectively, as 0, 0, 1, 3, 8 approximately. When the flutter coefficients are calculated on the basis of slender body theory,[22] we find

$$[b_{jk}] = \begin{bmatrix} 1 & -1 & 0.59 & -0.28 & 0.98 \\ 0 & 0.25 & -0.30 & 0.14 & -0.49 \\ 0 & 0 & 0.047 & -0.095 & 0.31 \\ 0 & 0 & 0.012 & 0.011 & -0.13 \\ 0 & 0 & -0.015 & 0.0022 & 0.21 \end{bmatrix}$$

(1) rigid translation
(2) rigid pitch
(3) fundamental elastic mode
(4) 1st overtone elastic mode
(5) 2nd overtone elastic mode

$$[c_{jk}] = \begin{bmatrix} 0 & -1.5 & 1.8 & -1.6 & 9.9 \\ 0 & 0 & -1.3 & 0.36 & -4.2 \\ 0 & 0 & -0.21 & -0.17 & 2.0 \\ 0 & 0 & 0.05 & -0.088 & -0.57 \\ 0 & 0 & -0.05 & 0.066 & 0.57 \end{bmatrix}$$

together with a symmetric matrix of virtual inertias and a diagonal generalized inertia matrix. Our object is to assess the relevance of each mode and the likelihood of flutter. Form first the symmetric damping matrix $b_{jk}^{(1)} = (b_{jk} + b_{kj})/2$ and, secondly, the skew-symmetric stiffness matrix $c_{jk}^{(2)} = (c_{jk} - c_{kj})/2$, which is easily done mentally. We notice that the former are, in general, quite small compared with the corresponding latter elements, which can, therefore, be expected to

† Taken from work currently sponsored by the AFOSR under contract No. AF49(638)-219.

dominate the magnitude of the energy circle radius for the various binary couplings between the five modes. It is clear too that the skew-symmetric components for the rigid-body modes (the first and second rows and columns) are significantly large. On this basis then, we are led to conclude that both rigid body modes can be expected to play a leading role in flutter of the coupled system. However, this in fact is not so, simply because all subdiagonal elements of all coefficients a (inertia), b, c, as well as the virtual mass coefficients are zero in columns 1 and 2—i.e., for the two rigid body modes. This means that in the flutter determinant all the corresponding δ_{jk}—see Eq. (1)—are zero so that these two modes are completely uncoupled from the elastic modes; they play no part in the flutter of the coupled system. The energy balance concept thus makes no explicit allowance for such partly-triangular flutter determinants; it essentially provides a *necessary* condition for flutter.

Deleting then the first two rows and columns of the coefficient matrices, we assess the remaining binary couplings, 3-4, 4-5, 3-5. A little mental arithmetic shows that the energy circle radii of the first two are of the same order whereas that of the third is somewhat larger, which suggests that mode 5 has an important role and should be included in a conventional flutter analysis. Such an analysis, however, reveals that the 3-5 and 4-5 binaries are always stable, that the 3-4 binary produces critical flutter conditions which, as may *now* be expected, differ slightly and only quantitatively from the critical flutter conditions for the 3-4-5 ternary coupled system. We conclude that although mode 5 is potentially capable of a flutter coupling with mode 3, the *structural* parameters are inappropriate to allow it—the ratio of modal stiffnesses, for example, is $(8/1)^2$.

This is not strictly a fair test inasmuch as the energy circle concept rightly is restricted to binary systems. More rigorously, Eq. (35) should be consulted in conjunction with the known results of the binary flutter analyses. Thus, for flight conditions which make the 3-4 binary critical, $e_{34} = 0$ and

$$e_{345} = -|e_{35}| - |e_{45}| + 0.05R_3^2 + 0.01R_4^2 + 0.2R_5^2 \tag{60}$$

since 4-5, 3-5 binaries are always stable. It is impossible to decide whether $e_{345} \gtrless 0$; i.e., whether the inclusion of mode 5 stabilizes or destabilizes the critical 3-4 binary.

Some Transient Effects

We consider a binary system and make the assumption, *ab initio*, that the introduction of time-dependence of the flutter coefficients need not cause deviations of the type of system motion—i.e., the motion (15) is valid. Substituting Eq. (15) into Eq. (13) and specializing to $n = 2$, we find

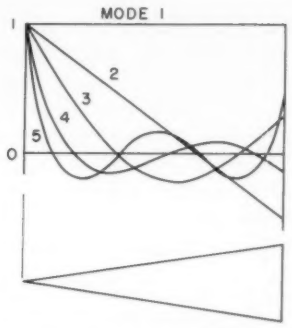

FIG. 13. Small aspect ratio chordwise-flexible delta wing modes.

$$-2(T + V)\int_0^{2\pi/\kappa} = \int_0^{2\pi/\kappa} (\dot{q}'A\dot{q} - q'\dot{C}q)dt + 4\pi k b_{11}\{R^2 + 2(\chi\cos\epsilon - \xi\sin\epsilon)R + \zeta\} \tag{61}$$

so that structural parameters now enter the equation of energy balance. To give some reality to the discussion, Eq. (61) is applied to a system subject to aerodynamic heating effects which are assumed to be manifest only by a time rate of change of the structural stiffness coefficients. Thus, we place $\dot{A} = 0$ and the elements of $\dot{c}$ equal to

$$\begin{aligned} \dot{c}_{jk} &= 0,\ j \neq k \\ c_{jj} &= \sigma_{jj} + s_{jj}e^{pt} \\ \dot{c}_{jj} &= ps_{jj}e^{pt} \end{aligned} \tag{62}$$

where σ_{jj}, s_{jj} are aerodynamic and structural stiffness, respectively. Eq. (61) reduces to

$$-(T + V)_0^{2\pi k} = \alpha R^2 + \beta R^2\cos 2\epsilon + \tau R^2\sin 2\epsilon + \delta R\cos\epsilon + \phi R\sin\epsilon + \iota = 0 \tag{63}$$

where

$$\begin{aligned} \alpha &= 2\pi k b_{22} - Ps_{22} \\ \beta &= -2Ps_{22}(p/2k)/[4 + (p/2k)^2] \\ \tau &= -(p/2k)\beta/2 \\ \delta &= 2\pi k(b_{12} + b_{21}) \\ \iota &= 2\pi k b_{11} - Ps_{11}\{1 + 2(p/2k)/[4 + (p/2k)^2]\} \\ P &= [e^{2\pi(p/2k)} - 1]/4 \end{aligned}$$

which is the polar equation of a conic in the $X = R\cos\epsilon$, $Y = R\sin\epsilon$ plane. Its nature is more easily seen if the restriction is made that $2\pi(p/2k)$ is small—i.e., if time variations of stiffness are not great, an assumption which accords with usual circumstance. Then

$$\left.\begin{aligned} \alpha &= \pi[2kb_{22} - (p/2k)s_{22}/2] \\ \beta &= 0 \\ \tau &= 0 \\ \delta &= 2\pi k(b_{12} + b_{21}) \\ \phi &= 2\pi(c_{12} - c_{21}) \\ \iota &= \pi[2kb_{11} - (p/2k)s_{11}/2] \end{aligned}\right\} \tag{64}$$

and Eq. (63) defines kinematically admissible flutter configurations by means of a second energy circle the characteristics of which differ from that of the conventional steady-state case only in relation to effective damping coefficients. Thus, by defining

$$(b_{jj})_{\text{eff}} = b_{jj} - (p/8k^2)s_{jj}; \quad j = 1, 2 \qquad (65)$$

the same energy circle is valid. Time-dependence thus appears as an effective damping which is positive or negative according as $p \lesseqgtr 0$—i.e., as the stiffness decreases or increases. An interesting result.

A simple application is to the two-dimensional binary flutter of a zero thickness wing for which a rigid pitch mode couples with a parabolic chordwise bending mode according to piston theory. The limiting condition $r^2 = 0$ leads to

$$(1 - 2a)^2 + (1/k)^2 = 36[2(1/3 - a + a^2) - s_{11}p/8k^2]\,[1/3 - s_{22}p/8k^2] \qquad (66)$$

for which it *is* possible to find real values of p. For $a = 1/2$ for example, p is real provided

$$(s_{11} - s_{22}/2)^2 + (1/k^2 - 2)s_{11}s_{22} \geq 0 \qquad (67)$$

Finally, we consider as a second example the two-dimensional wing bending-torsion flutter using zero thickness piston theory again. For a mid-chord pitch axis, the effective dampings are

$$(b_{11})_{\text{eff}} = (2/M) - (p/8k^2)(\mu M/3)k_0^2$$
$$(b_{22})_{\text{eff}} = (2/3M) - (p/8k^2)(\mu M/3)k_0^2\Psi/20$$

where k_0 and Ψ define the stiffnesses

$$c_{11} = (1/3)\mu M k_0^2 e^{pt}; \quad c_{22} = \Psi c_{11}/20$$

The condition for the vanishing of the energy circle, $r_0^2 = 0$, results in

$$(4/M - p\mu M k_0^2/4k^2)(4/M - 3p\mu M k_0^2\Psi/20k^2) = 12/(Mk)^2 \qquad (68)$$

Fig. 14 depicts a solution for the value of the modal stiffness ratio $\Psi = 5/3$, and illustrates the stabilizing influence of a negative rate of change with time of stiffness.

Conclusion

The equation of energy balance is but a partial integration of the equations of motion and as such is incapable of supplying the eigenvalues or the necessary and sufficient conditions for the existence of flutter. It does offer a means of deriving a necessary condition and as such provides an insight into the basic mechanism of flutter and an understanding of the significant characteristics of fluttering systems. For binary systems, it leads to the idea of ultimate stability and a concept of stability related to the capability of a neutrally stable system of absorbing energy. A criterion results which exposes in a specific way the influence of certain system parameters, and this requires as data simply the flutter coefficients as conventionally derived. For higher-order systems there appears to be no such simply applicable tool of assessment, although system behavior is often then approximated by certain binary couplings to an extent adequate for purposes of preliminary design.

Finally, such nonclassical effects as time-dependence arising from changing mass, altitude, aerodynamic heating are catered for; and there seems no reason why the influence of other force fields and other work functions, linear or nonlinear, should not be added to the conventional.

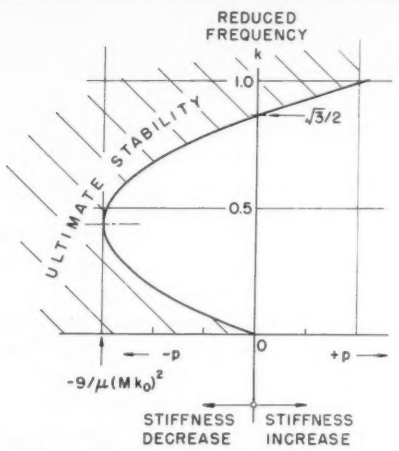

FIG. 14. Effect of time change of structural stiffness on two-dimensional supersonic wing bending-torsion flutter showing limiting reduced frequency as function of a stiffness variation of the form e^{pt}.

References

[1] Routh, E. J., *Dynamics of a System of Rigid Bodies*, Pt. II, 6th Ed., Chap. VII, p. 232; Dover Publn., Inc., New York, 1905.

[2] Rayleigh, Baron, *The Theory of Sound*, Vol. I, 2nd Ed., Chap. V, Arts. 82, 103; Dover Publn., Inc., New York, 1894.

[3] Frazer, R. A., and Duncan, W. J., *The Flutter of Aeroplane Wings*, Brit., ARC, R and M 1155, p. 42, 1928.

[4] Garrick, I. E., *Propulsion of a Flapping and Oscillating Airfoil*, NACA, TR 567, 1936.

[5] Ellis, E. L., and Duncan, W. J., Brit. RAE Rept. Aero 2036/AD, 1945.

[6] Barton, M. V., *Stability of an Oscillating Airfoil in Supersonic Airflow*, Journal of the Aeronautical Sciences, Vol. 15, No. 6, pp. 371–376, June, 1948.

[7] Greidanus, J. H., *Low Speed Flutter*, Readers' Forum, Journal of the Aeronautical Sciences, Vol. 16, No. 2, pp. 127–128, February, 1949.

[8] Duncan, W. J., *Flutter of Systems of Many Degrees of Freedom*, Aero. Quart., Vol. 1, Part 1, pp. 59–76, May, 1949.

[9] Rott, N., *Flügelschwingungsformen in ebener kompressibler Potentialströmung*, ZAMP, Vol. 1, Fasc. 6, pp. 380–410, November, 1950.

[10] Van de Vooren, A. I., *Theory and Practice of Flutter Calculations for Systems with Many Degrees of Freedom*, Doctoral Thesis, p. 89; Technische Hogeschool te Delft, Holland, April, 1952.

[11] Lambourne, N. C., *On the Conditions under which Energy can be Extracted from an Air Stream by an Oscillating Aerofoil*, Aero. Quart., Vol. 4, Pt. 1, pp. 54–68, August, 1952.

[12] Halfman, R. L., *Experimental Aerodynamic Derivatives of a Sinusoidally Oscillating Airfoil in Two-Dimensional Flow*, NACA Rept. 1108, 1952.

[13] Crisp, J. D. C., *On the Theory of Flutter Prevention for Wing-flap Systems*, Aust. ARL Rept. SM 259, January, 1958.

[14] Béatrix, C., *Méthode Énérgetique pour la Détection des Modes de Vibration Responsables du Risque de Flottement*, La Rech. Aéro., No. 58, pp. 41–48, May–June, 1957.

[15] Salaün, P., *Influence de L'amortissement Interne sur la Vitesse Critique de Flottement*, La Rech. Aero, No. 61, pp. 19–25, Nov.–Dec., 1957.

(*Continued on page 738*)

Some Effects of Sound-Reduction Devices on a Turbulent Jet

GILLES M. CORCOS*

Douglas Aircraft Company, Inc.

Summary

An account is given of an attempt to explain in simple terms how ejectors, corrugated nozzles, and multiple nozzles modify the turbulent mixing of a jet so as to generate less aerodynamic noise. Simple analytic and dimensional considerations lead to the conclusion that the noise reduction is due primarily to a decrease in turbulence levels in the mixing region. It is suggested that this is accomplished by accelerating the ambient air through a longitudinal pressure gradient before mixing it with the jet. Thus, a sheath of flowing air decreases the lateral jump in the mean axial velocity which is responsible for the turbulence level in the mixing region. An experiment at low speed with an ejector and a corrugated nozzle is reported. Mean velocity profiles and turbulent surveys were obtained. The results are in good agreement with expectations and provide strong support for the hypothesis.

Introduction

THE DESIGNER of a jet exhaust nozzle, attempting to minimize jet mixing noise without incurring performance penalties—i.e., loss of thrust and an increase in drag and weight—has had little help from analysis or from past experience. His approach has therefore been purely pragmatic. Considerable results have been achieved and it is of interest, in the wake of this progress, to seek a measure of understanding.

It is established that the major part of the noise generated by jet engines originates in the mixing of the high velocity exhaust gases with the air surrounding the jet. This mixing is turbulent and characterized by large velocity fluctuations and consequently by pressure fluctuations which in part propagate or radiate away from the jet. The magnitude of the pressure fluctuations in the jet is related to the magnitude of the velocity fluctuations there, and, as is shown in reference 1, the extent to which these pressure fluctuations propagate away depends on their frequency or time scale.

Several years ago, M. J. Lighthill[2] provided an analysis which yields the radiated noise at a point (or its stochastic description) in terms of the kinematics of a turbulent field such as a jet mixing region causing the noise. From an analytic standpoint this would solve the problem, were it not for the fact that the turbulent field which is assumed given in Lighthill's analysis is, in reality, not known. In other terms, our source of noise is identified but not given by that analysis or by any other. Since the problem is in fact not yet mathematically determinate (see, for instance, reference 3), the designer should not wait upon future progress in turbulence theory. Is it possible, instead, to measure the relevant quantities in the turbulent region and relate them to the geometry of the nozzle and the flow parameters? Here it seems that the terms identified in Lighthill's theory as the source terms cannot yet be measured practically[1] even if we overlook the difficulty of interpreting hot wire signals at the relevant mean velocities—i.e., transonically.

There are alternate identifications of the source (in terms of density, for instance) which may lead to practical measurements of its strength by optical means. Such measurements have not yet been reported, however, and in the meantime it is natural to seek a substitute—i.e., to associate more approximately the strength of the source of noise with a quantity which is readily measured in the mixing region and on which the effects of changes in the geometry of the nozzle can be easily traced. Such a substitute is proposed later.

Successful Devices

We shall briefly review modifications of exhaust nozzles which have been found successful to various degrees in that they generate less noise for a given thrust and mass flow than plain round nozzles do.

It has been verified that an ejector placed immediately at the exit of a plain nozzle is capable of decreasing the radiated noise energy by a factor as high as 5. This occurs only when the stream issuing from the ejector has reasonably uniform total pressure—i.e., when secondary and primary air have been sufficiently mixed. "Sufficient" mixing requires a long ejector (the ejector length should be approximately eight times its diameter).

Nozzles, the perimeters of which have been deeply corrugated so as to form lobes have been found much less efficient noise generators than comparable round nozzles. Here the gains are again of the order of 7 db. or a factor of 5.

Comparable figures have been quoted if the exhaust jet is subdivided in a number of parallel round nozzles placed a suitable distance apart from each other.

The gains obtained by ejectors and by corrugated nozzles are to a certain extent additive, in that a combination of a corrugated (or multiple) nozzle and an ejector reduce the aerodynamic noise of a jet still further. In fact, it has been found that even very

Received October 15, 1958.

* Formerly, Aerodynamics Engineer. Now, Assistant Professor of Aeronautical Sciences, University of California at Berkeley.

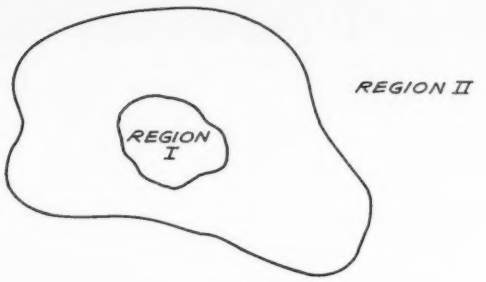

FIG. 1.

short ejectors were effective complements of corrugated nozzles.[4]

The Dependence of Aerodynamic Noise on Simple Flow Parameters

To help us discuss the role of various parameters characterizing our turbulent mixing process and the resulting noise (such as the lengths associated with the nozzle geometry, the mean and the turbulent velocities, characteristic frequencies, etc.) we will use the relation derived in reference 1, a low Mach Number approximation:

$$\nabla^2 p - (1/a_0^2)(\partial^2 p/\partial t^2) = (1/a_0^2)(\partial^2 p_{inc}/\partial t^2) \quad (1)$$

Eq. (1) gives the noise pressure field $p(x, y, z, t)$, in region II far enough away from the region of turbulent mixing, in terms of the local turbulent pressure fluctuations p_{inc} which are found in the region of turbulent mixing (region I) and which are closely given by incompressible relations (see Fig. 1). The right-hand side of Eq. (1) is the source of the radiated noise, and it can be seen that this term is large either when local turbulent fluctuations are large or when they are rapid. In fact, one should expect from the well-known solutions of the inhomogeneous wave equation (in the absence of boundaries) that the mean square noise pressure $\overline{p^2}$ at a distance will be proportional to the mean square of the local turbulent presssure and to a fourth power of a typical turbulent frequency ω^*. Thus,

$$\overline{p^2} \sim (1/a_0^4)\omega^{*4}\overline{p^2}_{inc}$$

Now $\overline{p^2}_{inc}$ will be taken proportional to u'^4 (where $u' = \sqrt{u^2}$ is the root mean square of the axial component of the fluctuating velocities) as is suggested in reference 1. In the present dimensional argument, no differentiation is made between the various components of the turbulent velocity fluctuations, and it is assumed that u' is sufficiently representative of the two other fluctuating components. Thus, we write

$$\overline{p^2} \sim (1/a_0^4)\omega^{*4}u'^4$$

Therefore, the noise generated can be expected to be reduced by reducing turbulent levels.

The typical frequency, ω^*, is undoubtedly also related to velocities in the turbulent region, but additional considerations must be adduced to decide whether the turbulent or the mean (say, jet exit) velocities are relevant. The distinction is important since a noise suppressing device is not permitted to alter appreciably the mean exit velocity (which would change the thrust or the mass flow of the engine). If, as Lighthill[5] argues, the turbulent velocities determine the frequencies which are relevant to the radiation of noise; i.e., if $\omega^* \sim u'/L$, where L is a characteristic dimension; then the sound level at a distance and, therefore, the total sound power output are indeed very sensitive functions of the turbulence level. since then $\overline{p^2} \sim u'^8$. Thus, it is reasonable to inquire first whether successful nozzle modifications result in a general decrease in the turbulence levels.

The Role of Length Parameters

The most obvious feature of corrugated and multiple nozzles is that they modify the length scales of the mixing process. For the same mass flow and the same thrust the "wetted perimeter" is increased, the axial distance over which a given amount of surrounding air is entrained is decreased, eddy sizes are decreased, etc. This may be misleading. It can be shown, for instance, that gains (reduction in noise output) realized by the substitution of multiple nozzles for one nozzle have very little to do with this change of scale.

A simple application of dimensional analysis indicates that for geometrically similar jets, the acoustic efficiency—i.e., the ratio

$$\frac{\text{Acoustic energy radiated by jet/Unit time}}{\text{Kinetic energy flux of the jet}}$$

depends on the diameter of the nozzle at most through the effect of changes in the Reynolds Number. We should expect that effect to be small over a wide range of Reynolds Numbers. Over the range of interest, Tyler's experiments[6] as well as those of Lassiter and Hubbard[7] have shown that changes in the Reynolds Number do not affect the acoustic efficiency of similar nozzles. Thus, if n small round jets have the same exit velocity and total exit cross-sectional area as one large round nozzle, they will generate together exactly as much sound power, provided they do not interfere with each other; this in spite of the fact that all length scales are different. Therefore, it is clearly the interference between contiguous nozzles which is responsible for the reduction in sound power, not the change of scale.

Thus, we have been led to the expectation that a decrease in the acoustic efficiency of a jet is closely related to a decrease in the turbulence levels within the jet. Now assuming this inference to be correct, why

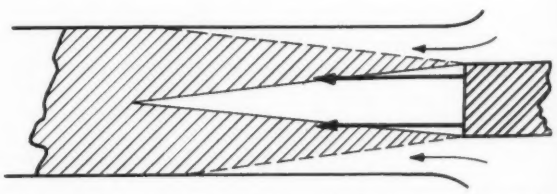

FIG. 2. An ejector accelerates secondary air before mixing it.

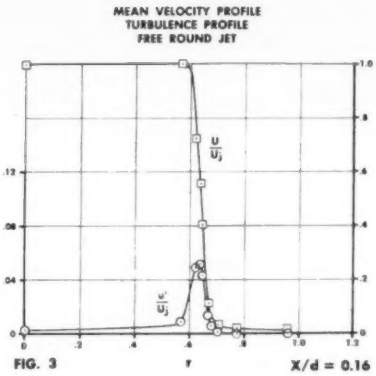

FIG. 3 X/d = 0.16

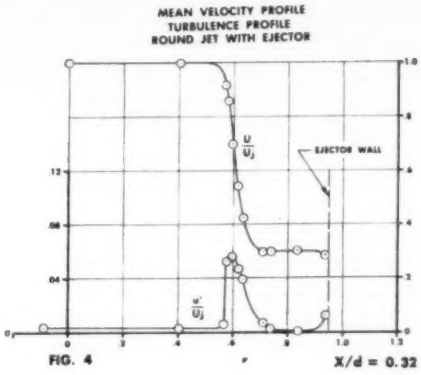

FIG. 4 X/d = 0.32

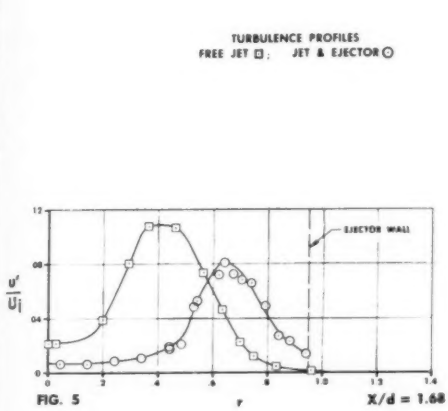

FIG. 5 X/d = 1.68

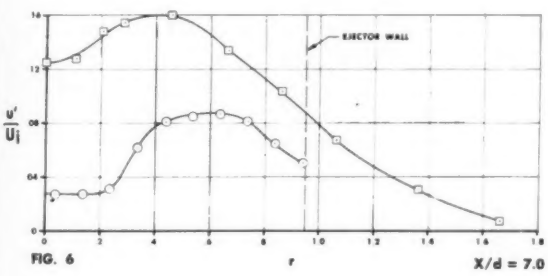

FIG. 6 X/d = 7.0

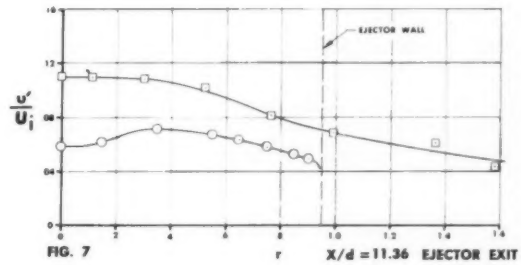

FIG. 7 X/d = 11.36 EJECTOR EXIT

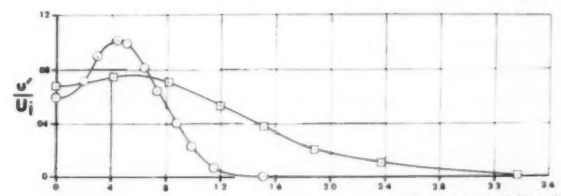

FIG. 8 X/d = 14.5 X'/D = 2

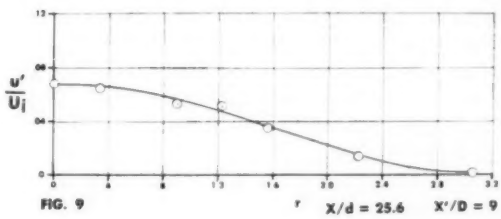

FIG. 9 X/d = 25.6 X'/D = 9

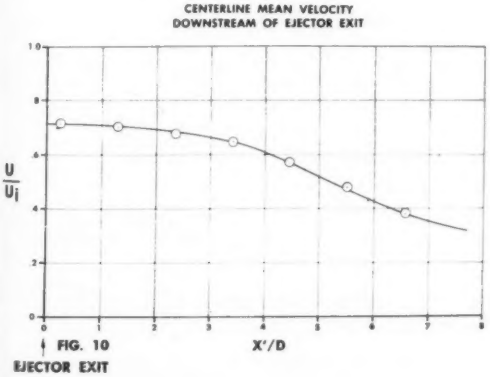

FIG. 10
EJECTOR EXIT

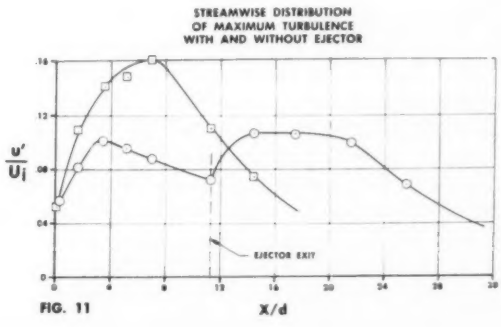

FIG. 11

would, say, an ejector depress turbulence levels? It was surmised that what determines the turbulence levels is the lateral mean jump in the axial velocity between the jet and its surroundings. For instance, if a nozzle discharging a jet at a velocity V_j were displaced axially in the opposite direction at the same speed, it seems intuitively clear that the turbulence levels would practically disappear. Now in an ejector the secondary stream is first accelerated as a potential flow by a longitudinal pressure gradient, a process which causes no turbulence and which decreases the velocity of the primary jet relative to its surroundings. The subsequent mixing is therefore characterized by a lower effective velocity so that turbulence levels might be expected to be lower than they are at corresponding stations of a free jet. A similar explanation can be advanced for multiple or corrugated nozzles. Again, the unmixed air surrounded by separate jets will acquire an axial velocity which will reduce the relative velocity of the jet with respect to its surroundings. (See Fig. 2.)

The foregoing hypotheses were tested in a low-speed experiment which will be reported presently.

Experimental Equipment and Methods

A one-horsepower vacuum cleaner discharged air through a diffuser to a cylindrical settling chamber. A smooth Fiberglas contraction section ended the settling chamber and formed a round nozzle 1.25 in. in diameter. In the first part of the experiment an ejector 14 in. long and 1.9 in. in diameter was secured to the end of the nozzle. The ejector was a thin piece of aluminum tubing properly flared out at the entrance end.

In the second part of the experiment, a four-lobe corrugated nozzle was used. An insert was made out of a piece of brass tubing the outside diameter of which was precisely equal to the inside diameter of the nozzle. One end of the tube was hammered into a four-lobe nozzle. The nominal Reynolds Number based on the diameter of the basic exit nozzle remained 40,000 for all the measurements. Both for the ejector and for the corrugated nozzle tests, the boundary layer inside the nozzle was made turbulent by tripping it with a thin cellophane tape, approximately one inch upstream of the nozzle exit or of the start of the corrugations.

Apart from a few total pressure traverses, the experiment consisted of hot-wire measurements of the turbulence levels u'/U (here u' is the root mean square of the fluctuating velocity in the x direction, U the mean velocity at the same point) and of U.

The hot-wire probes were small u' wires (single-wire stretched perpendicularly to the mean flow direction). Their length was 0.1 in. and their diameter 0.0001 in. The measurements were made by the constant temperature method. The amplifying and averaging equipment, the bridge, the compensation, and the data reduction followed conventional lines.

Even though the wires were calibrated and the calibration checked frequently, all measurements were taken in a comparative manner. A standard traverse was made immediately after each one or two traverses and compared to independent measurements of the same quantity. Thus repeatability was assessed and changes in the calibration easily detected. On the whole, the accuracy was satisfactory. It was found that most discrepancies arose out of inaccurate positioning of the probe especially far downstream of the nozzles. Many measurements were repeated with different wires.

Results and Discussion

Figs. 3–19 present a summary of the data obtained.† Both the mean velocity U at a point and the root mean square of the axial component of the velocity fluctuation u' are nondimensionalized with respect to the mean exit velocity U_j so that the turbulence traverses are essentially plots of the absolute value of the turbulent velocities.

The Ejector

The mean velocity profile at the entrance (x/d = 0.32, Fig. 4) shows that the secondary air has acquired a uniform velocity equal to $^3/_{10}$ of the jet exit velocity and the corresponding turbulence profile shows that no mixing has yet taken place. The spike approximately located at y = 0.6 in. is probably due in large part to the shedding of the turbulent boundary layer from the nozzle. For comparison, the mean velocity profile and turbulence profiles are given (Fig. 3) for the jet without an ejector. At the second station (x/d = 1.68, Fig. 5) the effect of the ejector on the turbulence levels is already apparent. The turbulence within the ejector rises to values which are of the order of 30 per cent lower than those which prevail in the corresponding sections of the free jet. The maximum has also been displaced away from the center of the jet. Succeeding traverses are similar. Within the ejector the highest turbulence level is reached four nozzle diameters downstream of the exit. Downstream of that point, turbulence levels decrease smoothly until the end of the ejector is reached. In the corresponding free jet the maximum turbulence level is reached approximately seven diameters downstream of the exit and it is considerably higher; the maximum turbulence within the ejector is approximately 68 per cent of what it is in the free jet. Strikingly, this is approximately the amount by which the lateral jump in the mean axial velocity has been reduced at the nozzle exit by the presence of the ejector.

At the ejector exit (Fig. 7) the turbulence level is still lower than it is at the same section in the free jet, this in spite of the fact that by then the core velocity of the free jet has decayed to values which are noticeably lower than the centerline velocity in the ejector.

Downstream of the ejector (Figs. 8, 9, and 10), the stream behaves somewhat as a free jet. The centerline

† For additional data, see reference 1.

AN ILLUSTRATION OF THE IMPORTANCE OF TURBULENCE MAXIMAE:
COMPARISON OF IDEALIZED NOISE SOURCE STRENGTH

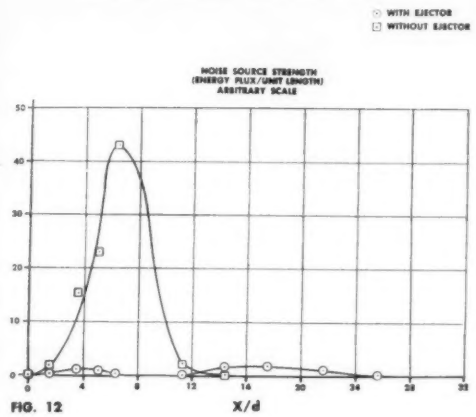

FIG. 12

THE EFFECT OF CRUCIFORM SPLITTER PLATES TURBULENCE PROFILES.

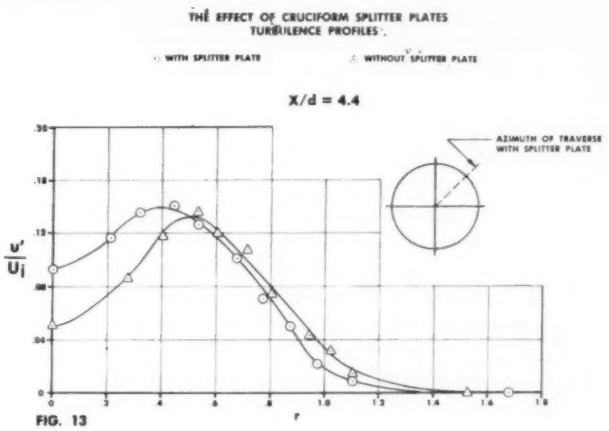

FIG. 13

MEAN VELOCITY PROFILES
CORRUGATED NOZZLE
θ = 0° ⊡
θ = 45° ⊙

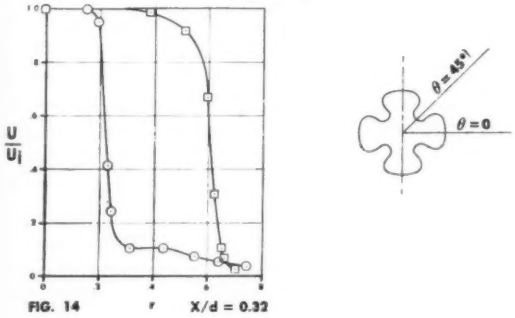

FIG. 14

DOWNSTREAM VARIATION OF MAXIMUM TURBULENCE
CORRUGATED NOZZLE
θ = 0° ⊡
θ = 45° ⊙

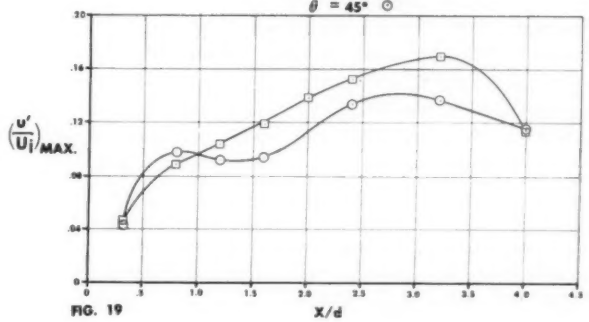

FIG. 19

TURBULENCE PROFILES
CORRUGATED NOZZLE
θ = 0° ⊡
θ = 45° ○

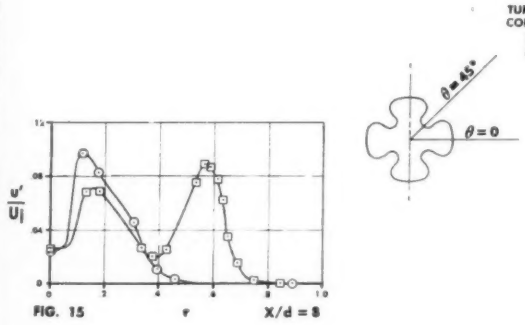

FIG. 15

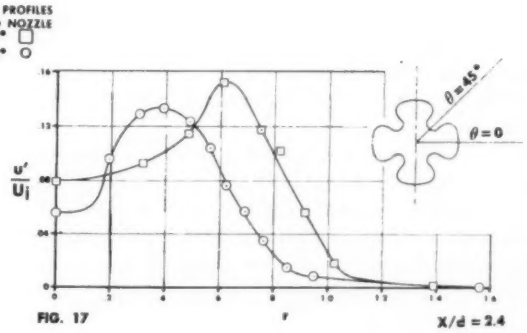

FIG. 17

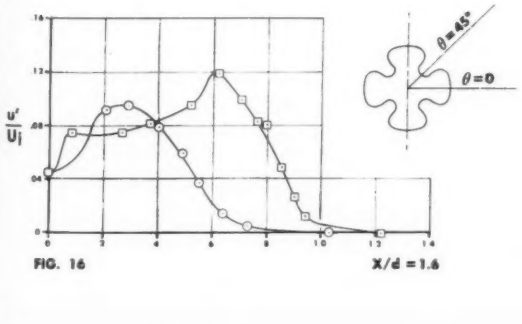

FIG. 16

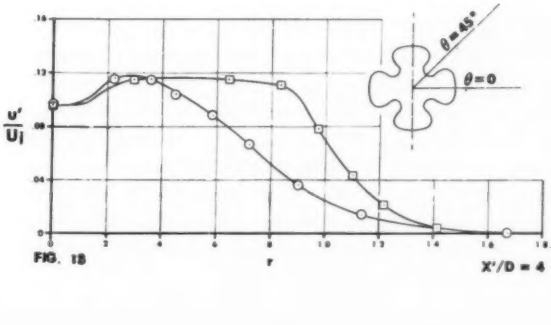

FIG. 18

velocity decreases little at first, and the turbulence levels rise to a value which is roughly the same as that for a free jet if one takes into account the reduced velocity of the "new" jet. For the ejector used in this experiment, the maximums reached within and downstream of the ejector were very nearly equal.

To point out the development of turbulence with downstream distance, the maximum turbulence occurring at each cross section has been plotted against downstream distance on Fig. 11.

To summarize the experiment: It has been verified that an ejector depresses the turbulence of a round jet. It can be argued that, on the other hand, turbulence levels have risen downstream of the ejector. This is true, and is a consequence of the inability of a jet plus ejector to entrain as much air in a given length as a simple jet. But this rise of turbulence levels far downstream is likely to be unimportant. It has been presented as plausible that the intensity of radiated noise was a function of a high power of the turbulence level. This means that everything else remaining the same, most of the noise comes from regions of highest turbulence and very little from other regions. Thus, a reduction of the maximum turbulence occurring anywhere in the jet would appear to be the most effective way to suppress its noise. To illustrate the point, assuming that the only way in which the ejector has changed the jet flow is by modifying the turbulence levels and using the tentative relation $\overline{p^2} \sim u'^8$, we have plotted on Fig. 12 a comparison of the x distribution of noise source strength on the basis of Fig. 11.

In view of the experiment reported above, it seems at least plausible that, as was presumed, turbulence levels are decreased because the effective velocity of the jet with respect to its surroundings is decreased. We have seen that both the lateral velocity jump at the nozzle exit and the maximum turbulence levels were reduced by roughly 30 per cent. In order to determine whether an ejector does not inhibit turbulence by restraining the lateral motion of the jet, two traverses were obtained at $x/d = 4.4$ (see Fig. 12). One was taken in a free round jet, the other in a jet which was trailed by two (cruciform) splitter plates. The latter traverse bisected one of the right angles formed by the splitter plates. The results show that the turbulence levels are not decreased by the splitter plates even though the lateral motion of the jet as a whole must be inhibited by them.

The Corrugated Nozzle

Figs. 14–19 show the results of hot wire traverses at eight stations downstream of the corrugated nozzle and at two azimuths: $\theta = 0$ traverses bisect the primary lobe, $\theta = 45°$ traverses bisect the secondary lobe, as shown on Fig. 14.

At the exit of the nozzle, the mean velocity is uniform across the nozzle and the turbulence levels are quite low except at the sharp boundary of the jet where they are again representative of the turbulence in the boundary layer shed from the nozzle walls.

The first mean velocity and turbulent traverses in the secondary lobe (Fig. 14, $\theta = 45°$) reveal that secondary air is entrained before it is mixed in a manner analogous to that discussed in connection with the ejector. The turbulence levels reach approximately the same value for the two azimuths at the first two stations. Downstream of the station $x/d = 0.8$; however, the traverses along the primary lobe show consistently higher turbulence levels than those along the secondary lobes. The maximum turbulence is reached for $x/d = 2.75$ ($\theta = 45°$) and $x/d = 3.25$ ($\theta = 0$). Further downstream, the difference between the traverses at the two azimuths seem to decrease. Fig. 19 is a plot of the maximum turbulence at a section as a function of downstream distance for the two azimuths. It exhibits two features of interest. The first has already been noted: wherever secondary air has been accelerated before mixing—i.e., in the secondary lobes—the turbulence levels are lower. To be sure, the reduction of the effective velocity jump and of the turbulence levels is smaller than it is for the ejector (compare Figs. 19 and 11). On the other hand, the corrugated nozzle used was rather shallow in comparison with those which have been found most successful in silencing jets. In addition, in a deeply corrugated nozzle, the fraction of the total perimeter of the jet which is affected by the accelerated secondary stream is larger. It seems that the lobes of a corrugated nozzle "interfere" with each other in that they compete for an insufficient local supply of secondary air in between them and thus cause a pressure drop which induces an axial velocity of the secondary air. In other words, secondary air is pumped from upstream in between the lobes of the jet. Hence, the effective velocity of part of the jet (the part contiguous to the secondary lobe) is reduced and this is probably the reason why turbulence levels in that region are observed to be lower than they would be in a round jet.

The second feature of the results summarized by Fig. 19 is that the corrugations have effectively changed the length scales of the mixing process. For instance, in a free round jet the mean velocity at the core begins to decay approximately 6 diameters downstream of the nozzle exit and the maximum turbulence is reached approximately 7 diameters downstream of the nozzle exit. In the corrugated nozzle tested, the centerline velocity decay starts 1.6 (original) diameters downstream of the nozzle exit and the maximum turbulence is reached approximately 3 diameters downstream. For a nozzle with a large number of corrugations, this effect is no doubt a great deal more pronounced. The success of very short ejectors used in conjunction with corrugated nozzles is due to this change of scale.

In conclusion, the experiments reported above provide evidence that a subsonic jet modified so as to radiate less aerodynamic noise for a given thrust and mass flow exhibits lower maximum turbulence levels than an unmodified jet. Experimental data further suggest a simple explanation for these results.

(*Continued on page 730*)

Hypersonic Viscous Flow Over Slender Cones†

L. TALBOT,* T. KOGA,** AND P. M. SHERMAN***

University of California at Berkeley, and University of Michigan

Summary

Viscous self-induced pressures on 3° semivertex angle cones were measured over the Mach Number range $3.7 < M_1 < 5.7$, and for values of the viscous interaction parameter in the range $0.5 < \bar{\chi}_c < 2.3$. The data were found to be in good agreement with results obtained by Talbot on 5° cones in the range $3.7 < M_1 < 4.1$, $0.9 < \bar{\chi}_c < 3.6$. All these data were correlated reasonably well by the viscous interaction parameter.

A new method for calculating self-induced pressures is presented which takes into account the interaction between boundary-layer growth and the inviscid flow field at the outer edge of the boundary layer. Pressures calculated by this method were only 10 to 20 per cent higher than the measured values.

Symbols

C = Chapman-Rubesin factor in relation $(\mu/\mu_2) = C(T/T_2)$
d = diameter of pressure orifice
K_c = similarity parameter, $M_1\theta_c$
K_2 = similarity parameter, $M_1\theta_2$
M = Mach Number
p = static pressure
r_c = cone radius
Re = Reynolds Number
t = bluntness of cone tip or thickness of leading edge of plate
T = gas temperature
u = gas velocity
x = distance measured from vertex along cone surface
y = distance normal to cone surface
γ = specific heats ratio
δ^* = boundary-layer displacement thickness, $\int_0^\infty [1 - (\rho u/\rho_2 u_2)]dy$
δ = boundary-layer thickness
μ = absolute viscosity
ν = kinematic viscosity
ρ = gas density
σ = Prandtl Number
Λ = mean free path
θ_δ = streamline inclination at outer edge of boundary layer
θ_c = cone semivertex angle
$\theta_2 = \theta_c + \theta_\delta$
$\bar{\chi}_c$ = viscous interaction parameter, $M_c^3(C/Re_{x_c})^{1/2}$

Subscripts

1 = free-stream conditions
2 = conditions at outer edge of cone boundary layer, taken to be functions of x
c = ideal flow conditions along surface of cone obtained for $x \to \infty$
w = wall conditions
aw = adiabatic wall

Examples of the notation used for the various Reynolds Numbers are: $Re_2/\text{in.} = u_2/\nu_2$, $Re_{t_1} = u_1 t/\nu_1$, $Re_{x_c} = u_c x/\nu_c$, etc.

Introduction

THE FLUID-DYNAMIC and thermodynamic phenomena associated with flight at hypersonic speeds have been the subject of intensive research in recent years. In this research one problem that has received considerable attention is the problem of the "self-induced pressure" effect, which is one aspect of a broader class of phenomena which can be described as "viscous interaction" phenomena.

Although the fundamental mechanism responsible for self-induced pressures is well understood, the analysis of the effect is rather complicated. The magnitude of the self-induced pressure is directly proportional to the rate of growth of the boundary layer. (See Fig. 1.) However, the growth of the boundary layer is determined by the pressure, Mach Number, etc., in the flow at the outer edge of the layer, and the values of these quantities depend on the magnitude of the displacement effect. It is seen, therefore, that we have to deal with a complex interaction phenomenon in which the boundary-layer "history" plays an important role. It will also be recognized that the phenomenon is, with regard to magnitude, more significant for thin bodies such as flat plates and slender cones than for thick bodies, since for thin bodies the changes in effective geometry due to boundary-layer growth will be proportionately larger.

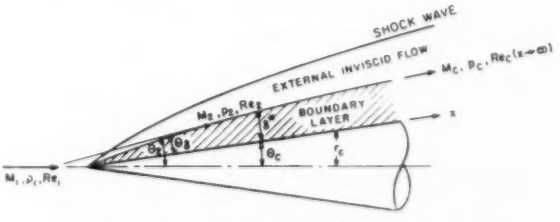

FIG. 1. Schematic of viscous flow over a cone.

Presented at the Aerodynamics—I Session, IAS 27th Annual Meeting, N.Y., Jan. 26–29, 1959.

† This work was sponsored by the National Advisory Committee for Aeronautics. An extended version is contained in NACA TN 4327.

* Associate Professor of Aeronautical Sciences, University of California, Berkeley.

** Professor of Engineering, University of Nagoya, Japan. Visiting Professor of Aeronautical Sciences, University of California, Berkeley, July-December 1956.

*** Research Engineer, University of Michigan, Ann Arbor.

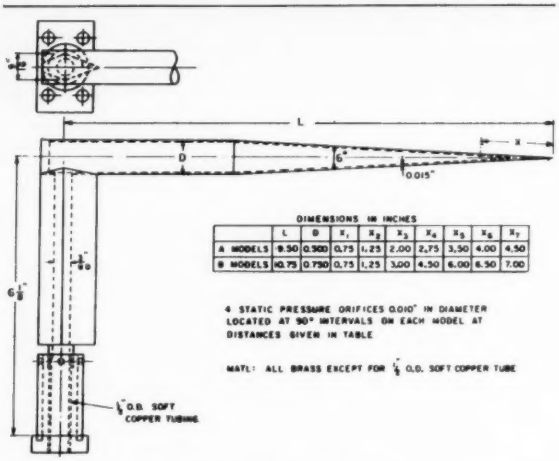
L
D
θ
x
0.015"
DIMENSIONS IN INCHES
4 STATIC PRESSURE ORIFICES 0.010" IN DIAMETER LOCATED AT 90° INTERVALS ON EACH MODEL AT DISTANCES GIVEN IN TABLE
MATL: ALL BRASS EXCEPT FOR ¼ O.D. SOFT COPPER TUBE
¼" O.D. SOFT COPPER TUBING

	L	θ	X_1	X_2	X_3	X_4	X_5	X_6	X_7
A MODELS	9.50	0.500	0.75	1.25	2.00	2.75	3.50	4.00	4.50
B MODELS	10.75	0.750	0.75	1.25	3.00	4.50	6.00	6.50	7.00

FIG. 2. Model specifications.

The particular problem considered in this paper is the self-induced pressure effect on a slender cone. In the first part of the paper new data are presented for pressures on 3° semivertex angle cones in the range of flow conditions $3.7 < M_1 < 5.8$; $650 < Re_{x_1} < 32{,}000$. Theories used for comparison with experiment are presented in the Appendixes.

Previous Experimental Results

The only data which have been available up to now for the viscous interacting air flow over a cone are the experiments of Talbot[1] and Baldwin.[2] Talbot's results were obtained in the Low Density Wind Tunnel of the University of California, the same wind tunnel used for the present work. His tests were carried out on 5° semivertex angle cones, in the Mach Number range $3.7 < M_1 < 4.1$, and at Reynolds Numbers which corresponded to the viscous interaction parameter range $0.91 < \bar{\chi}_c < 3.54$. Baldwin's data were obtained in the GALCIT 5″ × 5″ Hypersonic Wind Tunnel, Leg No. 1. His data were also for a 5° cone, at $M_1 = 5.8$, and over the viscous interaction parameter range $0.1 < \bar{\chi}_c < 1.6$.

Description of Present Experiments

Wind Tunnel

The experiments were conducted in the No. 4 Low Density Wind Tunnel of the Low Pressures Project of the University of California. This wind tunnel, which is an open-jet continuous-flow type employing axially symmetric nozzles, is described in detail elsewhere.[3] Two nozzles were used in the tests: the No. 8 nominal Mach 4 nozzle which produces flows in the range $3.7 < M_1 < 4.1$, $90 < Re_1/\text{in.} < 3{,}600$, and the No. 9 nominal Mach 6 nozzle, which produces flows in the range $5.5 < M_1 < 5.8$, $4{,}000 < Re_1/\text{in.} < 9{,}000$. Actual values of the flow parameters obtained in the test are listed in Table 1.

TABLE 1
Flow Conditions of Tests, $T_0 = 300°\text{K}$.

M_1	p_1 (μHg)	Re_1/in.	p_e/p_1 ($\theta_c = 3.03°$)
3.70	49.8	880	1.106
3.91	73.0	1,510	1.114
3.97	85.1	1,860	1.117
4.05	108.8	2,540	1.120
5.47	66.5	4,530	1.207
5.73	113.3	8,980	1.223

Models

All the cones tested were of 3° semivertex angle. Two sets of models were used, each set consisting of seven cones (see Fig. 2). The Type A cones had base diameters of 0.500 in., and the Type B cones had base diameters of 0.750 in. The longer Type B models were designed primarily to investigate the influence on the cone surface pressure of the expansion wave generated at the juncture of the conical surface and the cylindrical afterbody. Alignment of the cones in the flow was accomplished by adjustable set screws in the base support.

Subsequent to its use in the pressure measurement tests, Model B-7 was fitted with four copper-constantan thermocouples soldered in the cone surface at 2, 3, 4, and 5 in. from the vertex. This model provided information on the wall temperature of the cones, which was required for the boundary-layer calculations.

Some difficulty was encountered in producing models with sharp tips. The method of fabrication which was found most satisfactory was an acid etching process. After the cones had been machined to nearly their final dimensions, the tip regions were etched by a flat tool covered with a thin film of nitric acid. This method produced tips with diameters less than 0.001 in. However, the etching was not completely uniform. In the etched regions of the models, which extend back from the vertices about 0.4 in., some local variations in cone angle of several degrees were observed. Further back from the vertices all cone angles were found to be 3.03° ± 0.03°.

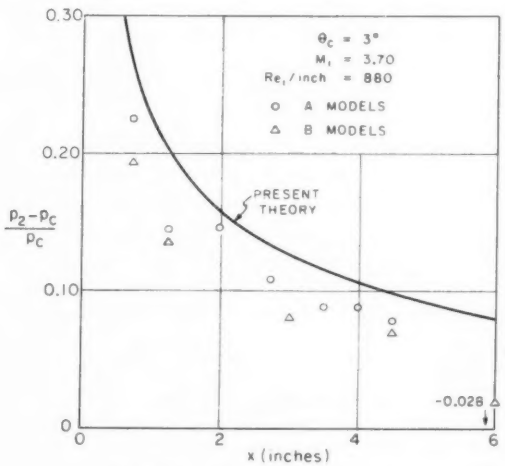

FIG. 3(a). 3° cone data, $M \sim 4$.

Instrumentation

Cone surface pressures were measured with a temperature-regulated thermistor manometer. The least count (0.1 mv) of the potentiometer used to measure the bridge unbalance of the thermistor measuring circuit corresponded to a pressure increment of about 0.02 micron Hg. Before each test the thermistor was calibrated statically against a precision McLeod gage. Analysis of the thermistor calibration data yielded a probable error in absolute pressure of about 1 per cent.

Wind-tunnel stagnation pressures were measured with a mercury manometer. Impact pressures were measured with a butyl phthalate oil manometer. Both manometers were equipped with magnifying optics which made it possible to locate the menisci to within 0.001 in.

Nozzle Calibration

Mach Numbers and static pressures in the test regions of the nozzles were determined by measuring stagnation and impact pressures, assuming the flow to be isentropic. For each flow condition of the tests, an axial impact pressure survey was made to determine the Mach Number and static pressure variations in the regions occupied by the models.

The tunnel-empty traverses in the No. 8 nozzle revealed a region about 8 in. in axial extent over which the Mach Number variation was less than 2 per cent and the static pressure variation less than 10 per cent. In the No. 9 nozzle the axial extent of the region over which the Mach Number and static pressure variations were less than these values was about 3.5 in.

Procedure

In the tests reported, all models were positioned so that their vertices were located at the same point in the flow. Correction was made for the axial gradients. Other tests were made with models positioned so that their respective pressure orifices were at the same axial location in the stream. The surface pressures obtained by this second method agreed quite well with those obtained by the first method. The correction for axial gradients in the stream was accomplished simply by using the local Mach Number (from tunnel-empty measurements) in the determination of the inviscid cone pressure p_c. It was found that this procedure gave consistent results provided the static pressure in the flow at the point where orifices were located did not differ by more than about 10 per cent from that at the vertex of the model. Consequently, in the No. 9 nozzle where the length of usable flow was about 3.5 in., models for which $x = 3.5$ in. were not used in the final tests. No difficulties arose on this score in the No. 8 nozzle. However, it was observed that the expansion wave reflection of the bow shock (the reflection occurring in the region of strong density gradient where the isentropic core merged with the nozzle boundary layer) affected the pressures measured on models B-6 and B-7. For this reason data are not reported at $M \approx 4$ for these models.

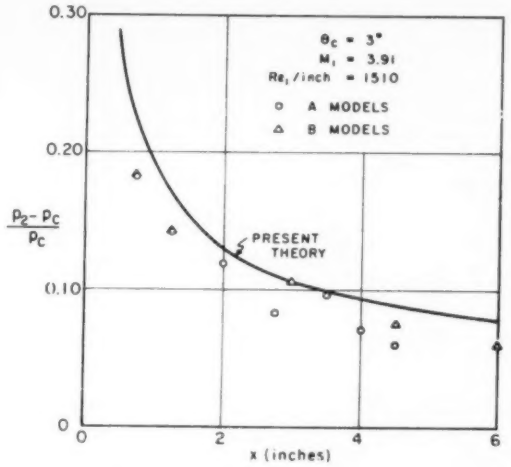

FIG. 3(b). 3° cone data, $M \sim 4$.

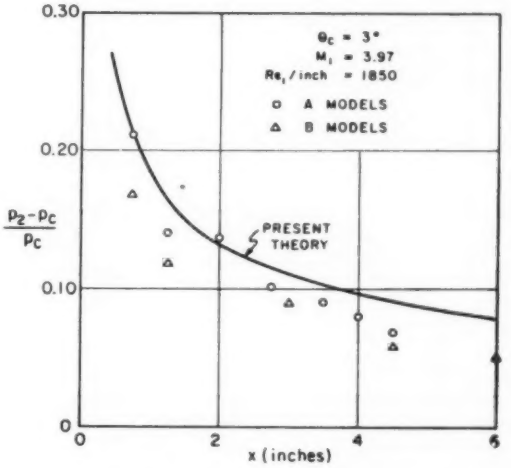

FIG. 3(c). 3° cone data, $M \sim 4$.

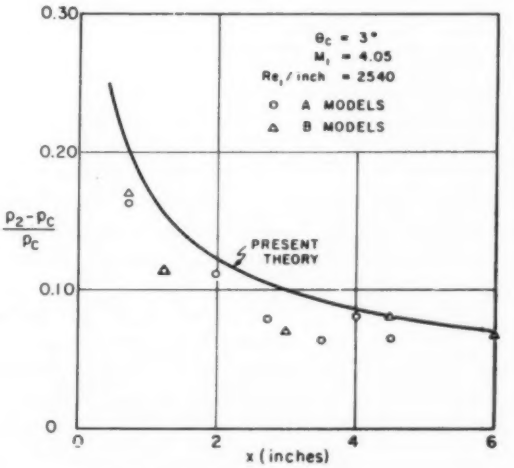

FIG. 3(d). 3° cone data. $M \sim 4$.

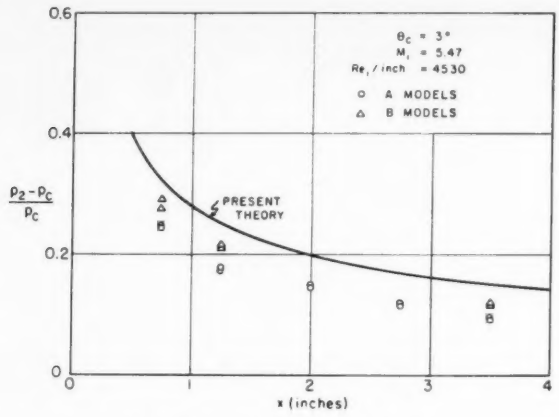

FIG. 4(a). 3° cone data, $M \sim 6$.

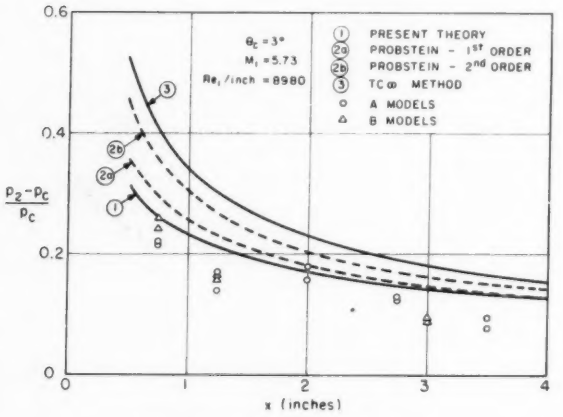

FIG. 4(b). 3° cone data, $M \sim 6$.

The temperature measurements made with Model B-7 showed the surface of the cone to be isothermal. The apparent recovery factor (based on inviscid flow conditions M_c, T_c behind the conical shock) was about 0.89; the increase over the theoretical value of 0.85 for the laminar boundary layer is due to heat conduction through the support from the model mounting, which was at essentially stagnation temperature.

Results

Results of the tests are given in terms of the induced pressure increment $p_2/p_c - 1$, where p_2 is the measured cone pressure and p_c the inviscid Taylor-Maccoll value. The inviscid flow values for the 3° cones were calculated from Van Dyke's second order theory,[4] since interpolation in the Kopal Tables[5] between 0° and 5° was not sufficiently accurate. The data at different flow conditions are shown plotted versus x in Figs. 3 and 4, and in Fig. 6 versus the hypersonic similarity parameter $\bar{\chi}_c = M_c^3(C/Re_{x_c})^{1/2}$ where M_c and Re_{x_c} are the Mach Number and Reynolds Number based on ideal Taylor-Maccoll flow conditions.

Numerical values for the induced pressure increment are in the range 0.06–0.30. The actual measured cone pressures varied between about 60 and 170 microns Hg. An error of 1 per cent in the measured pressure is equivalent to an error in the induced pressure increment of 5 per cent or more for most of the data, assuming the values of p_c to be exact, and from this it is estimated that the overall probable errors in $p_2/p_c - 1$ are between 5 and 15 per cent. Free-stream Mach Numbers are accurate to about 1 per cent; free-stream Reynolds Numbers are accurate to about 5 per cent.

In addition to the results of the present tests, two sets of data taken from reference 1 are shown in Fig. 5. In Fig. 6 all of the data from reference 1 on models A-1 through A-7 are plotted, and also Baldwin's 5° cone data are represented by a single line.

Discussion

Experimental Results

One conclusion which can be drawn from an examination of Figs. 3 and 4 is that the effect of the shoulder expansion did not extend far enough upstream in the cone boundary layer to influence the cone surface pressures, since the data obtained with the B models agree, within experimental scatter, with those obtained with the A models. We were not able to determine the extent of the region on the cone which is influenced by the shoulder expansion, because the reflection of the bow shock wave back onto the models obscured the effect. Models B-6 and B-7, which were designed to measure upstream influence, were those most affected by the reflected wave. In Fig. 3(a) it will be noted that the pressure orifices on model B-5 were also within the zone influenced by the reflection.

The scatter in the data is probably due to a combination of experimental error, imperfections in the orifices, and inaccuracies in the cone angle in the tip regions of the models. One may note that the reproducibility of the data was quite good, as evidenced by the comparisons shown in Figs. 4(a) and 4(b) between different sets of measurements made with both the A and the B models.

It can be seen from Fig. 6 that the parameter $\bar{\chi}_c$ provides a fairly good correlation for all of the data obtained in the University of California Low Density Wind Tunnel. The Mach 4 data for the 3° and 5° cones agree quite well; the Mach 6 data are slightly lower.

It is also seen from Fig. 6 that the induced pressure increments found by Baldwin are higher by a factor of about 2 than those obtained here. One suggestion which has been advanced is that the differences may be due in part to the influence of tip bluntness. It is true that the Reynolds Numbers based on tip diameter were higher in Baldwin's experiments than in ours; Baldwin's were mostly in the range $65 < Re_{t_1} < 230$, whereas all the Low Density Wind Tunnel data correspond to $Re_{t_1} < 9$. However, it seems unlikely that tip bluntness could account for much of the difference. The experiments on flat plates[6, 7] indicate that below about $Re_{t_1} = 80$ the plate can be considered as "sharp," and the effect of tip bluntness has been shown to be much less pronounced for cones than for flat plates.[8]

Comparisons Between Theory and Experiment

Three methods for calculating self-induced pressure have been employed in this report. The first, a new method devised by us, is presented and discussed in Appendix (A). The second, a method proposed by Probstein, is reviewed in Appendix (B), as is the third, which we have called the "TC_∞" method.

Figs. 3, 4, and 5 show that the present method for calculating self-induced pressures generally overestimates the data obtained in the Low Density Wind Tunnel by about 10–20 per cent. In contrast, the TC_∞ method and the Probstein second-order theory both give values greater by about a factor of 2 than the experimental results. The better agreement obtained with the present method is not surprising. Of the three methods it is the only one which accounts in even an approximate way for the true interaction effect, wherein the changes in the external flow due to the presence of the boundary layer feed back into the layer and alter its rate of growth. It seems likely that the discrepancies remaining between experiment and theory may be due mainly to the transverse curvature effect. [See Appendix (A).]

In Fig. 6 the results of the present theory are represented by a single straight line. (Actually, the individual curves of Figs. 3, 4, and 5 when plotted against $\bar{\chi}_c$ deviated about ±2–4 per cent from this mean line. The deviations seemed not to follow any particular trend, and were probably due mainly to accuracies introduced in the graphical parts of the analysis.) Again, in Fig. 6, the good agreement between the present theory and the Low Density Wind Tunnel data is clearly evident. Induced pressures have also been measured on 5° cones in helium[26] in the range $M_1 = 16$ to 18, and $0.8 < \bar{\chi}_c < 1.6$. A best fit through the higher points of these data is $(p_2 - p_c)/p_c \approx 1 + 0.25\ \bar{\chi}_c$, and if we correct to a $\gamma = 1.4$ gas by the theoretical weak-interaction factor[18] $\gamma(\gamma - 1)$, we obtain $(p_2 - p_c)/p_c \approx 1 + 0.13\ \bar{\chi}_c$, which may be compared with the best fit for the present data, $(p_2 - p_c)/p_c \approx 1 + 0.12\ \bar{\chi}_c$.

Hole Size Effect

It has been shown by Talbot[1] and by Rayle,[9] and others, that the apparent pressure sensed by a static pressure orifice increases with the diameter of the orifice. The phenomenon is due to mixing between the stream passing over the surface and the fluid confined within the orifice and pressure tubulation; the momentum transferred by the mixing sets up currents in the fluid within the orifice which give rise to the increase in pressure.

Ideally, a static pressure orifice should be as small as possible, both to minimize this hole size effect and to provide a truly localized pressure measurement. However, in rarefied gas flow if a pressure orifice is made small enough one encounters another effect, known as thermal transpiration, which can also result in errors in pressure measurement. Thermal transpiration occurs, for example, when an orifice whose diameter is small compared to the mean free path separates two regions of gas at different temperatures.[10] In this case, the pressure ratio is given by

$$p_1/p_2 = \sqrt{T_1/T_2} \tag{1}$$

The static pressure orifices used in the present experiments were 0.010 in. in diameter. For an orifice of this size, the pressure increment due to momentum mixing is completely negligible. However, there is the possibility that thermal transpiration effects may be important, since the boundary layer is a region of strong temperature gradient, and many of the molecules which enter the orifice from the gas stream come from regions in the boundary layer which are at temperatures different from the gas within the orifice.

We can make a rough estimate of the magnitude of the thermal transpiration effect in the following way. We assume the boundary-layer characteristics to be given with sufficient accuracy by Howarth's analysis.[11] For an insulated cone, with $\sigma = 1$ and $\mu/\mu_2 = T/T_2$,

$$\delta = (5.0/\sqrt{3})(1 + 0.08M_2^2)\sqrt{\nu_2 x/u_2} \tag{2}$$

$$T/T_{aw} = \{1 + 0.2M_2^2[1 - (u^2/u_2^2)]\}/(1 + 0.2M_2^2) \tag{3}$$

Now, let us also assume that the velocity distribution in the boundary layer is linear in y. Then the temperature T_Λ at a distance Λ_w from the wall is given by

$$T_\Lambda/T_{aw} = \{1 + 0.2M_2^2[1 - (\Lambda_w^2/\delta^2)]\}/(1 + 0.2M_2^2) \tag{4}$$

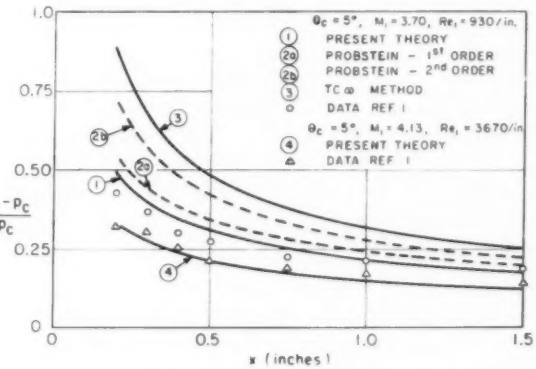

FIG. 5. 5° cone data, $M \sim 4$.

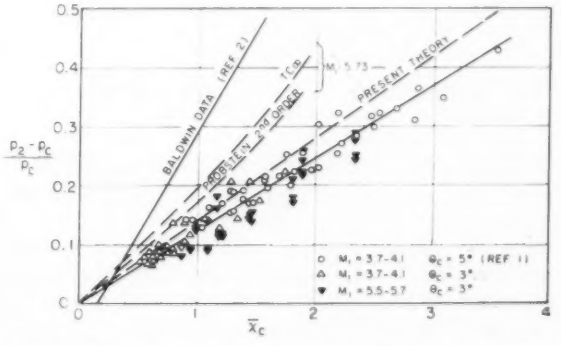

FIG. 6. Induced pressure increment vs. viscous interaction parameter $\bar{\chi}_c$.

We identify Λ_w with the mean free path of the gas at the wall.

As a specific example, let us take the following conditions:

$$M_2 = 5.5 \qquad x = 1 \text{ in.}$$
$$Re_2 = 10{,}000/\text{in.} \qquad T_{aw} = 270°\text{K.}$$
$$p_2 = 170\ \mu\text{Hg}$$

For these conditions $\Lambda_w = 0.011$ in., $\delta \approx 0.099$ in. Then from Eq. (1) we find $p_\Lambda/p_w = 0.994$, where we identify p_Λ as the pressure which we are attempting to measure and p_w as the pressure within the orifice which is presumably in error because of the thermal transpiration effect. It is seen that for this particular case the error is about 1/2 per cent. For the worst conditions, the error is found to be about 2 per cent. Actually, this analysis greatly overestimates the effect, since Eq. (1) is true only for $\Lambda_w/d \gg 1$. For the experiments $\Lambda_w/d \approx 1$, and in this range the pressure increment is less than 10 per cent of what it is in free molecule flow. One may conclude, therefore, that the pressures measured in the experiments were true static pressures, essentially uninfluenced by either momentum mixing or thermal transpiration hole size effects.

Appendix (A)

"Modified Tangent-Cone" Method

The assumptions usually made in the tangent-cone analysis for self-induced pressures are: (a) a region of inviscid flow exists between the outer edge of the boundary layer and the shock wave, and (b) the flow parameters, such as Mach Number, pressure, etc., at the edge of the boundary layer (subscript 2 in Fig. 1) can be obtained to satisfactory approximation by the tangent-cone (TC) method. The TC method consists of relating the local flow parameters on a body to the undisturbed flow ahead of the shock wave through conical flow theory (e.g., Taylor-Maccoll values), but using the local body inclination as the effective cone angle. In the case of self-induced pressures on a cone as shown in Fig. 1, the local effective cone angle is taken to be θ_2, the sum of the cone angle θ_c and the angle $\theta_\delta = \tan^{-1}(d\delta^*/dx)$.

Two computations are involved in utilizing the TC method for evaluation of self-induced pressures. First, the inviscid flow values must be obtained, for given effective cone angle θ_2, either from the exact solution (Kopal's Tables) or by one of several approximate methods[12, 13] which are available. Second, the boundary-layer displacement thickness must be evaluated, as a function of position along the cone surface, and here again several methods of varying accuracy and complexity are available. It will be noticed that the two computations are not independent. We are dealing with an interaction phenomenon—the boundary-layer growth determines the inviscid flow values at the outer edge of the boundary layer, but at the same time the rate of growth of the boundary layer is determined by these inviscid flow values. An accurate application of the TC method must include this interaction effect.

For the computations of the inviscid flow values, the exact Taylor-Maccoll results as computed by Kopal are employed. There are several supersonic and hypersonic flow approximations in analytic form which are accurate over different ranges of the similarity parameter $K_2 = M_1\theta_2$, but no single one is sufficiently accurate over the entire range of K_2 encountered in the tests reported here. The boundary-layer displacement thickness is calculated from the approximate formula of Monaghan,[14] which includes the effect of Prandtl Number and isothermal-wall heat transfer. It does not include the effects of pressure gradient or transverse curvature. To account in some measure for the variation in the external flow qualities along the outer edge of the boundary layer, local values of the external flow parameters are used to calculate M_2 and Re_{x_2}.

Monaghan's result, to which the Mangler[15] transformation correction has been applied, is

$$\delta^*/x = \sqrt{C/Re_{x_2}}\left((\pi/2)\left\{(T_w/T_2) - [\sigma(\gamma-1)/4]M_2^2\right\} - \left\{1 + \sigma^{1/3}[(T_w - T_{aw})/T_2]\right\}\right) \qquad \text{(A-1)}$$
$$\tan\theta_\delta = (d\delta^*/dx) \doteq (1/2)\cdot(\delta^*/x)$$

where $$T_{aw}/T_2 = 1 + [\sigma^{1/2}(\gamma-1)M_2^2/2] \qquad \text{(A-2)}$$

and the Chapman-Rubesin C is defined by

$$C = (\mu'/\mu_c)/(T'/T_c) \qquad \text{(A-3)}$$

The viscosity μ' is evaluated at the intermediate T' given by

$$T'/T_c = (T_w/T_c) - 0.468\sigma^{1/3}[(T_w - T_{aw})/T_c] - 0.273\sigma[(\gamma-1)/2]M_c^2 \qquad \text{(A-4)}$$

However, instead of using the Sutherland law, as recommended by Monaghan, the Bromley-Wilke[16] values are used for μ'/μ_c, since the Sutherland law is less accurate at the low free-stream temperatures encountered in our tests. The actual wall temperature T_w is determined by experiment.

For a given free-stream condition (M_1, p_1, etc.), a set of values of θ_2 are chosen, and for each of these values a range of values of θ_δ are computed, using local free-stream conditions determined by the tangent-cone method and Kopal's Tables. The angle θ_δ is a function of x, for each selected value of θ_2. Since the value of x appropriate to a particular value of θ_2 is that for which $\theta_2 - \theta_\delta = \theta_c$, by cross plotting one can obtain θ_2 as a function of x, and, hence, p_2/p_c as a function of x.

Accuracy of the Method

The accuracy of the TC calculation of the inviscid flow has been examined by Ehret[17] and Lees,[18] by comparing pressure distributions on pointed ogives with exact values from the method of characteristics. The

TC method yields surface pressures which are slightly higher than the exact values, the difference depending on the distance from the vertex of the ogive. At the vertex the two methods, of course, give identical results; farther back the deviation may be of the order of a few per cent. It is found that the TC method also overestimates the pressure for blunt power-law bodies.[19]

In the calculation for self-induced pressures the effect of boundary-layer growth on the external inviscid flow is approximated by increasing the effective local cone angle by θ_δ. Order of magnitude arguments concerning the accuracy of this approximation have been given by Lees and Probstein.[20] The error involved in replacing the actual streamline inclination in the external flow by θ_δ is estimated to be of order $(\delta/x)^2$, where δ is the boundary-layer thickness. It also turns out that the neglect of pressure gradient across the boundary layer is also justified provided $(\delta/x)^2$ is small.

The variation in external flow properties along the outer edge of the boundary layer is partially taken into account by using local values for M_2, Re_2, p_2, etc. But it will be noted that the expression for $d\delta^*/dx$ [Eq. (A-1)] is only approximate, since the terms involving dM_2/dx, dT_2/dx, and dRe_2/dx have been neglected. It turns out that for the present calculations these terms contribute an increment of about 5 per cent at most to θ_δ, and their neglect is not serious.

Two important effects which have not been included in the boundary-layer analysis are the effect of transverse curvature and the direct effect of the self-induced pressure gradient on the density and velocity distributions within the boundary layer. Both the transverse curvature and the pressure gradient tend to thin the boundary layer, and thus result in smaller values for the induced pressure increment. The transverse curvature effect has been studied by Probstein and Elliott.[21] Probstein[22] concludes from his analysis, which is valid for small δ^*/r_c, that transverse curvature does not appreciably alter the boundary-layer displacement thickness. However, much of our data were in the range $\delta^*/r_c = 1$ to 3, and for these values the transverse curvature effect almost certainly cannot be neglected. An estimate of transverse curvature effect in very simple form is given by Hill, et al.,[23] in the form

$$(d\delta^*/dx)_{tc} = (d\delta^*/dx)/\sqrt{1 + 2\delta^*/r_c}$$

where δ^* is the displacement thickness calculated by theory, neglecting transverse curvature, and $\delta_{tc}{}^*$ the actual displacement thickness. This correction is probably not valid for values of δ^*/r_c as large as those of the present tests, but we may note that for $\delta^*/r_c = 1$, a reduction of about 40 per cent in the induced pressure is predicted.

Appendix (B)

Probstein's Analysis for the Self-Induced Pressure Effect

Probstein[22] considers a Taylor series expansion of the surface pressure in the form

$$(p_2 - p_c)/p_c = (p_1/p_c)\{[\partial(p_c/p_1)/\partial\theta]_{\theta=\theta_c} \cdot \theta_\delta + (1/2!)[\partial^2(p_c/p_1)/\partial\theta^2]_{\theta=\theta_c} \cdot \theta_\delta{}^2 + \ldots\} \quad \text{(B-1)}$$

Now, for $K_c < 1$, which is the range encountered in the present tests, the Lees hypersonic approximation is not accurate, so that the values for the derivatives in (B-1) obtained by Probstein cannot be used. Probstein suggests that for $K_c < 1$ the ratio p_1/p_c be evaluated from the Kopal Tables, but that the derivatives be evaluated from the von Kármán[24] slender body result. However, this result is also not sufficiently accurate. Guided by Van Dyke's suggestions[25] for combined supersonic-hypersonic similarity, we found that a formula of the form

$$p_c/p_1 = 1 + (A_1\gamma M_1{}^2\theta_c{}^2/2)\ln(A_2/\theta_c\sqrt{M_1{}^2 - 1}) \quad \text{(B-2)}$$

could be made to fit the Kopal values and the Van Dyke second-order theory values for p_c/p_1 over the range $0.14 < \theta_c\sqrt{M_1{}^2 - 1} < 0.3$; $0 < \theta_c < 0.13$ radians. The constants found were $A_1 = 1.52$, $A_2 = 2.85$. Expression (B-2) was used to calculate the derivatives in Eq. (B-1), and expression (A-1) was used to evaluate θ_δ and $\theta_\delta{}^2$, except that inviscid flow values M_c, Re_c, and T_c, were used instead of the local values M_2, Re_2, and T_2.

We found that it was necessary to include at least two terms in the series. For example, with $M_1 = 3.70$, $\theta_c = 5°$,

$$\left.\begin{aligned}(p_1/p_c)[\partial(p_1/p_c)/\partial\theta]_{\theta=\theta_c} &= 3.5\\ (p_1/p_c)[\partial^2(p_1/p_c)/\partial\theta^2]_{\theta=\theta_c} &= 17\end{aligned}\right\} \quad \text{(B-3)}$$

We also performed a numerical differentiation of a curve constructed from cross-plots of the Kopal entries and the 3° values calculated by second-order theory, and obtained the values 3.8 and 38 for the above derivatives. The first of these values may be more accurate than that given in Eq. (B-3). Not much accuracy can be claimed for either set, however.

The results of the Probstein analysis are shown in Figs. 4(b) and 5. The curves entitled "1st Order" were obtained using only the first term in the series (B-1), those entitled "2nd Order" using two terms. It can be seen that for small angle cones (i.e., small K_c) the convergence of the series is slow. This slow convergence is already evident at $K_c = 1$, as can be seen from examination of the functions presented in reference 22.

As a check on the Probstein analysis, we also evaluated two induced pressure distributions by what we have called the "TC_∞" Method. In this method the boundary-layer slope θ_δ is calculated from the inviscid flow values T_c, M_c, and Re_c, rather than the local values of these quantities, but the tangent cone method with the Kopal values rather than the Probstein series is used to evaluate the pressure. The TC_∞ method, of course, gives the values that the Probstein method should converge to. As is evident in Figs. 4(b) and 5, the use of two terms in the Probstein series provides a fairly good approximation. But Probstein's

method is not very useful for $K_e < 1$, because it is difficult to obtain accurate values for the required derivatives.

References

[1] Talbot, L., *Viscosity Corrections to Cone Probes in Rarefied Supersonic Flow at Nominal Mach Number of 4*, NACA TN 3219, 1954.

[2] Baldwin, L. C., *Viscous Effects on Static Pressure Distribution or a Slender Cone at a Nominal Mach Number of 5.8*, GALCIT Hypersonic Wind Tunnel Memo No. 28, June 14, 1955.

[3] Maslach, G. J., and Sherman, F. S., *Design and Testing of an Axisymmetric Hypersonic Nozzle for a Low Density Wind Tunnel*, University of California Engineering Project Report HE-150-134, Series 23, Issue 17, February, 1956.

[4] Van Dyke, M. D., *Practical Calculation of Second Order Supersonic Flow Past Nonlifting Bodies of Revolution*, NACA TN 2744, 1952.

[5] Kopal, Z., *Tables of Supersonic Flow of Air Around Cones*, Tech. Report No. 1, Massachusetts Institute of Technology, Cambridge, 1947.

[6] Schaaf, S. A., Hurlbut, F. C., Talbot, L., and Aroesty, J., *Viscous Interaction Experiments at Low Reynolds Numbers*, ARS Journal, p. 527, July, 1959.

[7] Kendall, J. M., Jr., *An Experimental Investigation of Leading-Edge Shock Wave-Boundary Layer Interaction at Mach 5.8*, Journal of the Aeronautical Sciences, Vol. 24, No. 1, pp. 47–56, January, 1957.

[8] Blumer, C. B., Bradfield, W. S., and Scott, C. J., *The Effect of Cone Tip Blunting on the Supersonic Conical Laminar Boundary Layer*, Rosemont Aero. Lab. Engineering Memo 29, University of Minnesota, March, 1954.

[9] Rayle, R. E., Jr., *An Investigation of the Influence of Orifice Geometry on Static Pressure Measurements*, M.S. Thesis in Mechanical Engineering, Massachusetts Institute of Technology, 1949.

[10] Loeb, L. B., *Kinetic Theory of Gases*, 2nd Ed., McGraw-Hill Book Company, Inc., New York, 1934.

[11] Howarth, L., *Concerning the Effect of Compressibility on Laminar Boundary Layers and Their Separation*, Proc. Royal Soc. A, No. 1036, Vol. 194, pp. 16–42, 1948.

[12] Lees, L., *Note on the Hypersonic Similarity Law for an Unyawed Cone*, Journal of the Aeronautical Sciences, Vol. 18, No. 10, pp. 700–702, October, 1951.

[13] Probstein, R. F., and Bray, K. N. C., *Hypersonic Similarity and the Tangent-Cone Approximation for Unyawed Bodies of Revolution*, Journal of the Aeronautical Sciences, Vol. 22, No. 1, pp. 66–68, January, 1955.

[14] Monaghan, R. J., *An Approximate Solution of the Compressible Laminar Boundary Layer on a Flat Plate*, ARC R&M No. 2760, Great Britain, 1953.

[15] Howarth, L., (Ed.), *Modern Developments in Fluid Dynamics, High Speed Flow*, Vol. 1, Oxford University Press, p. 382, 1953.

[16] Bromley, L. A., and Wilke, C. R., *Viscosity Behavior of Gases*, Industrial and Engineering Chemistry, Vol. 143, p. 1641, July, 1951.

[17] Ehret, D. M., *Accuracy of Approximate Methods for Predicting Pressures on Pointed Nonlifting Bodies of Revolution in Supersonic Flow*, NACA TN 2764, August, 1952.

[18] Lees, L., *Hypersonic Flow*, Fifth International Aeronautical Conference, Los Angeles, pp. 241–276, 1955. Also available as GALCIT Publication No. 404.

[19] Kubota, T., *Inviscid Hypersonic Flow over Blunt-Nosed Slender Bodies*, Paper presented at 1957 Heat Transfer and Fluid Mechanics Institute, California Institute of Technology, Pasadena, Calif., June 19–21, 1957. See also GALCIT Hypersonic Research Project, Memorandum 40, June 25, 1957, and Lees, L., *Recent Developments in Hypersonic Flow*, Jet Propulsion, November, 1957.

[20] Lees, L., and Probstein, R. F., *Hypersonic Viscous Flow Over a Flat Plate*, Princeton University, Aero. Engrg. Lab. Report No. 195, April 20, 1952.

[21] Probstein, R. F., and Elliott, D., *The Transverse Curvature Effect in Compressible Axially Symmetric Laminar Boundary Layer Flow*, Journal of the Aeronautical Sciences, Vol. 23, No. 3, pp. 208–244, March, 1956.

[22] Probstein, R. F., *Interacting Hypersonic Laminar Boundary Layer Flow Over a Cone*, Technical Report AF 2798/1, Division of Engineering, Brown University, Providence, R.I., March, 1955.

[23] Hill, J. A. F., et al., *Mach Number Measurements in High-Speed Wind Tunnels*, AGARDograph 22, October, 1956.

[24] von Kármán, T., *The Problem of Resistance in Compressible Fluids*, Proc. 5th Volta Congress, pp. 210–271, Rome, 1935.

[25] Van Dyke, M. D., *A Study of Hypersonic Small-Disturbance Theory*, NACA TR 1194, 1954.

[26] Erickson, W. D., *Study of Pressure Distributions on Simple Sharp-Nosed Models at Mach Numbers From 16 to 18 in Helium Flow*, NACA TN 4113, October, 1957.

Some Effects of Sound-Reduction Devices on a Turbulent Jet

(*Continued from page 722*)

One cannot, on the strength of the present experiment alone, determine whether the turbulence values u'/U_j yield a sufficiently complete working index of the noise radiating efficiency of a jet. Still, reasons have been adduced to hope that the evaluation of the noise generating strength of a jet by its turbulence levels will prove adequate for engineering purposes. To establish the point, the type of measurements reported here should be made on a number of different nozzles with known noise generating efficiency.

What has been said in no way obviates the need for a more informative (and more difficult) study which might relate a more exact measure of the noise source strength with some integral property of the turbulent region

References

[1] Corcos, G. M., *Some Measurements Bearing on the Principle of Operation of Jet Silencing Devices*, Douglas Aircraft Company, Inc., Report No. SM-23114, March, 1958.

[2] Lighthill, M. J., *On Sound Generated Aerodynamically, I, General Theory*, Proc. Roy. Soc., Series A, Vol. 211, p. 564, 1952.

[3] Liepmann, H. W., *Aspects of the Turbulence Problem*, ZAMP, Vol. III, p. 407, 1952.

[4] Unpublished Douglas Aircraft Company, Inc., and NACA data.

[5] Lighthill, M. J., *On Sound Generated Aerodynamically, II, Turbulence As a Source of Sound*, Proc. Roy. Soc., Series A, Vol. 222, p. 1, 1954.

[6] Tyler, J. M., *Jet Noise*, SAE Preprint No. 287, 1954.

[7] Lassiter, L. W., and Hubbard, H. H., *Experimental Studies From Subsonic Jets in Still Air*, NACA TN 2757, 1952.

Heat Transfer in Separated Flows

HOWARD K. LARSON*

Ames Research Center, NASA

Summary

Results of an experimental heat-transfer investigation in regions of separated flow are presented and compared with the theoretical analysis of NACA TN 3792. The average heat transfer for both laminar and turbulent separated boundary layers was found to be from 35 to 50 per cent less than that for equivalent attached boundary layers. The overall scope of the measurements included Mach Numbers from 0.3 to 4.0 and Reynolds Numbers from 10^5 to 4×10^6. The results for laminar boundary layers agree well with the analysis of TN 3792. The results for turbulent boundary layers, however, disagree considerably. Results of velocity and temperature surveys in the separated turbulent boundary layer are presented and partially explain the discrepancy between the experiments and analysis. The maximum local heat-transfer rates were found to occur in the reattachment region of the separated boundary layers investigated. The effect of transition on heat transfer in the separated laminar boundary layers is described and data showing effects of Mach Number and wall temperature on the transition Reynolds Number of separated laminar flows are also included.

Symbols

A_{BL} = area of heated boundary layer: $\pi D\ell$ for axially symmetric models; $2b\ell$ for two-dimensional models, sq.ft.
b = span of two-dimensional models, ft.
c_p = specific heat of air, B.t.u./lb. °R.
D = diameter of axially symmetric models, ft.
$\bar{h}$ = average heat-transfer coefficient, $\bar{h} \equiv d(Q_{tot}/A_{BL})/dT_w$
ℓ = length of heated boundary layer, ft.
ℓ' = length of separated boundary layer, ft. ($\ell' = \ell$ for axially symmetric model, $\ell' = 2/3\,\ell$ for two-dimensional model)
L = model length, ft. (defined in Fig. 2)
M = Mach Number
Q_{tot} = total heat-transfer rate to heated portion of model, B.t.u./sec.
q = local surface heat-transfer rate, B.t.u./sec. ft.^{2}
$\bar{q}$ = average surface heat-transfer rate, B.t.u./sec. ft.^{2}
R_L = Reynolds Number, $R_L \equiv \rho_e u_e L/\mu_e$
R_{tr} = transition Reynolds Number, $R_{tr} \equiv \rho_\infty u_\infty \ell'/\mu_\infty$
S = separation location
$\overline{St}$ = average Stanton Number, $\overline{St} \equiv \bar{h}/\rho_e u_e c_p$
T = temperature, °R.
u = velocity in x direction, ft./sec.
x = longitudinal distance downstream of separation, ft.
y = radial distance from model surface, ft.
Y = depth of separated region, ft.
ρ = density, lb./cu. ft.
μ = coefficient of viscosity, lb./ft. sec.

Subscripts

A = attached boundary layer
aw = adiabatic wall
e = outer edge of separated or attached boundary layer
S = separated boundary layer
w = wall
∞ = free stream

Presented at the Aerodynamics—II Session, IAS 27th Annual Meeting, N.Y., Jan. 26–29, 1959.

* Aeronautical Research Scientist.

Introduction

A KNOWLEDGE of the effects of flow separation on heat transfer is an important consideration in the design of a variety of aerodynamic vehicles. In reference 1, Dr. D. R. Chapman of Ames Research Center presented an analysis of heat transfer in regions of separated flow. The results of that analysis indicate that separation of a laminar boundary layer reduces the average heat transfer whereas separation of the turbulent boundary layer can either increase or decrease the average heat transfer, depending on the Mach Number. Experimental heat-transfer data, appropriate for comparison with the results of the analysis, have not been available in the literature.

In order to provide experimental heat-transfer data for comparison with the analytical results, a wind-tunnel investigation was initiated. These experiments provided heat-transfer data for equivalent attached and separated boundary layers, thereby enabling a direct comparison of separated-flow heat transfer with attached-flow heat transfer. Additional observations of this investigation also provided an insight into some of the details of heat transfer in separated boundary layers.

This paper presents experimentally determined ratios of average heat transfer for separated boundary layers to average heat transfer for equivalent attached boundary layers and compares the results with the calculations of reference 1. Data were obtained for completely laminar boundary layers in supersonic flow. Since reference 1 indicated a large effect of Mach Number on heat transfer for separated turbulent flows, data for turbulent boundary layers were obtained over a range of subsonic and supersonic Mach Numbers. Qualitative measurements of the distribution of local heat-transfer rates were obtained and are presented for both separated laminar and turbulent flows. Utilization of fully laminar separated boundary layers (transition downstream of reattachment) depends on the transition Reynolds Number characteristics of these flows. Since aerodynamic heating problems are usually encountered at wall temperatures considerably lower than adiabatic, some recent measurements of the effect of wall temperature on separated boundary-layer transition are also included.

The writer recently became aware of the results presented in references 2–6. A short section is added at

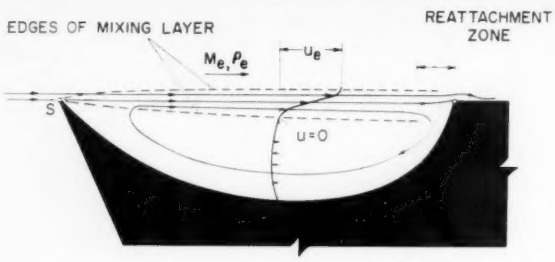

FIG. 1. Theoretical model.

the end of this paper for the purpose of comparing the present data with the results of those investigations.

Description of Analysis

The physical model used in the analysis of reference 1 is presented in Fig. 1. The theory analyzes the thin, separated boundary layer with the following assumptions: (a) the thickness of the boundary layer is zero at separation, or small compared with the depth of the separated region; (b) the length of the reattachment zone is small compared with the length of the separated boundary layer; (c) the pressure is constant along the separated layer; (d) the wall is isothermal; and (e) the low-speed air in the reverse-flow region is at wall temperature when drawn into the separated boundary layer at the zero velocity stream line.

The theory then calculates the average heat transfer for the separated boundary layer and compares it with the average heat transfer for an attached boundary layer with the same constant Mach Number, temperature, and pressure at the outer edge of the boundary layer, and the same constant wall temperature. Comparisons of the experimental results with the calculations of the analysis will be presented separately for laminar and turbulent flows after first describing the experimental method.

Experimental Method

Two types of electrically heated models were used in the experimental investigation. As shown at the left of Fig. 2, the axially symmetric models provided cylindrical attached and separated boundary layers of approximately the same mean, outer-edge flow properties and boundary-layer area. The two-dimensional wedge models, at the right, provided two-dimensional attached and separated boundary layers with approximately the same outer-edge flow properties and area. During the tests of both the axially symmetric and two-dimensional models, the attached- and separated-flow models were tested under nearly identical wind-tunnel flow conditions, thereby providing a direct comparison of heat transfer for separated boundary layers with heat transfer for attached boundary layers. Each of the two heated centerbodies of the axially symmetric models had eight individually heated segments. The forebody and afterbody were not heated and were thermally insulated from the heated centerbodies. During the tests, power was distributed among the eight segments to provide a constant wall temperature. The two-dimensional models were constructed of solid copper, and power to fore and aft electrical heaters was adjusted to provide a constant wall temperature. In order to provide true, two-dimensional data, guard heaters of identical cross section were mounted outboard on both sides of the models and capped with thin insulated plates to prevent crossflow in the separated region. A rear guard heater and the above described end guard heaters were removed when shadowgraphs of the flow pattern were taken.

The experimental data were obtained in the following manner: with the power distributed to provide constant wall temperature, the total power to the model was varied and plotted as a function of wall temperature. Fig. 3 presents some typical data plots from which the average heat-transfer coefficients, $\bar{h}$, were calculated. For the purposes of the present tests, the average heat-transfer coefficient is defined as $\bar{h} \equiv d(Q_{tot}/A_{BL})/dT_w$ and is equivalent to the customary definition, $\bar{h} \equiv Q_{tot}/A_{BL}(T_w - T_{aw})$, provided $\bar{h}$ is independent of T_w. In the course of the present tests, $\bar{h}$ was always found to be independent of T_w within the limits of experimental accuracy. The use of the present definition of $\bar{h}$ does not require a knowledge of

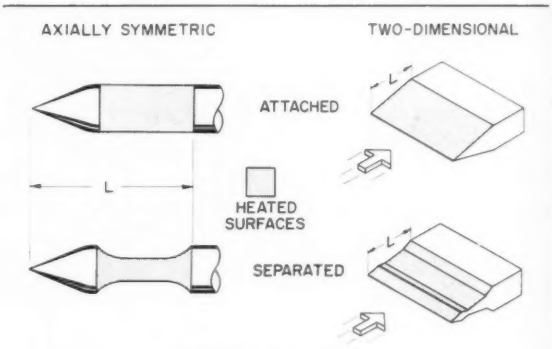

FIG. 2. Test models.

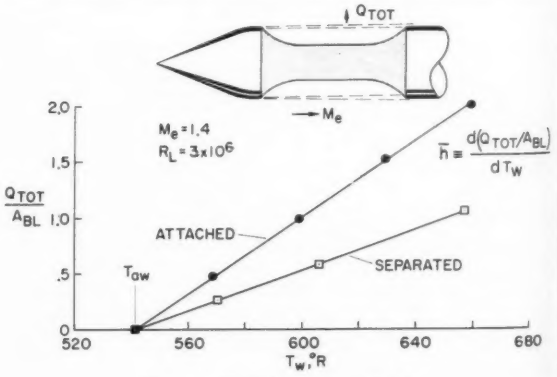

FIG. 3. Experimental method.

the adiabatic wall temperature. During most of the runs, power-off data were obtained and the measured adiabatic wall temperatures agreed well with extrapolations of the Q_{tot}/A_{BL} versus T_w plots to zero heat transfer.

For the purposes of comparing the experimental results with the analysis of reference 1, the data will be presented as the ratio of the average heat-transfer coefficients for separated and attached boundary layers, $\bar{h}_S/\bar{h}_A$, obtained with nearly identical outer-edge flow conditions. The Reynolds Number and the Stanton Number were calculated using mean flow properties at the outer edges of the boundary layers.

Comparison of Experimental Results for Laminar Boundary Layers With Theory

Axially Symmetric Models

Data obtained for the axially symmetric models are presented in Fig. 4, and compared with the results of reference 1. The measurements of $\bar{h}_S/\bar{h}_A$ at M_e = 3.1 and 4.0 agree well with the theory and appear to be reasonably independent of Mach Number and Reynolds Number up to the Reynolds Number at which transition begins in the reattachment region. At higher Reynolds Numbers, the increased values of $\bar{h}_S/\bar{h}_A$ are for transitional separated-flow data compared with laminar attached-flow data. Separation is observed to induce premature transition and at sufficiently high Reynolds Numbers, $R_L > 2 \times 10^6$, an increase rather than a reduction in average heat transfer was measured.

The interpretation of the agreement between the experimental results for completely laminar flow and reference 1 was considered open to question since the heated area of the separated-flow model was 35 per cent less than the heated area of the attached-flow model. In order to determine to what extent the reduction in heat transfer is due to the reduction in surface area, additional experiments were conducted with the two-dimensional models described in Fig. 2. The wetted-surface area lying beneath the separated boundary layer is, for this case, about 10 per cent greater than that for the attached boundary layer.

Two-Dimensional Models

Data obtained in the study of the two-dimensional boundary layers are presented in Fig. 5 and compared with theory. These data are for M_e = 3.0 and were obtained at a free-stream Mach Number of about 4. Only the rearward two-thirds chord of the separated-flow model was actually exposed to separated flow, and the results of reference 1 can be applied only to that portion of the surface for comparison of experiment with theory. Hence, the full theoretical reduction of 44 per cent would not be expected. Heat transfer for laminar attached boundary layers varies as $x^{-1/2}$, and the theoretical fractional reduction in heat transfer for this case would be $(\bar{h}_A - \bar{h}_S)/\bar{h}_A = 0.44(\sqrt{1} - \sqrt{1/3}) = 0.186$. The dashed line representing the analysis corresponds therefore to a value of $\bar{h}_S/\bar{h}_A = 0.814$. The data again agree well with the theory up to the Reynolds Number at which transition begins in the reattachment region. The present results then indicate that the average heat transfer for separated laminar boundary layers is reduced in accordance with the calculations of reference 1 and is apparently independent of the heated surface area lying beneath the separated boundary layer.

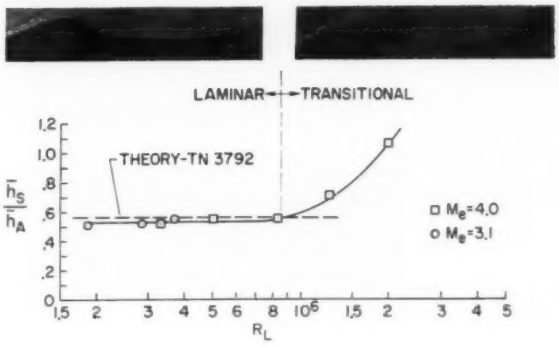

FIG. 4. Laminar heat transfer, axially-symmetric flow.

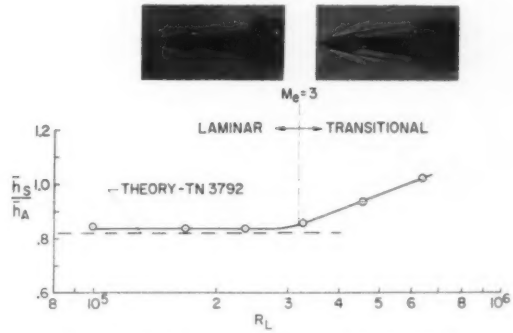

FIG. 5. Laminar heat transfer, two-dimensional flow.

Comparison of Experimental Results for Turbulent Boundary Layers With Theory

In order to obtain turbulent-boundary-layer data for comparison with the analysis, boundary-layer trips were fitted to the insulated forebody of the axially symmetric models described earlier. Two shadowgraphs typical of the turbulent flows investigated are presented in Fig. 6. It can be observed in both shadowgraphs that transition occurred just upstream of separation. This location of transition provided a minimum-thickness, turbulent boundary layer at separation in accordance with the assumptions of reference 1. Boundary-layer trip requirements are dependent on Mach Number and Reynolds Number. Wire trips of different wire diameters were employed in most cases in order to obtain transition just upstream of separation as flow conditions were varied. In one case,

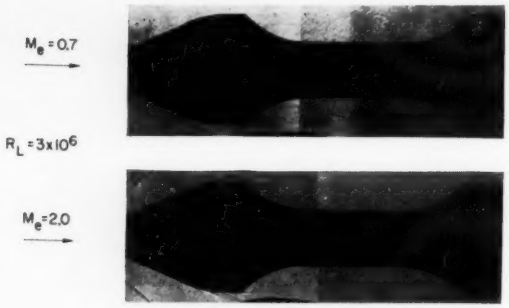

FIG. 6. Separated turbulent flow.

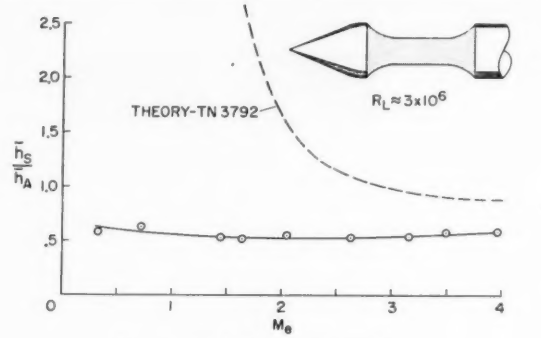

FIG. 7. Turbulent heat transfer.

$M_e = 0.7$ and $R_L = 3 \times 10^6$, a 1/16-in.-wide cellophane-tape trip was used. The same forebody and trips were used for the separated- and attached-flow models. Again, tests were performed under nearly identical wind-tunnel test conditions for both separated and attached boundary layers.

In contrast to the results for laminar boundary layers, the analysis of reference 1 indicated a large increase in heat transfer for turbulent boundary layers when separated at subsonic and low supersonic Mach Numbers. The analysis also indicated a large effect of Mach Number on $\bar{h}_S/\bar{h}_A$. The results of reference 1 and the experimental data are presented in Fig. 7. The experiments were performed at a constant Reynolds Number of about 3×10^6. In contrast to the excellent agreement of experiment with theory observed for laminar boundary layers, a large disagreement is evident for turbulent boundary layers, especially at the lower Mach Numbers.

In an attempt to shed some light on this large discrepancy, velocity and temperature profiles were measured in the separated, turbulent boundary layers with both heated and adiabatic walls. A shadowgraph taken during a probe survey at $M_e = 2.6$ is presented in Fig. 8 along with the pertinent thermal data. These data are typical of the probe studies conducted at other Mach Numbers and Reynolds Numbers. The temperature data are presented as the difference between the total temperatures measured by the probe with the wall heated and adiabatic. The plot in Fig. 8 shows how this temperature difference varied through the separated boundary layer. As discussed previously, reference 1 assumed that air in the low-velocity, reverse-flow region was drawn into the separated boundary layer at a temperature equal to wall temperature. If this assumption of the theory were correct, the probe would have measured $T_t = T_w$ at the zero velocity stream line. The lower portion of the probe survey indicates that the measured temperature difference is an order of magnitude less than that assumed by the theory. This large discrepancy in the temperature potential is one possible explanation of the disagreement found for the experimental and theoretical heat-transfer results. The probe surveys also show that the thickness of the separated boundary layer is greater than one-half the depth of the separated region, which may contribute to the difference since it is assumed in reference 1 that the thickness is relatively small. In view of these detailed studies, it is believed that theory must be modified to take into account the details of the reverse-flow region.

Effect of Reynolds Number

The effect of Reynolds Number on heat transfer in separated boundary layers is presented in Fig. 9. The data are plotted as average Stanton Number versus Reynolds Number for laminar and turbulent boundary layers. The results for laminar separated and attached boundary layers exhibit the same dependence on Reynolds Number, $\overline{St} \propto R_L^{-1/2}$, which is a well-known result for attached laminar boundary layers. Thus, the effect of separation on heat transfer is apparently independent of Reynolds Number, as discussed previously in this paper. The data for the attached turbulent boundary layer exhibit the usual Reynolds Number dependence, $\overline{St}_A \propto R_L^{-1/5}$. The separated-flow data, however, exhibit the trend, $\overline{St}_S \propto R_L^{-2/5}$, indicating that the reduction in heat transfer by separation increases with increasing Reynolds Number.

In order to explore further the dependence of Stanton

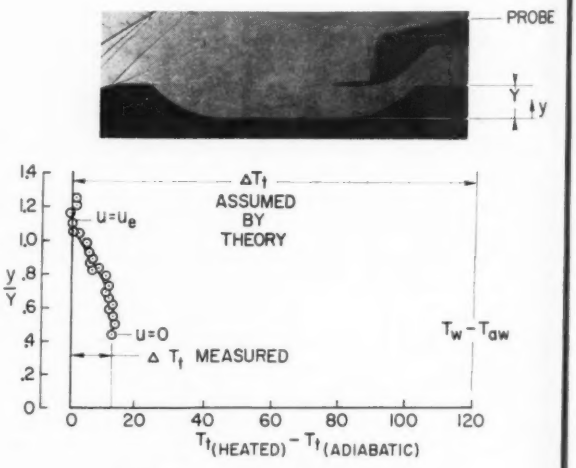

FIG. 8. Results of probe surveys.

Number on Reynolds Number, three additional tests were performed. The original configuration of Fig. 9 was tested at $M_e = 0.3$, and a larger diameter unheated forebody and afterbody were fitted to the two original heated centerbodies and data were obtained at $M_e = 2.6$. The resulting model configurations and experimental data are presented in Fig. 10. In each case, the Stanton Number exhibits a variation with Reynolds Number, $\overline{St}_S \propto R_L^{-2/5}$ in agreement with the earlier result.

A difference of about 30 per cent in the level of Stanton Numbers for the lower model, compared to the upper and center models, is apparent in Fig. 10 (data for $M_e = 2.6$), which requires some comment. As mentioned earlier, the lower model was assembled by adding a larger diameter, unheated forebody and afterbody to the heated centerbody of the original separated-flow model (top of Fig. 10). As a result, the lower model differed from the upper model in two respects: (a) the ratio of the depth of the separated region to the diameter of the separated boundary layer, Y/D, was considerably larger and would presumably result in lower reverse-flow velocities; (b) although not apparent in the sketches, portions of the lower model surface enclosed by separated flow (annular areas under reattachment and separation) were not heated whereas the entire surface between separation and reattachment was heated for the upper model. Both of these differences would probably result in lower measured Stanton Numbers for the lower model and the data, in fact, show considerably lower values for the lower model. The center model also differed from the upper model in two respects: (a) the ratio Y/D was less in this case, which would presumably result in higher reverse-flow velocities and, therefore, in higher Stanton Numbers; and (b) since the same unheated forebody and afterbody were used on the center model as were used on the lower model, portions of the model surface between reattachment and separation were unheated and would presumably tend to decrease the measured Stanton Numbers. It is possible that the opposing effects of the two differences, in this particular case, nearly compensate since the data of Fig. 10 indicate approximately equal Stanton Numbers for the center and upper models.

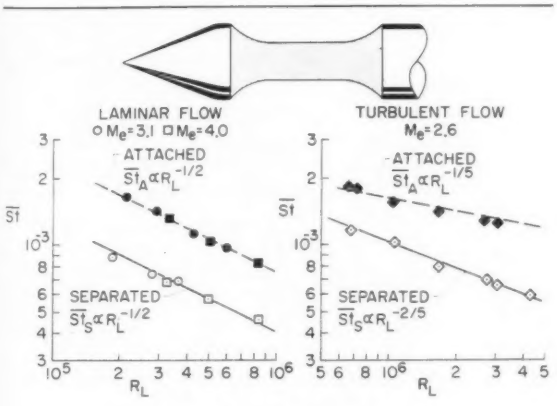

FIG. 9. Reynolds Number effect.

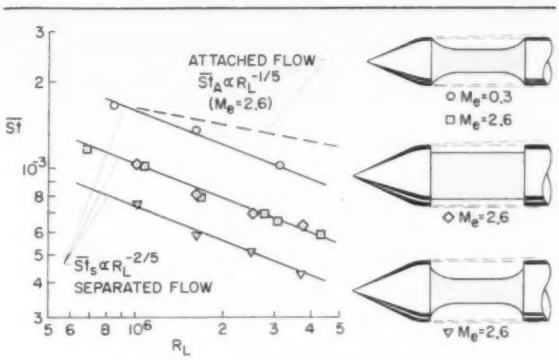

FIG. 10. Reynolds Number effect—turbulent flow.

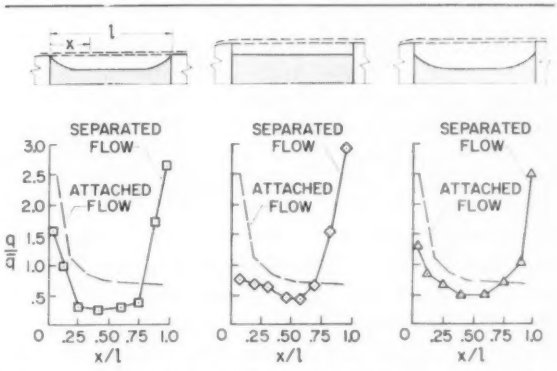

FIG. 11. Streamwise distribution of heat transfer. Laminar flow $M_e = 4$, $R_L = 0.4 \times 10^6$.

Streamwise Distribution of Heat Transfer

Knowledge of the distribution of heat-transfer rates over a surface is important to proper vehicle design. All of the data presented thus far have represented the average heat-transfer coefficients for constant wall temperature. The heated, axially symmetric centerbodies were equipped with eight heated segments of equal surface area. The measured distributions of heat to these eight segments were found to be repeatable and are believed to offer a good qualitative indication of the variation of local heat transfer on the heated surfaces.

Fig. 11 presents measured distributions of heat transfer for laminar separated boundary layers on the three configurations shown in Fig. 10. Data obtained at $M_e = 4.0$ for separated flow are presented as the ratio of the local heat transfer to the average over the heated surface, $q_S/\bar{q}_S$. For reference, the heat-transfer distribution for the attached boundary layer, $q_A/\bar{q}_A$, tested at the same outer-edge flow conditions, is shown as the dashed line. For the attached boundary layer, the maximum heat transfer was found to occur at the upstream portion of the heated surface and the local heat transfer decreased in the downstream direction which is the usual variation for attached boundary

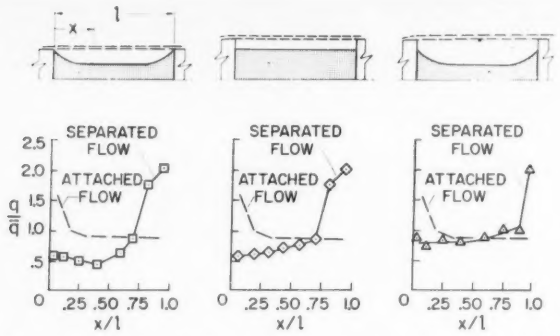

FIG. 12. Streamwise distribution of heat transfer. Turbulent flow $M_e = 2.6$, $R_L = 3 \times 10^6$.

layers. For each of the three models with separated boundary layers, however, the maximum heat transfer was found to occur at the portion of the heated surface farthest downstream. This result of maximum heating in the reattachment region was also observed at all Mach Numbers and Reynolds Numbers of the present tests.

The streamwise distribution of heat transfer was also measured for turbulent separated boundary layers on the same configurations discussed above. The results for turbulent boundary layers are presented in Fig. 12. Again, maximum heat transfer for the attached boundary layer is observed at the upstream portion of the heated centerbody. Separation of the turbulent boundary layer also resulted in maximum heat transfer in the region near reattachment for each of the three configurations, as shown in Fig. 12.

Some variations in the shape of the $q_S/\bar{q}_S$ plots are evident for the various model geometries and the detailed distribution of heat transfer may be influenced by the geometry of the separated region. The result of maximum heat transfer occurring in the reattachment region was observed for all separated flows of the present tests.

Transition of Separated Boundary Layers With Wall Temperatures Below Adiabatic

Practical applications of boundary-layer separation as a means of reducing heat transfer in laminar flow require a knowledge of the transition characteristics of separated boundary layers. This portion of the paper describes some measured effects of Mach Number and wall temperature on the Reynolds Number of transition of separated boundary layers. For the purposes of the present discussion, the transition Reynolds Number is defined as the maximum Reynolds Number, based on the length of separated boundary layer, ℓ', for which transition is just downstream of the reattachment region.

A strong influence of Mach Number on transition Reynolds Number was reported in reference 7, for the special case of adiabatic wall conditions. These data are presented in Fig. 13 as the shaded area. This area encompasses data obtained on a variety of two-dimensional models of which the sketches in Fig. 13 are typical. An increase in Mach Number is observed to increase the transition Reynolds Number from the order of 50,000 at $M = 0.3$ to about 400,000 at $M = 3$. This favorable effect of Mach Number may make separated laminar boundary layers of practical interest, especially at hypersonic Mach Numbers.

A knowledge of the effect of wall cooling, $T_w/T_{aw} < 1.0$, on transition is required since aerodynamic heating at hypersonic Mach Numbers is usually associated with wall temperatures much lower than the adiabatic wall temperature. In order to obtain this information, an experimental investigation was undertaken recently at Ames Research Center using ogive-cylinder models cooled internally with liquid nitrogen to a constant wall temperature. Some of the resulting data obtained by Stephen J. Keating, Jr., and the present writer are included in Fig. 13. Two separation lengths were required because of wind-tunnel stagnation pressure limitations. The data obtained for constant values of T_w/T_{aw} exhibit a favorable effect of Mach Number similar to that reported in reference 7. The effect of wall cooling at a constant Mach Number, however, is seen in Fig. 13 to decrease the transition Reynolds Number for separated boundary layers. This destabilizing effect of wall cooling is opposite to the stabilizing effect on attached boundary layers observed for moderate wall cooling by other investigators—e.g., references 8 and 9. The variable T_w data presented in Fig. 13 represent only a fraction of the temperatures and models investigated. The stabilizing effect of Mach Number and the destabilizing effect of $T_w < T_{aw}$ were observed in all cases.

Results of Other Investigations

Before the results of the various experiments (references 2–6) are compared, the types of flows studied will be briefly described. Rabinowicz[2] measured local heat-transfer rates on the base of a spike-hemisphere-cylinder for turbulent flow in a shock tube. Bloom and Pallone[3] measured local heat-transfer rates on two

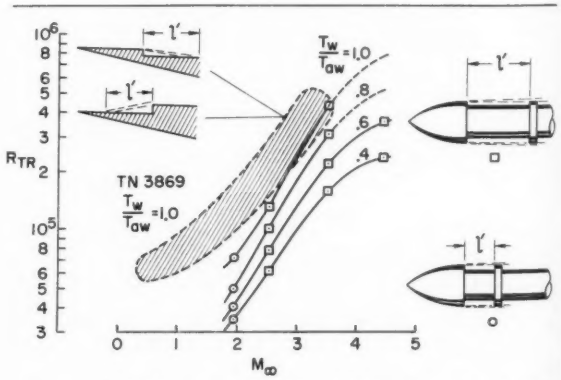

FIG. 13. Transition of separated laminar boundary layers.

afterbodies downstream of a blunt nose in a shock tunnel, and, for that investigation, transition apparently occurred in the separated boundary layer. Seban[4] and Emery[5] measured local heat-transfer rates in turbulent separated and reattached subsonic flows on two-dimensional plates downstream of a rod and two rearward-facing steps. Powers, Stetson, and Adams[6] measured local heat-transfer rates on the base and sting downstream of a hemisphere-cylinder using a shock tube. The separated boundary layers studied in reference 6 were either turbulent or laminar with transition apparently occurring in the reattachment region.

The experimental results of the above described studies are generally in agreement with the present paper, considering the variety of flows investigated. A comparison of the results of references 3–6 with the analysis of reference 1 is not discussed since the total or average heat transfer between separation and reattachment could not be calculated from their results. In each of these four investigations, approximately twofold variations in local heat transfer were measured in the regions of separated flow and are in qualitative agreement with the present data. In references 2 and 3, the separated boundary layers did not reattach to model surfaces. The two-dimensional separated turbulent boundary layers investigated in references 4 and 5 reattached on flat plates and the maximum heat-transfer rates were observed in the reattachment regions, in agreement with the results of the present paper. Reference 6 measured no distinguishable variations in local heat transfer within the separated region for either turbulent or transitional boundary layers. The measured average heat transfer for transitional flow was compared, in reference 6, with theoretical calculations of average heat transfer for attached flow reduced in accordance with reference 1. The comparison shows reasonable agreement between the data and theory considering the scatter of the data and the probable presence of transition in the reattachment region. The average heat-transfer measurements of reference 6 for separated turbulent flows were found to be about one-third of the theoretical calculations of that reference for equivalent attached turbulent boundary layers. This 67 per cent reduction in heat transfer due to separation is somewhat larger than the 50 per cent reduction reported in the present paper. This discrepancy may be the result of the considerably higher stagnation enthalpy levels of reference 6 and differences in the attached-flow heat-transfer values used for comparison (measured values in the present paper and theoretical values in reference 6).

The experiments of reference 6 gave no indication of high local heat-transfer rates in the reattachment region whereas relatively high local rates were observed for the present tests, and in references 4 and 5. One possible explanation may be the different types of axially symmetric separated flows studied in reference 6 and in the present paper. The conservation of boundary-layer mass would require a relatively thicker boundary layer at reattachment for the converging axially symmetric flow of reference 6 compared with the parallel flow of the present experiments, and the two-dimensional tests of references 4 and 5.

Concluding Remarks

Average heat transfer for separated laminar boundary layers was found to be about 56 per cent of that for equivalent attached laminar boundary layers, independent of Mach Number and Reynolds Number, in agreement with the analysis of reference 1. Average heat transfer for separated turbulent boundary layers was found to be about 60 per cent of that for equivalent attached boundary layers at a Reynolds Number of 3×10^6 and over a Mach Number range of 0.3 to 4.0—in considerable disagreement with the calculations of reference 1. The reduction in heat transfer due to separation of turbulent boundary layers was found to increase with increasing Reynolds Number within the limits of the present investigation and, if this trend continues to higher Reynolds Numbers, considerable reductions in average heat transfer may be possible through the mechanism of turbulent boundary-layer separation.

Data are also presented which demonstrate a favorable effect of increasing Mach Number and an adverse effect of decreasing wall temperature on separated boundary-layer transition. From these observations, the practicality of using separation as a means of reducing heat transfer for laminar boundary layers will probably depend strongly on the Mach Number of the flow and the ratio of wall temperature to adiabatic wall temperature.

In many applications, it may be desirable to have some control of the distribution of local heat-transfer coefficients. In all cases of the present investigation, maximum heat transfer was measured in the downstream, or reattachment, region of separated flows, whereas for attached flows, maximum heat transfer was measured at the farthest upstream portion of the heated surface as expected. In view of these results, single or multiple boundary-layer separations over a surface may permit some control of the distribution of local heat transfer and result in a reduction of the average heat transfer as well.

References

[1] Chapman, Dean R., *A Theoretical Analysis of Heat Transfer in Regions of Separated Flow*, NACA TN 3792, October, 1956.

[2] Rabinowicz, Josef, *Measurement of Turbulent Heat Transfer Rates on an Aft Portion and Blunt Base of a Hemisphere-Cylinder in the Shock Tube*, GALCIT Hypersonic Research Project Memo No. 41, 1957.

[3] Bloom, Martin H., and Pallone, Adrian, *Shroud Tests of Pressure and Heat Transfer Over Short Afterbodies With Separated Wakes*, Dept. of Aero. Eng. and Appl. Mech., Polytechnic Institute of Brooklyn (also available as WADC Tech. Note 58-185, 1958).

[4] Seban, R. A., *Heat Transfer and Flow with Separated and Reattached Boundary Layers as Produced by Surface Irregularities*, WADC Tech. Rep. 56-217, 1956.

[5] Emery, A., *Heat Transfer Downstream of a Step in a Plate*, M.S. thesis, University of California, Berkeley, Calif., 1958.

[6] Powers, William E., Stetson, Kenneth F., and Adams, Mac C., *A Shock Tube Investigation of Heat Transfer in the Wake of a Hemisphere-Cylinder, with Application to Hypersonic Flight*, Res. Rep. 30, Avco Research Laboratory, 1958.

[7] Chapman, Dean R., Kuehn, Donald M., and Larson, Howard K., *Investigation of Separated Flows in Supersonic and Subsonic Streams With Emphasis on the Effect of Transition*, NACA TN 3869, March, 1957.

[8] Jack, John R., Wisniewski, Richard J., and Diaconis, N. S., *Effects of Extreme Surface Cooling on Boundary-Layer Transition*, NACA TN 4094, October, 1957.

[9] Diaconis, N. S., Wisniewski, Richard J., and Jack, John R., *Heat Transfer and Boundary-Layer Transition on Two Blunt Bodies at Mach Number 3.12*, NACA TN 4099, October, 1957.

An Experimental Study of Jet-Flap Compressor Blades

(*Continued from page 702*)

[2] Falk, Theodore J., *Rotating Stall in Single-Stage Axial Flow Compressors*, M.S. thesis, Graduate School of Aeronautical Engineering, Cornell University, Ithaca, N.Y., September, 1956.

[3] Sinnette, John T., Jr., and Costello, George R., *Possible Application of Blade Boundary-Layer Control to Improvement of Design and Off-Design Performance of Axial-Flow Turbomachines*, NACA TN 2371, May, 1951.

[4] Katzoff, S., and Hannah, Margery E., *Further Comparisons of Theoretical and Experimental Lift and Pressure Distributions on Airfoils in Cascade at Low-Subsonic Speed*, NACA TN 2391, August, 1951.

[5] Sheets, H. E., *The Slotted-Blade Axial-Flow Blower*, ASME Diamond Jubilee Annual Meeting, Paper No. 55-A-156, November, 1955.

[6] Lockwood, Vernard E., Turner, Thomas R., and Riebe, John M., *Wind Tunnel Investigation of Jet-Augmented Flaps on a Rectangular Wing to High Momentum Coefficients*, NACA TN 3865, December, 1956.

[7] Clark, Edward L., Jr., *An Experimental Study of Jet-Flap Compressor Blades*, M.S. thesis, Graduate School of Aeronautical Engineering, Cornell University, Ithaca, N.Y., February, 1958.

[8] Cassidy, J. F., *Design and Calibration of a Cascade Wind Tunnel*, Graduate School of Aeronautical Engineering, Cornell University, Ithaca, N.Y. (to be published).

[9] Herrig, L. Joseph, Emery, James C., and Erwin, John R., *Effect of Section Thickness and Trailing-Edge Radius on the Performance of NACA 65-Series Compressor Blades in Cascade at Low Speeds*, NACA RM L51J16, December, 1951.

[10] Herrig, L. Joseph, Emery, James C., and Erwin, John R., *Systematic Two-Dimensional Cascade Tests of NACA 65-Series Compressor Blades at Low Speeds*, NACA RM L51G31, September 1951.

[11] Erwin, John R., and Emery, James C., *Effect of Tunnel Configuration and Testing Technique on Cascade Performance*, NACA Rep. 1016, 1951 (formerly, NACA TN 2028).

[12] Dean, R. C. Jr., *Aerodynamic Measurements;* Gas Turbine Laboratory, Massachusetts Institute of Technology, 1953.

[13] Scholz, N., *Über die Durchführung systematischer Messungen an ebenen Schaufelgittern*, ZFW, vol. 4, No. 10, October, 1956.

The Equation of Energy Balance for Fluttering Systems . . .

(*Continued from page 716*)

[16] Lanczos, C., *The Variational Principles of Mechanics;* University of Toronto Press, Toronto, 1949.

[17] Neumark, S., *Concept of Complex Stiffness Applied to Problems of Oscillations with Viscous and Hysteretic Damping*, Brit. RAE Rept. No. Aero 2592.

[18] Ashley, H., and Zartarian, G., *Piston Theory—A New Aerodynamic Tool for the Aeroelastician*, Journal of the Aeronautical Sciences, Vol. 23, No. 12, pp. 1109–1118, December, 1956.

[19] Dugundji, J., *Effect of Quasi-Steady Air Forces on Incompressible Bending-Torsion Flutter*, Journal of the Aeronautical Sciences, Vol. 25, No. 2, pp. 119–121, February, 1958.

[20] Acum, W. E. A., *Aerodynamic Forces on Rectangular Wings Oscillating in a Supersonic Airstream*, Brit. ARC 13,286, August, 1950.

[21] Walsh, J., Zartarian, G., and Voss, H. M., *Generalized Aerodynamic Forces on the Delta Wing with Supersonic Leading Edges*, Journal of the Aeronautical Sciences, Vol. 21, No. 11, pp. 739–748, November, 1954.

[22] Bisplinghoff, R. L., Ashley, H., and Halfman, R. L., *Aeroelasticity;* Addison-Wesley Publ. Co., Inc., Cambridge, Mass., 1955.

[23] Pines, S., *An Elementary Explanation of the Flutter Mechanism*, Proc. Nat. Special Meeting, IAS, Forth Worth, Tex., November 6–7, 1958.

[24] Pulos, John G., *An Energy Solution to the Three-Dimensional Flutter Problem*, thesis for degree of Master of Science in Applied Mechanics, Polytechnic Institute of Brooklyn, June, 1949.

Microcards for Volumes 1–5 Available

Microcards for Volumes 3–5 of the JOURNAL are now available (Vols. 1 and 2 were republished in this form earlier). All five volumes are priced at $5.50 each, and are obtainable through:

J. S. Canner & Company, Inc.
Boston, Roxbury 20, Mass.

An Actuator Disc Analysis of Inlet Distortion and Rotating Stall in Axial Flow Turbomachines†

HSUAN YEH*

University of Pennsylvania

Summary

The flow behind a rotor (or stator) blade row due to an arbitrary inlet distortion along both circumferential and spanwise directions is treated on the basis of classical actuator disc approximation. It is shown that, in general, the spanwise and the circumferential distortion waves interact, so that the combined influence is not the sum of the influences of the two simple types of distortions. Numerical examples are then given to show the influence of the various conventional design parameters. Also illustrated is the role played by the cascade characteristics, represented by the variations of loss and exit flow angle due to changing inlet flow angles. It is shown that both quantities exert a significant influence on the flow under inlet distortion.

Using the same approach to the problem of incipient stall, the analysis shows that theoretically there can be two types of self-induced distortion—a purely spanwise, axisymmetric type, and a traveling, circumferential plus spanwise type, the latter including a purely circumferential type as a special case. However, the analysis also indicates the interesting result that the purely circumferential type of traveling stall will, in all likelihood, precede the other types. One aspect of delaying the incipient traveling (rotating) stall can then be reduced to two extremely simple rules with respect to the desirable design parameters and cascade geometry.

Symbols

a = $\tan \alpha$
b = $\tan \beta = k + a$
k = a ratio of velocities. (With inlet distortion kU is the peripheral speed of rotor. With self-induced distortion kU is the speed of distortion propagation.)
L_y = circumferential length of cascade, hence also primary wave length of circumferential distortion
L_z = cascade blade span
m = number of half distortion waves in spanwise direction
M = defined by $\Delta\tilde{\omega} = 2M(\Delta\beta_1)$
n = number of full distortion waves in circumferential direction
N = defined by $\Delta \tan \beta_2 = N\Delta \tan \beta_1$
N^* = defined by $\Delta\beta_2 = N^*\Delta\beta_1$
P = pressure associated with the main flow
p = pressure perturbation
P_t = total pressure associated with the main relative flow
p_t = total-pressure distortion or perturbation
R = reaction ratio
$\Re$ = recovery ratio = $1 - (p_{t2}/p_{t1})$
U, V = main absolute velocities (see Fig. 1)
$\Delta U, \Delta V$ = absolute flow distortion
u, v, w = induced velocities
x, y, z = coordinates (see Fig. 1)
α_1, α_2 = absolute main flow angles, upstream or downstream of cascade
β_1, β_2 = relative main flow angles, upstream or downstream of cascade
$\Delta\beta_1, \Delta\beta_2$ = change of relative flow angles immediately upstream or downstream of cascade
δ = time lag in the response of $\Delta\tilde{\omega}$ and $\Delta\beta_2$ with $\Delta\beta_1$
ϵ = phase change of exit distortion compared to inlet distortion
λ_n = wave number for circumferential distortion = $2\pi n/L_y$
μ_m = wave number for spanwise distortion = $m\pi/L_z$
ν_{mn} = $\lambda_n/(\mu_m^2 + \lambda_n^2)^{1/2}$
$\tilde{\omega}$ = total-pressure loss coefficient of cascade
φ = velocity potential of induced velocities
ϕ = flow coefficient
ψ = work coefficient

Subscripts

1 for upstream of cascade
2 for downstream of cascade
3 for downstream of a stator in a complete rotor-stator stage

Received April 23, 1958. Revised and received June 20, 1959.

† This work was performed at the Flight Propulsion Laboratory Department of General Electric Company during the summer of 1957 and was published as a General Electric Report R57AGT628, September 13, 1957. The author wishes to express his gratitude to Dr. L. H. Smith, Jr., for many stimulating discussions on the aerodynamics of turbomachinery and to J. F. Klapproth and A. H. Perugi for their constant encouragement through the progress of this work.

* Professor of Mechanical Engineering.

Introduction

ALTHOUGH the aerodynamic design of compressors today is based mainly on an axisymmetric and steady flow model, there are certain nonaxisymmetric and nonsteady flow phenomena which can no longer be ignored. Among these are inlet flow distortion and rotating stall.

One type of inlet distortion can still be considered axisymmetric and steady; this is the purely spanwise distortion analyzed by Smith.[1] Another type, that of a purely circumferential distortion,** has been investigated by Ehrich[2] and by Rannie and Marble.[3] It appears that a unified treatment of distortions consisting of both spanwise and circumferential wave patterns

** The author's attention was called by the reviewer of this paper to a recent publication on purely circumferential inlet distortion by Katz[11] who presented some interesting analytical and experimental results for the case of a rectangular depression of the upstream total pressure.

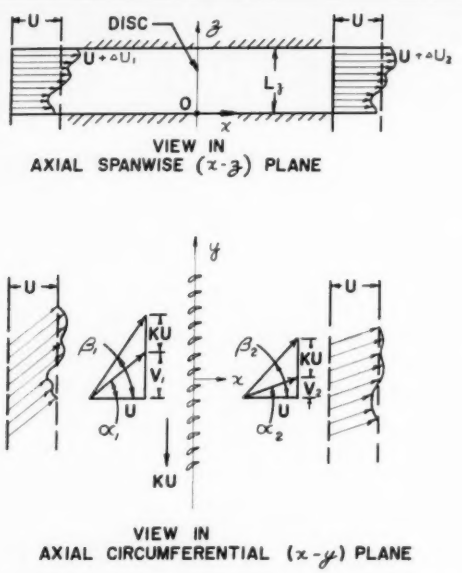

FIG. 1. Isolated plane cascade of finite span with spanwise and circumferential inlet distortions.

is possible; such a treatment would then include purely spanwise and purely circumferential distortions as special cases. It is shown in this analysis that the spanwise and the circumferential distortion waves interact so that the combined influence is not the sum of the influences of the two simple distortions. Numerical examples are shown for various values of the conventional design parameters—i.e., flow coefficient, work coefficient, and reaction ratio. Also illustrated is the influence of the cascade characteristics, represented by the variations of loss and exit flow angle with a changing inlet flow angle.

Compared to inlet distortion, the problem of rotating stall has received much greater attention since its first description by Iura and Rannie.[4] Various theories have been proposed, the majority of which use a small perturbation approach,* such as the ones by Emmons, et al.,[5] Sears,[6] Marble,[7] Stenning, et al.,[8] Yeh,[9] and Rannie and Marble.[3] Since a small perturbation approximation is used in the theories mentioned above, it is clear that they apply strictly for an *incipient* stall which is identified in reference 3 as a self-induced distortion.

It is shown in this analysis that theoretically there can be two types of self-induced distortion—a purely spanwise and, therefore, axisymmetric type and a traveling, circumferential plus spanwise type, the latter including a traveling, purely circumferential type as a special case. It is further shown that the purely circumferential type would in all probability occur first. The influence of the conventional design parameters on self-induced distortion is then discussed in some detail.

* Analyses without the assumption of small perturbation have been made by Fabri and Siestrunck[12] and Kriebel.[13] See a literature survey by Emmons, Kronauer, and Rockett.[14]

Analysis

We shall consider the case of a plane cascade of infinite blades and of finite span between two walls (Fig. 1). The cascade itself is approximated by an actuator disc located at $x = 0$. The coordinate axes are chosen as follows (see Fig. 1): x represents the axial direction, y the circumferential direction, and z the spanwise direction. The region upstream of the cascade is denoted by the subscript 1, and that downstream of the cascade by subscript 2. (Equations without subscripts apply to both regions.)

The undistorted or main absolute velocities are denoted by U along x and V along y. The absolute main flow angle α is, therefore, $\alpha = \tan^{-1} V/U$. The rotor blade velocity is represented by kU, where k is the reciprocal of the conventional flow-coefficient ϕ. (For a stator, $k = 0$.) The relative main flow angle β is, therefore, $\beta = \tan^{-1}[(V + kU)/U]$. It is clear that $\tan \beta = k + \tan \alpha$. The main flow is assumed to be uniform along the span (as well as in the circumferential direction), hence the blades are untwisted. However, the turning of main flow across the cascade need not be small.

The inlet distortion is represented by the velocity components ΔU_1 along x and ΔV_1 along y far upstream at $x = -\infty$. These velocity components are, in general, functions of both y and z; in a turbomachine this means a combined circumferential and spanwise inlet distortion. Due to this inlet distortion, the velocity far downstream at $x = +\infty$ will be distorted by an amount ΔU_2 and ΔV_2. (At present we shall leave the question open as to whether $\Delta V_1 = \Delta U_1 \tan \alpha_1$, $\Delta V_2 = \Delta U_2 \tan \alpha_2$.) Thus;

Velocity far upstream:

$$U + \Delta U_1(-\infty, y, z), \quad V_1 + \Delta V_1(-\infty, y, z), \quad 0$$

Velocity far downstream:

$$U + \Delta U_2(+\infty, y, z), \quad V_2 + \Delta V_2(+\infty, y, z), \quad 0$$

In the following it will be assumed that the velocity distortion is small compared to the main velocities. It is then possible to consider that, in the *entire* upstream or downstream region, the velocity perturbation consists of (1) the distortion velocities ΔU and ΔV carried along by the main velocities such that

$$\Delta U = \Delta U(x \tan \alpha - y, z), \quad \Delta V = \Delta V(x \tan \alpha - y, z)$$

and (2) an additional induced velocity field represented by

$$u = u(x, y, z), \quad v = v(x, y, z), \quad w = w(x, y, z)$$

The purpose of this analysis is to find this induced velocity field which will then yield the exit distortion ΔU_2 and ΔV_2, all under a given inlet distortion ΔU_1 and ΔV_1 which, as will be seen later, may be arbitrarily prescribed.

Basic Equations

Substituting the velocity components

$$U + \Delta U(x \tan \alpha - y, z) + u(x, y, z)$$
$$V + \Delta V(x \tan \alpha - y, z) + v(x, y, z)$$
$$w(x, y, z)$$

into the incompressible, nonviscous equations of motion and retaining only the first-order terms, we obtain

$$U(\partial u/\partial x) + V(\partial u/\partial y) = -(1/\rho)(\partial p/\partial x) \quad (1)$$

$$U(\partial v/\partial x) + V(\partial v/\partial y) = -(1/\rho)(\partial p/\partial y) \quad (2)$$

$$U(\partial w/\partial x) + V(\partial w/\partial y) = -(1/\rho)(\partial p/\partial z) \quad (3)$$

In the above equations, $p = p(x, y, z)$ is the pressure perturbation.

The continuity equation for incompressible flows gives

$$(\partial u/\partial x) + (\partial v/\partial y) + (\partial w/\partial z) = 0 \quad (4)$$

After canceling out p in any pair of the first three equations, we obtain three equations of the form

$$U[\partial(\ )/\partial x] + V[\partial(\ )/\partial y] = 0$$

where ( ) represents any one of the three vorticity components

$$[(\partial u/\partial y) - (\partial v/\partial x)], \quad [(\partial v/\partial z) - (\partial w/\partial y)], \quad [(\partial w/\partial x) - (\partial u/\partial z)]$$

Physically it merely means that the vorticity is carried by the main velocity only and not by the induced velocities, a well-known result of linearization. Since u, v, w are zero at $x = \pm\infty$, their vorticity must be zero everywhere. Hence, we can define a potential φ such that

$$u = \partial\varphi/\partial x, \quad v = \partial\varphi/\partial y, \quad w = \partial\varphi/\partial z \quad (5)$$

Substituting into the continuity equation, the result is a Laplace equation for φ. Keeping the appropriate boundary conditions in mind, the solution for φ_1 upstream of the cascade and for φ_2 downstream of the cascade are as follows:

$$\left.\begin{aligned} \varphi_1 &= \sum_m \sum_n A_{mn} e^{\sqrt{\mu_m^2 + \lambda_n^2}\,x + i\lambda_n y} \cos \mu_m z \\ \varphi_2 &= \sum_m \sum_n B_{mn} e^{-\sqrt{\mu_m^2 + \lambda_n^2}\,x + i\lambda_n y} \cos \mu_m z \end{aligned}\right\} \quad (6)$$

where

$\mu_m = m\pi/L_z$, L_z = blade span, $m = 0, 1, 2, 3, \ldots$

$\lambda_n = 2n\pi/L_y$, L_y = primary wave length along y, $n = 0, 1, 2, 3, \ldots$

The coefficients A_{mn} and B_{mn} are in general complex numbers. From Eq. (5),

$$u_1 = \sum_m \sum_n A_{mn} \sqrt{\mu_m^2 + \lambda_n^2} \times e^{\sqrt{\mu_m^2 + \lambda_n^2}\,x + i\lambda_n y} \cos \mu_m z \quad (7)$$

$$v_1 = \sum_m \sum_n A_{mn} i\lambda_n e^{\sqrt{\mu_m^2 + \lambda_n^2}\,x + i\lambda_n y} \cos \mu_m z \quad (8)$$

$$w_1 = -\sum_m \sum_n A_{mn}\mu_m e^{\sqrt{\mu_m^2 + \lambda_n^2}\,x + i\lambda_n y} \sin \mu_m z \quad (9)$$

with similar expressions for u_2, v_2, w_2. It is seen that $w = 0$ at the walls (where $z = 0, L_z$) as required.

Matching Conditions at Actuator Disc

For the remaining part of this analysis, we shall use the subscript 1 for $x = -0$ and subscript 2 for $x = +0$, these being the stations immediately upstream and immediately downstream of the actuator disc. Considering a *single* upstream two-dimensional wave in y and z represented by

$$u_1 = A_{mn} \sqrt{\mu_m^2 + \lambda_n^2}\, e^{i\lambda_n y} \cos \mu_m z \quad (10a)$$

with corresponding expressions for v_1, w_1, and a *single* downstream two-dimensional wave represented by

$$u_2 = B_{mn} \sqrt{\mu_m^2 + \lambda_n^2}\, e^{i\lambda_n y} \cos \mu_m z \quad (10b)$$

with corresponding expressions for v_2, w_2, we obtain, from Eqs. (7) and (8), the following important relations:

$$v_1 = i\nu_{mn} u_1, \quad v_2 = -i\nu_{mn} u_2 \quad (11)$$

where

$$\nu_{mn} \equiv \lambda_n/\sqrt{\mu_m^2 + \lambda_n^2} = (2n/L_y)/\sqrt{(2n/L_y)^2 + (m/L_z)^2}$$

The first matching condition at the disc is continuity. This requires

$$\Delta U_1 + u_1 = \Delta U_2 + u_2 \quad (12)$$

The second matching condition is that the spanwise velocity should undergo no change across the actuator disc—i.e.,

$$w_1 = w_2 \quad (13)$$

This condition is probably unimportant when $\mu_m \ll \lambda_n$, since w would then be much smaller than the other induced velocities u and v. (Notice that w is identically zero at the walls.) On this aspect more will be said later.

If Eq. (13) is valid, then a comparison of Eq. (9) for w_1 and a corresponding equation for w_2 shows that $A_{mn} = B_{mn}$ if $m \neq 0$. Then,

$$u_1 = -u_2, \quad v_1 = v_2 \quad (13')$$

For $m = 0$, Eq. (13) is identically satisfied since $w_1 = w_2 = 0$.

Cascade Characteristics

In steady-state cascade testing, a cascade of fixed geometry (stagger, solidity, camber, etc.) is subjected to various inlet flow angles β_1. Considering β_1 as the independent variable, the following quantities are the dependent variables: (1) exit flow angle β_2, (2) loss of total pressure (this is usually represented by a loss coefficient $\bar{\omega}$ defined as the ratio of total-pressure loss to inlet dynamic pressure), and (3) static pressure rise.

Any two of the above three quantities are sufficient to determine the third. For our purpose we shall choose the first two—i.e., β_2 and $\tilde{\omega}$.

Consider first the exit flow angle β_2. For small variations, we can represent a function by a linear relation. Thus,

$$\Delta\beta_2 = N^*(\Delta\beta_1) \tag{14}$$

where N^* is the slope in the β_2 versus β_1 curve at the cascade operating point. It is fairly simple to relate $\Delta\beta_1$ and $\Delta\beta_2$ to the velocity perturbations. From

$$\tan(\beta + \Delta\beta) = \frac{U\tan\beta + \Delta V + v}{U + \Delta U + u}$$

we get

$$\Delta\tan\beta = [(\Delta V + v)/U] - [(\Delta U + u)/U]\tan\beta$$

Hence,

$$\Delta\beta = \cos^2\beta(\Delta\tan\beta) = (\cos^2\beta/U)\,[(\Delta V + v) - (\Delta U + u)\tan\beta]$$

Eq. (14) then gives

$$(\Delta V_2 + v_2) - (\Delta U_2 + u_2)\tan\beta_2 = N[(\Delta V_1 + v_1) - (\Delta U_1 + u_1)\tan\beta_1] \tag{15}$$

where $N \equiv N^*\cos^2\beta_1/\cos^2\beta_2$. Notice that Eq. (15) is equivalent to

$$\Delta\tan\beta_2 = N\,\Delta\tan\beta_1$$

Hence, N is the slope in the $\tan\beta_2$ versus $\tan\beta_1$ curve. At design condition N is usually small, but may not be negligible especially for low solidities.

Making use of Eq. (11), Eq. (14) or (15) can finally be written as

$$\Delta U_2\tan\beta_2 - \Delta V_2 + (\tan\beta_2 + i\nu_{mn})u_2 = N[\Delta U_1\tan\beta_1 - \Delta V_1 + (\tan\beta_1 - i\nu_{mn})u_1] \tag{16}$$

Next consider the change of relative total pressure across the cascade. (By relative total pressure we mean the sum of the static pressure and the dynamic pressure due to velocities relative to the blade.) The relative total pressure at either side of the cascade consists of a main relative total pressure P_t (due to main flow alone) and a total-pressure perturbation p_t. Thus,

$$P_t + p_t = P + p + (1/2)\rho[(U + \Delta U + u)^2 + (V + \Delta V + v)^2] \approx P + p + (1/2)\rho(U^2 + V^2) + \rho[U(\Delta U + u) + V(\Delta V + v)]$$

Since by definition

$$P_t = P + (1/2)\rho(U^2 + V^2)$$

it follows

$$p_t = p + \rho[U(\Delta U + u) + V(\Delta V + v)]$$

But from Eq. (1) and $\partial u/\partial y = \partial v/\partial x$, it can be shown that

$$p + \rho(Uu + Vv) = 0$$

(This merely means that the induced flow is a potential flow, and, hence, will not change the total pressure.) Thus, the relative total-pressure perturbation due to the velocity perturbation is

$$p_t = \rho(U\Delta U + V\Delta V) \tag{17}$$

The loss of relative total pressure across the cascade can be expressed as

$$(P_{t1} + p_{t1}) - (P_{t2} + p_{t2}) = (\tilde{\omega} + \Delta\tilde{\omega})(\rho/2) \times [(U_1 + \Delta U_1 + u_1)^2 + (V_1 + \Delta V_1 + v_1)^2]$$

where $\tilde{\omega}$ is the loss coefficient for the main flow and $\Delta\tilde{\omega}$ is the change of $\tilde{\omega}$ due to the inlet-angle perturbation as a result of velocity perturbations. Now, for the main flow alone,

$$P_{t1} - P_{t2} = \tilde{\omega}(\rho/2)(U_1^2 + V_1^2)$$

Hence,

$$p_{t1} - p_{t2} = \Delta\tilde{\omega}\,\frac{\rho}{2}\,U_1^2(1 + \tan^2\beta_1) \times \left[1 + 2\tilde{\omega}\left\{\frac{(\Delta U_1 + u_1) + \tan\beta_1(\Delta V_1 + v_1)}{\Delta\tilde{\omega}U_1(1 + \tan^2\beta_1)}\right\}\right]$$

The second term in the above brackets is of the order of $\tilde{\omega}/(\Delta\tilde{\omega}/2\Delta\beta_1)$. It turns out in later calculations that, when the loss begins to exert a significant influence, $\Delta\tilde{\omega}/2\Delta\beta_1$ is of the order 1, whereas $\tilde{\omega}$ is still one order of magnitude smaller than 1. Thus it appears permissible, for the sake of reducing the amount of mathematical calculation, to drop the second term in the brackets and let

$$p_{t1} - p_{t2} = \Delta\tilde{\omega}(\rho/2)U_1^2(1 + \tan^2\beta_1)$$

We now substitute p_{t1} and p_{t2} in the above equation in terms of perturbation velocities by Eq. (17). Furthermore, for small changes of β_1 (i.e., small $\Delta\beta_1$), $\Delta\tilde{\omega}$ can be expressed as a linear function of $\Delta\beta_1$; i.e.,

$$\Delta\tilde{\omega} = 2M\Delta\beta_1 \tag{18}$$

where M is one-half of the slope of the $\tilde{\omega}$ versus β_1 curve. The resulting equation after these substitutions is

$$(\Delta U_2 + \Delta V_2\tan\beta_2) - (\Delta U_1 + \Delta V_1\tan\beta_1) - i\nu_{mn}k(u_2 + u_1) = M[\Delta U_1\tan\beta_1 - \Delta V_1 + (\tan\beta_1 - i\nu_{mn})u_1] \tag{19}$$

Eq. (16) and (19) represent the cascade characteristics.

Solutions

In the foregoing we have derived the three Eqs. (12), (16), and (19). In addition, there is also Eq. (13′) for $m \neq 0$. Given the inlet distortion ΔU_1 and ΔV_1, the main flow angles α_1, α_2, β_1, β_2, and the cascade characteristics N and M, we should be able to solve for the exit distortions ΔU_2 and ΔV_2. The best way to do this is to consider separately the following four cases.

To simplify future writing we shall introduce the symbols

$a_1 = \tan \alpha_1, \quad a_2 = \tan \alpha_2, \quad b_1 = \tan \beta_1, \quad b_2 = \tan \beta_2$

Case (1)—Purely Spanwise Distortion

In this case $n = \lambda_n = \nu_{mn} = 0$. From Eqs. (12) and (13′),

$$\Delta U_1 - \Delta U_2 = 2u_2 = -2u_1$$

Using the above relation to eliminate u_1 and u_2 in Eqs. (16) and (19), we obtain two equations for the two unknowns ΔU_2 and ΔV_2:

$$\left.\begin{aligned}(b_2 - Nb_1)\Delta U_2 - 2\Delta V_2 = \\ (Nb_1 - b_2)\Delta U_1 - 2N\Delta V_1\end{aligned}\right\} \qquad \left.\begin{aligned}(2 - Mb_1)\Delta U_2 + 2b_2\Delta V_2 = \\ (2 + Mb_1)\Delta U_1 + 2(b_1 - M)\Delta V_1\end{aligned}\right\} \tag{20}$$

This pair of equations can easily be solved. The results can be considerably simplified if we separate the two types of inlet distortions: (a) the distortion velocity parallel to the main flow, and (b) the distortion velocity perpendicular to the main flow. Any other types of inlet distortion can then be obtained by a combination of these two basic types.

(1a) *The Inlet Distortion Velocity Parallel to the Main Flow*—For this case we have $\Delta V_1 = \Delta U_1 a_1$. The solution to Eq. (20) then becomes

$$\left.\begin{aligned}\frac{\Delta U_2}{\Delta U_1} &= \frac{[M(2k - b_1) + 2(1 + a_1b_1)] + b_2(2kN - Nb_1 - b_2)}{2 - Mb_1 + b_2(b_2 - Nb_1)} \\ \frac{\Delta V_2}{\Delta U_1} &= \frac{(b_2 - Nb_1)[M(2k - b_1) + 2(1 + a_1b_1)] - (2 - Mb_1)(2kN - Nb_1 - b_2)}{2[2 - Mb_1 + b_2(b_2 - Nb_1)]}\end{aligned}\right\} \tag{21}$$

If in addition $N = M = 0$, Eqs. (21) reduce to

$$\Delta U_2/\Delta U_1 = [2(1 + a_1b_1) - b_2^2]/(2 + b_2^2), \qquad \Delta V_2/\Delta U_1 = b_2(2 + a_1b_1)/(2 + b_2^2) \tag{22}$$

Thus, although the inlet distortion velocity is parallel to the inlet main absolute velocity, the direction of the exit distortion velocity is, in general, neither along the main exit absolute velocity nor along the main exit relative velocity. On account of this, the exit flow (including the distortion) will have slightly different directions at different spanwise locations.

For the simple case represented by Eqs. (22), it is of interest to examine one complete stage in a multistage machine. The exit distortion of the rotor given by Eqs. (22) becomes the inlet distortion to the following stator if the interaction between the two blade rows is neglected. The exit distortion of the stator can be obtained from Eqs. (22) by letting $k = 0$. Using the subscript 3 for stator exit, then the exit distortions ΔU_3, ΔV_3 for a complete stage of repeated stage design (i.e., $a_3 = a_1$) are

$$\left.\begin{aligned}\frac{\Delta U_2}{\Delta U_1} &= \frac{(2 - a_1^2)[2(1 + a_1b_1) - b_2^2] + 2a_2b_2(2 + a_1b_1)}{(2 + a_1^2)(2 + b_2^2)} \\ \frac{\Delta V_3}{\Delta U_1} &= \frac{a_1[4(1 + a_1b_1) - 2b_2^2 + a_2b_2(2 + a_1b_1)]}{(2 + a_1^2)(2 + b_2^2)}\end{aligned}\right\} \tag{23}$$

Another quantity of interest is the total-pressure perturbation at rotor exit as a ratio of the same quantity at inlet. For the simplified case $N = M = 0$ represented by Eqs. (22), this ratio is

$$\frac{p_{t2}}{p_{t1}} = \frac{(1 + a_1b_1)(2 + a_2b_2) - kb_2}{(1 + a_1^2)(2 + b_2^2)} \tag{24}$$

A more general expression for this ratio, including the influence of the parameters N and M, can be derived in a similar manner. The significance of this ratio is as follows: The closer this ratio is to 0, the more is the tendency of the stage to smooth out any inlet distortion. Smith[1] has defined a "recovery ratio" $\mathcal{R} \equiv 1 - (p_{t2}/p_{t1})$. If $\mathcal{R} = 0$, a total-pressure distortion upstream of the rotor will be fully carried over to the downstream. If $\mathcal{R} = 1$, the upstream distortion will be completely smoothed out, and the downstream flow will experience no distortion in total pressure. If $\mathcal{R} > 1$, an upstream

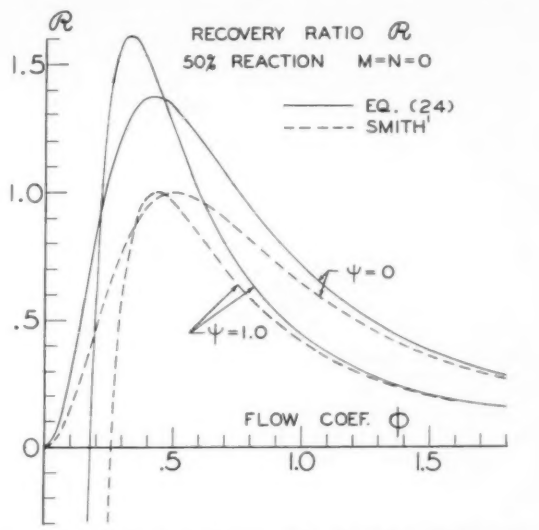

FIG. 2. Recovery of purely spanwise distortion, 50 per cent reaction, $M = N = 0$, (inlet distortion velocity parallel to main flow).

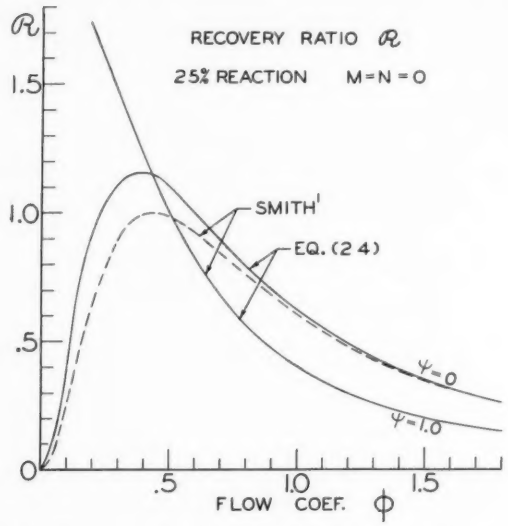

FIG. 3. Recovery of purely spanwise distortion, 25 per cent reaction, $M = N = 0$, (inlet distortion velocity parallel to main flow).

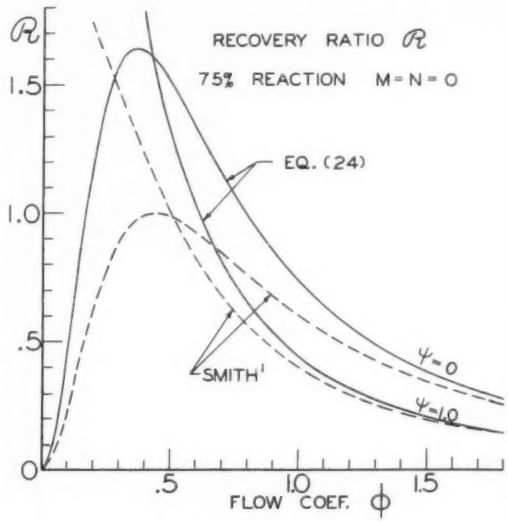

FIG. 4. Recovery of purely spanwise distortion, 75 per cent reaction, $M = N = 0$, (inlet distortion velocity parallel to main flow).

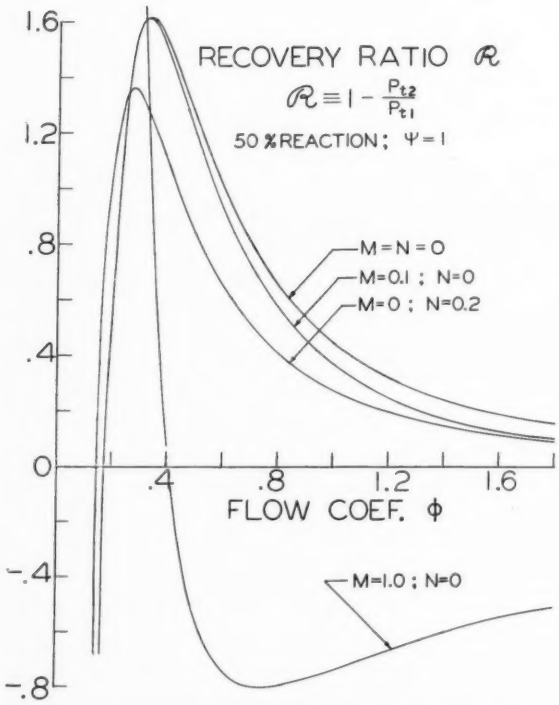

FIG. 5. Influence of variation of loss and exit flow angle on recovery of purely spanwise distortion, 50 per cent reaction, $\psi = 1$, (inlet distortion velocity parallel to main flow).

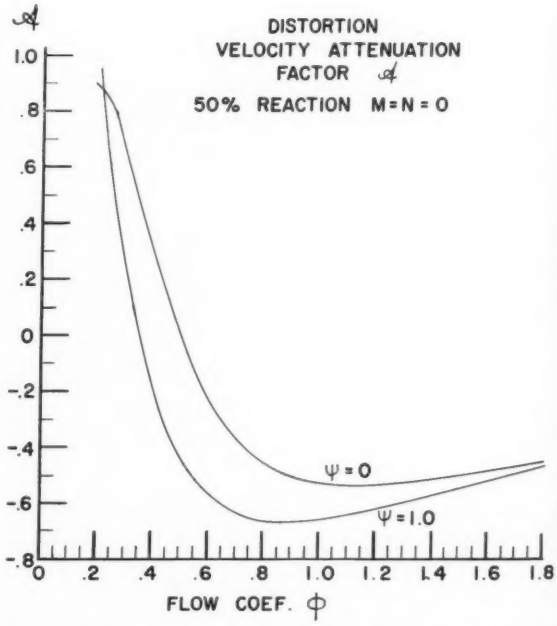

FIG. 6. Attenuation of purely spanwise distortion, 50 per cent reaction, $M = N = 0$, (inlet distortion velocity perpendicular to main flow).

total-pressure defect (or excess) will become a total-pressure excess (or defect) at downstream. Conversely, if $\mathfrak{R} < 0$, an upstream velocity distortion will become worse downstream. Thus it seems that a recovery ratio in the neighborhood of 1 would be highly desirable in an axial flow turbomachine.

Since Smith's results [Eqs. (2), (3), and Figs. 5–7 of reference 1] are obtained on the basis of somewhat different assumptions, it is interesting to compare his results with those of the present analysis. For this purpose we shall adopt the following conventional parameters:

Flow coefficient $\Phi = 1/k$

Work coefficient $\Psi = \text{Work}/[(kU)^2/2] = (2/k)(a_1 - a_2) = (2/k)(b_1 - b_2)$

Reaction ratio $R = (b_1 + b_2)/2k = 1 + [(a_1 + a_2)/2k]$

These parameters take the place of the angles α_1, α_2, β_1, β_2 or their tangents a_1, a_2, b_1, b_2. For 50 per cent reaction (Fig. 2), 25 per cent reaction (Fig. 3), and 75 per cent reaction (Fig. 4), the recovery ratio $\mathfrak{R}$ is plotted against the flow coefficient ϕ for two values of ψ: $\psi = 0$ and $\psi = 1$. In each case, the solid lines are calculated from Eq. (24) and the dotted lines are based on Eqs. (7), (8), and (9) of reference 1. It can be seen that the two different analyses yield qualitatively similar results; although, in the range where the recovery ratio reaches its peak, its value is higher and occurs at somewhat lower flow coefficient in this analysis than in reference 1. (It is interesting to note that for 25 per cent reaction and $\psi = 1$, the two analyses give identical results.) As pointed out by Smith, his results show that (1) the flow coefficient should be around 0.5 or somewhat less, (2) light loading is generally desirable especially at higher flow coefficients, and (3) the recovery ratio is not a strong function of reaction ratio. These results are again approximately valid on the basis of this analysis.* One could, however, modify slightly the first two conclusions as follows: (1) the flow coefficient should be around 0.5 or somewhat more, and (2) light loading allows somewhat higher flow coefficients for full recovery.

The above conclusions are for $N = M = 0$—i.e., the cascade exit angle and the loss are assumed to be independent of the inlet angle. To find out the influence of the variation of loss, two cases $M = 0.1$ and $M = 1.0$ are used to calculate the recovery ratio for 50 per cent reaction, $\psi = 1$, using the exit velocity distortions as given by the more general Eqs. (21). These two values of M correspond to an increase of loss coefficient $\bar{\omega}$ by 0.0035 and 0.035, respectively, per degree increase of inlet flow angle. (The larger figure represents, therefore, a considerable stall.) The results are compared to the previous case of $M = 0$ in Fig. 5. It appears that the influence of a mild M is to decrease the recovery ratio somewhat, but does not change the main characteristics or the conclusions of the previous paragraph. On the other hand, with a severe M the recovery ratio is negative almost all the way. It would appear, therefore, that no practical recovery is attainable under severe stall.

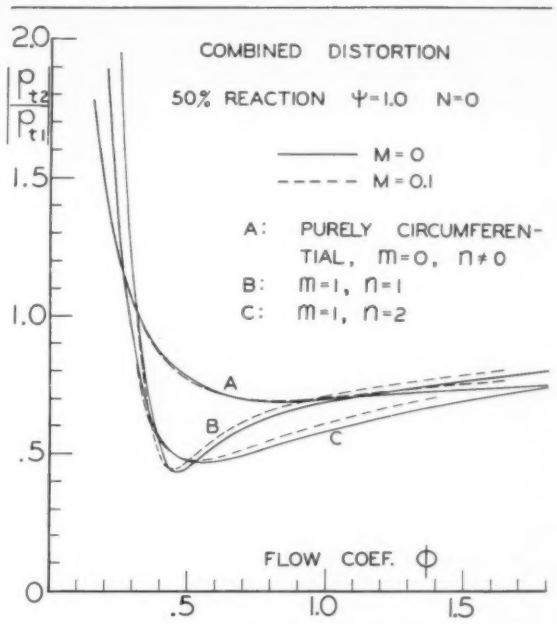

FIG. 7. Ratio of total-pressure perturbation for combined circumferential and spanwise distortion, 50 per cent reaction, $\psi = 1$, $N = 0$, $L_y/L_z = 3\pi$.

The influence of N is investigated next, again for the case of 50 per cent reaction and $\psi = 1$. Here a value of $N = 0.2$ is compared to $N = 0$. ($N = 0.2$ corresponds to a compressor cascade of solidity around 0.6 at reasonable stagger and incidence.) It is seen in Fig. 5 that N tends to reduce recovery ratio for all practical values of ϕ. The combined influence of N and M at design condition seem to suggest that for best recovery of spanwise distortions, the flow coefficient should be in the neighborhood of 0.4 to 0.5.

Although the results represented by Eqs. (20) to (24) are derived for a single wave given by Eq. (10) with $n = 0$, $m = 1, 2, 3 \ldots$, the fact that these results are independent of m means that all wave lengths of the radial distortion are attenuated or amplified by the same factor. This, plus the fact that there is no phase shift in exit distortion (compared to inlet distortion), enables us to conclude that the relative profile of any radial inlet distortion is preserved at the exit, and only its magnitude is modified by a constant factor. How

* The essential difference between the two analyses is as follows. The analysis of reference 1 assumes that the flow perturbation at blade trailing edge is the same as that at far downstream, whereas this analysis assumes that the flow at blade trailing edge is the same as that immediately behind the actuator disc. The truth of the matter must lie somewhere between these two assumptions. Presumably the assumption of reference 1 works better for blades with low aspect ratio, whereas the assumption in this analysis works better for blades with high aspect ratio. It is significant, therefore, that both analyses reach roughly the same conclusion with respect to the desirable values for flow coefficients.

ever, as pointed out previously, the exit flow angle will change by slightly different amounts along the span. As will be seen later, these conclusions are quite different from the case of a circumferential distortion.

(1b) *The Inlet Distortion Velocity Perpendicular to the Main Flow**—For this case we have $\Delta V_1 = -\Delta U_1/a_1$. The solution to Eq. (20) then becomes

$$\left.\begin{aligned}\frac{\Delta U_2}{\Delta U_1} &= \frac{b_2[N(2 + a_1b_1) - a_1b_2] + [M(2 + a_1b_1) - 2k]}{a_1[2 - Mb_1 + b_2(b_2 - Nb_1)]} \\ \frac{\Delta V_2}{\Delta U_1} &= \frac{(b_2 - Nb_1)[M(2 + a_1b_1) - 2k] - (2 - Mb_1)[N(2 + a_1b_1) - a_1b_2]}{2a_1[2 - Mb_1 + b_2(b_2 - Nb_1)]}\end{aligned}\right\} \tag{25}$$

If, in addition, $N = M = 0$,

$$\Delta U_2/\Delta U_1 = (-a_1b_2^2 - 2k)/a_1(2 + b_2^2), \qquad \Delta V_2/\Delta U_1 = b_2(a_1 - k)/a_1(2 + b_2^2) \tag{26}$$

Since $p_{t1} = 0$ when the inlet distortion velocity is perpendicular to the main flow, it is impossible to define an attenuation factor on the basis of total-pressure distortions. One alternative is to define a velocity attenuation factor $\mathfrak{a}$ as the ratio of the exit velocity distortion *in the direction of the exit main flow* to the inlet distortion velocity (which is perpendicular to the main flow). For the simple case $N = M = 0$,

$$\mathfrak{a} = -[\sin\alpha_1 \cos\alpha_2/a_1(2 + b_2^2)]k[2 + b_2(a_1 + a_2)] \tag{27}$$

This attenuation factor $\mathfrak{a}$ is plotted for 50 per cent reaction blading, with $\psi = 0$ and $\psi = 1$. (See Fig. 6.) It is seen that here again the flow coefficient should be around 0.5 for the least downstream distortion in total pressure, corresponding to a vanishing $\mathfrak{a}$.

Case (2)—Purely Circumferential Distortion

In this case $m = \mu_m = 0$, $\nu_{mn} = 1$. The three available Eqs. (12), (16), and (19) contain four unknowns ΔU_2, ΔV_2, u_1, u_2. For an inlet distortion $\Delta V_1 = a_1\Delta U_1$, which is moreover steady in the absolute frame of reference, the flow at exit is also steady. A consideration on continuity and equations of motion at far downstream then shows that

$$\Delta V_2 = a_2\Delta U_2 \tag{28}$$

Making use of this relation, Eqs. (12) and (16) can now be used to solve for u_1 and u_2. The results are

$$\left.\begin{aligned}u_1 &= \frac{(Nk - b_2 - i)\Delta U_1 + (a_2 + i)\Delta U_2}{(b_2 - Nb_1) + i\,(1 + N)} \\ u_2 &= \Delta U_1 - \Delta U_2 + u_1\end{aligned}\right\} \tag{29}$$

Substituting u_1 and u_2 into Eq. (19), we can solve for ΔU_2:

$$\Delta U_2/\Delta U_1 = (A + iB)/(C + iD) \tag{30}$$

where

$$\begin{aligned}A &= (1 + a_1b_1 + Mk)(b_2 - Nb_1) + Mb_1(Nk - b_2) + (k - kN - M) \\ B &= (1 + a_1b_1 + Mk)(1 + N) + kN(2k - b_1 - M) - kb_2 + M(b_2 - b_1) \\ C &= (1 + a_2b_2)(b_2 - Nb_1) - M(1 + a_2b_1) + k(1 - N) \\ D &= 1 + a_2^2 + k^2 + M(a_2 - b_1) + N(1 + a_2b_2 - kb_1)\end{aligned}$$

For a stator, $k = 0$ and $a = b$. Hence, across a stator,

$$\Delta U_3/\Delta U_2 = (A_s + iB_s)/(C_s + iD_s) \tag{31}$$

where

$$\begin{aligned}A_s &= (1 + a_2^2)(a_3 - Na_2) - M(1 + a_2a_3) \\ B_s &= (1 + a_2^2)(1 + N) + M(a_3 - a_2) \\ C_s &= (1 + a_3^2)(a_3 - Na_2) - M(1 + a_2a_3) \\ D_s &= (1 + a_3^2)(1 + N) + M(a_3 - a_2)\end{aligned}$$

The product of Eqs. (30) and (31) gives the attenuation for a complete stage consisting of a rotor and a stator. (For a repeated stage in a multistage machine, $a_3 = a_1$.)

For the specially simple case when both $N = M = 0$, Eq. (30) becomes

$$\frac{\Delta U_2}{\Delta U_1} = \frac{(1 + a_1b_1)b_2 + k + i(1 + a_1b_1 - kb_2)}{(1 + a_2b_2)b_2 + k + i(1 + k^2 + a_2^2)} \tag{32}$$

This equation can be written in an alternate form: $\Delta U_2/\Delta U_1 = |\Delta U_2/\Delta U_1|e^{i\epsilon_r}$ (33)

where

$$\left|\frac{\Delta U_2}{\Delta U_1}\right| = \left\{\frac{(1 + a_1^2)(1 + b_1^2)\,(1 + b_2^2)}{(1 + a_2^2)[4k^2 + (1 + b_2^2)^2]}\right\}^{1/2} \tag{34}$$

and

$$\tan\epsilon_r = \frac{k\{(1 + b_2^2)(2 + a_1b_1 + a_2b_2) + 2k^2 - 2(1 + a_1b_1)(1 + a_2b_2)\}}{k^2(b_2^2 - 3 - 2a_1b_1 - 2a_2b_2) - (1 + b_2^2)(1 + a_1b_1)(1 + a_2b_2)} \tag{35}$$

* Dr. L. H. Smith, Jr., has pointed out to the author that such distortion velocity may arise due to the upstream secondary flow.

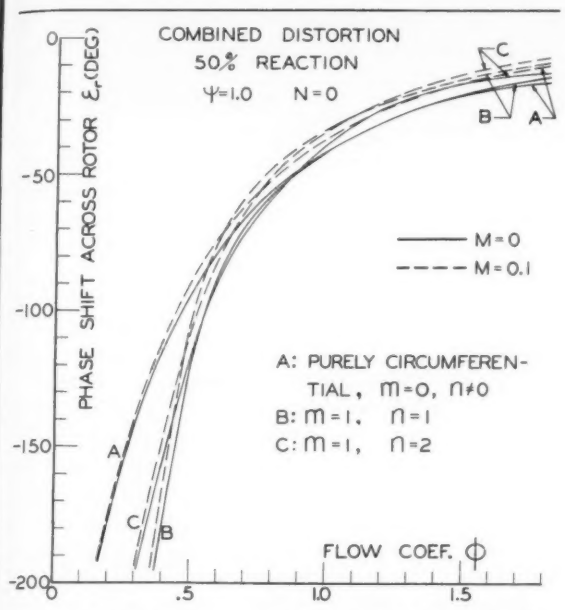

FIG. 8. Phase shift across rotor for combined circumferential and spanwise distortion, 50 per cent reaction, $\psi = 1$, $N = 0$, $L_y/L_z = 3\pi$.

Eqs. (34) and (35) have been obtained by Ehrich.[2] The quantity $|\Delta U_2/\Delta U_1|$ represents the attenuation on the *magnitude* of the exit distortion of the rotor, whereas ϵ_r represents a *phase shift* in the circumferential direction.

Calculations based on these equations will be included in the more general case to be described next. It might be remarked that Eqs. (34) and (35) show that both the attenuation and the phase shift are independent of the inlet distortion wave number λ_n. When the inlet distortion consists of many different wave numbers, the exit distortion will not in general maintain the same shape, since a constant phase shift ϵ for all wave numbers means that waves of different wave numbers will be displaced relative to one another.

Case (3)—Combined Spanwise and Circumferential Distortion With $\mu_m \ll \lambda_n$

When the spanwise wave number μ_m is much less than the circumferential wave number λ_n, corresponding to a distortion velocity gradient which is comparatively mild spanwise and comparatively severe circumferentially, we would expect the induced velocities $w \ll u \approx v$. For such cases it is reasonable to assume that Eq. (13) can be ignored. We, therefore, have the four equations (12), (16), (19), and (28), from which the four unknowns u_1, u_2, ΔU_2, ΔV_2 can be solved. The results are as follows.

Across a rotor:

$$\Delta U_2/\Delta U_1 = (A + iB)/(C + iD) \qquad (36)$$

where

$$A = (1 + a_1b_1 + Mk)(b_2 - Nb_1) + Mb_1(Nk - b_2) + \nu_{mn}^2(k - kN - M)$$

$$B = \nu_{mn}\{(1 + a_1b_1 + Mk)(1 + N) + (2k - M)(Nk - b_2) + (kb_2 - kNb_1 - Mb_1)\}$$

$$C = (1 + a_2b_2)(b_2 - Nb_1) - Ma_2b_1 + \nu_{mn}^2(k - kN - M)$$

$$D = \nu_{mn}\{(1 + a_2b_2 - kb_1)N + M(a_2 - b_1) + 1 + k^2 + a_2^2\}$$

Across a stator:

$$\Delta U_3/\Delta U_2 = (A_s + iB_s)/(C_s + iD_s) \qquad (37)$$

where

$$A_s = (1 + a_2^2)(a_3 - Na_2) - M(\nu_{mn}^2 + a_2a_3)$$
$$B_s = \nu_{mn}\{(1 + a_2^2)(1 + N) + M(a_3 - a_2)\}$$
$$C_s = (1 + a_3^2)(a_3 - Na_2) - M(\nu_{mn}^2 + a_2a_3)$$
$$D_s = \nu_{mn}\{(1 + a_3^2)(1 + N) + M(a_3 - a_2)\}$$

In particular, if $M = 0$, Eq. (37) shows that

$$\Delta U_3/\Delta U_2 = (1 + a_2^2)/(1 + a_3^2) \quad \text{across a stator} \qquad (38)$$

Comparing the above equations with Eqs. (30) and (31) previously derived, it can be seen that Eqs. (30) and (31) are a special case of Eqs. (36) and (37) with $\nu_{mn} = 1$.

The ratio of total-pressure perturbation is

$$p_{t2}/p_{t1} = (\Delta U_2/\Delta U_1)[(1 + a_2^2)/(1 + a_1^2)] = |p_{t2}/p_{t1}|e^{i\epsilon_r} \quad \text{across a rotor} \qquad (39)$$

$$p_{t3}/p_{t2} = (\Delta U_3/\Delta U_2)[(1 + a_3^2)/(1 + a_2^2)] = |p_{t3}/p_{t2}|e^{i\epsilon_s} \quad \text{across a stator} \qquad (40)$$

where $\Delta U_2/\Delta U_1$ and $\Delta U_3/\Delta U_2$ are given by Eqs. (36) and (37). As a check, one notes that for $M = 0$, $p_{t3} = p_{t2}$ and $\epsilon_s = 0$ across a stator.

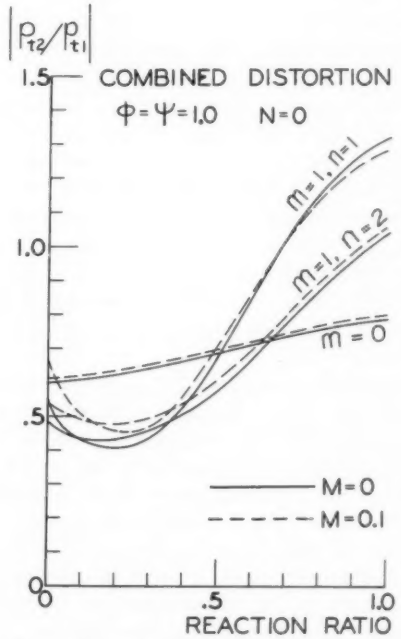

FIG. 9. Ratio of total-pressure perturbation for combined circumferential and spanwise distortion $\phi = \psi = 1$, $N = 0$, $L_y/L_z = 3\pi$.

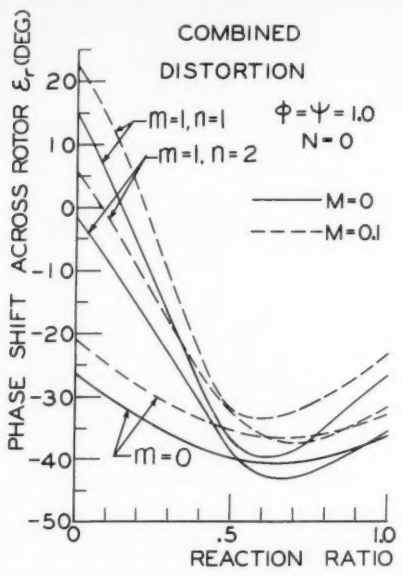

FIG. 10. Phase shift across rotor for combined circumferential and spanwise distortion, $\phi = \psi = 1$, $N = 0$, $L_y/L_z = 3\pi$.

In order to find the influence of ν_{mn}, let us consider a machine of hub-tip radius ratio of 0.5, which gives $L_y/L_z = 3\pi$ where L_y is the circumference at pitch radius and L_z is the span. Then

$$\nu_{0n} = 1, \quad \nu_{m0} = 0, \quad \nu_{11} = \nu_{22} = 0.2076,$$
$$\nu_{21} = 0.1055, \quad \nu_{12} = 0.3907, \quad \text{etc.} \quad (41)$$

Fig. 7 presents $|p_{t2}/p_{t1}|$ across the rotor calculated from Eqs. (39) and (36) for a 50 per cent reaction stage with $\psi = 1$, $N = 0$, and two values of M; 0 and 0.1. It appears that all curves reach a minimum value at around $\phi = 0.5$. Also, the curves for $m = n = 1$ and $m = 1$, $n = 2$ are lower than that for $m = 0$ for the usual values of ϕ, the difference being especially pronounced near $\phi = 0.5$. Thus, it appears that a combined spanwise and circumferential distortion is attenuated more than a purely circumferential one. Also, the curve for ν_{12} is significantly lower than that for ν_{11}, meaning that more circumferential "wiggles" in inlet distortion are helpful in recovery. Fig. 7 also shows that a small nonzero M increases somewhat the exit distortion. This is similar to a purely spanwise distortion.

Fig. 8 presents the phase shift ϵ_r across the rotor as defined by Eq. (39). It shows that the phase shift may vary from slightly negative to $-180°$ or more depending strongly on the value of ϕ. For $\phi > 0.7$, the case of combined spanwise and circumferential distortion does not differ much from that of a purely circumferential distortion. However, at $\phi = 0.5$ or less, the former may give considerably more phase shift than the latter. The introduction of M appears to reduce the absolute amount of phase shift.

In order to examine the influence of reaction ratio R, a calculation is made on $\phi = \psi = 1$, with varying R from 0 to 1. The pressure perturbation $|p_{t2}/p_{t1}|$ is shown on Fig. 9 for $N = 0$ and two values of M; 0 and 0.1. The phase shift for these cases are shown on Fig. 10. It appears that the exit distortion increases with reaction ratio; lower reaction thus appears preferable on this account. The interaction of spanwise distortion with circumferential ones shows up in a rather complicated manner. The influence of M is to increase the exit distortion. Considerable variation of phase shift is exhibited with respect to reaction ratio R and ν_{mn}.

Since a small value of $M(= 0.1)$ does not appear to exert much influence on $|p_{t2}/p_{t1}|$ and phase shift, a larger value of $M = 1$ is chosen, for the case of purely circumferential distortion, 50 per cent reaction, $\psi = 1$, $N = 0$. The results are plotted on Fig. 11 for $|p_{t2}/p_{t1}|$ and on Fig. 12 for the phase shift. As far as the distortion magnitude is concerned, Fig. 11 shows that for $\phi < 0.62$, M reduces the exit distortion and hence gives better recovery, whereas the reverse is true for $\phi > 0.62$. Fig. 12 shows that the absolute magnitude of phase shift is decreased considerably by a large M.

The influence of the variation of exit leaving angle is next considered in the same Figures. Comparing the two curves $N = 0$ and $N = 0.2$ (both for 50 per cent reaction, $\psi = 1$, $M = 0$) we find that the influence of N is quite significant. For $\phi < 0.88$, N reduces the exit distortion. The reverse is true for $\phi > 0.88$. Also, N reduces considerably the absolute magnitude of phase shift for all values of ϕ.

Since both N and M exert strong influence on $|p_{t2}/p_{t1}|$ as well as ϵ_r, the accurate prediction of the flow downstream of an *arbitrary* inlet distortion consisting of many waves may be quite difficult even on the basis of this simple theory.

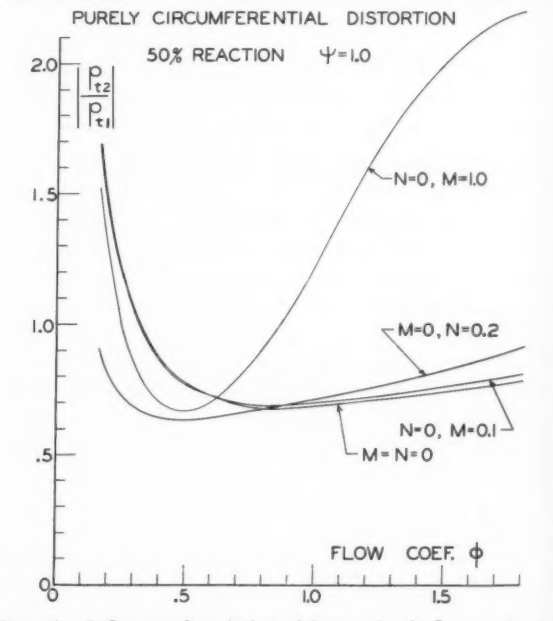

FIG. 11. Influence of variation of loss and exit flow angle on ratio of total-pressure perturbation for purely circumferential distortion, 50 per cent reaction, $\psi = 1$, $N = 0$.

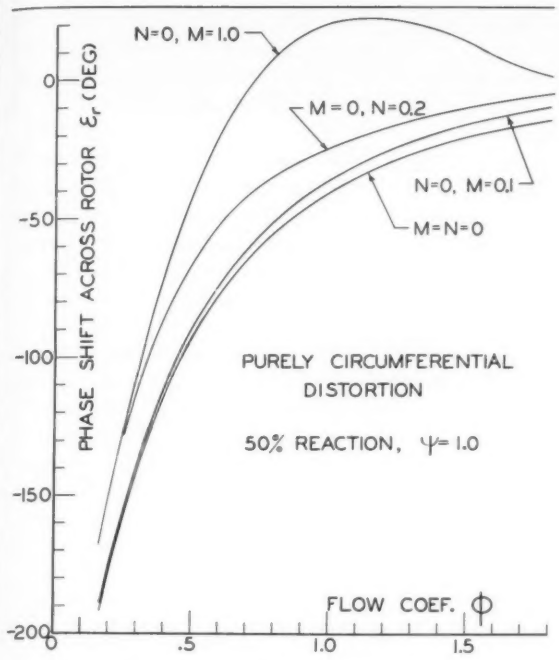

FIG. 12. Influence of variation of loss and exit flow angle on phase shift across rotor for purely circumferential distortion, 50 per cent reaction, $\psi = 1$, $N = 0$.

Although Eq. (36) will not apply for $\lambda_n \ll \mu_m$, it is interesting to examine the limiting case as $\lambda_n \to 0$ and $\nu_{mn} \to 0$. Then Eq. (36) yields

$$\frac{\Delta U_2}{\Delta U_1} = \frac{(1 + a_1b_1 + Mk)(b_2 - Nb_1) + Mb_1(Nk - b_2)}{(1 + a_2b_2)(b_2 - Nb_1) - Ma_2b_1} \tag{42}$$

which is a real number. Thus the phase shift along the circumferential direction decreases to zero as the distortion velocity gradient becomes more severe spanwise than circumferentially. This must be true since for the limiting case of purely spanwise distortion, the phase shift has been shown to be zero. [See case (1).] In particular, for $M = 0$ Eq. (42) gives

$$\Delta U_2/\Delta U_1 = (1 + a_1b_1)/(1 + a_2b_2) \tag{43}$$

and

$$p_{t2}/p_{t1} = (1 + a_1b_1)(1 + a_2^2)/(1 + a_2b_2)(1 + a_1^2) \tag{44}$$

Case (4)—Combined Spanwise and Circumferential Distortion With $\lambda_n \ll \mu_m$

When the circumferential wave number λ_n is much less than the spanwise wave number μ_m, corresponding to a distortion velocity gradient which is comparatively mild circumferentially and comparatively severe spanwise, $w \approx u \gg v$. Here Eq. (13) or its equivalent (13′) must be fulfilled. We now have the four equations, (12), (13′), (19), and (28), for the four unknowns, u_1, u_2, ΔU_2, and ΔV_2. The solution is

$$\frac{\Delta U_2}{\Delta U_1} = \frac{2(1 + a_1b_1) - M(b_1 - 2k - i\nu_{mn})}{2(1 + a_2b_2) - M(b_1 - i\nu_{mn})} \tag{45}$$

For $M = 0$, this equation becomes identical to Eq. (43). Although both Eq. (45) and Eq. (42) reduce to Eq. (43) for $M = 0$, the value of u_1 and v_1 are not the same in the two cases. For the case represented by Eq. (45), $u_1 = -u_2 = (\Delta U_2 - \Delta U_1)/2$; these induced and distortion velocities in turn determine the exit flow angle which is not otherwise restricted. On the other hand, for the case represented by Eq. (42), u and v must vary in such a way that the specified relation Eq. (16) between the exit angle and the inlet angle be obeyed. Since our practical interest is in the ratio $\Delta U_2/\Delta U_1$, the fact that u, v differs in these two cases is probably of secondary importance.

We may now conclude that the solution represented by Eqs. (36)–(40) appears to be generally applicable for *all* distortion wave patterns except a purely spanwise distortion. Its applicability to a purely circumferential distortion has been demonstrated by letting $\mu_m = 0$ and $\nu_{mn} = 1$; Eq. (36) then reduces to Eq. (30). On the other hand, by letting $\lambda_n = 0$ and $\nu_{mn} = 0$, it has been shown that Eq. (36) becomes identical to Eq. (45) at least for $M = 0$. Thus, although Eq. (36) is strictly true only for $\mu_m \ll \lambda_n$, it appears also to be a reasonable approximation for $\lambda_n \ll \mu_m$, thereby covering all distortion wave patterns (except a purely spanwise one).

Self-Induced Distortion

In the foregoing we have evaluated the exit velocity distortion for inlet distortions of various wave forms. It might appear at first glance that if the inlet distortion is zero, the exit distortion would have to be zero. This is indeed the case under normal conditions. Under certain special conditions, however, there is a possibility of an exit velocity distortion even if there is no inlet distortion. In fact, there can be two different

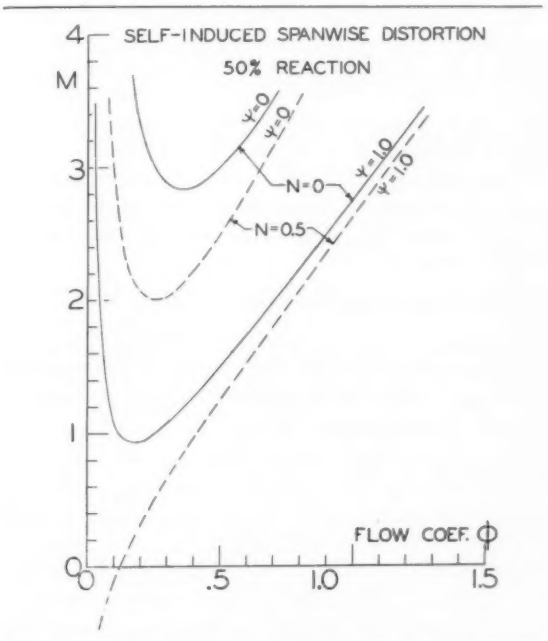

FIG. 13. Self-induced spanwise distortion, 50 per cent reaction.

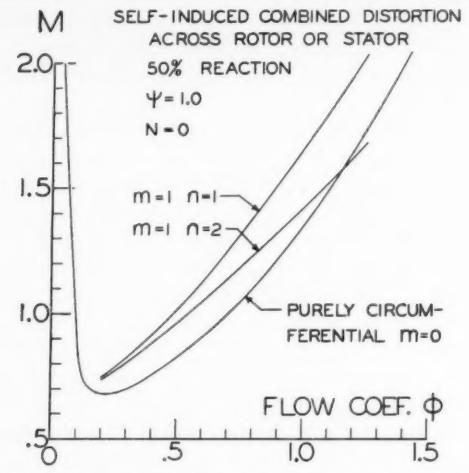

FIG. 14. Self-induced combined spanwise and circumferential distortion, 50 per cent reaction, $\psi = 1.0$, $N = 0$, $L_y/L_z = 3\pi$.

types of such "self-induced" exit distortions—a purely spanwise type and a circumferential plus spanwise type. The latter also includes the purely circumferential distortion as a special case, and, as will be shown, *must* travel or "rotate" with respect to the blades.

Purely Spanwise Self-Induced Distortion

This type of self-induced distortion can theoretically happen after either a rotor or a stator. It occurs when the determinant formed by the coefficients in the left-hand side of the pair of Eqs. (20) vanishes—i.e.,

$$M = [2 + b_2(b_2 - Nb_1)]/b_1 \tag{46}$$

Since M varies from approximately zero to large values when the inlet angle β_1 or its tangent b_1 varies, there always exits a situation for which the above equation is satisfied for any given cascade. Fig. 13 shows the necessary value of M for such self-induced distortion to occur for 50 per cent reaction blading with $\psi = 0$ and $\psi = 1$ and with $N = 0$ (solid curves) and $N = 0.5$ (dotted curves). However, as will be seen later, the onset of circumferential self-induced distortion will probably have the effect of suppressing this kind of spanwise distortion.

Traveling Self-Induced Distortion; Rotating Stall

Consider next the possibility of having self-induced distortions along both the circumferential and spanwise directions. Eq. (36) shows that for such a distortion to occur, we must have $C = D = 0$; i.e.,

$$\left.\begin{aligned}(1 + a_2b_2)(b_2 - Nb_1) - Ma_2b_1 + \\ \nu_{mn}^2(k - kN - M) = 0\\ (1 + a_2b_2 - kb_1)N + M(a_2 - b_1) + \\ 1 + k^2 + a_2^2 = 0\end{aligned}\right\} \tag{47}$$

This pair of equations can be used to solve for M and N in terms of the flow angles. It is clear that, except by sheer coincidence, M and N cannot *both* satisfy the requirements at the *same* flow angles. (The presence of ν_{mn} does not help the situation since it can only assume certain discrete values.) Hence, a *stationary* self-induced distortion along the circumferential direction *cannot* happen.

The possibility arises, however, of an *unsteady*, self-induced distortion. When there is no distortion in the inlet absolute flow, kU loses its significance as the peripheral speed of the blades. Instead, kU is still the relative velocity between the (exit) distortion and the blades, but now becomes a dependent variable of the problem. From the relation $a = b - k$ (which now becomes the definition for a), a is now the tangent of the main flow angle when viewed on a frame of reference which travels with the distortion. Eqs. (47) can now be used to solve k and M (or N). The results are

$$M = \frac{(1 + a_2b_2)(b_2 - Nb_1) + \nu_{mn}^2k(1 - N)}{\nu_{mn}^2 + b_1a_2} \tag{48}$$

and k is the root of the following equation:

$$(1 + a_2^2)[\nu_{mn}^2(1 + b_2^2) + (\nu_{mn}^2 + b_1^2)N] - kb_1(1 + \nu_{mn}^2 + 2a_2^2) + a_2b_2(1 - \nu_{mn}^2)(1 + a_2b_2) = 0 \tag{49}$$

This equation can be reduced to a cubic equation for k:

$$Ek^3 + Fk^2 + Gk + H = 0 \tag{50}$$

where

$$\begin{aligned}E &= -2b_1\\ F &= 4b_1b_2 + b_1^2N + b_2^2 + \nu_{mn}^2(1 + N)\\ G &= -(b_2 + b_1)(1 + \nu_{mn}^2 + 2b_2^2) - 2Nb_2(\nu_{mn}^2 + b_1^2)\\ H &= (1 + b_2^2)[b_2^2 + Nb_1^2 + \nu_{mn}^2(1 + N)]\end{aligned}$$

For the special case of a purely circumferential self-induced distortion, $\nu_{mn} = 1$, and Eq. (49) yields an extremely simple solution for k:

$$k = [(1 + b_2^2) + (1 + b_1^2)N]/2b_1 = (1 + N^*)/2b_1\cos^2\beta_2 \tag{51}$$

Substituting into Eq. (48), we obtain, after much simplification,

$$M = [(1 + b_2^2) + N(1 - b_1b_2)]/b_1 \tag{52}$$

Eqs. (51) and (52) have been obtained by the author in a previous report;[9] they are, respectively, Eq. (27) and Eq. (30) of reference 9. In fact, one can introduce a phase lag δ in the response of the exit flow angle and loss coefficient to a variation of inlet flow angle by using, instead of M and N, $Me^{i\delta}$ and $Ne.^{i\delta}$ The result as given in reference 9 is

$$k = \frac{1 - b_1\tan\delta + N^*\sec\delta}{2\cos^2\beta_2(b_1 + \tan\delta)} \tag{53}$$

$$M = [(1 + b_2^2)/(1 + b_1^2)]\sec\delta\{b_1 + [2k/(1 + b_2^2)] - N^*(\sin\delta + b_2\cos\delta)\} \tag{54}$$

These equations reduce to Eqs. (51) and (52) for $\delta = 0$.

The necessary M as given by Eqs. (48) and (50) for self-induced combined circumferential and spanwise distortions is plotted in Fig. 14 for 50 per cent reaction, $\psi = 1$, and $N = 0$. It can be seen that for almost the

entire range of ϕ the necessary M for the purely circumferential type is lower than that for other types involving both spanwise and circumferential self-induced distortion. This shows that *the purely circumferential type will occur first* and, hence, is the only type that requires further investigation. This simplifies matters enormously. For the purely circumferential type, calculations are made on 50 per cent reaction (Fig. 15) and 75 per cent reaction (Fig. 16) with $\psi = 0$ and $\psi = 1$ and with $N = 0$ (solid curves) and $N = 0.5$ (dotted curves). These results show that, for 50 per cent reaction with $N = 0$, the minimum values of M are around 2 at $\phi \approx 0.5$ for $\psi = 0$ and around 0.66 at $\phi \approx 0.25$ at $\psi = 1$. At other values of ϕ, the necessary M would be still higher. Now, even the smaller value $M \approx 0.66$ (corresponding to an increase of $\bar{\omega}$ of 0.023 per degree increase of inlet flow angle) is large enough to indicate that the cascade is near stall. For this reason the self-induced circumferential distortion can be identified as an incipient "rotating *stall*." However, for the somewhat extreme case of $N = 0.5$, corresponding to very low solidity, the necessary M actually vanishes at $\phi = 0.14$ for $\psi = 1$. The self-induced distortion at that region is then definitely not a stall phenomenon. It so happens that $\phi = 0.14$ is much too low for ordinary compressor cascades, and this may be the reason that the experimental evidence of such a non-stall type of traveling distortion has not been reported in literature.

Comparing Eqs. (46) and (52), it can be seen that unless $N > 1$, which is highly improbable, the necessary M for purely circumferential distortion is less than that for purely spanwise distortion. One may thus conclude that *the purely circumferential type of self-induced distortion always occurs first.* The consequent nonuniformity in the circumferential direction would in all likelihood tend to suppress the self-induced spanwise distortion.

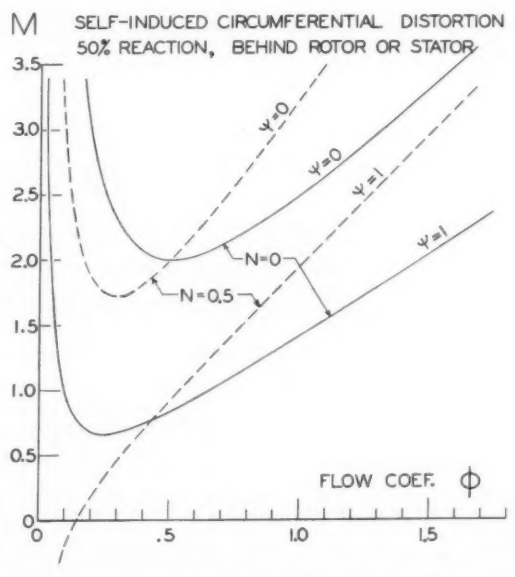

FIG. 15. Self-induced circumferential distortion, 50 per cent reaction.

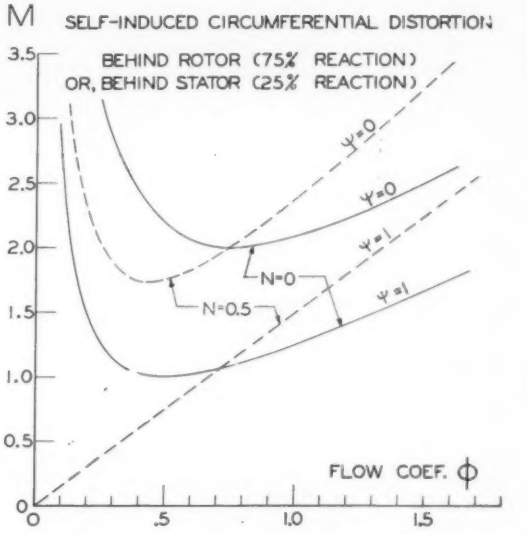

FIG. 16. Self-induced circumferential distortion, 75 per cent reaction.

Velocity of Rotating Stall

As mentioned before, kU is the velocity of travel of the self-induced exit distortion *relative* to the blade, irrespective of whether the blade is a rotor or stator. For the general case of distortion waves along both the circumferential and the spanwise directions, k can be evaluated from Eq. (50). For the simple case of a purely circumferential distortion, k is given by Eq. (53) with an assumed time lag and by Eq. (51) without a time lag. Now the purely circumferential distortion, when occurring at the onset of stall, has been identified as a "rotating stall" and, as such, has been investigated by a number of researchers, both theoretically and experimentally. It is pertinent to compare the results in the present analysis with those of the other authors. This is done in the Appendix.

Delay of Rotating Stall by Cascade Geometry

Since the self-induced circumferential distortion or "rotating stall" is considered harmful to blades, it is of interest to find out if some cascade geometry might not be able to delay rotating stall better than others. The answer to this problem lies in Eq. (52), which gives the values of M that are necessary for rotating stall to make its appearance. If the necessary M is very large, say approaching ∞, then rotating stall may never occur. Unfortunately, this would require extremely low or high flow coefficients, as shown in Figs. 15 and 16. For the practical range of compressor cascade geometry, rotating stall occurs at an inlet angle at which the actual M value of the cascade reaches the necessary M of Eq. (52). The delay of rotating stall, therefore, requires the simultaneous consideration of two problems—how to increase the necessary M and how to decrease the actual M. In the following an attempt will be made to answer the first question.

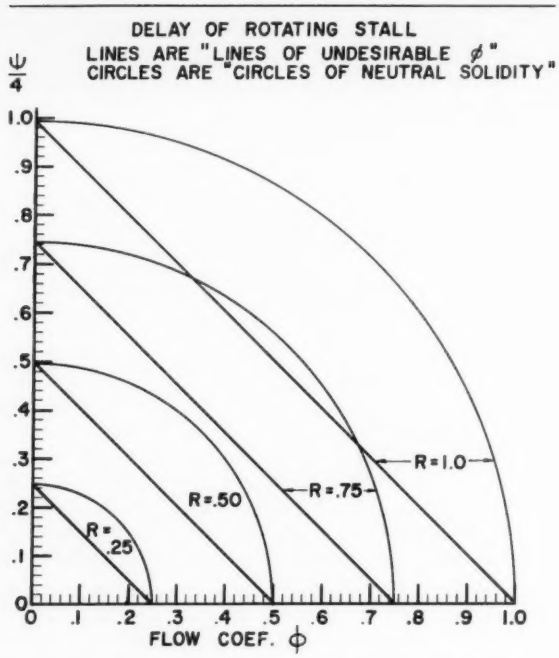

FIG. 17. Delay of self-induced circumferential distortion or incipient rotating stall.

(The second question can only be answered by comparing the actual M and N values of different cascades, based on the results of cascade testing.) First consider the influence of N on the necessary M for rotating stall. (It is probably safe to assume that, other things being equal, lower solidity corresponds to higher N and vice versa.) Now Eq. (52) shows that if $b_1b_2 > 1$, higher N will decrease the necessary M and, hence, promote rotating stall. The reverse is true if $b_1b_2 < 1$. At $b_1b_2 = 1$, the value of N will have no influence. Expressing in terms of the conventional design parameters ϕ, ψ, and R, it can be shown that the condition $b_1b_2 = 1$ is equivalent to

$$\phi^2 + (\psi/4)^2 = R^2$$

If ϕ and $\psi/4$ are used to represent the coordinate axes, the above equation describes a circle with center at the origin and with radius equal to the reaction ratio R. (See Fig. 17.) These circles might be called "circles of neutral solidity," in the sense that, if the combination of ϕ and ψ lie outside of the particular circle corresponding to the value of R of the cascade stage, rotating stall can be delayed by increasing N or decreasing solidity. On the other hand, if the design parameters lie inside of this circle then it is better to have a smaller N by using a higher solidity. For 50 per cent reaction blading, the usual values of ϕ and ψ appear to lie outside of the "circle of neutral solidity," hence lower solidity will most likely serve to prohibit rotating stall. On the other hand, for 75 per cent reaction, it is likely that some combinations of design parameters may lie inside the circle. For such cases, lower solidity might make the matter a little worse, somewhat contrary to usual expectations.

With the influence of solidity out of the way, we now may consider the value of M with $N = 0$. Eq. (52) then gives

$$M = (1 + b_2^2)/b_1 = [\phi^2 + (R - \psi/4)^2]/\phi(R + \psi/4)$$

With fixed R and ψ, we can differentiate M with respect to ϕ and set the derivative equal to zero. This will give us the worst possible choice of ϕ (corresponding to minimum necessary M) for the given combination of R and ψ. It turns out that such undesirable values of ϕ can be described by the simple relation $\phi + (\psi/4) = R$. These are straight lines in the ϕ versus $\psi/4$ plane, with intercepts equal to R at both coordinate axes. These lines might be called "lines of undesirable ϕ" in the sense that, if the parameters ϕ, ψ, and R lie *on* these lines, the resistance to rotating stall is the least. The obvious alternative is to stay as far away from these lines as possible in either side of them. Fig. 17 shows, perhaps unnecessarily, such a plot. It must be emphasized that the values of ϕ, ψ, and R are the ones corresponding to the operating (off-design) condition at which rotating stall is likely to occur; they may differ considerably from the design values.

Appendix

For the purely circumferential type of self-induced distortion, its velocity of propagation has been derived and given as Eq. (53) with an assumed time lag and Eq. (51) without a time lag. These results are compared below with some of the previous ones obtained by other investigators.

Comparison With Previous Theories

For the special case of $N^* = 0$, Eq. (53) becomes

$$k = \frac{1 - \tan\delta \tan\beta_1}{2\cos^2\beta_2(\tan\beta_1 + \tan\delta)}$$

This can be compared with Sear's channel theory[6] which gives

$$k = \frac{1 - \tan\delta \tan\beta}{\cos^2\beta[2\tan\beta + (1 - \tan^2\beta)\tan\delta]}$$

(In Sear's theory, β implies β_1; however, no distinction is made between β_1 and β_2.) On the other hand, Eq. (53) yields, for $\delta = 0$, the previous Eq. (51),

$$k = (1 + N^*)/2\cos^2\beta_2 \tan\beta_1 \qquad (51)$$

This can be compared with Marble's theory[7] which gives

$$k = \frac{(\cos^2\beta_2/\cos^2\beta_1) + N^*}{2\cos^2\beta_2 \tan\beta_1}$$

If both N^* and δ are zero, the comparison is as follows:

$$\text{Present work} \quad K = 1/2\cos^2\beta_2 \tan\beta_1 \qquad (51a)$$

$$\text{Sears}^6 \text{ and Marble}^7 \quad k = 1/2\cos^2\beta_1 \tan\beta_1$$

To compare the present results with Stenning's theory,[8] we take Stenning's result for incipient stall (long wave length):

TABLE 1

β_1	β_2	k	$2k \cos^2 \beta_2$
Stenning, Kriebel, and Montgomery			
Stator, Solidity = 1.0			
63.8°	47.5°	0.63	0.58
65.5°	49°	0.695	0.60
67.2°	50°	0.74	0.61
68.5°	52°	0.72	0.54
Stator, Solidity = 0.5			
64.8°	56°	0.78	0.49
68.5°	57°	0.87	0.52
Rotor			
67°	43°	0.85	0.91
71°	48°	0.85	0.76
Costilow and Huppert			
Rotor			
53°–55°	25°	0.48–0.52	0.79–0.85
55°–57°	26°	0.46–0.50	0.75–0.81

$$k = 2(1 - C_p)/\sin 2\beta_1 \approx 1/\cos^2 \beta_2 \tan \beta_1$$

if C_p is taken approximately to be $1 - (\cos^2 \beta_1/\cos^2 \beta_2)$. This gives a value of k equal to twice the value given by Eq. (51a). However, since N^* in Eq. (51) lies between 0.1 to 0.5, the value of k given by Eq. (51) does not differ quite so much from Stenning's results. (In another derivation assuming downstream mixing, Stenning obtained a different result which reduces to Eq. (51a) exactly for long wave length.)

The result of Rannie and Marble[3] agrees completely with Eq. (51) for the case of $N = 0$. When N is non-zero, there appears a discrepancy between Eq. (51) and the corresponding equation of reference 3.

Comparison With Experiments

Although a number of experimental results on stall propagation have been reported, relatively few would apply to the present analysis, which is based on an isolated rotor or stator and also restricted to incipient, small-amplitude stall.

The data given in Table 1 for incipient stall propagation in a single rotor or stator are gathered (or estimated if not directly available) from two sources—Stenning, Kriebel, and Montgomery[8] and Castilow and Huppert.[10]

Comparing these experimental data with Eq. (51), it appears that they follow the prediction reasonably well. In fact, these data can all be explained without the introduction of a time lag, for they lie within the curves of Eq. (51) $N = 0$ and 0.5. (See Fig. 18.) The only exception is the case of the rotor of Stenning, et al., in which the experimental value appears to correspond to $N^* \approx 1$. Perhaps by coincidence, a search of the rotor performance (β_2 versus β_1) of reference 8 turns out that N^* is indeed fairly large (around 0.8).

In the paper by Rannie and Marble,[3] a comparison between theory and experiments (Fig. 3 of reference 3) shows that their experimental values of k are higher by 10 to 15 per cent than their theoretically predicted values. The equation used in their theory, Eq. (7.1) of reference 3, appears to be the same as Eq. (51) of this analysis but with $N^* = 0$. If one takes N^* to be 0.10 to 0.15, which are reasonable values for the cascade

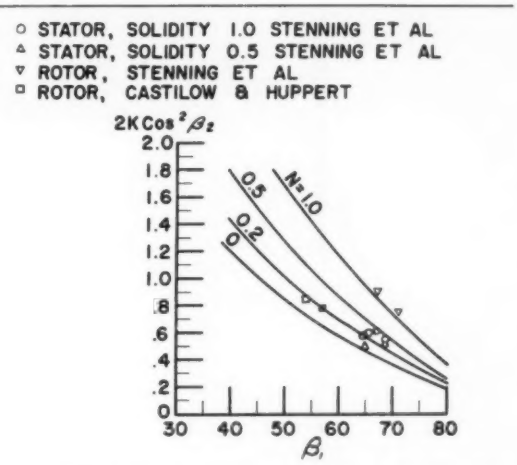

FIG. 18. Comparison of theoretical velocity of propagation of incipient stall with experiments.

of their investigation, there would be almost complete agreement between theory and experiment.

References

[1] Smith, L. H., Jr., *Recovery Ratio—A Measure of the Loss Recovery Potential of Compressor Stages*, Trans. ASME, Vol. 80, No. 3, pp. 517–524, April, 1958.

[2] Ehrich, F., *Circumferential Inlet Distortions in Axial Flow Turbomachinery*, Journal of the Aeronautical Sciences, Vol. 24, No. 6, pp. 413–417, June, 1957.

[3] Rannie, W. D., and Marble, F. E., *Unsteady Flows in Axial Turbomachines*, ONERA, Comptes Rendus des Journées Internationales de Sciences Aeronautiques, Part 2, pp. 1–21, Paris, May 27–29, 1957.

[4] Iura, T., and Rannie, W. D., *Experimental Investigations of Propagating Stall in Axial-Flow Compressors*, Trans. ASME, Vol. 76, pp. 463–471, April, 1954.

[5] Emmons, H. W., Pearson, C. E., and Grant, H. P., *Compressor Surge and Stall Propagation*, Trans. ASME, Vol. 77, pp. 455–467, May, 1955.

[6] Sears, W. R., *Rotating Stall in Axial Compressors*, ZAMP, Vol. 35, No. 6, pp. 429–455, 1955.

[7] Marble, F. E., *Propagation of Stall in a Compressor Blade Row*, Journal of the Aeronautical Sciences, Vol. 22, No. 8, pp. 541–554, August, 1955.

[8] Stenning, A. H., Kriebel, A. R., and Montgomery, S. R., *Stall Propagation in Axial Compressors*, NACA TN 3580, June, 1956. See also, Stenning, A. H., and Kriebel, A. R., *Stall Propagation in a Cascade of Airfoils*, Trans. ASME, Vol. 80, May, 1958.

[9] Yeh, H., *The Theory of Stall Propagation and its Applications to Axial Flow Compressors*, Technical Report R56 AGT 528, General Electric Company, September, 1956.

[10] Costilow, E. L., and Huppert, M. C., *Rotating Stall Characteristics of a Rotor with High Hub-Tip Radius Ratio*, NACA TN 3518.

[11] Katz, R., *Performance of Axial Compressors with Asymmetric Inlet Flows*, Daniel and Florence Guggenheim Jet Propulsion Center, California Institute of Technology, June, 1958.

[12] Fabri, J., and Siestrunck, R., *Rotating Stall in Axial Flow Compressors*, Journal of the Aeronautical Sciences, Vol. 24, pp. 805–812, 1957.

[13] Kriebel, A. R., *Stall Propagation in a Cascade of Airfoils*, Journal of the Aeronautical Sciences, Vol. 23, No. 9, p. 897, September, 1956.

[14] Emmons, H. W., Kronauer, R. E., and Rockett, J. A., *A Survey of Stall Propagation—Experiment and Theory*, ASME Preprint 58-A-150.

Readers' Forum

BRIEF REPORTS of investigations in the aerospace sciences and discussions of papers published in the JOURNAL are presented in this special department. Entries must be restricted to a maximum of 1,300 words or the equivalent of one JOURNAL page including formulas and illustrations. Publication is completed as soon as possible after receipt of the material. The Editorial Committee does not hold itself responsible for the opinions expressed by the correspondents.

Contents

Integration of Some Thermal Differential Equations ..... B. SAELMAN 754

On an Exact Solution of Incompressible, Inviscid, Hypersonic, Stagnation-Point Flow for a Sphere ..... KOON-SANG WAN 755

Comments on "The Heating of Slabs With Arbitrary Heat Inputs" ..... WILLIAM SQUIRE 756

Note on the Calculation of Equilibrium Skin Temperatures ..... HANS C. VETTER 757

On the Integral of Moment of Pressure in Supersonic Flow ..... LU TING 758

Column End-Fixity Versus End-Restraint ..... PAUL E. SANDORFF 759

Comments on "A New Solution to the Laminar Boundary-Layer Equations" ..... M. Z. v. KRZYWOBLOCKI 760

Further Remarks on Matrix Interpolation of Flexibility Influence Coefficients ..... WILLIAM P. RODDEN 760

Visual Supersonic Flow Patterns by Means of Smoke Lines V. P. GODDARD, J. A. MCLAUGHLIN, AND F. N. M. BROWN 761

The Compressible Laminar Boundary Layer With Constant Injected Mass Flux at the Surface ..... ALAN Q. ESCHENROEDER 762

A Perturbation Analysis of Shock Flow in a Nozzle ..... ROY GUNDERSEN 763

The Effect of Temperature on Pressures Measured in a Hypersonic Wind Tunnel ..... WESTON M. HOWARD 764

Acoustical Instability of Jets and Wakes for Mach Numbers Above Two ..... ERIK MOLLÖ-CHRISTENSEN 765

Generalized Spectral Representation in Aeroelasticity ..... ARTHUR K. CROSS 766

A Two-Cell Vortex Solution of the Navier-Stokes Equations ..... ROGER D. SULLIVAN 767

On the Accuracy of an Approximate Theory for the Ablation of Glassy Materials—A Reply ..... HANS A. BETHE AND MAC C. ADAMS 768

Integration of Some Thermal Differential Equations

B. Saelman

Design Weight Engineer, Lockheed Aircraft Corporation, Burbank, Calif.

May 13, 1959

SYMBOLS

T_r = boundary-layer recovery temperature, °R.
T = skin temperature, °R.
T_e = skin equilibrium temperature, °R.
T_a = ambient temperature, °R.
T_o = initial skin temperature, °R.
r = recovery factor
a = acceleration Mach Number/sec.
a_0 = initial acceleration Mach Number/sec.
M_0 = initial Mach Number
t = time, sec.
R = resistance, sec. (°R.)/B.t.u.
C_n = capacitance, B.t.u./°R.
m = heating rate, °R./sec.
ϵ = emissivity
σ = Stephan-Boltzman constant
q = heat flow, B.t.u./sec.
h_b = heat-transfer coefficient, B.t.u./ft.²(hr.), °R.

MANY OF THE EQUATIONS describing thermal relationships are solved by the finite-difference methods. However, there are some important equations in this category for which closed solutions exist. Some of these are presented below.

For accelerated flight, we have the following relationships:

$$a = a_0 - ct \tag{1}$$

$$T_r = T_a\{1 + r[a_0 t - (ct^2/2) + M_0]^2\} \tag{2}$$

The differential equation of the thermal relationship is

$$(T_r - T)/R = Cn(dT/dt) \tag{3}$$

Combining Eqs. (1)–(3) and integrating with the initial condition, $T = 0$ when $t = 0$,

Contributors Please Note

Readers' Forum items must be confined to the equivalent of one page in the *Journal*. Contributions that exceed this limit will be returned to the authors for condensation and rewrite. To avoid inconvenience and delay, please adhere to the following specifications:

(1) Five, double-spaced, typewritten, manuscript pages (8 1/2 by 11 in.), including wide margins, formulas, and headings, equal one printed page.

(2) For every illustration, deduct at least one-half or as much as one manuscript page, depending on the size of the illustration.

$$T = kT_a\left\{\frac{rc^2}{4k}t^4 - \left(\frac{ra_0c}{k} + \frac{rc^2}{k^2}\right)t^5 + \left[\frac{r(a_0^2 - M_0c)}{k} + \frac{3ra_0c}{k^2} + \frac{3rc^2}{k^3}\right]t^2 + \left[\frac{2a_0M_0r}{k} - \frac{6rc^2}{k^4} - \frac{6ra_0c}{k^3} - \frac{2r}{k^2}(a_0^2 - M_0c)\right]t + \left[\frac{2r(a_0^2 - M_0c)}{k^3} + \frac{6ra_0c}{k^4} + \frac{6rc^2}{k^5} + \frac{rM_0^2}{k} - \frac{2a_0M_0r}{k^2} + \frac{1}{k}\right]\right\} + \beta e^{-kt} \quad (4)$$

where
$$k = 1/RC_n \quad (5)$$

$$\beta = -kT_a\left\{\frac{1}{k} + \frac{2r(a_0^2 - M_0c)}{k^3} + \frac{rM_0^2}{k} + \frac{6ra_0c}{k^4} + \frac{6rc^2}{k^5} - \frac{2ra_0M_0}{k^2}\right\} \quad (6)$$

When speed is constant, $a_0 = c = 0$ and

$$T = T_a(1 + rM_0^2)(1 - e^{-kt}) = T_r(1 - e^{-kt}) \quad (7)$$

During acceleration, the recovery temperature, T_r, can sometimes be expressed

$$T_r = mt \text{ (see Fig. 1) } t < t_1 \quad (8)$$

Substituting Eq. (8) into Eq. (3) and integrating

$$T = (m/k)(kt - 1) + (m/k)e^{-kt} \quad t < t_1 \quad (9)$$

and
$$T_1 = (m/k)(kt_1 - 1) + (m/k)e^{-kt_1} \quad (10)$$

and
$$T_r = \bar{T}_r \quad \text{constant for} \quad t > t_1 \quad (11)$$

Substituting Eq. (11) into Eq. (3) and integrating

$$T = \bar{T}_r - (\bar{T}_r - T_1)e^{k_1(t_1 - t)} = \bar{T}_r - (m/k)(1 - e^{-kt_1})e^{k_1(t1 - t)} \quad t > t_1 \quad (12)$$

The temperature difference can be expressed

$$T_\Delta = \bar{T}_r - T = (m/k)(1 - e^{-kt_1})e^{k(t1 - t)} \quad (13)$$

This is a maximum at $t = t_1$

$$T_{\Delta max} = (m/k)(1 - e^{-kt_1}) \quad (14)$$

Introducing the radiation term

$$q = A\sigma\epsilon T^4 \quad (15)$$

$$q = (T_r - T)/R = C_n(dT/dt) + A\sigma\epsilon T^4 \quad (16)$$

The integral of Eq. (16) is

$$t = -\int \frac{dT}{(\sigma\epsilon/C_n)T^4 + kT - kT_r} = \int \frac{AdT}{T - a} + \int \frac{BdT}{T - b} + \int \frac{(CT + D)dT}{eT^2 + fT + g} \quad (17)$$

where a and b are real roots of

$$(A\sigma\epsilon/C_n)T^4 + kT - kT_r = 0$$

$$t = -\left(A\log(T - a) + B\log(T - b) + (C/2e)\times \log|eT^2 + fT + g| + \{2[D - (Cf/2e)]/\sqrt{4eg - f^2}\}\times \tan^{-1}[(2eT + f)/\sqrt{4eg - f^2}]\right) \quad (18)$$

Since this expression involves T as the independent variable, the radiation term is usually neglected and integration of the differential equation leads to the convenient expression, given below, with the temperature expressed as a function of time:

$$T = T_r - (T_r - T_o)e^{-kt} \quad (19)$$

Neglecting the capacitance term in Eq. (16)—i.e., assuming all of the heat input is equal to the amount of heat radiated, we have

$$h_bA(T_r - T_e) = A\sigma\epsilon T_e^4 \quad (20)$$

Expressing
$$T_e^4 = [T_r - (T_r - T_e)]^4 \quad (21)$$

Expanding $[T_r - (T_r - T_e)]^4$, neglecting terms involving powers of $T_r - T_e$ greater than unity, and solving,

$$T_e = [T_r + 3(\sigma\epsilon/h_b)T_r^4]/[1 + 4\sigma(\epsilon/h_b)T_r^3] \quad (22)$$

This approximation is valid when $T_r - T_e$ is small.

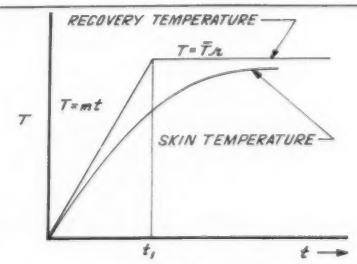

FIG. 1.

On an Exact Solution of Incompressible, Inviscid, Hypersonic, Stagnation-Point Flow for a Sphere*

Koon-Sang Wan
Research Associate Professor of Applied Mechanics, Polytechnic Institute of Brooklyn, Freeport, N.Y.
April 10, 1959

THE PURPOSE OF THIS NOTE is to present an exact solution for an inviscid hypersonic flow at the stagnation point of a sphere. The density ρ of the flow in the "shock layer" is assumed to be constant and is equal to $\rho/\rho_\infty = 1/k$ (see references 1 and 2) where the value of k depends on the free-stream Mach Number M_∞ and the ratio of the specific heats $\gamma = C_p/C_v$.

Under these assumptions, the governing equations can be written as, in spherical coordinates (see Fig. 1),

$$(1/r^2)(\partial/\partial r)(r^2u) + (1/r\sin\theta)(\partial/\partial\theta)(v\sin\theta) = 0 \quad (1)$$

$$u(\partial u/\partial r) + (v/r)(\partial u/\partial\theta) - (v^2/r) = -(1/\rho)(\partial p/\partial r) \quad (2)$$

$$u(\partial v/\partial r) + (v/r)(\partial v/\partial\theta) + (uv/r) = -(1/r\rho)(\partial p/\partial\theta) \quad (3)$$

The boundary conditions are: (1) at $r = a$, $\theta = 0°$; $u = 0$, $v = 0$; (2) at $r = a$, $u = 0$, and (3) at $r = a + \delta(\theta) \cong a + \delta^*$; i.e., near the stagnation point,

$$u = u_\infty\{-[1 + (k - 1)\sin^2\beta]\cos\theta + (1 - k)\sin\beta\cos\beta\sin\theta\} \cong -ku_\infty\cos\theta \quad (4)$$

$$v = u_\infty\{[1 + (k - 1)\sin^2\beta]\sin\theta + (1 - k)\sin\beta\cos\beta\cos\theta\} \cong u_\infty\sin\theta \quad (5)$$

$$p = p_\infty + \rho_\infty u_\infty^2(1 - k)\sin^2\beta \cong p_\infty + p_\infty u_\infty^2(1 - k)\cos^2\theta \quad (6)$$

by using the oblique shock conditions and where

$$\beta = 90° - \theta + [1/(a + \delta)](d\delta/d\theta) \cong 90° - \theta$$

The solution of this problem can be obtained by assuming

$$u = f(r)\cos\theta, \quad v = g(r)\sin\theta \quad (7)$$

Substituting these into Eq. (1) yields

$$2g = -(1/r)(d/dr)(r^2f) \quad (8)$$

By cross-differentiating Eqs. (2) and (3) to eliminate p and using

* The results obtained here are identical with those obtained by Lighthill,[3] but the approach used here is slightly different.

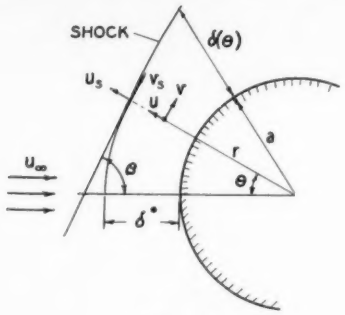

FIG. 1.

relation (8), one can obtain another relation between f and g as

$$r(d^2g/dr^2) + 2(df/dr) = 0 \tag{9}$$

The solutions of f and g are, therefore,

$$f(r) = A_1 + A_2r^2 + (A_3/r^3),$$
$$g(r) = -A_1 - 2A_2r^2 + (1/2)(A_3/r^3)$$

Hence,
$$u = [A_1 + A_2r^2 + (A_3/r^3)] \cos\theta \tag{10}$$
$$v = [-A_1 - 2A_2r^2 + (1/2)(A_3/r^3)] \sin\theta \tag{11}$$

and

$$p/\rho = A_4 + (1/2)[A_1A_2r^2 + (A_1A_3/r^3) + A_2r^4 + 7A_2A_3(1/r) - (1/4)(A_3^2/r^6)] - (1/2)[3A_1A_2r^2 + 3A_1A_3(1/r^3) + 2A_2^2r^4 + 9A_2A_3(1/r) + (3/4)(A_3^2/r^6)] \cos^2\theta \tag{12}$$

The unknown constants A_1, A_2, A_3, A_4, and δ^* are now determined by the boundary conditions and obtained as

$$\left.\begin{aligned} \bar{A}_1 &= A_1/u_\infty = (1 - 4k/3k \\ \bar{A}_2 &= A_2(a + \delta^*)^2/u_\infty = -(1 - k)^2/5k \\ \bar{A}_3 &= A_3/[u_\infty(a + \delta^*)^3] = 2(1 - k)(6k - 1)/15k \\ A_4 &= k(p_\infty/\rho_\infty) - (1/2)u_\infty^2[\bar{A}_1\bar{A}_2 + A_1\bar{A}_3 + \bar{A}_2^2 + 7\bar{A}_2\bar{A}_3 - (1/4)\bar{A}_3^2] \end{aligned}\right\} \tag{13}$$

and

$$-3(1 - k)^2\sigma^5 + (5 - 20k)\sigma^3 + 2(1 - k)(6k - 1) = 0 \tag{14}$$

an equation determining the value of $\sigma = a/(a + \delta^*)$ and, hence, δ^*. Since k is related to M_∞, therefore u, v, and p within the shock layer and near the stagnation point are completely determined for a given M_∞ from Eqs. (10)–(14).

It is of interest to compute the values of δ^*/a vs. M_∞. The results of such computations are shown in Figs. 2 and 3 together with results from experiments and theory by Li and Geiger for the purpose of comparison. They show that the present results check

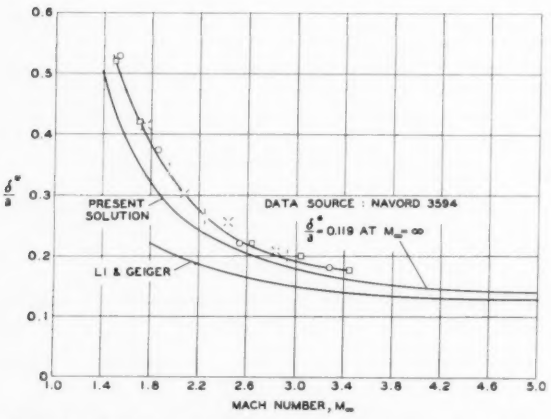

FIG. 2. Shock detachment distance (spheres tested in air).

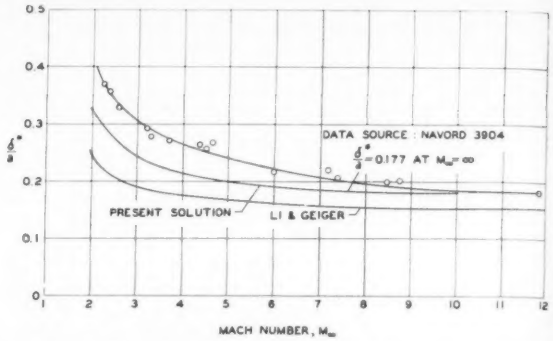

FIG. 3. Shock detachment distance (sphere tested in monatomic gases).

more closely with the experiment than those of Li and Geiger. This is expected since the effect of curvature is included in the present solution, as was also pointed out by Li and Geiger. The pressure coefficient at $r = a$ has also been computed vs. θ. The results are in good agreement with those from experiments and theory of Li and Geiger near the stagnation point.

REFERENCES

[1] Hayes, W. D., *Hypersonic Flow Fields at Small Density Ratio*, The Ramo-Wooldridge Corporation, May, 1955.

[2] Li, T. Y., and Geiger, R. E., *Stagnation Point of a Blunt Body in Hypersonic Flow*, Journal of the Aeronautical Sciences, Vol. 24, No. 1, pp. 25–32, January, 1957.

[3] Lighthill, M. J., *Dynamics of a Dissociated Gas, Part I, Equilibrium Flow*, J. Fluid Mech., Vol. 2, Part I, pp. 1–32, January, 1957.

Comments on "The Heating of Slabs With Arbitrary Heat Inputs"

William Squire*
Southwest Research Institute, San Antonio, Texas
May 19, 1959

IN A RECENT COMMUNICATION, Goodman[1] described the application of a "heat-balance integral" method to heat conduction problems including those with nonlinear boundary conditions. The basic advantage of the method is that approximate solutions of a partial differential equation are obtained by solving an ordinary differential equation. This note shows that an approximation method due to Shvets[2] gives analogous results and points out the need for further investigation of these methods.

The basic problem to be considered is the partial differential equation

$$\partial^2u/\partial x^2 = \partial u/\partial t \tag{1}$$

subject to the initial condition

$$u(x, 0) = 0 \tag{2}$$

and the boundary conditions

$$u(0, t) = 0 \tag{3a}$$

and
$$\partial u(0, t)/\partial x = -f(z, t) \tag{3b}$$

where $z(t)$ is the surface temperature, $u(0, t)$.

The solution is approximated by

$$u^n = \sum_{k=0}^{k=n} u_k \tag{4}$$

n being an integer ≥ 1 and k an integer ≥ 0. The partial solutions, u_k, satisfy the equation

* Formerly of Bell Aircraft Corporation, Buffalo, N.Y.

$$\partial^2 u_k/\partial x^2 = \partial u_{k-1}/\partial t \tag{5a}$$

and the sequence is started by

$$\partial^2 u_0/\partial x^2 = 0 \tag{5b}$$

This gives rise to polynomials in x so u^n cannot satisfy Eq. (3a). Therefore this boundary condition is replaced by

$$u^n(\delta, t) = 0 \tag{6a}$$

and the additional condition

$$(\partial u^n/\partial x)(\delta, t) = 0 \tag{6b}$$

is imposed to determine $\delta(t)$, the distance the heat penetrates the slab. Two boundary conditions are needed to determine the integration "constants" of Eq. (5) and two conditions are needed to determine δ and z as functions of t. There are three possible choices† which are shown in Table 1 where the corresponding u_0, u_1, and equations for δ and z are also listed.

We cannot present a detailed discussion of the solutions of the equations for δ and z here but we will show that marked differences exist in the predictions of the different approximations. For the case where f is a function of t only, Goodman obtains

$$\delta = (12F/f)^{1/2} = 3z/f \tag{7}$$

where

$$F(t) = \int_0^t f(t)dt$$

The supplementary equations of Case 2 can be integrated to give

$$\delta = (4F/f)^{1/2} \tag{8}$$

which is similar in form but with a less accurate numerical coefficient. On the other hand, Case 2 gives

$$\delta = \left(12\int_0^t F^2 dt \Big/ F^2\right)^{1/2} = 2F/z \tag{9}$$

Eq. (9) appears to be superior from a logical point of view since it gives δ as an expression which is inherently positive while Eq. (7) changes sign when f or z change sign. Dr. Goodman has found‡ that his method is not suitable for pulse-type inputs and seems to break down when f' changes sign.

On the other hand, if we consider the case where

$$f(t) = t^n \tag{10}$$

the exact solution is

$$z = \{n!/[n + (1/2)]!\}\, t^{n + (1/2)} \tag{11}$$

Goodman's method gives

$$z = [4/3(1 + n)]^{1/2} t^{n + (1/2)} \tag{12}$$

while Case 1 gives

$$z = \{[1 + (2/3)n]^{1/2}/(1 + n)\} t^{n + (1/2)} \tag{13}$$

A comparison shows Goodman's method is in closer agreement with the exact solution.

It, therefore, would be desirable to investigate the various approximations further in order to determine their relative advantages for different types of problems and to put them on a sound mathematical basis.

† Shvets' paper deals primarily with boundary-layer problems, and the treatment of heat conduction is very concise. The author interpreted it as Case 1. Dr. Goodman, to whom the author is indebted for an interesting correspondence, interpreted it as Case 2. This led the author to consider all three possibilities.

‡ Private communication.

TABLE 1

CASE	INTEGRATION CONDITIONS	SUPPLEMENTARY CONDITIONS	PARTIAL SOLUTIONS	EQUATIONS FOR z AND δ (FIRST ORDER)
I	$u_0(0,t) = z(t)$	$\frac{\partial u^n}{\partial x}(0,t) = -f(z,t)$	$u_0 = z(1 - x/\delta)$	$f = 3/2\,\frac{z}{\delta} + \frac{1}{4}\,\delta z'$
	$u_n(0,t) = 0$	$\frac{\partial u^n}{\partial x}(\delta,t) = 0$	$u_1 = \frac{x\delta z'}{2}\left(\frac{x}{\delta} - 1\right)$	$2f = \delta' z + \delta z'$
	$u_k(\delta,t) = 0$		$-\frac{x\delta^2}{6}\left(\frac{z}{\delta}\right)'\left(\frac{x^2}{\delta^2} - 1\right)$	
II	$\frac{\partial u_0}{\partial x}(0,t) = -f(z,t)$	$u^n(0,t) = z(t)$	$u_0 = -f\cdot(x - \delta)$	$z = f\delta - \frac{(f\delta)'}{2}\delta^2 + \frac{f'}{6}\delta^3$
	$\frac{\partial u_n}{\partial x}(0,t) = 0$	$\frac{\partial u^n}{\partial x}(\delta,t) = 0$	$u_1 = \frac{(f\delta)'}{2}(x^2 - \delta^2)$	$f = (f\delta)'\delta - \frac{f'}{2}\delta^2$
	$u_k(\delta,t) = 0$		$-\frac{f'}{6}(x^3 - \delta^3)$	
III	$u_0(0,t) = z(t)$	$u^n(\delta,t) = 0$	$u_0 = z - fx$	$z = f\delta - \frac{f'}{2}\delta^2 + \frac{f'}{6}\delta^3$
	$u_n(0,t) = 0$	$\frac{\partial u^n}{\partial x}(\delta,t) = 0$	$u_1 = \frac{f'}{2}x^2 - \frac{f'}{6}x^3$	$f = z'\delta - \frac{f'}{2}\delta^2$
	$\frac{\partial u_0}{\partial x}(0,t) = -f(z,t)$			
	$\frac{\partial u_n}{\partial x}(0,t) = 0$			

NOTE: $f' = \frac{\partial f}{\partial t} + z'\frac{\partial f}{\partial z}$ k IS AN INTEGER ≥ 0 n IS AN INTEGER ≥ 1

REFERENCES

[1] Goodman, T. R., *The Heating of Slabs With Arbitrary Heat Inputs*, Readers' Forum, Journal of the Aero/Space Sciences, Vol. 26, No. 3, pp. 187–188, March, 1959.

[2] Shvets, M. E., *Method of Successive Approximation for the Solution of Certain Problems in Aerodynamics*, NACA TM 1286, April, 1951, (translation, Prikl. Mat. Mek., Vol. 13, No. 3, pp. 257–66, 1949).

Note on the Calculation of Equilibrium Skin Temperatures

Hans C. Vetter
Aerodynamics Engineer, Douglas Aircraft Company, Inc., El Segundo, Calif.

May 21, 1959

THIS NOTE presents a method for the rapid estimation of equilibrium skin temperatures that result from aerodynamic heating in both the real-gas and ideal-gas regimes. Heretofore, the calculation of equilibrium temperatures has relied on a graphical or analytical determination of the roots of a fourth-order equation. The present method reduces the problem to the reading of a design chart for ideal-gas flow and to a quickly converging iteration method using the same design chart for real-gas flows.

IDEAL GAS

The heat-balance equation for an ideal gas is

$$h(T_r - T_e) + \alpha G = \epsilon\sigma T_e^4 \tag{1}$$

The first term on the left of Eq. (1) is the aerodynamic heating input, the second is an irradiation term, and the surface-radiation term appears on the right. By defining

$$\tau^3 = h/\epsilon\sigma$$

Eq. (1) may be rewritten, as follows:

$$(T_e/\tau)^4 + (T_e/\tau) = (T_r + \alpha G/h)/\tau \tag{2}$$

The roots of Eq. (2) may be calculated for all possible values of the right-hand term, and the results plotted to form a design curve for the determination of equilibrium temperatures. Actually, it is much easier to plot the right-hand term versus T_e/τ. A plot of Eq. (2) is shown in Fig. 1.

A temperature-dependent heat-transfer coefficient may be handled by iteration, but it is often sufficient to make the initial evaluation of h at a temperature somewhat lower than the recovery value.

REAL GAS

The appropriate heat-balance equation for aerodynamic heating with real-gas effects but neglecting hot-gas radiation is

$$C_H \rho V(i_r - i_e) + \alpha G = \epsilon\sigma T_e^4 \tag{3}$$

Here, C_H is the Stanton Number, ρ the density, V the velocity, and i the enthalpy. Now, the following definitions are made:

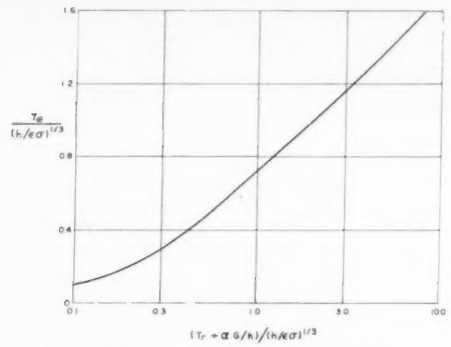

FIG. 1. Chart for determining equilibrium temperature.

$$h' = C_H \rho V c_{p_0}$$
$$i_e = c_{p_0} T_e + \Delta i_e$$
$$T_r' = i_r/c_{p_0} - \Delta i_e/c_{p_0}$$

where c_{p_0} is the ideal-gas value of the specific heat. Using these definitions, Eq. (3) may be written as follows:

$$h'(T_r' - T_e) + \alpha G = \epsilon\sigma T_e^4 \tag{4}$$

Eq. (4) has exactly the same form as Eq. (1), with the exception that T_r' is a function of T_e. Hence, Eq. (4) may be put into the generalized form of Eq. (2) using the primed quantities in place of the unprimed quantities. By assuming Δi_e to be zero, a first estimate of T_e may be calculated from the design chart that may then be used to calculate a second approximation to T_r'. By using this value of T_r', a better estimate of T_e may be made, etc., until the desired accuracy is achieved. A temperature-dependent Stanton Number may, of course, be included in the iteration.

If real-gas effects are not large ($\Delta i_e \ll i_r$), but not negligible, one iteration is sufficient to determine the equilibrium temperature. In addition, it is often sufficient to use the following approximation:

$$T_e = T_{e_1} + \Delta T_e$$
$$h_1' = h_0' + \Delta h_1'$$
$$\Delta T_e \cong (\partial T_e/\partial h')\Delta h_1' + (\partial T_e/\partial T_r')\Delta T_r'$$

whence

$$\Delta T_e \cong \{[(i_r/C_{p_0}) - T_{e_1}]\Delta h_1' - h_0'(\Delta i_e/C_{p_0})_1\}/(h_0' + 4\epsilon\sigma T_{e_1}^3)$$

where the subscript 1 refers to an evaluation at $T_e = T_{e_1}$, and h_0' is the initial estimate of h'. The above approximation is based on the observation that the equilibrium temperature, as calculated from Eq. (4), differs from that calculated from Eq. (1) by only a small difference in the "effective" recovery temperature ($\Delta T_r' = -\Delta i_e/C_{p_0}$).

On the Integral of Moment of Pressure in Supersonic Flow*

Lu Ting
Research Associate Professor, Polytechnic Institute of Brooklyn, Freeport, N.Y.
May 21, 1959

IN THIS PAPER, the integral of the moment of the disturbance pressure along the line of the interaction of a Mach plane with the cylindrical surface whose generator is parallel to the undisturbed stream, is shown to be related to the integral of the moment of the prescribed normal velocity along the same line. It is derived by the generalized integral relationship which relates the integral of disturbance pressure to that of the prescribed normal velocity.[1, 2]

As shown in Fig. 1, a cylindrical surface $y = f(s)$, $z = g(s)$, is placed in a supersonic stream with its generator parallel to the x-axis, which is the direction of the undisturbed supersonic flow with velocity U and Mach Number M. $q_n(x, s)$ represents the prescribed small normal velocity on the cylindrical surface with $q_n = 0$ for $x < 0$. It will be assumed that for any given Mach plane, $x + B(y \cos\omega + z \sin\omega) = X$, there exist two finite values of $K_1(X)$ and $K_2(X)$ with $K_1 > K_2$, such that ahead of the Mach plane, the disturbance potential due to q_n is confined inside the region $K_1 > z > K_2$; i.e.,

$$\varphi[x \leq X - B(y \cos\omega + z \sin\omega), y, z] = 0 \tag{1}$$

for $\infty > z \geq K_1(X)$ and $K_2(X) \geq z > -\infty$. This assumption is usually valid for a finite range of ω. The generalized integral relationship states:

$$\iint_S p(x, y, z)\mathbf{n}\cdot\boldsymbol{\omega}\, dS = (\rho U/B)\iint_S q_n\, dS \tag{2}$$

where $p(x, y, z)$ is the disturbance pressure; $\mathbf{n}$ is the unit vector normal to the cylindrical surface, $\boldsymbol{\omega} = \cos\omega\,\mathbf{j} + \sin\omega\,\mathbf{k}$; $\mathbf{j}$, $\mathbf{k}$ are the unit vectors parallel to y and z axis; and S represents the domain of integration on the cylindrical surface ahead of the Mach plane. Eq. (2) can be written as

$$\int_{s_1}^{s_2} ds \int_0^{x^*(s)} dx\; p[x, f(s), g(s)](n_y \cos\omega + n_z \sin\omega) = (\rho U/B)\int_{s_1}^{s_2} ds \int_0^{x^*(s)} q_n(x, s)\, dx \tag{3}$$

where $x^*(s) = X - B[f(s)\cos\omega + g(s)\sin\omega]$; s_1 and s_2 are the arc lengths on the cylindrical surface corresponding to the points $z = K_1$ and $z = K_2$, respectively; and n_y, n_z are the y and z components of the normal $\mathbf{n}$ which is a function of s only. Differentiation of Eq. (3) with respect to ω yields:

$$B\int_{s_1}^{s_2} ds\; p(x^*, f, g)(\mathbf{n}\cdot\boldsymbol{\omega})(f\sin\omega - g\cos\omega) - \iint_S p(x, f, g)(n_y \sin\omega - n_z\cos\omega)dS = \rho U\int_{s_1}^{s_2} ds\; q_n(x^*, s)(f\sin\omega - g\cos\omega)$$

which is equivalent to

$$\int_T ds(\mathbf{n}\cdot\boldsymbol{\omega})(y\sin\omega - z\cos\omega)p = (1/B)\times \iint_S (\mathbf{n}\times\boldsymbol{\omega}\cdot\mathbf{i})p\, dS + (\rho U/B)\int_T ds\,(y\sin\omega - z\cos\omega)q_n \tag{4}$$

where the line integrals are carried out along the line T, which is the line of intersection of the Mach plane (X, ω) and the cylindrical surface.

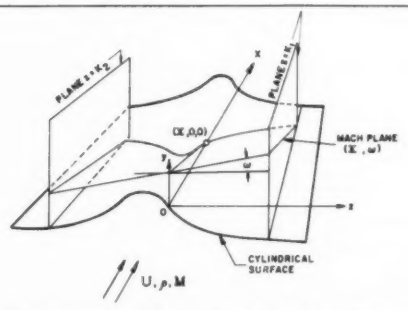

FIG. 1. The generalized integral relationship of pressure and that of moment of pressure.

* This research was supported by the USAF through the Air Force Office of Scientific Research, Air Research and Development Command, under Contract No. AF 49(638)-217, Project No. 9781.

The author wishes to express his sincere thanks to Prof. Antonio Ferri for many stimulating discussions and suggestions.

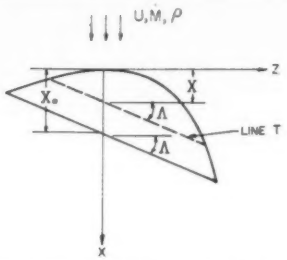

FIG. 2. Planar wing at yaw with a straight trailing edge.

Eq. (4) is the general relationship which involves the integral of moment of pressure. Eq. (4) is now applied to a planar system. Fig. 2 shows a wing planform with all edges supersonic and a straight trailing edge. The wing is yawed at an angle Λ. The total lift and center of pressure can be calculated readily by virtue of Eqs. (2) and (4). For the planar system with $\mathbf{n} = \mathbf{j}$ and $y = 0$, Eqs. (2) and (4) become

$$\cos\omega \iint_S p\,dS = \iint_S q_n\,dS(\rho U/B) \tag{5}$$

and

$$B\cos^2\omega \int_T zp\,dz = -\sin\omega \iint_S p\,dS + \rho U \int_T z\,q_n\,dz = \rho U\left[-(\tan\omega/B)\iint_S q_n\,dS + \int_T z\,q_n\,dz\right] \tag{6}$$

For $\omega = -\arcsin(\tan\Lambda/B)$, the line T is parallel to the trailing edge and S is the area of the upper surface (or lower surface) of the wing ahead of the line T. For $X = X_0$, the line T_0 coincides with the trailing edge, and the total lift acting on the upper surface of the wing is

$$L^+ = -\iint_A p^+\,dA = -(\rho U/B\cos\omega)\iint_A q_n{}^+\,dA \tag{7}$$

where the superscript $+$ refers to the upper surface. The location $(\mathbf{z}, \mathbf{x})$ of the center of pressure acting on the line T is obtained from Eq. (6):

$$\mathbf{z}(X) = \left(\int_T dz\,p^+\,z\Big/\int_T dz\,p^+\right)\left[\left(B\int_T z\,q_n{}^+dz - \tan\omega \times \iint_S q_n{}^+\,dS\right)\Big/B\cos\omega\int_T q_n{}^+dz\right] \tag{8}$$

and $\mathbf{x}(X) = X + \mathbf{z}\tan\Lambda$ where the relationship

$$\cos\omega\int_T p^+\,dz = (\rho U/B)\int_T q_n\,dz$$

is deduced from Eq. (2).[1] The location of the center of pressure on the upper surface of the wing is simply

$$\begin{aligned} x_c{}^+ &= \int_0^{X_0} - \mathbf{x}(X)\left(\int_T dz\,p^+\right)dX/L^+ \\ &= \int_0^{X_0}\mathbf{x}(X)\left(\int_T q_n{}^+dz\right)dX\Big/\iint_A q_n{}^+\,dA \\ z_c{}^+ &= \int_0^{X_0}\mathbf{z}(X)\left(\int_T q_n{}^+dz\right)dX\Big/\iint_A q_n{}^+\,dA \end{aligned} \tag{9}$$

Similar results can be obtained for the lower surface. Additional applications to planar and nonplanar systems are presented in reference 3.

REFERENCES

[1] Ting, Lu, *Some Integrated Properties of Solutions of the Wave Equations With Nonplanar Boundaries*, Quart. Appl. Math., Vol. 16, No. 4, pp. 373–384, January, 1959.

[2] Ting, Lu, *Pressure Distribution on Dihedral Wings at Supersonic Speed*, PIBAL Rep. No. 397, Polytechnic Institute of Brooklyn, January, 1958.

[3] Ting, Lu, *On the Integral of Moment of Pressure in Supersonic Flow*, PIBAL Report No. 449, Polytechnic Institute of Brooklyn, April, 1959.

Column End-Fixity Versus End-Restraint

Paul E. Sandorff
Associate Professor of Aeronautics and Astronautics, Massachusetts Institute of Technology, Cambridge, Mass.

May 21, 1959

IN A RECENT REPORT published here, Neffson[1] has made a creditable presentation of a problem that recurs repeatedly in practice and in the literature. The earliest solution of this problem with which the writer is familiar is that of Osgood,[2] who, employing the same fundamental beam-column theory, derived a method and a chart whereby the critical load could be expressed from the end-moments applying to an elastically-restrained test column. Osgood references earlier work by Prager and Zimmerman, which was limited to consideration of elastic columns. Wozniak[3] presented a solution to the inverse problem of determining the end-moments, in the presence of a lateral load, when the end-fixity coefficient is established. Most certainly unknown to Neffson is reference 4, which employed in part the identical derivation as reference 1 and presented the suggested curves of end-fixity coefficient vs. end-restraint factors, where the latter are established by the relative rigidities of the column and the adjacent restraining structure. Deserving of mention is the unpublished report of Ensrud, Kastan, and Wignot[5] on working methods for all aspects of beam-column structures, including those continuous over many supports and with various types of lateral loads and restraint conditions. There are undoubtedly others whom the writer regrets being unable to credit.

Hitherto unpublished is the much improved and extended chart expressing column end-fixity in terms of end-restraints, due to C. H. Heilbron, presented herewith as Fig. 1.

A typical problem which is greatly simplified by use of such a chart is the determination of a proper test length, at, say, $c = 3.5$ for a structure which, in service, is stated to have "end-fixity conditions corresponding to $c = 2.0$ at one end and to $c = 1.5$ at the other." Such improperly stated specifications may be trans-

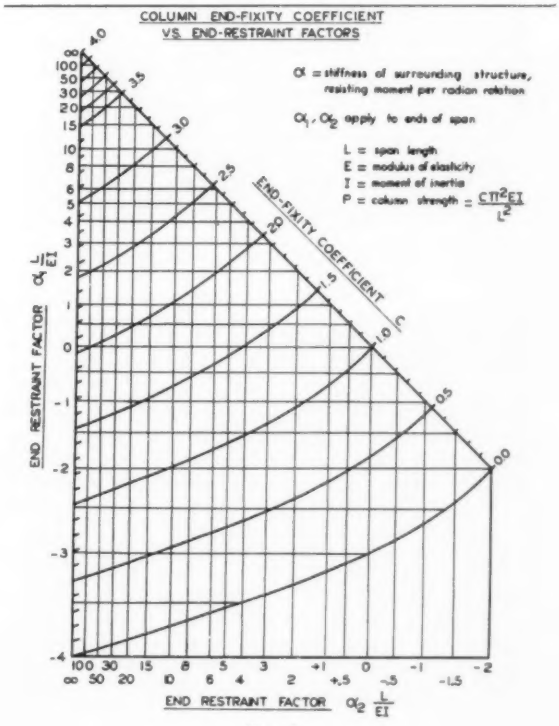
COLUMN END-FIXITY COEFFICIENT
VS. END-RESTRAINT FACTORS
α = stiffness of surrounding structure, resisting moment per radian rotation
α_1, α_2 apply to ends of span
L = span length
E = modulus of elasticity
I = moment of inertia
P = column strength = $C\pi^2EI/L^2$
END-FIXITY COEFFICIENT C
END RESTRAINT FACTOR $\alpha_1 \frac{L}{EI}$
END RESTRAINT FACTOR $\alpha_2 \frac{L}{EI}$

FIG. 1.

lated, "if end-restraints were symmetrical and equal to α_1, c would be 1.0; if both were equal to α_2, c would be 2.0." From Fig. 1, equal end-restraint factors corresponding to $c = 2.0$ are $\alpha_1 L/EI = \alpha_2 L/EI = 3.4$; corresponding to $c = 1.0$, $\alpha_1 L/EI = \alpha_2 L/EI = 0$. The actual end-fixity which corresponds to $\alpha_1 L/EI = 0$ and $\alpha_2 L/EI = 3.4$, is $c = 1.44$. The proper test length is therefore, $\sqrt{3.5/1.44}$ times as large as the actual structure.

The chart extends into the regions of negative end-restraint, so that it may be used to advantage when destabilizing influences are exerted by the adjacent structure. It is, therefore, suitable for the solution of multispan columns as suggested in reference 4. A typical problem concerns a column of constant section continuous over a central support, but, for example, with one bay half the length of the other, and where all supports are assumed to furnish restraint corresponding to $c = 1.5$. Simultaneous instability requires that $c_{ab}/c_{bc} = (L_1/L_2)^2 = 1/4$. By trial and error, a solution is quickly found whereby the proper increment of stiffness is exchanged at the central support; it is $\alpha_a L/EI = 1.4$; $\alpha_{-b} L/EI = 1.4 - 3.6 = -2.2$, $\alpha_{+b} L/EI = 1.4 + 2(3.6) = 8.6$, $\alpha_c L/EI = 1.4$, and $c_{ab} = 0.50+$, $c_{bc} = 2.01$.

References

[1] Neffson, B. A., *Beam Columns on Elastic Supports*, Readers' Forum, Journal of the Aero/Space Sciences, Vol. 26, No. 4, pp. 255–256, April, 1959.

[2] Osgood, W. R., *Column Strength of Tubes Elastically Restrained Against Rotation at the Ends*, NACA Rep. No. 615, 1938.

[3] Wozniak, F. B., *Beam-Column End Moments for Known Fixity*, Aviation, Vol. 40, No. 1, p. 52, January, 1941.

[4] Sandorff, P. E., *Notes on Columns*, Journal of the Aeronautical Sciences, Vol. 11, No. 1, pp. 1–12, January, 1944.

[5] Ensrud, A. F., Kastan, H., and Wignot, J. E., *The Beam Column—An Introduction to the Problem of General Instability*, Lockheed Aircraft Corporation Rept. No. 5048, June 5, 1945.

Comments on "A New Solution to the Laminar Boundary-Layer Equations"

M. Z. v. Krzywoblocki
Professor, University of Illinois, Urbana, Ill.

May 21, 1959

HASSAN[1] proposed a generalization of Görtler's solution of plane and steady laminar boundary-layer equations for a certain class of outer pressure distributions. The remarks below refer to both these propositions, and, as a matter of fact, to many similar and analogous propositions of this kind. The equations of a boundary layer are nonlinear partial differential equations which are usually associated with two-curve boundary conditions. In the theory of differential equations, one distinguishes two main processes: (1) formal construction of a solution satisfying the prescribed boundary conditions; (2) proof of existence and, possibly, of uniqueness of a solution—i.e., proof that a solution actually exists and satisfies boundary conditions, regardless of its form (closed or derivable by means of a limiting process). In both processes, one may attempt to derive a solution and a proof in an infinitesimal neighborhood of the boundary curve (local solution or solution in the small) or in a finite region (solution in the large). Up to the present time, there do not exist any proofs of the nature of process (2) referring to the boundary-layer equations in question. Consequently, all the attempts and efforts referring to these equations can only be classified as processes belonging to category (1). Since there is no existence proof, one cannot investigate whether a solution constructed by some method is exact, convergent, approximate, or asymptotic (this may be even divergent). A possible comparison may be made with physical (experimental) test results. The classical mathematical approach to the field of differential equations is one of demonstrating that the problem in question has at least one solution (sometimes proving uniqueness). In many cases, an investigator may well seek a series or numerical solution even though he is not certain it is obtainable in the manner chosen (or at all). The purpose may be an application or it may be one of experimental arithmetic—i.e., a calculation which may help in an effort to guess a correct statement of the proposition in question. If one believes that there is a probability of a success and if one can verify that his final result is an adequate approximation to a solution, then there may be no reason to insist on furnishing a firm proof. But the status of the entire question of the so-called new and old solutions, supposedly known as exact or rigorous, etc., should be always explained and discussed, and it is believed that these few remarks may help to understand it a little better.

An interesting contribution to the problem in question in the incompressible-fluid flow domain was furnished by Rheinboldt who proved that if in a certain region $[0 \leqq x \leqq x_0; 0 \leqq y \leqq \infty]$ the stream function ψ is an analytic function of x, then the boundary condition at infinity is always automatically satisfied and does not need to be taken into account. But to this end the function ψ must be representable by an absolutely convergent power series in x. In the existing texts and collective works (Princeton Series, Oxford Series, etc.) on boundary-layer theory, the description and explanation of these fundamentals is usually neglected.

References

[1] Hassan, H. A., *A New Solution to the Laminar Boundary-Layer Equations*, Journal of the Aero/Space Sciences, Readers' Forum, Vol. 26, No. 3, pp. 189–190, March, 1959.

[2] Görtler, H., *A New Series for Calculation of Steady Laminar Boundary-Layer Flows*, J. Rational Mech. and Analysis, J. Math. and Mech., Vol. 6, No. 1, pp. 1–66, January, 1957.

Further Remarks on Matrix Interpolation of Flexibility Influence Coefficients†

William P. Rodden*
Research Specialist, Vibration, Flutter and Acoustics, North American Aviation, Inc., Los Angeles, Calif.

May 21, 1959

IN CARRYING OUT an aeroelastic analysis by collocation methods, it is assumed that both structural and aerodynamic influence coefficients are known. The aerodynamic influence coefficients have been defined[1] as relating the forces acting at the control points to the deflections of the *same* control points. Since the structural influence coefficients normally are determined for loads acting at the panel points of the structure, it becomes necessary to unify the control points of both the structural and the aerodynamic systems in order to obtain a consistent aeroelastic analysis. It is the nature of aerodynamic theories that a transformation of control points is not convenient, whereas the transformation of the structural control points can be carried out readily.

We will generalize the results of Schmitt[2] in order to eliminate the dependence on the least-squares interpolation method. We denote the structural net by p and the aerodynamic net by k. We are given the structural matrix $[a_p]$ such that

$$\{h_p\} = [a_p]\{F_p\} \tag{1}$$

and we seek an equivalent set such that

$$\{h_k\} = [a_k]\{F_k\} \tag{2}$$

The problem is to relate $\{F_p\}$ to $\{F_k\}$. We choose to make the relationship structurally equivalent rather than statically equivalent because of the greater accuracy of the outboard

† The present analysis is an outgrowth of a private communication with Dr. Alfred F. Schmitt, and the author wishes to acknowledge his very helpful and stimulating comments.

* Now Engineering Specialist, Dynamics Branch, Norair Division of the Northrop Corporation, Hawthorne, Calif.

deflections which are more important in an aeroelastic analysis. By structurally equivalent we mean that the set of forces $\{F_k\}$ produces the same deflection mode $\{h_p\}$ as does the original set $\{F_p\}$. Therefore, there is some matrix $[C_{pk}]$ that defines the structural equivalence.

$$\{h_p\} = [C_{pk}]\{F_k\} \tag{3}$$

By Maxwell's Law of Reciprocity

$$\{h_k\} = [C_{kp}]\{F_p\} \tag{4}$$

where $[C_{kp}]$ is the transpose of $[C_{pk}]$. From Eqs. (1) and (4),

$$\{h_k\} = [C_{kp}][a_p]^{-1}\{h_p\} \tag{5}$$

and from Eqs. (3) and (5),

$$\{h_k\} = [C_{kp}][a_p]^{-1}[C_{pk}]\{F_k\} \tag{6}$$

By identifying Eqs. (2) and (6), we find

$$[a_k] = [C_{kp}][a_p]^{-1}[C_{pk}] \tag{7}$$

To determine $[C_{pk}]$, we assume a deflection interpolation matrix can be found.

$$\{h_k\} = [I_{kp}]\{h_p\} \tag{8}$$

By identifying Eqs. (5) and (8), we find

$$[I_{kp}] = [C_{kp}][a_p]^{-1} \tag{9}$$

from which $$[C_{pk}] = [a_p][I_{pk}] \tag{10}$$

Substituting Eq. (10) into Eq. (7) yields the desired form of the transformation.

$$[a_k] = [I_{kp}][a_p][I_{pk}] \tag{11}$$

The result Eq. (11) is that obtained by Schmitt if the interpolation matrix of Eq. (8) is found from the least-squares method. However, Eq. (8) shows that there are a number of methods obtaining the elements of $[I_{kp}]$. These methods can be divided into two classes: interpolation-in-the-large in which the entire surface is fitted with a single set of functions—e.g., Schmitt suggests that product combinations of the normal modes of a uniform cantilever beam provide satisfactory functions for plate-like wing surfaces, and interpolation-in-the-small in which each small region is fitted with functions appropriate to the significant boundary conditions and structural discontinuities in the region (in this manner, the elements of $[I_{kp}]$ are found a row at a time). It appears that the latter choice is the more reliable for, although a practical surface is uniform for the most part, there are always a sufficient number of structural discontinuities to be bothersome. The interpolation-in-the-small can be carried out using double polynomial functions ($x^m y^n$) either by the Lagrangian method (which has been found to be grossly inaccurate for interpolation-in-the-large) or by the least-squares method. The least-squares method is more general since it includes the Lagrangian fit as a limiting case.

References

[1] Rodden, William P., *A Matrix Approach to Flutter Analysis and Related Aeroelastic Problems*, paper presented to a Specialist Meeting of the IAS, Los Angeles, Calif., December 9, 1958 (available as Fairchild Fund Paper No. FF-23).

[2] Schmitt, Alfred F., *A Least Squares Matrix Interpolation of Flexibility Influence Coefficients*, Readers' Forum, Journal of the Aeronautical Sciences, Vol. **23**, No. 10, p. 980, October, 1956.

Visual Supersonic Flow Patterns by Means of Smoke Lines

V. P. Goddard, J. A. McLaughlin, and F. N. M. Brown
University of Notre Dame, Notre Dame, Ind.
May 26, 1959

THE CONSIDERABLE SUCCESS enjoyed here at Notre Dame in extending the useful top speed of three-dimensional smoke-tunnels[1] from a bare 20 ft. per sec. to more than 200 ft. per sec. resulted in a doubt that any upper limit of speed for smoke tunnels existed. The radical increase in useful speed in the subsonic tunnel was achieved rather simply by severe reduction ratios, heavy antiturbulence screening, and introduction of the smoke upstream of this screening. The same technique of design was applied to the supersonic tunnel, and the doubt was confirmed; smoke pictures can be taken at least as high as 1,325 ft. per sec.

The techniques for producing and photographing supersonic flow patterns have not yet been fully perfected. However, they are at a point which enables a realization of the potentialities of this type of aerodynamic study in the supersonic flow regime.

It is the purpose of this article to present and describe these techniques. Pictures are included of flow patterns about a wedge and a sphere (see Figs. 1 and 2).

TUNNEL

The Notre Dame supersonic pilot tunnel was designed by the Foelsch method.[2] It is an indraft type tunnel capable of continuous operation at Mach 1.38. The working section is approximately 4 in. long with a cross-sectional area of 6.25 sq. in. The entire side walls are of 3/4 in. lucite to enable visualization and schlieren setups along the full length of the nozzle.

The reduction cone was designed by the Smith and Wang curves.[2] It has a reduction ratio to the throat of the tunnel of 96 to 1 and is 3 ft. in length. There are 6 antiturbulence screens of fine-mesh nylon at the upstream end of the reduction cone spaced 3/4 in. apart.

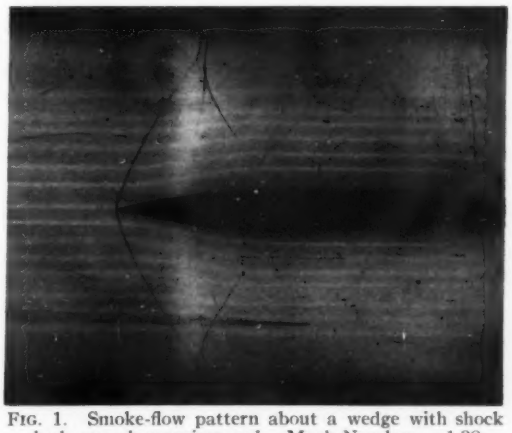

FIG. 1. Smoke-flow pattern about a wedge with shock shadowgraph superimposed. Mach Number = 1.38.

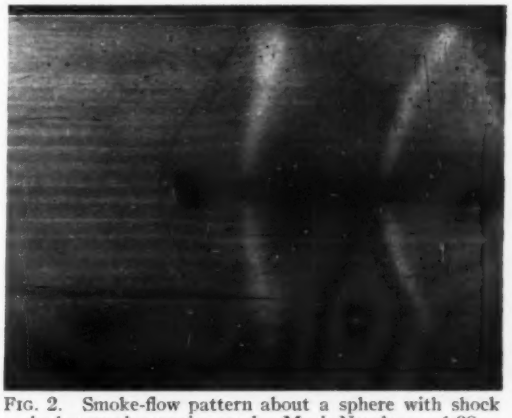

FIG. 2. Smoke-flow pattern about a sphere with shock shadowgraph superimposed. Mach Number = 1.38.

Smoke System

The smoke is produced according to techniques devised by Brown.[4] Wheat straw is coked, and the resulting smoke is cooled and filtered before introduction.

Lighting and Photography

The light source for both shock shadow and smoke filaments was a short-interval flash lamp synchronized with the shutter of a modified schlieren camera. The effective exposure was about 20 microsec.

To make pictures of the shock shadow, the short-interval lamp was substituted for the usual steady light source. A cover with a pin-hole opening was placed over the light to produce a point source. The knife edges were omitted, and the image of the point source was focused on the shutter diaphragm.

The pictures of the smoke lines were made with the same modified schlieren camera, but two short-interval lamps were placed behind and upstream of the working section. Both lamps were aimed at the model. The angle of the beam with respect to the back wall of lucite was just larger than the critical angle of that material. Tungsten 160 film was used, and the desired contrast was obtained by underexposing and overdeveloping.

The accompanying pictures were made through the two negatives—the smoke-filament negative and the shock-shadow negative. This is justifiable because the negatives were identical in scale, a steady-state flow condition existed, and both negatives were made with smoke flowing. The random marks on the pictures are due to scratches on the lucite tunnel walls.

Future Plans

The current pictures are, perhaps, acceptable, but it is believed that they can be considerably improved. To this end, a new nozzle is under construction which permits introduction of the light through a lucite plate sandwiched in the lower nozzle block. This will permit full utilization of the polarization property and, at the same time, diminish the illumination of the background.

Since the level of turbulence appears to be a function of the reduction ratio and the screening, the optimum will be sought. The reduction ratio and the number of screens and screen spacing will be varied independently to this end. It is hoped an optimum combination can be found to enable taking pictures of the quality now being obtained with the subsonic smoke tunnel here at Notre Dame.

References

[1] Brown, F. N. M., *An American Method of Photographing Flow Patterns*, Aircraft Eng., Vol. 24, No. 280, pp. 164–169, June, 1952.

[2] Foelsch, Kuno, *A New Method of Designing Two-dimensional Laval Nozzles for a Parallel and Uniform Jet*, Report No. NA-46-235-2, North American Aviation, Inc., May 27, 1946.

[3] Smith, R. H., and Wang, Chi-Teh., *Contracting Cones Giving Uniform Throat Speeds*, Journal of the Aeronautical Sciences, Vol. 11, No. 4, pp. 356–360, October, 1944.

[4] Brown, F. N. M., *A Photographic Technique for the Mensuration and Evaluation of Aerodynamic Patterns*, Photographic Eng., Vol 4, No. 3, pp. 146–156, 1953.

The Compressible Laminar Boundary Layer With Constant Injected Mass Flux at the Surface

Alan Q. Eschenroeder
Cornell University, Ithaca, N.Y.

May 26, 1959

Analyses of the steady compressible laminar boundary layer on a flat plate with fluid injection have been done by Low[1] for injection velocity proportional to the reciprocal of the square root of the distance from the leading edge and by Lew and Fanucci[2] for uniform injection velocity. Certain problems in mass-transfer cooling with combustion require a compressible solution for uniform mass flux from the surface because the wide variation of fluid density precludes the use of constant injection velocity as a boundary condition when fluid is supplied uniformly to a porous wall boundary.

Under the assumption that the product of density and viscosity is a constant, the uniform mass flux case can be solved in terms of an existing incompressible solution by Lew and Fanucci.[2] Basically, their transformation procedure is followed with redefinitions of variables. The boundary-layer equation for the x-component of momentum after the von Mises transformation reduces to

$$\partial u'/\partial x' = (\partial/\partial\psi')[u'(\partial u'/\partial\psi')] \tag{1}$$

u' is the nondimensional downstream velocity (referred to the free-stream velocity U_1), x' is the nondimensional downstream distance from the leading edge (referred to a typical downstream length L), and ψ' is a nondimensional stream function defined by

$$\rho' u' = 1/\sqrt{Re_L}(\partial\psi'/\partial y'); \quad \rho' v' = -(1/\sqrt{Re_L})(\partial\psi'/\partial x') \tag{2}$$

where ρ' is the nondimensional density (referred to the density at free-stream conditions ρ_1), y' is the nondimensional normal distance (referred to L), v' is the nondimensional normal velocity (referred to U_1), and Re_L is a Reynolds Number $\rho_1 U_1 L/\mu_1$. The boundary conditions become

$$u'(0, \psi') = 1; \quad u'(x', \infty) = 1; \quad u'[x', f'(x')] = 0 \tag{3}$$

where $f'(x')$ is given by

$$f'(x') = -\sqrt{Re_L}\int_0^{x'} \rho_0' v_0'(x')dx' \tag{4}$$

The subscript 0 refers to conditions at the wall surface. Further transformations following the method of reference 3 with consistent redefinitions of variables lead to the equation

$$\sqrt{V'}(\partial^2 V'/\partial\tau'^2) + (\partial V'/\partial\tau')\left[2\sigma'\tau' - \left(\sqrt{V'}/\tau'\right) + \tau'^3\right] - 2\sigma'\tau'^2(\partial V'/\partial\sigma') = 0 \tag{5}$$

where $V' = 4u'^2$ and the two independent variables are related to the original variables by the equations

$$\sigma'^2 = 2[-(\rho_0 v_0/\rho_1 U_1)]^2(\rho_1 U_1 x/\mu_1) \tag{6}$$

and

$$2\sigma'\int_0^{\tau'} \tau' d\tau'/\sqrt{V'} = -(\rho_0 v_0/\mu_1)\int_0^y (\rho/\rho_1)dy \tag{7}$$

The boundary conditions governing Eq. (5) are

$$V'(\sigma', 0) = 0 \text{ and } V'(\sigma', \infty) = 4 \tag{8}$$

Eq. (5) with these boundary conditions is formally identical to the problem solved numerically in reference 3; therefore, the tabulated results of that reference can be utilized for the compressible case with uniform mass flux if the definitions expressed in Eqs. (6) and (7) are used. As a check, it can be shown that the normal distance in reference 3 is given by

$$\int_0^y (\rho/\rho_1)dy$$

according to the familiar Dorodnitzyn-Howarth transformation, which should be implicit in the present method.

The friction coefficient c_f defined by

$$c_f = \mu_0(\partial u/\partial y)]_0/(1/2)\rho_1 U_1^2 \tag{9}$$

can also be found. For various values of σ', Lew and Fanucci[2] have tabulated a starting coefficient d_2 which gives the friction coefficient for the compressible case with uniform mass flux by the relationship

$$c_f = d_2/2\sqrt{2\rho_1 U_1 x/\mu_1} \tag{10}$$

The detailed steps of the transformations and the derivation of Eq. (10) are found in Appendix A of reference 4.

References

[1] Low, G. M., *The Compressible Laminar Boundary Layer with Fluid Injection*, NACA TN 3404, March, 1955.

[2] Lew, H. G., and Fanucci, J. B., *The Laminar Compressible Boundary Layer over a Flat Plate with Suction or Injection*, Journal of the Aeronautical Sciences, Vol. 22, No. 9, pp. 589–597, September, 1955.

[3] Lew, H. G., and Fanucci, J. B., *An Exact Solution of the Laminar Boundary Layer with Zero Pressure Gradient and Homogeneous Injection*, A. F. Technical Report No. 6, Pennsylvania State University, July, 1955.

[4] Eschenroeder, A. Q., *Flame Stabilization in the Boundary Layer on a Porous Flat Plate*, Doctoral thesis, Cornell University, June, 1959.

A Perturbation Analysis of Shock Flow in a Nozzle*

Roy Gundersen
Assistant Professor of Mathematics,
Illinois Institute of Technology, Chicago, Ill.
May 23, 1959

BY THE USE of a linearization based on small area variations, the motion of a plane shock generated by a uniform compressive piston motion has been solved for the case of a slowly converging or diverging one-dimensional channel.[1] In the present paper, these results are extended to the case where the channel presents a throat. With $E(x)$ the cross section of the tube, it is convenient to let $E(x) = E_0 + k(x - a)^2$, where E_0 is the original uniform cross section, a is a constant, and k is a small parameter.

At $t = 0$, a uniform shock is introduced at $x = 0$, and it is assumed that the piston is pushed continuously with uniform velocity, and the original shock velocity is W. Utilization of the general solution for the nonisentropic perturbation of a constant state gives the shock-velocity perturbation $\bar{W}(t)$.

$$E_0\bar{W}(t) = [u_2c_2M_1kat/(k_1 + M_1k_2 - M_1c_2k_3\nu^{-1})] - \{[u_2kc_2^2M_1(M_1^3 + M_1 + 2m)t^2]/[2k_1(1 + M_1^2) + 4M_1k_2 - 4c_2k_3M_1\nu^{-1}]\} \quad (1)$$

where the rest state in front of the shock is denoted by the subscript 0 and the perturbed flow behind the shock by the subscript 2, u and c are the fluid and sound velocities, $W_2 = W - u_2$, $M_0 = W/c_0$, $M_1 = W_2/c_2$, $m = u_2/c_2$, $\nu = 2c_v\gamma(\gamma - 1)$ with c_v the specific heat at constant volume, γ the adiabatic index and k_1, k_2, and k_3 depend upon the Mach Numbers defined above.

For $\gamma = 7/5$ and the shock strength defined as the pressure ratio $P_2/P_0 = z$, Eq. (1) becomes

$$E_0\bar{W}(t) = \{[6(z + 6)(z - 1)zkatc_0^2]/(27z^2 + 65z + 6)\} - \{[3(z - 1)(z + 6)(39z^2 - 8z + 18)c_0^3kt^2] \div [14(9z^2 + 31z + 9)(42z + 7)^{1/2}]\} \equiv R_1c_0^2kat - R_2c_0^3kt^2 \quad (2)$$

which is a quadratic function of t with zeros at $t = 0$ and t_1 where $c_0t_1/a = 28z(9z^2 + 31z + 9)(42z + 7)^{1/2}/(27z^2 + 65z + 6)(39z^2 - 8z + 18)$. $\bar{W}(t)$ is zero at $t = 0$, increases to a maximum at $t_1/2$, and decreases to zero at t_1. For larger t, $\bar{W} < 0$, increasing in absolute value. Table 1 gives values of t_1, R_1, and R_2 for several shock strengths.

The position of the point where $\bar{W}(t) = 0$ is given in Table 2.

For a shock strength less than about 2.2, $\bar{W} > 0$ throughout the entire nozzle. For $z > 2.2$, the maximum point lies upstream of the throat and moves farther upstream for increasing z with a limiting position of about $0.72a$ for a very strong shock. If the tube is of constant cross section after the nozzle, the shock will asymptotically become uniform.

For the case $a = 0$—i.e., cross-sectional perturbation $E_1 = kx^2$—the pressure perturbation directly behind the shock is given by

$$\bar{P}_2 = -(P_2 - P_0)E_1E_0^{-1}K_6$$

where

$$2(\gamma - 1 + 2M_0^{-2})^2(M_1^2 + M_1 + 2m)/(\gamma + 1)^2K_6 = M_1(1 + M_1)^2(1 + M_0^{-2}) + 4M_1^3 + 2mM_1^2(1 - M_0^{-2}) - M_1(\gamma - 1 + 2M_0^{-2})\gamma^{-1}\{4(1 - M_1^2)[(\gamma + 1)(1 - M_0^{-2})]^{-1} + m^2 - 2 + 2(\gamma - 1)/(\gamma - 1 + 2M_0^{-2})\} \quad (3)$$

K_6 is a monotonic decreasing function of shock strength, and for $\gamma = 7/5$, $0.5 \geqq K_6 > 0.361$.

Eq. (3) may be interpreted as a differential relation between shock strength and area, viz.,

$$-E^{-1}\frac{dE}{dz} = 1/(z - 1)K_6(z) = \frac{(3\gamma^3 + 5\gamma^2 + \gamma - 1)z^3 + (13\gamma^3 + 21\gamma^2 + 11\gamma + 3)z^2 + (13\gamma^3 + 7\gamma^2 - 9\gamma - 3)z + (3\gamma^3 - \gamma^2 - 3\gamma + 1)}{2(z - 1)(R_3z^2 + R_4z + R_5)[(\gamma - 1)z + \gamma + 1]} + \frac{2(\gamma - 1)\gamma^{-1}[(\gamma + 1)^2z^2 + 2(\gamma^2 - 1)z + (\gamma - 1)^2]}{(z - 1)(R_3z^2 + R_4z + R_5)} + \frac{2[(\gamma^2 - 1)\gamma^{-1}(z - 1)[(\gamma + 1)z + \gamma - 1]}{[(\gamma - 1)z + \gamma + 1](R_3z^2 + R_4z + R_5)}$$

with $R_3 = 3\gamma^2 + 4\gamma + 1$, $R_4 = 4\gamma^2 - 6\gamma - 2$, $R_5 = (\gamma + 1)^2$

Integration yields $Eg(z) =$ constant where

$$\exp\left\{\frac{\gamma^3 - 77\gamma^2 - 109\gamma - 31}{4R_3(z + 22\gamma - \gamma^2)^{1/2}}\tan^{-1}\frac{R_3z + R_4/2}{\gamma(7 + 22\gamma - \gamma^2)^{1/2}}\right\} g(z) = (z - 1)^2[(\gamma - 1)z + \gamma + 1]^{\frac{3 - \gamma}{4(\gamma - 1)}}[R_3z^2 + R_4z + R_5]^{\frac{(5 - 7\gamma)}{8(3\gamma - 1)}}$$

For the particular area variation under consideration, this relation gives an approximate description of the motion of the shock in terms of the cross-sectional area.

TABLE 1

z	c_0t_1/a	R_1	R_2
1	2	0	0
4	0.96390	1.0315	1.0702
8	0.62578	2.0870	3.3350
10	0.54758	2.5745	4.7016

TABLE 2

z	x
1	$2a$
4	$1.8216\,a + 0.14973\,ka^3/E_0$
8	$1.6557\,a + 0.13621\,ka^3/E_0$
∞	$1.4359\,a + 0.089090\,ka^3/E_0$

* This work was supported by a grant from the National Science Foundation.

REFERENCE

[1] Gundersen, Roy, *The Flow of a Compressible Fluid With Weak Entropy Changes*, J. Fluid Mech., Vol. 3, Part 6, pp. 553–581, March, 1958.

The Effect of Temperature on Pressures Measured in a Hypersonic Wind Tunnel*

Weston M. Howard
Aerodynamics Engineer, Boeing Airplane Company, Pilotless Aircraft Division, Seattle, Wash.
June 4, 1959

THERMAL CREEP, a gaseous flow phenomenon which occurs at the boundary of a surface and a gas at low pressure, can be of considerable importance in hypersonic testing. An important effect of thermal creep is the buildup of a pressure gradient along the length of a tube. Thus, appreciable error may result at high temperatures and low pressures when attempting to measure pressures on the surface of a hypersonic-wind-tunnel model, since the pressure-lead tubes are generally small and have an axial temperature gradient due to high model-surface temperatures.

Theory for regions of relatively large and small Knudsen Numbers (in the measuring tube) has been derived and is well established.[1-3] However, some doubt exists concerning the transition region where the Knudsen-Number range is approximately 0.1 to 10. For this transition region, a semi-empirical equation, based on experiments with hydrogen, was derived by Knudsen.[4, 5]

The three equations and their regions of applicability are given below.

$$dp/p = [3.8Kn^2/(1 + 4Kn)](dT/T), \quad Kn < 0.1 \qquad (1)$$

$$dp/p = (1/2)\{1 + [2.46\,(Kn + 3.15)/Kn\,(Kn + 24.6)]\}^{-2} \times (dT/T), \quad 0.1 \lesssim Kn \lesssim 10 \qquad (2)$$

$$dp/p = (1/2)(dT/T), \quad Kn > 10 \qquad (3)$$

where K_n = Knudsen Number, ratio of mean-free-path length to tube inside radius
p = pressure
T = temperature

* The work discussed in this paper was carried out at the Guggenheim Aeronautical Laboratory, California Institute of Technology, under the sponsorship and with the financial support of the Office, Chief of Ordnance.
The author wishes to express his appreciation to Dr. H. T. Nagamatsu for his guidance throughout this investigation.

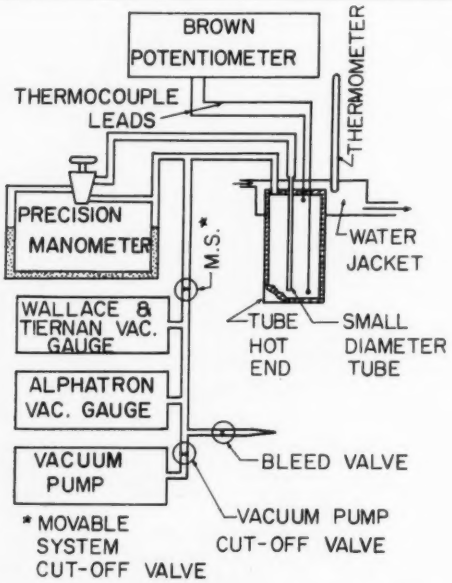

FIG. 1. Schematic diagram of pressure gradient test apparatus and instrumentation.

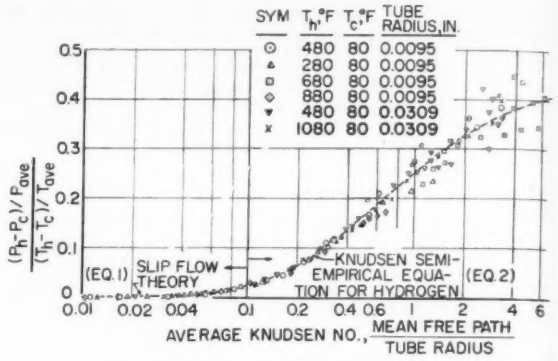

FIG. 2. Experimentally determined effect of thermal gradients on the pressure measured through circular tubes.

In order to check the theory for the range of Knudsen Numbers which might be encountered in hypersonic-wind-tunnel testing, an experimental program was planned and carried out. The test apparatus consisted of stainless-steel tubes of inside radius 1.3 in., 0.0095 in., and 0.0309 in. The tube lengths were about 11 in. Provisions were made for evacuating the tubes and for heating one end and cooling the other. The large tube served as a reference, since no appreciable pressure gradient would be built up for such a large-diameter tube. Therefore, the pressure drop for the small-diameter tubes could be found by comparing the small-tube cold-end pressure with the large-tube reference pressure. A schematic diagram of the apparatus and overall system is shown in Fig. 1.

The results are most clearly described by plotting the data in the form

$$[(p_h - p_c)/p_{ave.}]/[(T_h - T_c)/T_{ave.}]$$

vs. average Kn, as shown in Fig. 2 where

$( )_h$ refers to hot-end conditions
$( )_c$ refers to cold-end conditions
$( )_{ave.}$ refers to average conditions

As can be seen from the plot, the data fall reasonably close to the theoretical curves (except for point scatter at large values of Kn) even with the rather crude assumption that dp and dT can be represented by the large increments $p_h - p_c$ and $T_h - T_c$. The scatter increases rapidly with Kn due, of course, to the fact that the pressure differential is divided by the average pressure, which is very small for large Knudsen Numbers. Also, drift and outgassing are more detrimental at the low pressures. Therefore, correlation with theory is questionable for Kn greater than 2. However, it appears that the data would follow Knudsen's transition curve up to a somewhat larger Knudsen Number if more precise measurements were made.

Based on these results, it seems reasonable to assume that Eqs. (1) and (2) are sufficiently accurate for use in applying temperature corrections to pressure-test data. The corrections can then be made either by using the equations, or by reading the ordinate from Fig. 2 (after calculating the Knudsen Number). It should be noted that Kn is the average value in the tube; therefore, for the case of large corrections, several iterations should be made, each time using the new average value of Kn and $p_{ave.}$

REFERENCES

1 Kennard, E. H., *Kinetic Theory of Gases*, 1st Ed., pp. 327–333; McGraw-Hill Book Co., Inc., New York, 1938.
2 Loeb, L. B., *The Kinetic Theory of Gases*, 2nd Ed., pp. 353–364; McGraw-Hill Book Co., Inc., New York, 1934.
3 Kavanau, L. L., *Base Pressure Studies in Rarefied Supersonic Flows*, Institute of Engineering Research Technical Report No. HE-150-125, p. 57, University of California, November, 1954.
4 Knudsen, M., *Eine Revision der Gleichgewichtsbedingung der Gase. Thermische Molekularströmung*, Ann. d. Phys., Vol. 31, p. 205, 1910.
5 Knudsen, M., *Thermischer Molekulardruck in Rohren*, Ann. d. Phys., Vol. 83, p. 797, 1927.

Acoustical Instability of Jets and Wakes for Mach Numbers Above Two

Erik Mollö-Christensen
Associate Professor of Aeronautics and Astronautics, Massachusetts Institute of Technology, Cambridge, Mass.
July 8, 1959

RIBNER[1] AND MILES[2] have shown that a discrete interface between two moving media may be unstable to supersonic disturbances when the Mach Number difference between the two media exceeds two.

This note points out that for a planar ideal jet the acoustical instability will lead to sound emission at one frequency $f = aM/4h\sqrt{M^2 - 4}$ and with wave fronts making an angle with the upstream direction of $\sin^{-1}(2/M)$.

Instability of a Single Interface

Consider a planar interface between two streams moving in opposite directions with Mach Numbers M_1 and M_2, respectively, relative to the coordinate system (Fig. 1). A stationary disturbance as shown represents a pressure field of the form:

$$\left.\begin{aligned} y \geq 0;\ p_1(x, y) &= AF(x + \beta_1 y) = (1/\beta_1)\rho_1 a_1 M_1 v_1(x + \beta_1 y) \\ y < 0;\ p_2(x, y) &= BF(x + \beta_2 y) = (1/\beta_2)\rho_2 a_2 M_2 v_2(x + \beta_2 y) \end{aligned}\right\} \quad (1)$$

where a = velocity of sound, v = vertical velocity, ρ = density, $\beta_i = \sqrt{M_i^2 - 1}$; $i = 1,2$, and A and B are constants. The subscripts 1 and 2 refer, respectively, to the upper and lower medium.

The pressure-vertical velocity relation is that given by Ackeret (see reference 3) for small disturbances on a steady uniform supersonic flow where a linear approximation can be used and no viscosity is present.

The boundary conditions at the interface are:

$$p_1 = p_2 \text{ at } y = 0 \quad (2)$$
(zero pressure difference)

$$v_2/a_1 M_1 = v_2/a_2 M_2 \text{ at } y = 0 \quad (3)$$
(no difference in streamline slope)

Substituting Eq. (1) into Eqs. (2) and (3), one obtains:

$$-A + B = 0$$
$$(a_2^2\rho_2 M_2^2\beta_1/a_1^2\rho_1 M_1^2\beta_2)A - B = 0$$

The condition for a nontrivial solution for A and B is that the determinant of this set of equations vanishes, which yields:

$$a_2^2\rho_2 M_2^2\beta_1/a_1^2\rho_1 M_1^2\beta_2 = 1$$

Expressing M_2 in terms of M_1 and M, one can then solve for M_1 in terms of a_1, a_2, ρ_1, ρ_2 and M. For the special case of $a_2 = a_1$ and $\rho_2 = \rho_1$, one finds Solution 1: $M_1 = M_2 = M/2$, and two other solutions, of which one or both are real for $M > 2$. We will refer to these as Solutions 2 and 3. It is interesting to note that Solution 1 is valid to the second order in streamline slope, since the second-order correction is a function of Mach Number and streamline slope only, and thus is the same above and below the interface, M_1 being equal to M_2. Solutions 2 and 3 do not exist in the second-order approximation.

FIG. 1.

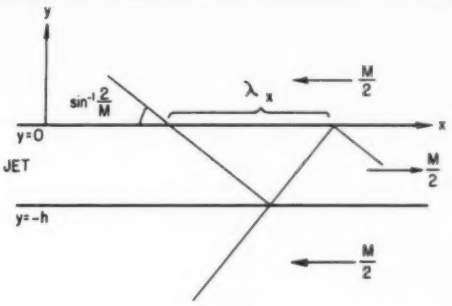

FIG. 2.

Using the second-order relation between vertical velocity v and pressure p, one obtains:[3]

$$p_1 = (\rho_1 a_1 M_1 v_1/\beta_1) + \left(\{[(\gamma + 1)M_1^4 - 4\beta_1^2]\rho_1 v_1^2\}/4\beta_1^4\right);\quad y \geq 0$$
$$p_2 = (\rho_2 a_2 M_2 v_2/\beta_2) + \left(\{[(\gamma + 1)M_2^4 - 4\beta_2^2]\rho_2 v_2^2\}/4\beta_2^4\right);\quad y < 0$$

Substituting this into the boundary conditions, one obtains for $\rho_1 = \rho_2$ and $a_1 = a_2$:

$$\left(\{4\beta_1^3 a_1 M_1 + [(\gamma + 1)M_1^4 - 4\beta_1^2]\, v_1(x)\}/4\beta_1^4\right) =$$
$$\left(\{(4\beta_2^3 a_2 M_2^3/M_1) + [(\gamma + 1)M_2^4 - 4\beta_2^2]M_2^2 v_1(x)/M_1^2\}/4\beta_2^4\right)$$

The only solution for M_1 and M_2 independent of v_1 is $M_1 = M_2$, which gives $v_1 = v_2$, which corresponds to the previous Solution 2. The previous Solutions 2 and 3 must, therefore, be limited to much smaller amplitudes than Solution 1, and the latter will dominate. The disturbance will thus be a planar wave limited in amplitude, due to effects of terms of third and higher orders in streamline slope.

It should also be remarked that these disturbances are only unstable for Mach Numbers between $M = 2$ and $M = 2\sqrt{2}$, as shown by Miles.[2] Above $M = 2\sqrt{2}$ they are neutrally stable, but the presence of another interface will cause disturbances to interact and become unstable also for $M \geq 2\sqrt{2}$. There being no length scale in the present arrangement, the wave length and wave form of the disturbances are arbitrary.

Next, introduce a length scale by considering a two-dimensional ideal jet between two interfaces at $y = 0$ and $y = -h$.

Instability of an Ideal Jet

On each of the interfaces, the disturbances considered above can exist. A disturbance of one layer will now impinge on the other layer and create a disturbance, which will be reflected. As shown in Ribner's paper,[1] this reflection will be infinitely strong. Nonlinear effects of third order in streamline slope will, however, limit the reflection to some finite amplitude, and a periodic disturbance pattern will be formed (Fig. 2).

The period in x will be λ_x:

$$\lambda_x = 4h\cot[\sin^{-1}(2/M)] = 2h\sqrt{M^2 - 4}$$

With respect to an observer at rest in the medium outside the jet, these waves will move in the x-direction with a velocity $aM/2$, and their fundamental frequency $\omega/2\pi$ is thus:

$$2\omega h/2\pi aM = 1/2\sqrt{M^2 - 4}$$

The angle θ between the wave-front normal and the downstream direction is

$$\theta = \cos^{-1}(2/M)$$

These waves will probably not be simply harmonic. The exact wave form will have to be determined using nonlinear theory, including terms of at least third order in streamline slope.

Application to Real Jets

In real jets, the shear layer has finite thickness. The analysis given above should be approximately valid when the shear-layer

thickness is small compared to the wave length of the disturbances—i.e., to the jet thickness h.

With the disturbances there will be associated Reynolds stresses in the shear layer; their net effect will be to exert a net shearing stress on the layer. The direction of this shearing stress can be found by considering the drag on the ripples in the interface caused by the traveling disturbances. On the outside faces of the jet, this drag acts opposite to the direction of flow in the jet; it thus will tend to slow down the jet.

References

[1] Ribner, H. S., *Reflection, Transmission, and Amplification of Sound by Moving Medium*, J. Acoust. Soc. Am., Vol. 29, No. 4, pp. 435–441, April, 1957.

[2] Miles, J. W., *On Reflection of Sound at Interface of Relative Motion*, J. Acoust. Soc. Am., Vol. 29, No. 2, pp. 226–227, February, 1957.

[3] Liepmann, H. W., and Roshko, A., *Elements of Gasdynamics*; John Wiley and Sons, New York, 1957.

[4] Powell, A., *On the Mechanism and Reduction of Choked Jet Noise*, ARC 15, 823, FM 1858, December, 1952.

Generalized Spectral Representation in Aeroelasticity

Arthur K. Cross

Norair Division, Northrop Corporation, Los Angeles, Calif.

June 4, 1959

ALTHOUGH a few fragmentary specialized results of the general technique treated in this note have appeared in the literature,[1] it is believed that the results of this general method are useful enough to justify the brief development and catalog of these results presented below.

This general technique, Generalized Spectral Representation, (abbreviated GSR hereafter) is a straightforward generalization of the so-called Spectral theorem[2] (sometimes referred to as the Schmidt-Hilbert theorem in integral-equation terminology). It will be shown that GSR permits the expansion of matrices associated with various physical systems. The analytical basis and applications (with particular reference to aeroelasticity) are discussed below.

Analytical Basis of GSR

Consider the $(n \times n)$ matrices G, E, F of rank m where

$$G = E^{-1}F,\ E^{+} \equiv (E^{*})^{t} = E,\ F^{+} \equiv (F^{*})^{t} = F \qquad (1)$$

(where the superscripts $*$, t, $+$ denote complex conjugation, transposition, and hermitian conjugation, respectively). Then, it is well known that m eigenvectors X_j exist which satisfy the following equations:

$$FX_j = \lambda_j EX_j, \quad 1 \leq j \leq m \leq n \qquad (2)$$

$$X_i^{+}FX_j = \lambda_j X_i^{+}EX_j = N_j\lambda_j\delta_{ij}, \quad 1 \leq j \leq m, 1 \leq i \leq m \qquad (3)$$

where, clearly, the hermiticity of E and F guarantee the reality of λ_j and N_j. Let the unit rank projection operators be denoted by P_j:

$$P_j \equiv X_jX_j^{+}E/N_j = X_jX_j^{+}F/\lambda_jN_j, \quad 1 \leq j \leq m \qquad (4)$$

Then, the following properties of the P_j's result from Eqs. (1) to (3):

$$P_iX_j = \delta_{ij}X_j, \quad P_iP_j = \delta_{ij}P_j \qquad (5)$$

$$G = \sum_{i=1}^{m} \lambda_iP_i, \quad T(G) = \sum_{i=1}^{m} T(\lambda_i)P_i \qquad (6)$$

(where the ordinary scalar power series $T(\lambda)$ exists). Hence,

$$\left.\begin{aligned} E^{-1} &= \sum_{i=1}^{m} \lambda_iX_iX_i^{+}/X_i^{+}FX_i \\ F^{-1} &= \sum_{i=1}^{m} \lambda_i^{-1}X_iX_i^{+}/X_i^{+}EX_i \end{aligned}\right\} \qquad (7)$$

Practical Applications of GSR in Aeroelasticity

So-called mass and stiffness matrices are often calculated in aeroelastic practice by means of matrices containing data supplied by tabulated functions or known problem geometry and diagonal matrices containing data based on statically determined elastic and inertial properties of the system under consideration. The latter matrices are pre- and post-multiplied by the former, and the resulting mass and stiffness matrices are used to determine modal frequencies and deflections. Conversely, Eqs. (7) provide a reverse process for determining, for instance, an EI or GJ distribution (or "effective distributions" for systems for which an elastic axis assumption is unrealistic) based on vibration data. Such information may be used to determine directly the compatibility of observed vibration data and statically determined stiffness data. An analogous but less practical procedure exists for inertial data. The rest of this note is concerned with two brief expositions of the first of these reverse processes and a discussion of other regions of application of GSR.

Although the following results hold quite generally, to fix ideas consider a case where the symbols C^{zz}, $C^{z\gamma}$, $C^{\gamma z}$, C^{pp} denote the $(m \times m)$ vertical, vertical-roll, roll-vertical, roll, and twist submatrices of a $(3m \times 3m)$ flexibility matrix C. Numerical integration of well-known formulas for the elements of these matrices provides a sequence of matrix operations by which the above matrix sequence may be obtained: $W_6U(EI)^{-1}W_1U^tW_6$, $W_7U(EI)^{-1}W_2V^tW_8$, $W_8V(EI)^{-1}W_2U^tW_7$, $V(EI)^{-1}W_3V^t$, $V(GJ)^{-1}W_4V^t$ (where the ij^{th} elements of U and V are, respectively, $(y_j - y_{j-1})\sum_{k=1}^{i}\delta_{kj}$ and $\sum_{k=1}^{i}\delta_{kj}$, y_i is the i^{th} wing station numbering from the zero station in the direction of positive y, and the W_i are weighting matrices). Furthermore, let h, h', and α denote the $(m \times 1)$ (bending, bending slope, and torsion) submatrices of the $(3m \times 1)$ matrix H. Then, if q_0 is the (3×1) matrix of zero station deflections, the following matrix formulation of the equations of motion (*in vacuo*) defines the $(3m \times 3)$ matrix L_0:

$$\underline{H} \equiv H - L_0q_0 = \omega^2C\underline{M}H \quad (\underline{M} = \text{mass matrix}) \qquad (8)$$

The system dynamic loads balance equations define the (3×3) and $(3 \times L)$ matrices L_1 and L_2:

$$L_1q_0 = -L_2T$$

$$T \equiv \left[\sum_{1}^{m} m_ih_i,\ \sum_{1}^{m} S_{\alpha i}\alpha_i,\ \sum_{1}^{m} I_{xi}h_i',\ \sum_{1}^{m} I_{xyi}\alpha_i, \text{ etc.}\right]^{t} \qquad (9)$$

(T, of course, is an $(L \times 1)$ matrix).

Finally, if the $(L \times 3m)$ matrix L_3 is constructed such that

$$L_3H = T \qquad (10)$$

and the matrices T and q_0 are eliminated between Eqs. (8)–(10), there results

$$\omega^{-2}H = KC\underline{M}H,\ K = I - L_0(L_1 + L_2L_3L_0)^{-1}L_2L_3 \qquad (11)$$

Then, according to Eqs. (2) and (7),

$$C = K^{-1}\sum_{i=1}^{3m} \omega_i^{-2}H_i\underline{H}_i^{t}/\underline{H}_i^{t}\underline{M}H_i \qquad (12)$$

The diagonal $(m \times m)$ matrices (EI) and (GJ) are then found by application of inverses of the known matrices U, U^t, V, V^t, W_i to appropriate submatrices of C. It is assumed above that the test modes H_i have been orthogonalized by one of the standard methods—e.g., the Kennedy-Pancu technique—and decoupled from the mount frequencies. If measured cantilever modes are used, $K = I$. The required orthogonality of the H_i and the $\underline{H}_i$ [see Eq. (12)] follows from Eq. (8).

A completely analogous procedure utilizing uniform beam modes is outlined below. First, let v_0 and v be $(3 \times m/2)$ and $(m/2 \times m/2)$ matrices of which the ij^{th} elements are, respectively, the i^{th} rigid free vertical deflection shape evaluated at station j and the i^{th} elastic free bending mode shape evaluated at station

j. Then, let $\underline{v}^t = [v^t_0, v^t, 0]$ and $\underline{n}^t = [n^t_0, 0, n^t]$ where $\underline{v}$ and $\underline{n}$ are $[(m+3) \times m/2]$ matrices and n_0 and n are $(3 \times m/2)$ and $(m/2 \times m/2)$ torsional counterparts of v and v_0.

Then, the generalized mass matrix B may be calculated as follows:

$$B = \underline{v}M\underline{v}^t + \underline{v}S_\alpha\underline{n}^t + \underline{n}S_\alpha\underline{v}^t - \underline{v}S_r\underline{v}'^t - \underline{v}'S_r\underline{v}^t + \underline{v}'I_x\underline{v}'^t + \underline{n}I_y\underline{n}^t - \underline{v}'I_{xy}\underline{n}^t - \underline{n}I_{xy}\underline{v}'^t \quad (13)$$

Then let P be the $(m \times m/2)$ matrix of which the ij^{th} element is the i^{th} free test mode shape at station j (the bending component thereof) with an analogous definition holding for the torsional component matrix Q which has the same dimensions. Furthermore, let Z^t, z^t, and Ω denote $m \times (m+3)$, $(m \times m)$ and $(m \times m)$ matrices, respectively, where

$$\left.\begin{aligned} Z^t &\equiv [-z^tB_{eo}B_{oo}^{-1}, z^t], \quad \Omega z^t\underline{B}_{ee} \equiv z^tA_{ee} \\ \Omega &\equiv [\delta_{ij}\omega^2_j], \quad (\underline{B}_{ee} \equiv B_{ee} - B_{eo}B^{-1}_{oo}B_{oe}) \end{aligned}\right\} \quad (14)$$

and

$$A_{ee} = \{\underline{v}''(EI)\underline{v}''^t + \underline{n}'(GJ)\underline{n}'^t\}_{ee} \quad (15)$$

The ee, oe, eo, oo subscripts represent $(m \times m)$, $(3 \times m)$, $(m \times 3)$, (3×3) submatrix indices, and, as usual, the primes denote span differentiation.

Since $$Z^tB = PM\underline{v}^t + PS_\alpha\underline{n}^t + QS_\alpha\underline{v}^t - P'S_r\underline{v}^t + \text{etc.} \quad (16)$$

B can be eliminated between Eqs. (13) and (16), and the resulting columns z_i of z used to determine A_{ee} in accord with Eqs. (7). Then, the diagonal matrices (EI) and (GJ) are calculated by applying inverses of the known v'', v''^t, n', n'^t to appropriate submatrices of A_{ee}.

The usefulness of Eq. (6) for sweeping procedures is obvious if it is noted that successive iterates of $G - \sum_1^k \lambda_i P_i$ converge to $\lambda_{k+1}X_{k+1}$. If G is the unit matrix, which has unity eigenvalues and arbitrary eigenvectors, $F = E$, and Eq. (7) provides a convenient expansion of E^{-1} in terms of any easily constructed set of X_i orthogonal with respect to E. In actual calculations, Eqs. (6) and (7) are most conveniently utilized after conversion into matrix product form.

It is interesting to note that although there are points of similarity and, in some special cases, coincidence of the operators P_i and the "normalized annihilator products" of Sylvester,[3] in general these operators differ. Indeed, the GSR of the single annihilator product (rank $= \sigma$ if $G \neq I$) corresponding to a spectral multiplicity of order σ is given by Eq. (6). In such a case, there exist infinitely many sets of σ P_j's corresponding to the fact that any of the infinity of sets of orthogonal Cartesian bases spanning the σ dimensional subspace (of the m dimensional configuration space associated with the metric tensor E) associated with the above spectral multiplicity forms principal axes of the quadric determined by F.

Simple arguments can be constructed from the latter circumstance which show that whereas close eigenvalues of G are relatively insensitive to small changes in G, its eigenvectors are sensitive in a manner that increases without bound as the roots coalesce. The failure to observe (during vibration test) theoretical mode shapes associated with two close frequencies should thus not be unexpected. The techniques described above can be used to determine the important component of error by comparing the modal contributions to the stiffness distributions based on vibration data with the modal contributions to the assumed distributions (calculated using theoretical modes).

References

[1] Bisplinghoff, R., Ashley, H., and Halfman, R., *Aeroelasticity*, pp. 95, 168; Addison Wesley Publishing Co., Inc., Cambridge, Mass., 1955.

[2] Riesz, F., and Sz.-Nagy, B., *Functional Analysis*, p. 272; Frederick Ungar Publishing Co., New York, 1955.

[3] Sylvester, J., *Mathematical Papers*, Vol. IV, p. 215; Cambridge University Press, Cambridge, England, 1904.

A Two-Cell Vortex Solution of the Navier-Stokes Equations*

Roger D. Sullivan

Aeronautical Research Associates of Princeton, Princeton, N.J.

June 26, 1959

BURGERS[1, 2] has discussed an exact solution of the Navier-Stokes equations for a three-dimensional vortex. In terms of a cylindrical coordinate system (r, θ, z) with the radial, tangential, and axial velocity components designated by u, v, and w, respectively, it can be written

$$u = -ar, \quad w = 2az, \quad v = (\Gamma/2\pi r)[1 - e^{-(ar^2/2\nu)}] \quad (1)$$

where a and Γ are constants (Γ being the circulation at infinity), and ν is the kinematic viscosity. Recently, Rott[3, 4] has considered the same solution in more detail, including an extension to the case of v varying with time, and determination of pressure and temperature distributions.

An analog to Burgers' solution with two cells has been found in the course of a study of a family of solutions in which u and v are functions of r only and w is a function of r multiplied by z. By "two cells" is meant that the flow does not simply spiral in toward the axis and out along it, as shown in Fig. 1(a), but has a region of reverse flow near the axis, as shown in Fig. 1(b). This solution is given by

$$u = -ar + 6(\nu/r)[1 - e^{-(ar^2/2\nu)}] \quad (2)$$

$$w = 2az\,[1 - 3e^{-(ar^2/2\nu)}] \quad (3)$$

$$v = (\Gamma/2\pi r)[H(ar^2/2\nu)/H(\infty)] \quad (4)$$

where H is defined by

$$H(x) = \int_0^x \exp\left\{-t + 3\int_0^t [(1 - e^{-\tau})/\tau]d\tau\right\} dt$$

The pressure for the two-cell case is

$$p = p_0 - (\rho/2)\{4a^2z^2 + a^2r^2 + 36(\nu^2/r^2) \times [1 - e^{-(ar^2/2\nu)}]^2\} + \rho\int_0^r (v^2/r)dr \quad (5)$$

where v is given by Eq. (4), while for the one-cell case it is

$$p = p_0 - (\rho/2)[4a^2z^2 + a^2r^2] + \rho\int_0^r (v^2/r)dr$$

with v given by Eq. (1). It is to be noted that for both cases the axial pressure gradient is

$$\partial p/\partial z = -4\rho a^2 z$$

* This research was supported by the USAF through the AFOSR of the ARDC, under Contract No. AF 49(638)-255. Reproduction in whole or in part is permitted for any purpose of the United States Government.

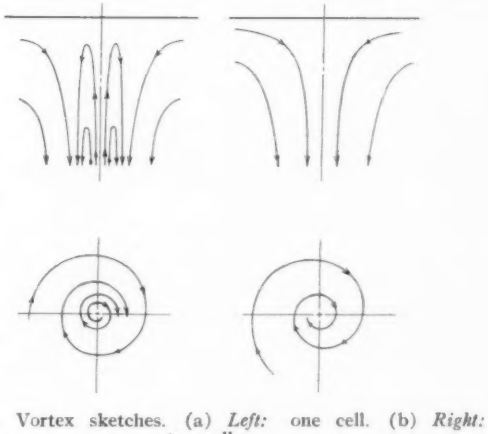

FIG. 1. Vortex sketches. (a) *Left:* one cell. (b) *Right:* two cells.

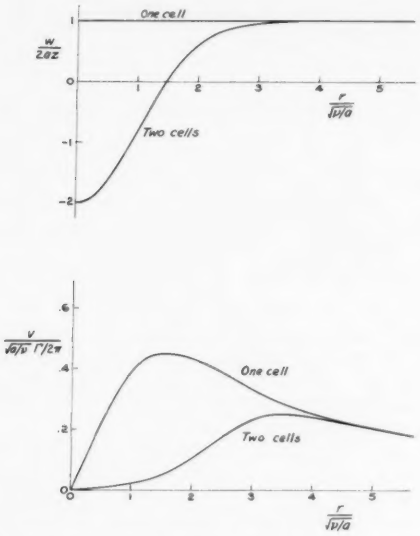

FIG. 2. Velocity distributions. (a) *Top*: axial velocity. (b) *Bottom*: tangential velocity.

and that Eqs. (2), (3), (4), and (5) all reduce, for large r, to the corresponding expressions for the one-cell case.

The distribution of w with r for the two cases is shown in Fig. 2(a), and that of v in Fig. 2(b). A marked reduction in the maximum value of v for the two-cell as compared with the one-cell case is evident, and there is a large region near the axis where v can be considered negligible in the two-cell case in comparison with the one-cell case.

Burgers calculated the dissipation, using only the terms in v, and found the result to be of the third order in velocities and independent of viscosity. The same is found to be true in the two-cell case.

REFERENCES

[1] Burgers, J. M., *Application of a Model System to Illustrate Some Points of the Statistical Theory of Free Turbulence*, Proc. Acad. Sci. Amsterdam, Vol. 43, No. 1, pp. 2–12, 1940.

[2] Burgers, J. M., *Advances in Applied Mechanics*, "A Mathematical Model Illustrating the Theory of Turbulence," Vol. 1, pp. 197–199; Academic Press, 1948.

[3] Rott, Nicholas, *On the Viscous Core of a Line Vortex*, ZAMP, Vol. 9b, No. 5/6, pp. 543–553, 1958.

[4] Rott, Nicholas, *On the Viscous Core of a Line Vortex II*, ZAMP, Vol. 10, No. 1, pp. 73–81, 1959.

Change of Address

It is important that the Institute be notified of changes in address 30 days in advance of publishing date to ensure receipt of every issue of the JOURNAL and AERO/SPACE ENGINEERING. Notices should be sent directly to:

Institute of the Aeronautical Sciences, Inc.
2 East 64th Street, New York 21, N.Y.

On the Accuracy of an Approximate Theory for the Ablation of Glassy Materials—A Reply

Hans A. Bethe and Mac C. Adams
Avco-Everett Research Laboratory, Everett, Mass.
June 24, 1959

IN A RECENT NOTE, Sutton[1] compared several approximate theories with his numerical results for the case of a glass which melts and flows without evaporation. He concluded: (1) our theory[2] predicts an ablation rate which is too large by as much as 25 per cent, and (2) this same theory will yield significant errors when calculating the amount of melt which vaporizes. These same conclusions were also quoted in a recent paper by Lees.[3] Unfortunately, Sutton's comparison was made incorrectly, and both conclusions are wrong.

To make the comparison, he chose a surface temperature of 4,000°F. and then calculated the heat-transfer and ablation rates for this given temperature. His results indicated that our theory led to ablation rates which were too large, by about 25 per cent. However, it should be noted the corresponding heat-transfer rates were also larger by about 35 per cent. He, therefore, compared ablation rates for two *different* heat-transfer rates, and the comparison is not meaningful.

The comparison should have been made for equal heat-transfer rates, since the heat-transfer rate and not the surface temperature is the boundary condition for a given flight situation. For equal heat-transfer rates, our approximate theory gives an ablation rate which is 2 per cent larger than given by Sutton's numerical results. The surface temperature is then 3,660°F. instead of 4,000°F. This agreement is even closer than should be expected, since the appendix[2] gives a second-order correction of 4 per cent for this particular glass. Clearly, we are discussing small numbers, and Sutton's numerical results check our theory quite adequately.

Now, regarding the second point, our theory becomes even more accurate for situations where some of the melt vaporizes. This is true for two reasons. First, the vapor pressure is a strong function of temperature, and there is a condition of compatibility between the vapor pressure and the gas boundary layer. As a consequence of these conditions, the surface temperature is fixed by the vapor pressure and not vice versa, as stated by Sutton. Second, the error, due to the approximation that the melt absorbs energy appropriate to the surface temperature ($\eta = 1$), becomes insignificant; with evaporation, this energy constitutes only a small fraction of the total energy absorbed.

We wish to call attention to a report[4] which compares our theory with quartz ablation experiments performed in an air arc wind tunnel. The experimental data scatter above and below the theory by less than 8 per cent.

REFERENCES

[1] Sutton, G. W., *A Comparison of Several Approximate Theories of Melting Ablation*, Journal of the Aero/Space Sciences, Vol. 26, No. 6, pp. 397–398, June, 1959.

[2] Bethe, Hans A., and Adams, Mac C., *A Theory for the Ablation of Glassy Materials*, Journal of the Aero/Space Sciences, Vol. 26, No. 6, pp. 321–328, June, 1959.

[3] Lees, L., *Similarity Parameters for Surface Melting of a Blunt Nosed Body in a High Velocity Gas Stream*, J. ARS, Vol. 29, No. 5, pp. 345–353, May, 1959.

[4] Adams, Mac C., Powers, W. E., and Georgiev, Steven, *An Experimental and Theoretical Study of Quartz Ablation at the Stagnation Point*, Avco-Everett Research Laboratory, Research Report 57, June, 1959.

REQUIREMENTS *for* CONTRIBUTIONS
to the publications of the
INSTITUTE *of the* AERONAUTICAL SCIENCES

The Institute of the Aeronautical Sciences invites both members and nonmembers from any country to submit papers for publication in the JOURNAL OF THE AERO/SPACE SCIENCES and AERO/SPACE ENGINEERING. The Institute, following the practice of other societies, does not pay for contributions.

The following directions for the preparation of papers, if followed by authors, will save correspondence, avoid the return of papers for changes, minimize the work of preparation for the printer, and save the expense due to the charges made for "author's corrections."

MANUSCRIPTS: The original typewritten copy of the paper is desired. **To expedite review, an additional copy of both the manuscript and figures should be submitted.** The manuscript must be double or triple spaced on one side of white paper sheets, consecutively numbered. There should be wide margins to allow for the marking of directions to the printer. Correcting, changing, or adding to papers after they are in type is costly. It is, therefore, imperative that papers submitted be in final form. Typographical errors may be corrected on proofs, but if authors wish to add material, they may do so at their own expense. In mailing, drawings may be rolled, but manuscripts should be sent flat. Send by first-class mail (register if you wish for your own protection) to the Editorial Office, Institute of the Aeronautical Sciences, 2 East 64th Street, New York 21, N.Y. All manuscripts will be examined by the Editorial Committee and by the Editor. Authors will be advised as promptly as possible whether the paper is acceptable for publication.

TITLES: The title of the paper should be brief. The name and initials of the author should be written as he prefers. The use of the full name of an author is advocated because of the frequent duplication of initials and surnames which sometimes makes it difficult to establish the identity of the author. This is particularly important for large annual indexing and abstracting services. All titles and degrees or honors are omitted. The name of the organization with which the author is associated should be placed after his name on a separate line. The date on which the paper is received will be inserted by the Editor. The author's title or position should be indicated in a footnote.

SUMMARIES OR ABSTRACTS: An abstract to be printed at the beginning should accompany each article. It should be adequate as an *index* and as a *summary*. It should contain a statement of major conclusions reached, since summaries in many cases constitute the only source of information used in compiling scientific reference indexes. Abstracts printed in other journals, especially foreign, in most cases consist of summaries from printed papers. The summary should explain as adequately as possible the major conclusions to a nonspecialist in the subject and should contain from 100 to 300 words, depending on the length of the paper.

SUBHEADINGS: Subheadings should be inserted by the author at frequent intervals. The work of editorial preparation will be simplified by the author's provision of many subheadings.

MATTER USUALLY DELETED: Photographs or illustrations of little technical interest and not showing advances in general practice. Too detailed tabular matter (general results of such tables may be included in the text). Lengthy descriptions of materials or processes or of preliminary experiments of theories that preceded final results; salient features only are of interest.

REFERENCES: References should be numbered consecutively and grouped together at the end of the manuscript, with only the corresponding number being mentioned in the text. The arrangement should be as follows. For books: [1]Durand, W. F., *Aerodynamic Theory*, 1st Ed., Vol. 1, p. 23; Julius Springer, Berlin, 1934. For magazines: [1]England, C. R., Crawford, A. B., and Mumford, W. W., *Some Results of a Study of Ultra-Short-Wave Transmission Phenomenon*, Proc. IRE, Vol. 20, No. 12, pp. 481–482, March, 1933. Please give author, title, edition, volume, number, page, publisher, and place and date of publication as indicated. Omission of one required fact causes much extra editorial work and possible inaccuracies.

ILLUSTRATIONS: Illustrations should accompany manuscripts, and each should always be referred to in the text by number. Drawings or graphs should not be larger than 12 × 16 inches, and must be made with jet black India ink on white paper or tracing cloth, the latter being preferred. *Do not use typewriter for lettering.* The smallest lettering on 8 × 10 inch figures should be no less than $^1/_4$ inch high. Cross-section paper (white with black lines) may be used, but it should not have more than 4 lines per inch. If finer ruled paper is used, the major division lines should be drawn in with black ink, omitting the finer divisions. In the case of finely ruled paper, only blue-lined paper can be accepted. *Tracing paper and blueprints* are not acceptable. Lettering and all markings must be large enough to be readable after reduction to single-column width ($3^1/_{16}$ in.). Mail rolled or flat; never fold. Drawings that cannot be reproduced (including pencil drawings) will be returned to the author for redrawing, thus delaying publication of the paper. Photographs should be distinct and show clear black and white contrasts. They must be on glossy white paper. Avoid round or oval photographs.

CAPTIONS AND LEGENDS: Legends or captions must accompany each drawing or photograph submitted. If written on the drawing or photograph, they should be placed below and well outside the part to be reproduced. Each table should have a caption such as Table 1, Table 2, Table 3, etc. Captions should be complete in themselves so as to make the data intelligible to the reader without reference to the text. A duplicate list of captions for figures should be included as the last page of the manuscript. Use "Fig. 1" (not Figure 1), "Figs. 3 and 4," etc., in both the text and the numbering of illustrations. In the text, "Eq. (1)" or "Eqs. (1) and (2)" is used, not "Equation (1)." In captions, legends, and in table headings, write all words in full; do not abbreviate, except for "Fig." and "Eq."

MATHEMATICAL WORK: Formulas may be typewritten or carefully written in pen and ink, the writing to be large enough so that it can be marked for the printer. Considerable space for marking should be allowed above and below all equations. All complicated equations should be repeated on separate sheets with plenty of space left for marking. The solidus should be used for simple fractions appearing within the text. Make all expressions clear to the typesetter. Greek letters used in formulas should be clearly designated by name in the margin of the manuscript. The difference between capital and lower-case letters should be clearly distinguished and care taken to avoid confusion between zero (0) and the letter (o), between the numeral (one), and the letter (ell) and the prime (′), between alpha and a, kappa and k, u and mu, v and nu, n and eta. All subscripts and exponents should be clearly distinguished. Avoid complicated exponents and subscripts. Dots and bars over letters or mathematical expressions should also be avoided. When it is necessary to repeat a complicated expression, it should be represented by some convenient symbol.

SYMBOLS AND ABBREVIATIONS: The symbols recommended in the American Standard Association "Letter Symbols for Aeronautical Sciences," ASA Y10.7—1954, should be used wherever practicable All symbols should be clearly written and carefully checked Standard abbreviations should be used, and it should be noted that most abbreviations are lower case, such as m.p.h., b.m.e.p., i.h.p., b.hp., hp., etc.

CORPORATE MEMBERS

OF THE

INSTITUTE OF THE AERONAUTICAL SCIENCES

AC SPARK PLUG DIVISION, GENERAL MOTORS CORPORATION

ACADEMY OF AERONAUTICS

ADAMS RITE MANUFACTURING COMPANY

AEROJET-GENERAL CORPORATION

AEROLAB DEVELOPMENT COMPANY

AERONCA MANUFACTURING CORPORATION

AERONUTRONIC SYSTEMS, INC.

AEROQUIP CORPORATION

AGAWAM AIRCRAFT PRODUCTS, INC.

ALLIED RESEARCH ASSOCIATES, INC.

ALLISON DIVISION, GENERAL MOTORS CORPORATION

ALUMINUM COMPANY OF AMERICA

AMERICAN AIRLINES, INC.

AMERICAN BOSCH ARMA CORPORATION

AMERICAN STEEL & WIRE DIVISION, UNITED STATES STEEL CORPORATION

AMOCO CHEMICALS CORPORATION

AMPHENOL-BORG ELECTRONICS CORPORATION

ANDERSON, GREENWOOD & CO.

ARDE ASSOCIATES

ASSOCIATED AVIATION UNDERWRITERS

AVCO RESEARCH LABORATORY

AVIEN, INC.

AVRO AIRCRAFT LIMITED

BAKER STEEL & TUBE COMPANY

BEECH AIRCRAFT CORPORATION

BELL AIRCRAFT CORPORATION

BENDIX AVIATION CORPORATION

BOEING AIRPLANE COMPANY

BOOZ, ALLEN & HAMILTON

THE BRISTOL AEROPLANE COMPANY (U.S.A.) INC.

BULOVA RESEARCH AND DEVELOPMENT LABORATORIES, INC.

CANADAIR, LTD.

THE CESSNA AIRCRAFT COMPANY

CHANCE VOUGHT AIRCRAFT, INCORPORATED

THE CHASE MANHATTAN BANK

CHICAGO AERIAL INDUSTRIES, INC.

THE CLEVELAND PNEUMATIC INDUSTRIES, INC.

CONSOLIDATED CONTROLS CORPORATION

CONTINENTAL MOTORS CORPORATION

CORNELL AERONAUTICAL LABORATORY, INC.

CURTISS-WRIGHT CORPORATION

DANIEL, MANN, JOHNSON, & MENDENHALL

DAYSTROM, INC.
DAYSTROM-WESTON SALES DIVISION

THE DECKER CORPORATION

DEL MAR ENGINEERING LABORATORIES

DELCO-REMY DIVISION, GENERAL MOTORS CORPORATION

DOAK AIRCRAFT COMPANY, INC.

DOUGLAS AIRCRAFT COMPANY, INC.

DZUS FASTENER COMPANY, INC.

EASTERN AIR LINES, INC.

EATON MANUFACTURING COMPANY

EDO CORPORATION

ELASTIC STOP NUT CORPORATION OF AMERICA

ELECTROL INCORPORATED

ENGINEERING SUPERVISION COMPANY

ESSO STANDARD OIL COMPANY

FAIRCHILD CAMERA AND INSTRUMENT CORPORATION

FAIRCHILD ENGINE AND AIRPLANE CORPORATION

THE FIRESTONE TIRE & RUBBER COMPANY

THE GARRETT CORPORATION

GENERAL APPLIED SCIENCE LABORATORIES, INC.

GENERAL DYNAMICS CORPORATION

GENERAL ELECTRIC COMPANY

GENERAL PRECISION EQUIPMENT CORPORATION

G. M. GIANNINI & CO., INC.

GIANNINI PLASMADYNE CORPORATION

THE B. F. GOODRICH COMPANY

GOODYEAR AIRCRAFT CORPORATION

GRUMMAN AIRCRAFT ENGINEERING CORPORATION

HYDRO-AIRE CO.

INSURANCE COMPANY OF NORTH AMERICA COMPANIES

INTERNATIONAL BUSINESS MACHINES CORPORATION

THE INTERNATIONAL NICKEL COMPANY, INC.

ITT LABORATORIES, DIVISION OF INTERNATIONAL TELEPHONE AND TELEGRAPH CORPORATION

JANITROL AIRCRAFT DIVISION, SURFACE COMBUSTION CORPORATION

JOHNS-MANVILLE SALES CORPORATION

EARLE M. JORGENSEN CO.

WALTER KIDDE & COMPANY, INC.

KOLLSMAN INSTRUMENT CORPORATION

LAVELLE AIRCRAFT CORPORATION

LEAR, INCORPORATED

C. W. LEMMERMAN, INC.

LIBRASCOPE, INCORPORATED

THE LIQUIDOMETER CORPORATION

LOCKHEED AIRCRAFT CORPORATION

LOEWY-HYDROPRESS DIVISION OF BALDWIN-LIMA-HAMILTON CORPORATION

LONGINES-WITTNAUER WATCH COMPANY, INC

THE MARQUARDT CORPORATION

THE MARTIN COMPANY

MARTIN STEEL PRODUCTS CORPORATION

McDONNELL AIRCRAFT CORPORATION

MELETRON CORPORATION

MID-CONTINENT MANUFACTURING, INC.

MINNEAPOLIS-HONEYWELL REGULATOR COMPANY

NATIONAL CREDIT OFFICE, INC.

NORTH AMERICAN AVIATION, INC.

NORTHROP CORPORATION

NUCLEAR DEVELOPMENT CORPORATION OF AMERICA

PAN AMERICAN WORLD AIRWAYS, INC.

THE RALPH M. PARSONS COMPANY

PESCO PRODUCTS DIVISION, BORG-WARNER CORPORATION

PHILLIPS PETROLEUM COMPANY

PIASECKI AIRCRAFT CORPORATION

RADIO CORPORATION OF AMERICA
ASTRO-ELECTRONIC PRODUCTS DIVISION
DEFENSE ELECTRONIC PRODUCTS

REPUBLIC AVIATION CORPORATION

ROHR AIRCRAFT CORPORATION

PAUL ROSENBERG ASSOCIATES

RYAN AERONAUTICAL COMPANY

SANDBERG-SERRELL CORPORATION

SHAFER BEARING DIVISION, CHAIN BELT COMPANY

SHELL OIL COMPANY

SIMMONDS AEROCESSORIES, INC.

SOCONY MOBIL OIL COMPANY, INC.

SOLAR AIRCRAFT COMPANY

SOUTHWEST PRODUCTS CO.

SPACE TECHNOLOGY LABORATORIES, INC.

R. DIXON SPEAS ASSOCIATES

SPERRY GYROSCOPE COMPANY DIVISION OF SPERRY RAND CORPORATION

STANDARD OIL COMPANY OF CALIFORNIA

STANDARD OIL COMPANY (INDIANA)

STANDARD-THOMSON CORPORATION
CLIFFORD MANUFACTURING DIVISION

STANLEY AVIATION CORPORATION

THIOKOL CHEMICAL CORPORATION

THOMPSON RAMO WOOLDRIDGE INC.

TRANS WORLD AIRLINES, INC.

TURBO PRODUCTS, INC.

UNION CARBIDE CORPORATION

UNITED AIR LINES, INC.

UNITED AIRCRAFT CORPORATION

UNITED STATES AVIATION UNDERWRITERS, INC.

VARD, INC.

VERTOL AIRCRAFT CORPORATION

VITRO CORPORATION OF AMERICA

WESTERN GEAR CORPORATION

WESTINGHOUSE ELECTRIC CORPORATION

WYMAN-GORDON COMPANY

YOUNG RADIATOR COMPANY

ME

LIBRARY

JOURNAL OF THE

AERO/SPACE SCIENCES

VOLUME 26 DECEMBER, 1959 NUMBER 12

PURDUE UNIVERSITY
DEC 7 1959
LIBRARY

CONTENTS

An Appreciation ..... THE EDITORS 769

Space Vehicle Environment ..... CARL GAZLEY, JR., W. W. KELLOGG, AND E. H. VESTINE 770

Photothermoelastic Investigation of Transient Thermal Stresses in a Multiweb Wing Structure ..... GEORGE GERARD AND HERBERT TRAMPOSCH 783

A Linear Perturbation Method for Stability and Flutter Calculations on Hypersonic Bodies ..... MAURICE HOLT 787

An Investigation of Optimal Zoom Climb Techniques ..... HENRY J. KELLEY 794

Thermal Buckling of Circular Cylindrical Shells Under Circumferential Temperature Gradients ..... DAVID ABIR AND S. V. NARDO 803

Heat Transfer to Separated and Reattached Subsonic Turbulent Flows Obtained Downstream of a Surface Step ..... R. A. SEBAN, A. EMERY, AND A. LEVY 809

Viscous Hypersonic Similitude ..... WALLACE D. HAYES AND RONALD F. PROBSTEIN 815

Buckling of a Cylindrical Shell Under a Circumferential Band Load ..... D. O. BRUSH AND F. A. FIELD 825

Readers' Forum 831

Index to Volume 26 853

Published by
INSTITUTE OF THE AERONAUTICAL SCIENCES, INC.